Innovative Observational Global and Regional Ocean Water Mass, Circulation, and Mixing Analyses

Paige D. Lavin

A dissertation

submitted in partial fulfillment of the

requirements for the degree of

Doctor of Philosophy

University of Washington

2021

Reading Committee:

Gregory C. Johnson, Chair

Stephen C. Riser

Susan L. Hautala

Program Authorized to Offer Degree:

School of Oceanography

University of Washington

Abstract

Innovative Observational Global and Regional Ocean Water Mass, Circulation, and Mixing Analyses

Paige D. Lavin

Chair of the Supervisory Committee:
Dr. Gregory C. Johnson
School of Oceanography

This dissertation applies novel methodology to existing oceanographic datasets in order to gain new insights into the circulation and mixing of water masses at both regional and global scales. Given the boom of in-situ data from programs such as Argo over the last two decades, in addition to the rising prevalence and accessibility of novel methods such as machine learning, we hope to build on the foundational understanding of these processes obtained from analyses of previous, sparser datasets. We investigate the water mass properties, circulation, and inferred near-bottom mixing of the ocean from a mean state perspective. This allows us to use as many observations as possible in our analyses of these important features of the ocean and to get at the "baseline" behavior of the ocean.

The first portion of this dissertation focuses on using conductivity-temperature-depth (CTD) and velocity measurements from Argo floats to assess the mean transport of the Alaskan Stream (AS). This current is a western boundary current at the north edge of the North Pacific subpolar gyre that flows west-southwestward along the south side of Alaska and the Aleutian Island Arc to strongly influence physical and biological processes downstream in the Sea of Okhotsk and the Bering Sea. Since the start of the Argo program, a sufficient number of Argo floats have sampled the AS such that we are now able to quantify the zonal evolution of this current by mapping Argo data to across-current transects at a number of locations along the current's extent. Alongshore absolute geostrophic transports in the top 2000 dbar (obtained by combining mean absolute 1000-dbar velocities from float displacements with the geostrophic velocity fields) were found to generally increase to the west. Full-depth transports are estimated by fitting a barotropic and the first two baroclinic modes calculated from a climatology to the absolute geostrophic velocities in the upper 2000 dbar and applying the velocities from these fits from 2000 dbar to the seafloor. As it flows west from its formation region the full-depth AS becomes stronger, more barotropic, and narrower. Mean concentrations of the relatively warm, salty, oxygen-poor, and nutrient-rich Pacific Equatorial Water in the AS decrease westward as more water is entrained from the offshore gyre. This work introduces a number of new methods for using Argo data to analyze the volume transports and water mass structure of a boundary current.

In the second part of this dissertation, we developed a new global bottom water climatology using a novel machine learning-based method that we hope can be applied to other sparse oceanographic datasets in the future. The most recent global synthesis of mean bottom water properties relied on expert hand-contouring to create maps from sparse shipboard measurements. Here we created a new bottom water climatology by using random forest regression followed by

objective mapping to map the sparsely sampled quantities of temperature, salinity, oxygen, silicate, nitrate, and phosphate to a 0.5-degree grid based on smoothed ETOPO-2 bathymetry. We applied the regressions in an iterative manner, using the new maps of the better sampled fields (e.g., temperature) to help improve the prediction of the more sparsely sampled fields (e.g., silicate), an approach we have named the "stacked" random forest and objective mapping method. Using these maps, we are able to trace the flow of North Atlantic Deep Water and Antarctic Bottom Water globally from their source regions, through several topographic choke points such as various sills and fracture zones, and along the rest of the seafloor. The new, high-quality oxygen and nutrient maps produced here illustrate the influence of a variety of regional biogeochemical processes on the bottom water property distributions, which have been difficult to resolve in previous, coarser-resolution global analyses of the bottom waters. Lastly, we performed a global census of the bottom waters in temperature-salinity and oxygen-salinity space to improve our understanding of how different water masses mix and are affected by biogeochemical processes along the seafloor.

The final set of analyses included here aims to provide a description of different dynamical bottom mixed layer (BML) regimes found throughout the North Atlantic Ocean. We have adapted a quantitative approach from the surface mixed layer literature for identifying BMLs in high-resolution CTD profiles known as the split-and-merge method. This method automatically identifies not only the BML but also the important overlying layer known as the stratified mixing layer (SML) in these profiles. Under certain conditions, weakly-stratified BMLs over sloped topography may act as conduits for diapycnal upwelling of bottom waters, an important mechanism for closing the global meridional overturning circulation. We performed k-means clustering on the thickness and mean stratification values for the identified BMLs and SMLs along with information about the underlying bathymetry (e.g., slope and roughness) to

identify dynamically similar BMLs in our dataset that may play a role in the diapycnal upwelling of bottom waters.

TABLE OF CONTENTS

LIST OF FIGURES

LIST OF TABLES

ACKNOWLEDGEMENTS

This work would not have been possible without the guidance, mentoring, and friendship of my advisor Gregory Johnson. He has helped me to become a better scientist in a million little ways: from always ensuring we use the highest-quality data for our analyses, to improving my scientific writing, to allowing me to pursue my interests in machine learning and climate policy, and so much more. I will forever be grateful for his continual support and encouragement over my graduate career.

I would also like to extend my sincere gratitude to my committee: Stephen Riser, Mark Warner, Susan Hautala, and Cecilia Bitz. The diversity of perspectives they brought to my projects during my time at UW enriched my science in more ways than they can know and I thoroughly enjoyed getting the opportunity to interact with them all throughout graduate school. Though she was not technically on my committee, I would like to thank LuAnne Thompson for being my greatest source of support and guidance when I was on campus. Not only did she serve as my fellowship sponsor, but she also adopted me into her lab group and always checked in on me when I was in my UW office.

Over the years I was extremely fortunate to be a part of a number of wonderful scientific and professional communities, each of which provided exactly the support I needed at different times. I would like to thank my colleagues in the School of Oceanography, Atmospheric Sciences, the PCC, SWMS, MPOWIR, and at PMEL for being such a meaningful part of my graduate career.

Lastly, the personal support of my family, especially my husband and my parents, was absolutely instrumental in getting me through the rollercoaster of graduate school and I could not have done it without them.

DEDICATION

To my parents, Mark and Kathy, for helping me fall in love with the ocean at a young age and instilling the confidence in me to achieve my dreams.

Chapter 1. INTRODUCTION

Over the past few decades our physical and biogeochemical sampling of the subsurface ocean has grown substantially, enabling us to not only improve our understanding of key processes in the ocean but to also monitor changes in this important part of the climate system (e.g., Roemmich, Alford, et al., 2019; Talley et al., 2016). In this dissertation, we use a mixture of data from autonomous and shipboard observing platforms to gain insights into the mean state of a number of important circulation, water mass, and mixing regimes in the ocean at both regional and global scales.

The Alaskan Stream is an integral part of the circulation in the North Pacific, acting as a western boundary current at the northern boundary of the subpolar gyre. The intense flow of this current begins near Kodiak Island and then continues westward along the Aleutian Island Arc until it bifurcates near the dateline with a portion turning northward into the Bering Sea while the rest continues westward to join the Kamchatka Current. Downstream in the Sea of Okhotsk and the Bering Sea the relative warm and salty waters of the Alaskan Stream can impact the ecosystems, sea ice cover, and sea level of these basins.

Many previous studies quantified the volume transports of the Alaskan Stream at various locations along its extent by analyzing hydrographic, mooring, current meter, and satellite altimeter data. In Chapter 2 of this dissertation, we compute absolute geostrophic volume transports for the upper 2000 dbar at 5° longitude intervals along this current from 140°W to 175°W by combining shipboard- and Argo-based conductivity-temperature-depth (CTD) measurements with deep velocity data from the Argo floats and using a novel approach to map these data to across-current transects. Additionally, we estimate the below-2000 dbar transports at

these locations by fitting a barotropic and the first two baroclinic modes calculated from a climatology to the absolute geostrophic velocities in the upper 2000 dbar and then applying the velocities from these fits from 2000 dbar to the seafloor. We also evaluated the concentration of the nutrient-rich Pacific Equatorial Water over the extent of the current.

The deep ocean is the most sparsely sampled part of the ocean (de Lavergne, Madec, Capet, et al., 2016), making detailed, global analyses of this region difficult. However, recent work (e.g., Berg et al., 2019; Giglio et al., 2018) has shown that machine learning methods can help us to extract new insights from sparse oceanographic datasets that were not possible, or just much more difficult, to infer using more classical methods. Since the deep ocean plays a role in the storage of excess heat and carbon from climate change, we focus on using machine learning methods to advance our understanding of both the lateral motion of the waters in this depth range as they spread from sites of bottom water formation and of the variability in near-bottom stratification, which may influence how these waters upwell diapycnally to mid-depths and then along isopycnals to the surface (e.g., Ferrari et al., 2016; Marshall & Speer, 2012). These are both critically important pieces of the meridional overturning circulation.

The most recent detailed, global analysis of bottom waters was performed by Mantyla & Reid (1983) who expertly hand-contoured maps of density, temperature, salinity, oxygen, and silicate to infer pathways of along-bottom circulation. In Chapter 3 of this dissertation, we produce updated maps of density, temperature, salinity, oxygen, silicate, phosphate, and nitrate by combining the dataset used by Mantyla & Reid (1983) with the greatly increased number of shipboard observations made since that time. Furthermore, instead of hand-contouring these data we develop a new machine learning-based method that we named the “stacked” random forest and objective mapping approach that quantitatively takes advantage of high-resolution bathymetric

data and relations among various water properties to perform the mapping. These new maps enable us to describe the spreading pathways of the newly-formed Antarctic Bottom Water (AABW) and North Atlantic Deep Water (NADW) in greater detail and to examine locations where regional physical and biogeochemical processes may have a substantial influence on the bottom water property distributions.

To help to address the question of where these bottom waters upwell across diapycnals to begin their return journey to the surface, in Chapter 4 we use shipboard CTD data to study bottom mixed layers in the North Atlantic. Recent modeling and theoretical studies (e.g., Ferrari et al., 2016; de Lavergne, Madec, Le Sommer, et al., 2016; McDougall et al., 2017) have suggested that these layers, when present over sloped topography, may be the site of substantial upward diapycnal transport of bottom waters. We modify the split-and-merge method from the surfaced mixed layer literature (Thomson & Fine, 2003) to automatically identify the bottom mixed layer and overlying stratified mixing layer in CTD profiles. Information about the thickness and stratification of these layers is combined with information about the underlying bathymetry in an unsupervised clustering method from machine learning known as k-means clustering in order to identify dynamical regimes of interest in these potentially important layers. Lastly, Chapter 5 summarizes the results of Chapters 2, 3, and 4 and discusses avenues for further research.

Chapter 2. ZONAL EVOLUTION OF ALASKAN STREAM STRUCTURE AND TRANSPORT QUANTIFIED WITH ARGO DATA

(A version of this chapter was published by the Journal of Geophysical Research: Oceans. Copyright (2016), American Geophysical Union: Logan, P. D., & Johnson, G. C. (2017). Zonal evolution of Alaskan Stream structure and transport quantified with Argo data. *Journal of Geophysical Research: Oceans, 122*(2), 821–833. https://doi.org/10.1002/2016JC012302)

2.1 INTRODUCTION

The Alaskan Stream (AS) is a narrow (~50 km), fast (surface velocities > 60 cm s^{-1}), deep (>3000 m) current that makes up the northern limb of the north Pacific subpolar gyre (Favorite, 1967; Stabeno and Reed, 1991). The eastern boundary current of this gyre is the Alaska Current. Near Kodiak Island, the Alaska Current turns southwestward and intensifies, transforming into the AS, which flows approximately to 180° longitude along the shelf break. From Kodiak Island to around 180°, the AS is a western boundary current, supported by the Aleutian Island Arc. However, west of 180° the Aleutian Island Arc turns up to the northwest. When the orientation of this boundary changes, the AS splits, with part of its flow turning northward into the Bering Sea and the rest of its flow continuing westward as a free jet to join the Kamchatka Current.

The Aleutian Arc contains a number of passes that connect the AS to the Bering Sea. Most of these passes east of 180° are fairly shallow with northward volume transports typically <1 Sv (1 Sv = 10^6 m^3 s^{-1}) (Stabeno et al., 2005). However, there are two deeper (>400 m) passes closer to 180°: Amukta (172°W) and Amchitka (180°), which see transports into the Bering Sea of ~4.5 Sv (Stabeno et al., 2005; Ladd and Stabeno, 2009) and ~3 Sv, respectively (Stabeno and Reed,

1992; Reed and Stabeno, 1993). On average, the total transport through these passes into the Bering Sea is <10 Sv (Stabeno et al., 2005). The majority of this flow joins the northeastward flowing Aleutian North Slope Current. These flows through the Aleutian passes are important because the AS contains near-surface waters that are relatively warm and fresh compared to those offshore (in the gyre interior). These warm, fresh waters can affect Bering Sea ecosystems and sea level (Reed and Stabeno, 1994; Mordy et al., 2005; Ladd and Stabeno, 2009; Ezer and Oey, 2010). Furthermore, the AS carries this anomalous water into the Kamchatka Current and eventually the Sea of Okhotsk. Interannual variations in the volume transport of the AS have been shown to affect the amount of AS water that reaches the Sea of Okhotsk. This variability leads to changes in nutrients, fish stocks, sea ice cover, and dense shelf water formation in this marginal sea (Uehara et al., 2014; Prants et al., 2015).

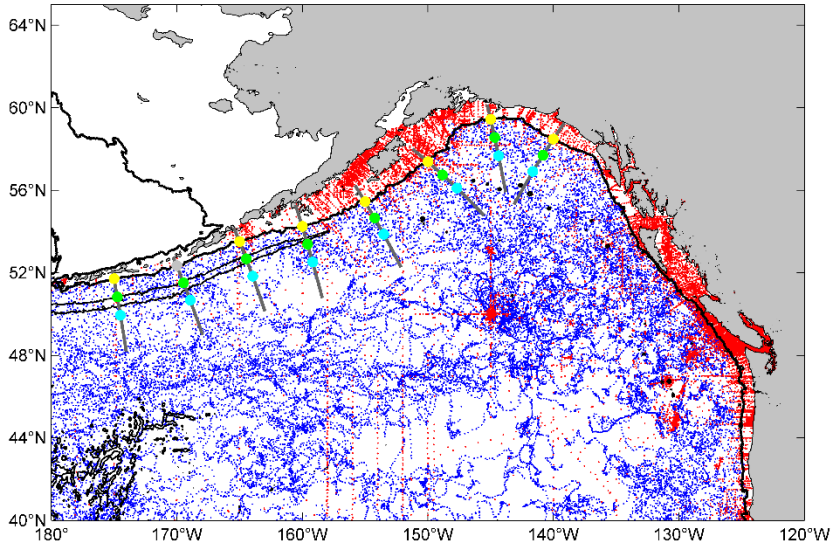

Figure 2.1. Locations of Argo (blue dots) and WOD13 (red dots) CTD profiles used in the analysis with 1000-m (thick black contours) and 6000-m (thin black contours) isobaths. Locations of the eight-mapped sections (thick gray lines) are shown to 400 km offshore with the 1000-m isobath (yellow circles), 100 km (green circles), and 200 km (cyan circles) offshore distances indicated.

Numerous efforts have been made to quantify volume transports of the AS using hydrographic, mooring, current meter, and satellite altimeter data. An early comprehensive study of the structure of the AS and its volume transport estimated its geostrophic transport referenced to 1000 db to be ~6 Sv between 165°W and 175°E based on hydrographic data (Favorite, 1967). Conductivity-temperature-depth (CTD) instrument casts down to 3000 db taken at a number of locations from 149°W to 180° in 1981 were used to estimate geostrophic transports referenced to 3000 db. These calculations suggested that the AS strengthens westward with transports growing from ~15 Sv at 149°W to ~21 Sv at 180° (Reed, 1984). However, this work likely underestimated the total AS volume transport between 160°W and 180° since the casts only went down to 3000 db and thereby did not include the component of AS transport in the nearshore, deep (>3000 dbar) Aleutian Trench (Figure 2.1) within this longitude range. Further work to investigate the deep structure of the AS in 1981 using current meter and CTD data provided an estimate of 28 Sv for its full-depth transport at 175°W (Warren and Owens, 1988). Over the next two decades several new estimates of the AS's full-depth volume transport were made using hydrographic, ADCP, and mooring data, ranging from 8 Sv to 39 Sv (Roden, 1995; Onishi and Ohtani, 1999; Reed and Stabeno, 1999; Chen and Firing, 2006). Recently, estimates were made using moorings at ~169°W, yielding mean transports of 19 Sv for 2001–2002 and 21 Sv for 2003–2004 (Stabeno and Hristova, 2014). All of these previous transport estimates used data that were somewhat limited in their spatial and temporal extent, something we improve upon in the present study by using several years of Argo float profile and deep velocity data over a wide range of longitudes.

Analyzing the mean behavior of the AS is further complicated by the presence of long-lived mesoscale eddies in the Gulf of Alaska. These eddies have been identified in both in-situ and satellite altimeter data (Musgrave et al., 1992; Crawford et al., 2000). Anticyclonic eddies tend to

dominate the eddy field within the AS and typically form near Sitka, Yakutat, or the Kenai Peninsula. They slowly (mean velocity ~2 km day^{-1}) carry warm, salty anomalies southwestward along the shelf break and thereby contribute significantly to the heat and freshwater transports out of the Alaskan shelf region (Ueno et al., 2009; Lyman and Johnson, 2015). These eddies are a potential source of noise when estimating mean transports or conditions. The use of data over a wide range of times and locations helps to mitigate this noise by averaging over multiple eddies.

The upper waters of the AS are composed of two main water masses, Pacific Equatorial Water (PEW) and Pacific Subarctic Upper Water (PSUW) (Tibby, 1941; Todd et al., 2012). PEW is relatively warm, salty, oxygen-poor, and nutrient-rich. It flows to the Gulf of Alaska along the North American coast via the California Undercurrent (CUC). PSUW is relatively cool and fresh. It feeds into the Alaska Current from the interior via the North Pacific Subarctic Current. Previous work tracked the signature of PEW to Unimak Pass (~165°W) using a number of hydrographic lines along the coasts of Oregon, Washington, British Columbia, and Alaska (Thomson and Krassovski, 2010). This analysis showed PEW concentrations of ~40% in the CUC at the Newport, Oregon line, slowly eroding northward along the Canadian coast and then westward along the Aleutian Islands, with PEW concentrations closer to ~10%–15% in the AS by Unimak Pass (~165°W).

We use the high-quality and relatively abundant Argo CTD profiles and deep displacement data in the North Pacific from 2000 to June 2014, supplemented by historical CTD data, to estimate the long-term mean velocities and transports of the AS at 5° longitude resolution from 140°W to 175°W. This analysis allows us to quantify the downstream evolution of this important boundary current and to place into context the large variability of historical estimates (6–39 Sv, see above). By combining these transport estimates with those of the PEW concentrations made from these

Argo T-S data within the current, we estimate the PEW transports within the AS and trace the signal of PEW 10° further west than previous work (Thomson and Krassovski, 2010).

2.2 Data and Methods

We downloaded all available Argo data in the region from 180°W–120°W, 40°N–62°N on 11 June 2014 (http://www.usgodae.org/argo/argo.html). Adjusted values from delayed-mode scientific quality-control were used if available, otherwise the real-time values were accepted. Only data flagged as "good" were included in this analysis. Given our focus on the AS, we discarded any profiles located north of the Aleutian Island chain, leaving 30,117 profiles (Figure 2.1, blue dots). To increase data coverage on the continental slope, we supplemented these Argo data with high resolution CTD/XCTD profile data reported by the United States and Canada from the NCEI (formerly NODC) World Ocean Database 2013 (WOD13) within the study region noted above (data downloaded on 7 April 2015; http://www.nodc.noaa.gov/OC5/WOD/pr_wod.html). Full profiles were initially retained if their salinity and temperature flags were good. Then, the salinity, temperature, and depth flags were checked for each sampling level within each profile and that level's data (not the full profile) were discarded if flagged. Any profiles with less than 20 pressure levels of good data or located on land according to ETOPO-2 (Smith and Sandwell, 1997) were discarded, leaving 58,200 profiles (Figure 2.1, red dots). We combined these Argo and high-resolution shipboard CTD data to form the full dataset (88,317 total profiles), with the shipboard CTD data dominating the total number of profiles from 1967–2005 and Argo dominating after 2005 (Figure 2.2).

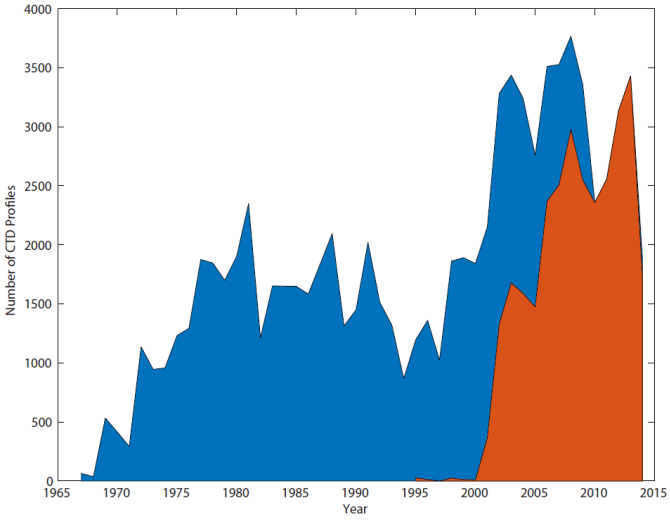

Figure 2.2. Number of CTD profiles used in the analysis by source (Argo in orange, WOD13 in blue) for each year between 1967 and 2014.

For all profiles, any levels where salinity was equal to 0 were removed. Profiles with a shallowest measurement deeper than 20 dbar were discarded to improve the chances that the mixed layer was sampled. Since there is much more structure in the surface waters than at depth, we required higher-resolution sampling nearer to the surface. To meet this requirement, profiles containing any vertical sample spacing exceeding

$$gap_{max} = 20\ dbar + 0.1 p_{mid} \tag{2.1}$$

were removed, where p_{mid} is the pressure halfway between the two pressure levels whose gap is being tested. Absolute salinity, conservative temperature, and potential density relative to the surface were calculated for the remaining 85,159 profiles using v3.05.5 of the 2010 TEOS equation of state (IOC et al., 2010). These quantities were then linearly interpolated onto a regular pressure grid from 0 to 2000 dbar at 10 dbar intervals. If the original profile did not have values at 0 dbar then the values for these quantities at the shallowest sample were applied to the surface level as well.

We performed further quality control on these data, applying an interquartile range filter to conservative temperature and absolute salinity distributions within 5° latitude by 5° longitude boxes. If there were more than 50 values on a given pressure surface, we found the interquartile range (*IQR*): the difference between the values one-fourth ($q_{i,\,1/4}$) and three-fourths ($q_{i,\,3/4}$) of the way along the distribution. Profiles that contained values of the variable (q) outside of:

$$q_{i,1/4} - 1.5 \times IQR < q_i < q_{i,3/4} + 1.5 \times IQR \tag{2.2}$$

on any pressure level (i) were discarded.

Data from the early years of CTD use, roughly 1967–1975, can be less reliable than data from later years. Our quality-control statistics reflect this issue. We discarded 13% of the data from 1967–1975 but only 6% of the data from 1976–2014. We chose to retain the remaining data from 1967–1975 to allow for more averaging of some of the "noise" from mesoscale eddies (e.g., Ueno et al., 2009; Lyman and Johnson, 2015) in the conservative temperature and absolute salinity fields. However, none of our AS transport estimates changed significantly with respect to their uncertainties when we computed them omitting data prior to 1976.

The AS does not flow strictly westward, so we adopted an along-/across-stream coordinate system for the velocity and transport estimates. We first assumed that the AS generally flows parallel to the 1000-m isobath (e.g., Stabeno and Reed, 1991). Since the angle of this isobath varies along the length of the AS, at each "central longitude" of our analysis (located at 5° intervals from 140°W to 175°W) we found the geographic locations of the 1000-m isobath within ±2.5° long. of that central longitude, fit a line to those locations, and calculated the angle of that line relative to parallels of latitude (φ, Table 2.1). The latitude and longitude of all the data points were then converted to along- and across-stream distances for each central longitude. The origin of the

transformed coordinate system for each central longitude was located at the position of the 1000-m isobath at that longitude.

Table 2.1. Angle of 1000-m isobath relative to parallels of latitude at each central longitude (φ) and degrees of freedom (N) for Argo data at each central longitude assuming a 60-day decorrelation timescale.

Central Longitude	140°W	145°W	150°W	155°W	160°W	165°W	170°W	175°W
φ	–29.7°	10.9°	45.8°	29.2°	16.3°	21.2°	22.1°	10.5°
N	19	24	26	24	22	20	22	23

After transforming the data coordinate system at each central longitude, we applied a locally weighted regression (loess) smoothing algorithm (Cleveland and Devlin, 1988) to the conservative temperature, absolute salinity, and potential density data on each pressure level. We assumed an along-current scale of x_{spn} = 500 km and an across-current scale of y_{spn} = 200 km to map the dataset to 5-km resolution across-current sections at the eight central longitudes (Figure 2.1). Additionally, given the short across-current scales over the narrow and steep continental slope, we chose to add a bottom depth term (bd_{spn}) to the loess smoother (equations (2.3–2.5)) to shorten the across-current scale over steep bottom slopes, similarly to previous work (Davis, 2005) (Figure 2.3). The value of bd_{spn} varied for each mapped point i and was set to either 1000 m or twice the bottom depth at that mapped location ($bd_{map,i}$), whichever value was greater. The loess weighting term W thus became

$$W(x, y, bd) = (1 - q_i^3)^3 \; if \; q_i < 1, \tag{2.3}$$

where

$$q_i = \left(\frac{x_{data} - x_{map,i}}{x_{spn}}\right)^2 + \left(\frac{y_{data} - y_{map,i}}{y_{spn}}\right)^2 + \left(\frac{bd_{data} - bd_{map,i}}{bd_{spn}}\right)^2. \tag{2.4}$$

We chose to keep the bottom depth term linear in the smoothing polynomial:

$$M = [1 + x + x^2 + y + y^2 + x * y + bd]. \quad (2.5)$$

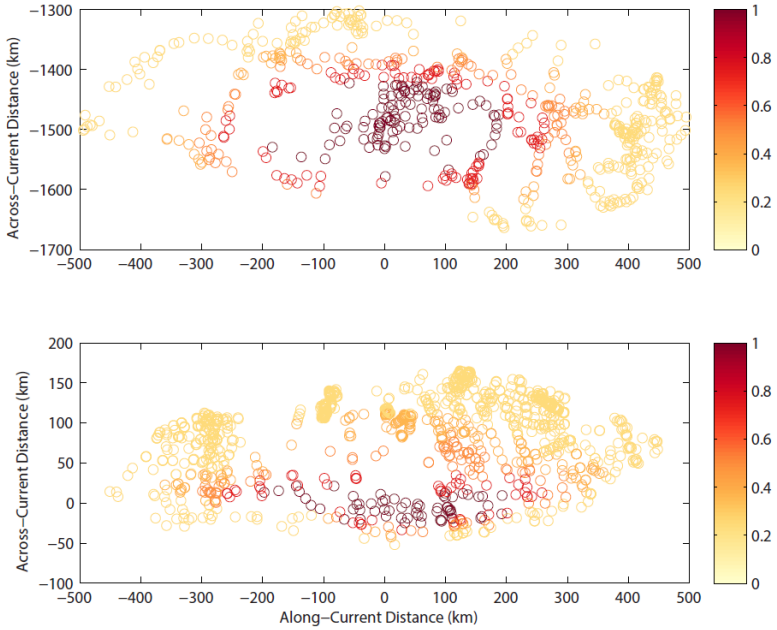

Figure 2.3. Loess weighting terms (W) at (a) an offshore location over the abyssal plain and (b) at a nearshore location centered on the 1000-m isobath where topography is steep.

We calculated the geostrophic velocities for each of the eight mapped sections. For all locations along each section with bottom pressure ≥ 1000 dbar, we initially referenced geostrophic velocities to a 1000-dbar level of no motion. For locations with bottom pressure <1000 dbar, we referenced the geostrophic velocities using the adjacent offshore geostrophic velocity at the deepest common level (DCL) of the location being referenced, marching inshore up the slope. In the small regions between the DCL and the seafloor along the steep continental slope, commonly referred to as the "bottom triangle" areas (which are actually more complicated shapes at the resolution of the ETOPO-2 bathymetry), we applied the adjacent offshore geostrophic velocity at each level within the bottom triangle while moving inshore. We defined the inshore edge of the AS to be at the 200-m isobath to separate our analysis of the offshore AS from the Alaska Coastal Current. This separation may be somewhat artificial, as while the Alaska Coastal Current is largely

confined to the shelf and strongly affected by river outflows and other nearshore processes, it does interact with the AS, especially near Kayak Island and around deep canyons in the Gulf of Alaska.

To estimate absolute geostrophic velocity fields (Figure 2.4), we chose to combine the density data with Argo float parking-depth displacement data from an update of YoMaHa'07 (Lebedev et al., 2007), downloaded on 16 July 2014 (http://apdrc.soest.hawaii.edu/projects/yomaha/). Again, focusing on the AS, we only used displacement data in the region from 180°W–120°W, 40°N–62°N, and south of the Aleutian Islands. We discarded any displacements with bad time inversion/duplication or velocity flags and any floats with a parking pressure outside of 1000 ± 100 dbar. To eliminate displacement data from potentially grounded floats, we discarded any points where the bottom depth at the last fix of the previous cycle or the bottom depth at the first fix of the current cycle was shallower than 1000 m. Last, we visually examined the trajectories of any floats that contained any velocities > 20 cm s^{-1} and discarded displacement data from four floats with trajectories that we deemed physically unrealistic (WMO IDs: 2900312, 2900428, 2900434, and 2900527). These unrealistic motions may have been caused by bad surface ARGOS position fixes. While some of those bad fixes appear to affect only a few displacements, we conservatively chose to discard the entire trajectories for these four floats. The remaining 17,677 displacement-based 1000-dbar velocities were rotated into the along/across-stream coordinates described above for each central longitude's across-current transect. The along-stream components of the 1000-m velocities were then mapped onto the same 5-km resolution transects as the geostrophic velocities using the same loess smoother described above. Next, we added the resulting absolute velocities at 1000 dbar to the geostrophic velocities that we had earlier referenced to a 1000-dbar level of no motion (i.e., at locations with bottom pressures ≥ 1000 dbar). Again, for locations with bottom pressures <1000 dbar, the geostrophic

velocities were referenced to the adjacent offshore geostrophic velocity at the DCL, marching inshore up the slope. The adjacent offshore velocities at each level were again applied to the bottom triangles below the DCL while moving inshore. Adding in the absolute velocities at 1000 dbar substantially changed the velocity values from the geostrophic calculation referenced to zero velocity at 1000 dbar. These differences are even more evident in the volume transport estimates.

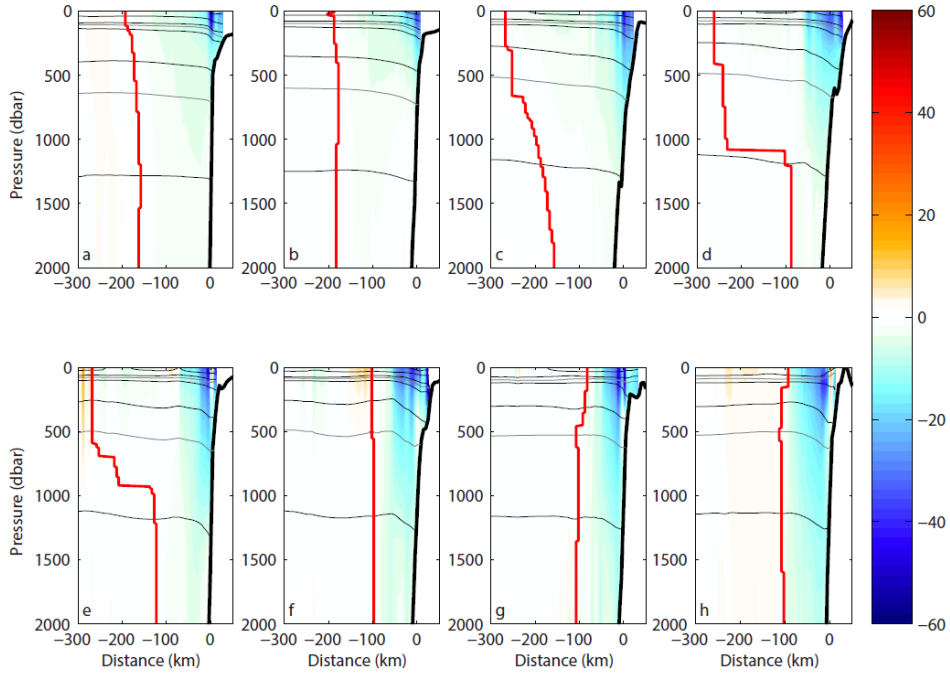

Figure 2.4. Sections of absolute geostrophic velocity (cm s^{-1}) in color with negative values indicating downstream (nominally southwestward) flow at each of the 8 central longitudes (140°W–175°W, a-h). Isopycnals are contoured at 0.5 kg m^{-3} (solid gray lines) with 26.2 and 27.2 kg m^{-3} (dotted gray lines) added. Location of the current edge for each pressure level (thick red line) is defined in the text.

We calculated the alongshore transport of the AS in the upper 1000 dbar at each of the central longitudes using both the geostrophic velocities assuming zero velocity at 1000 dbar and the absolute geostrophic velocities, but calculated the transport for the upper 2000 dbar only using the absolute geostrophic velocities (Figure 2.5). For the transport calculations, the offshore edge

of the current at each pressure level was set to the location of the maximum cumulative alongshore transport when integrating offshore from the 200-m isobath (Figure 2.4, red lines).

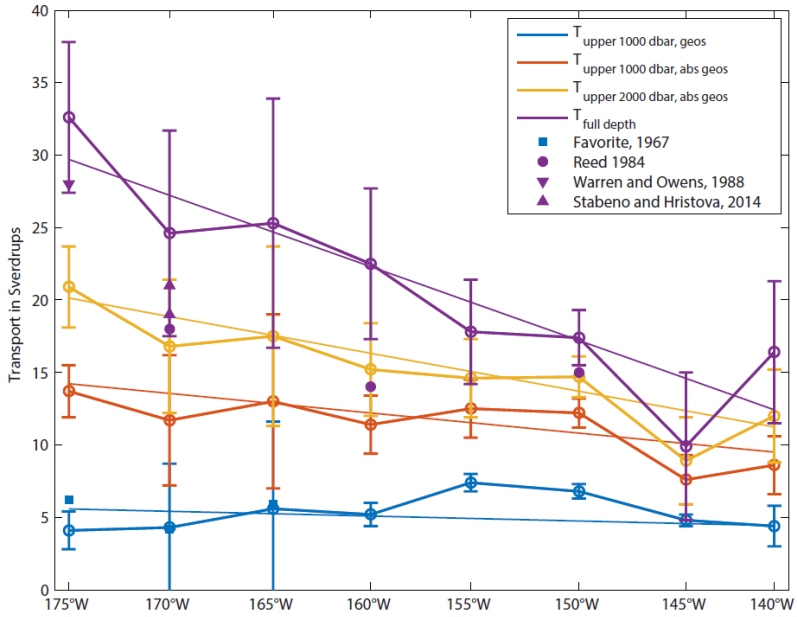

Figure 2.5. Estimates of AS geostrophic transports relative to a 1000-dbar level of no motion in the upper 1000 dbar (blue), absolute geostrophic transports in the upper 1000 dbar (red), absolute geostrophic transports in the upper 2000 dbar (yellow), and full-depth transports (purple) at each central longitude with the 5%–95% confidence intervals (error bars) and linear weighted least squares fits (thin lines). The x-axis is distance along the 1000-m isobath from its location at 140°W but is labeled with the 8 central longitudes. Selected transport estimates from literature shown by the shaded symbols with citations in the legend, color-coded by the type of transport they represent.

To estimate velocities and transports at pressures >2000 dbar, we fit absolute geostrophic velocity profiles in the upper 2000 dbar to the barotropic and first two baroclinic modes. We used the mean profiles of density from the 1/4°-resolution full-depth World Ocean Atlas (WOA) 2013 climatology (downloaded on 20 August 2015; Boyer et al., 2013; https://www.nodc.noaa.gov/OC5/woa13/) to calculate the first two baroclinic modes (Gill, 1982). We used least squares fits to find the amplitudes of the barotropic and baroclinic modes at each

location with bottom pressure >2000 dbar along the eight sections. These three modes alone accounted for >94% of the variance in the absolute geostrophic velocities in the upper 2000 db at the across-current distance of the most inshore edge of the current (Figure 2.4, red lines) at all of the central longitudes (Figure 2.6). Since the mode-derived velocities were nearly constant for the bottom few pressure levels at each location, we applied velocities at the DCL to all levels deeper than the DCL (i.e., in the bottom triangles). We combined these mode-based velocities below 2000 dbar with the absolute geostrophic velocities above 2000 dbar to generate eight full-depth velocity sections along the current, which allowed us to make estimates of the full-depth transport of the AS (Figure 2.5; Table 2.2).

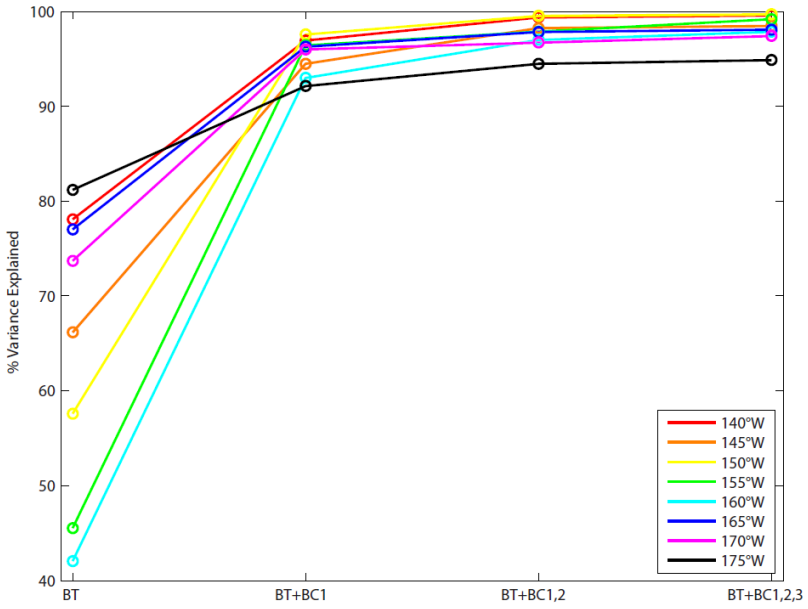

Figure 2.6. Percent variances of absolute geostrophic velocities in the upper 2000 dbar explained by a barotropic mode and 0–3 baroclinic modes calculated from the WOA 2013 climatology. Values shown are for the fits at the across-current distance of the most inshore edge of the current (Figure 2.4, red lines) for each central longitude (see legend), a location chosen to lie within the AS, but also in deep water where the modes are applied.

Table 2.2. Mean values and 5%–95% confidence intervals at each central longitude of: alongshore geostrophic and absolute geostrophic transports in the top 1000 dbar, alongshore absolute geostrophic transports in the top 2000 dbar, mode-based alongshore transports below 2000 dbar, alongshore full-depth transports, alongshore geostrophic and absolute geostrophic transports of PEW for $26.2 < \sigma\theta < 27.2$ kg m-3, total alongshore absolute geostrophic transports for $26.2 < \sigma\theta < 27.2$ kg m-3, and percentages of PEW transports with respect to the total volume transport for $26.2 < \sigma\theta < 27.2$ kg m-3. All transports have units of Sv (1 Sv = 106 m3 s-1), with positive values indicating westward/southwestward (along-stream) flow. Units for the slopes of the linear trends are either Sv per hundred km or % per hundred km. Bolded slope values indicate trends significantly different from zero at the 5%–95% confidence interval.

Central Long.	140°W	145°W	150°W	155°W	160°W	165°W	170°W	175°W	Slope of Lin. Trend
$T_{top\ 1000\ dbar,\ geos}$	4.4 ± 1.4	4.8 ± 0.4	6.8 ± 0.5	7.4 ± 0.6	5.2 ± 0.8	5.6 ± 6.0	4.3 ± 4.4	4.1 ± 1.3	0.03 ± 0.17
$T_{top\ 1000\ dbar,\ abs\ geos}$	8.6 ± 2.0	7.6 ± 1.7	12.2 ± 1.0	12.5 ± 2.0	11.4 ± 2.0	13.0 ± 6.0	11.7 ± 4.5	13.7 ± 1.8	**0.19 ± 0.15**
$T_{top\ 2000\ dbar,\ abs\ geos}$	12.0 ± 3.2	8.9 ± 3.0	14.7 ± 1.4	14.6 ± 2.7	15.2 ± 3.2	17.5 ± 6.2	16.8 ± 4.6	20.9 ± 2.8	**0.36 ± 0.15**
$T_{below\ 2000\ dbar}$	4.4 ± 2.0	1.0 ± 2.3	2.7 ± 0.9	3.2 ± 1.6	7.3 ± 3.0	7.8 ± 5.0	7.8 ± 5.2	11.7 ± 2.7	**0.33 ± 0.21**
$T_{full\ depth}$	16.4 ± 4.9	9.9 ± 5.1	17.4 ± 1.9	17.8 ± 3.6	22.5 ± 5.2	25.3 ± 8.6	24.6 ± 7.1	32.6 ± 5.2	**0.71 ± 0.27**
$T_{PEW,\ geos}$	1.1 ± 0.4	1.3 ± 0.1	1.5 ± 0.1	1.5 ± 0.1	0.9 ± 0.2	1.1 ± 1.1	0.7 ± 0.5	0.7 ± 0.2	–0.03 ± 0.03
$T_{PEW,\ abs\ geos}$	1.8 ± 0.5	1.6 ± 0.3	2.3 ± 0.2	2.1 ± 0.3	1.7 ± 0.3	1.9 ± 1.1	1.4 ± 0.6	1.5 ± 0.3	–0.02 ± 0.03
$T_{in\ \sigma\theta\ range,\ abs\ geos}$	10.3 ± 2.8	9.9 ± 1.8	16.9 ± 1.2	17.9 ± 2.4	15.2 ± 2.4	17.5 ± 9.3	14.8 ± 6.0	17.5 ± 2.6	0.27 ± 0.30
PEW % of Vol T	17.8 ± 0.3	16.2 ± 0.3	13.7 ± 0.2	11.8 ± 0.4	10.9 ± 0.6	10.7 ± 1.4	9.6 ± 0.8	8.5 ± 0.5	**–0.41 ± 0.09**

To estimate the volume transport uncertainties, we applied Jackknife resampling (Efron and Stein, 1981). The quasi-Lagrangian decorrelation time scale for deep (1800 dbar) Argo

temperature data is ~60 days on average (Johnson et al., 2015). To determine the degrees of freedom (*N*) in our Argo dataset at each central longitude, we counted the number of 60-day periods sampled within a 200-km along-stream by 200-km across-stream box centered at the location of the 1000-m isobath at each central longitude (Table 2.1). We resampled the dataset at each central longitude *N* times, removing a unique fraction $\frac{1}{N}$ of the Argo/shipboard CTD profile data and Argo displacement-based velocity data within the maximum possible range of the loess smoother for each resampling. We then ran the entire transport calculation for each resampling at each central longitude, starting with the loess filtering steps. We estimated the standard error (*SE*) for each of our transport estimates (*T*) at each central longitude as

$$\mathrm{SE(T)_{jack}} = \sqrt{\frac{N-1}{N}\sum_{i=1}^{N}\left(T_i - \frac{1}{N}\sum_{i=1}^{N}T_i\right)^2}, \tag{2.6}$$

following delete-one Jackknife formalism. For each transport estimate, we computed 5%–95% confidence intervals from these standard error estimates assuming a Student's t-distribution and using the appropriate degrees of freedom at each central longitude (Figure 2.5). These error estimates may be bit conservative given that the addition of the shipboard CTD data increases our degrees of freedom—particularly within 140°W–155°W where there are a significant number of these profiles.

To quantify the concentrations and transports of the warm and salty (also nutrient-rich and oxygen-poor) PEW we calculated spice (π) (McDougall and Krzysik, 2015) for our mapped fields at each central longitude. We defined PEW and PSUW using temperature-salinity curves from the September fields of the Monthly Isopycnal and Mixed-layer Ocean Climatology (MIMOC) sigma-coordinate climatology (Schmidtko et al., 2013; http://www.pmel.noaa.gov/mimoc/) at 0°, 113.5°W for PEW and 46.5°N, 171.5°E for PSUW. We computed the spice values for these two water masses as a function of potential density (σ_θ). These two water masses act as sufficient

bounds on our data from 140°W to 175°W within $26.2 < \sigma_\theta < 27.2$ kg m^{-3} (Figure 2.7). Maximum wintertime mixed layer densities of $\sigma_\theta \approx 26.2$ kg m^{-3} in the Gulf of Alaska set the lighter limit of the density range (Johnson et al., 2012) and there is very little PEW for $\sigma_\theta > 27.2$ kg m^{-3}. Therefore, we analyzed the concentrations of PEW only for $26.2 < \sigma_\theta < 27.2$ kg m^{-3}. To determine how much of the water at each location is composed of PEW, we subtracted π of PSUW from π at that location, both for a given σ_θ (i), and then divided the result by the difference between the PEW and PSUW π values for that σ_θ (i) (equation (2.7)).

$$F_{PEW,i} = \frac{\pi_{AS,i} - \pi_{PSUW,i}}{\pi_{PEW,i} - \pi_{PSUW,i}} \quad (2.7)$$

We multiplied these values of the fraction of PEW at each data point (Figure 2.8) by the alongshore velocity fields detailed above to determine the PEW volume transport along the current every 5° longitude from 140°W to 175°W (Figure 2.9; Table 2.2). We calculated the quotient of the PEW transport and the total transport in the PEW σ_θ-range to generate a volume-transport-weighted mean concentration at each central longitude (Figure 2.9; Table 2.2), allowing us to determine what percentage of the total volume transport in this range is of PEW over the AS's extent.

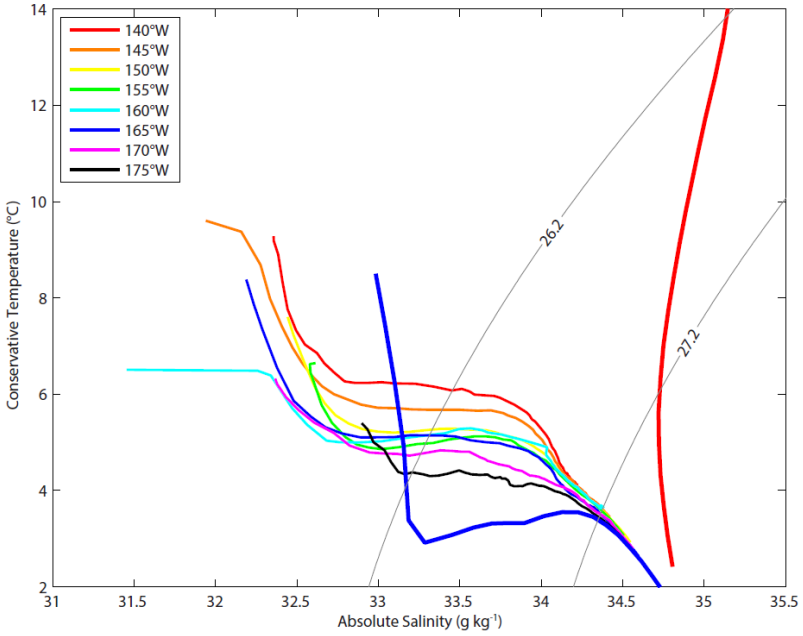

Figure 2.7. T-S curves defining PEW (thick blue line; 0°, 113.5°W) and PSUW (thick red line; 46.5°N, 171.5°E) from the September MIMOC climatology (Schmidtko et al., 2013) and T-S curves for AS water at the 1000-m isobath for each central longitude (see legend). Isopycnals bounding the PEW density range shown (kg m^{-3}; dotted gray lines).

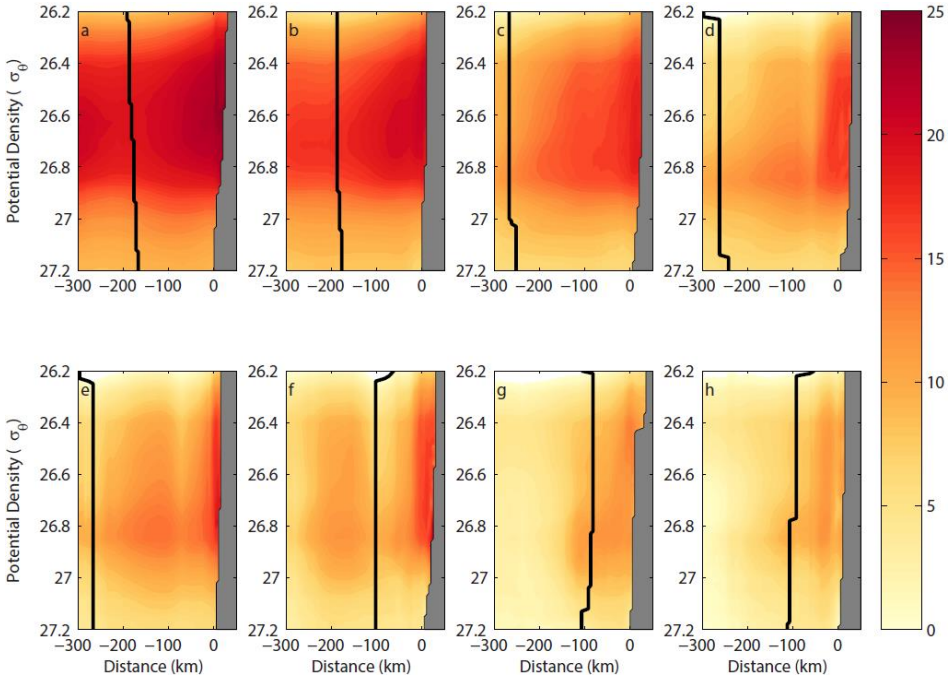

Figure 2.8. Sections of PEW concentrations versus across-current distance and potential density in the AS at central longitudes (140°W–175°W, a-h) with current edges as defined in the text (thick black lines) and topography (gray regions) indicated.

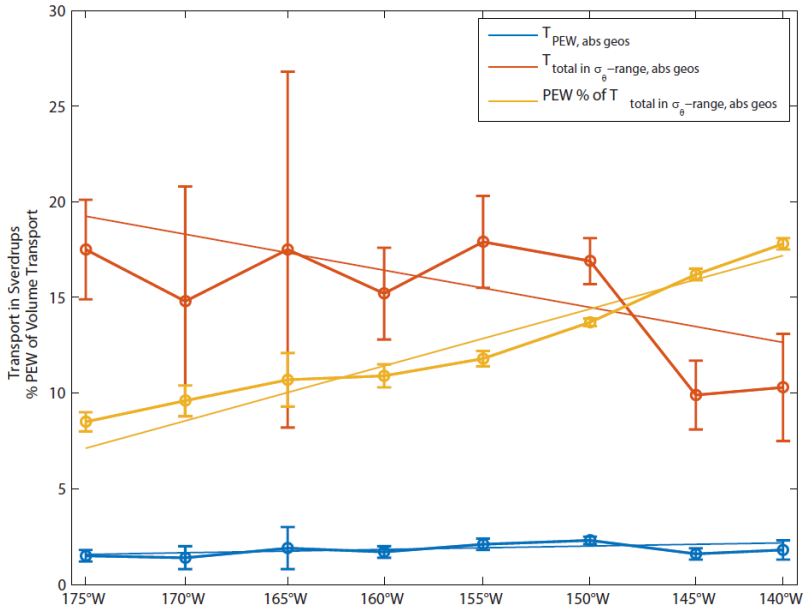

Figure 2.9. Total volume transport in PEW σ_θ-range (red), total PEW transport in PEW σ_θ-range (blue), and percentage of total transport in PEW σ_θ-range of PEW (yellow) at each central longitude with the 5%–95% confidence intervals (error bars) and the linear weighted least squares fits to the data (thin lines). The x-axis convention follows Figure 2.5.

2.3 RESULTS

By generating eight cross-sections of the AS from our data, we are able to examine the evolution of this current as it moves westward from its formation region (140°W–150°W), to its commonly defined start at Kodiak Island (~153°W), to near where it transitions to a boundary-free jet at 180°. This analysis provides us with a robust picture of the AS's long-term mean density and velocity fields, which have been difficult to obtain from previous work based on shipboard hydrographic and mooring data alone. We also build on previous analyses of PEW concentrations in the AS (Thomson and Krassovski, 2010) by examining its signal farther west and estimating the volume transports of this water mass by the AS.

2.3.1 *Density and Velocity Structure*

The vertical and horizontal structure of the AS changes significantly between its formation region (140°W–150°W) and 175°W, near where it leaves the boundary to flow westward in the interior as a free jet (Figure 2.4). Though its narrow (~50 km), high-velocity (>60 cm s^{-1}) core remains just offshore of the 1000-m isobath along its entire extent, the core's dimensions change as it gets farther westward. As mesoscale eddies propagate through the AS its core will be interrupted, typically moving offshore. Here, we are presenting an analysis of the AS at its mean position. Between the formation region of the current (140°W–145°W, Figures 2.4a and 2.4b) and the canonical start of the current near Kodiak Island (150°W–155°W, Figures 2.4c and 2.4d), the core of the AS broadens and deepens. The deep (pressure > 1000 dbar) velocities then continue to strengthen downstream all the way to 175°W. The location of the offshore current edge (Figure 2.4, red lines) indicates significant narrowing of the current at all depths (most notably those shallower than 1000 dbar) between 160°W and 165°W. The current then remains relatively narrow and barotropic between 165°W and 175°W. This increasingly barotropic structure of the current from 160°W to 165°W appears in the vertical modes as well (Figure 2.6). At 160°W, the barotropic mode explains ~42% of the variance of the velocity in the upper 2000 dbar while at 165°W it explains ~77% of the variance. The core of the AS also seems to split in two at 160°W with a precursor to this split appearing at 155°W, as a small region of weaker westward velocity within the core region.

2.3.2 *Volume Transports*

The volume transport of the AS shows significant variation from east to west (Figure 2.5; Table 2.2). Geostrophic transports in the top 1000 dbar referenced to a 1000-dbar level of no motion (blue line, Figure 2.5; Table 2.2) increase from 4.4 ± 1.4 Sv at 140°W to 7.4 ± 0.6 Sv at 155°W

and then decrease to 4.1 ± 1.3 Sv at 175°W. Adding the absolute velocities at 1000 dbar to obtain absolute geostrophic transports in the upper 1000 dbar (red line, Figure 2.5; Table 2.2) results in values that increase rapidly from 8.6 ± 2.0 Sv at 140°W to 12.5 ± 2.0 Sv at 155°W and then continue to increase more slowly to 13.7 ± 1.8 Sv at 175°W. The absolute geostrophic transports for the upper 2000 dbar (yellow line, Figure 2.5; Table 2.2), the mode derived transports for pressure > 2000 dbar (Table 2.2), and the estimates of full-depth transport (purple line, Figure 2.5; Table 2.2), which are the sum of these first two sets of transport estimates, all exhibit strong increasing trends from 140°W to 175°W.

2.3.3 *Pacific Equatorial Water Distribution and Transport*

We quantify distributions of PEW within the AS as far west as 175°W (Figure 2.8), 10° further west than previous work (Thomson and Krassovski, 2010). The core of PEW is centered on σ_θ = 26.6 kg m^{-3} with peak concentrations around 24% at 140°W. This result is consistent with previous work at this longitude, which found peak concentrations of ~23% in a core at σ_θ = 26.55 kg m^{-3} (Thomson and Krassovski, 2010). This high-PEW core then erodes moving westward, apparently splitting into two cores at 155°W with a 16% peak centered on σ_θ = 26.7 kg m^{-3} closer to the 1000-m isobath and a 14% peak centered on σ_θ = 26.85 kg m^{-3} farther offshore. Between 165°W and 170°W, the cores of PEW erode even further, leading to fairly constant PEW concentrations around 12% for 26.2 < σ_θ <27.2 kg m^{-3} at both 170°W and 175°W.

We combine PEW concentrations with geostrophic and absolute geostrophic transports (Section 2.3.2) to make estimates of the geostrophic and absolute geostrophic volume transports of PEW by the AS (Figure 2.9; Table 2.2). As detailed below, both estimates of PEW transport show no statistically significant along-stream variation from 140°W to 175°W, with mean values

of about 1 and 2 Sv, respectively. However, the fraction of the total transport that is of PEW in this σ_θ-range decreases by a factor of 2 (from 17.8% ± 0.3% at 140°W to 8.5% ± 0.5% at 175°W).

2.4 DISCUSSION

The extensive spatial and temporal distribution of Argo data in the Gulf of Alaska, complemented by historical CTD data, allow robust estimates of volume transports of the AS at eight locations along its longitudinal extent, revealing that its structure and transports change substantially from 140°W to 175°W (Figures 2.4 and 2.5; Table 2.2). The current increases in strength and becomes more barotropic while it narrows from east to west (Figure 2.4). Though our full-depth estimates are generally higher than those found in the literature, most of these prior estimates fall within (or very close to) our 5%–95% confidence bounds (Figure 2.5). We expect some differences between our long-term mean values of the transport and those derived from shorter records given the strong variability of this current on weekly to interannual timescales and the influence of strong mesoscale eddies (Musgrave et al., 1992; Crawford et al., 2000; Ueno et al., 2009; Stabeno and Hristova, 2014; Lyman and Johnson, 2015). The slight dip in transport seen at 170°W may be due to the presence of significant passes close to this location (e.g., Samalga and Amutka passes) through which some AS water can flow into the Bering Sea. This feature is discernible in the historical estimates as well.

We examine trends in AS transports from east (140°W) to west (175°W), and find statistically significant increases in all of them except the geostrophic transport in the upper 1000 dbar and the PEW transports (Table 2.2). We compute these trends using linear weighted least squares fits versus the distance along the 1000-m isobath from its location at 140°W to its location at each central longitude. This result provides strong support for previous suggestions of increasing full-depth and deep (>2000 dbar) transports moving westward along the AS based on analysis of

hydrographic data alone (Reed, 1984). The statistically significant differences between the geostrophic and absolute geostrophic transports suggest that adding in the absolute velocities at 1000 dbar is a critical step in accurately computing total volume transports in the AS. This result differs from a previous finding that including deep displacement data from Argo did not significantly change the velocity structure (Freeland, 2006). That work also suggested that the AS accelerates only to 165°W, not 175°W. These differences are likely due to use of a quasi-geostrophic model that did not allow flow through the Aleutian passes and reliance on it and interior Argo data to infer the behavior of this boundary current in that previous study.

As noted above, the absolute geostrophic PEW transport within the AS shows little variation from 140°W (1.8 ± 0.5 Sv) to 175°W (1.5 ± 0.3 Sv), which might initially seem surprising given the statistically significant decreasing trend in the concentrations of PEW seen over this range (Figure 2.9; Table 2.2). However, this result is less surprising when considered in conjunction with the trends of increasing transport of the AS from east to west. These results imply that in the mean, the AS is losing little of its PEW to either the Bering Sea or the gyre interior. Instead, the AS is gaining significant amounts of water from the gyre interior as the current flows westward, leading to decreased concentrations of PEW, but stronger total transports and nearly constant PEW transports. This finding advances our knowledge of the fate of PEW in the North Pacific and may help us better understand the effects of this water on the Bering Sea ecosystem.

Robust estimates of the full-depth volume transports of the AS could improve regional circulation models, some of which currently assume constant transport along the length of the AS (e.g., Ezer and Oey, 2010). Taking the strengthening of the mean transports along the extent of the AS into account is important since the effects of AS transport on the Bering Sea shelf have been shown to be highly nonlinear, with increases in AS transport within certain ranges causing

warming along the shelf while increases within other ranges causing cooling on the shelf (Ezer and Oey, 2010). More accurately modeling the mean state of the AS might also improve our understanding of the nonlinear interactions between the AS and the Bering Sea, as well as the impacts of variable AS transports on physical and biological processes in the Sea of Okhotsk. Additionally, having a snapshot of the mean structure of the AS should provide context for future observations, when examining its seasonal and interannual variability and the influence of mesoscale eddies.

2.5 ACKNOWLEDGEMENTS

Argo data were collected and made freely available by the International Argo Program and the national programs that contribute to it (http://www.argo.ucsd.edu, http://argo.jcommops.org). The Argo Program is part of the Global Ocean Observing System. Data used in this study can be downloaded from the URLs given in the text. We thank two anonymous reviewers for their helpful comments. P.D.L. and G.C.J. are supported by the Climate Observation Division, Climate Program Office, National Oceanic and Atmospheric Administration (NOAA), U.S. Department of Commerce and NOAA Research. Pacific Marine Environmental Laboratory Contribution Number 4550.

Chapter 3. A NEW GLOBAL BOTTOM WATER CLIMATOLOGY FOR TRACING ABYSSAL FLOW PATHWAYS AND EXPLORING BOTTOM WATER TRANSFORMATIONS

3.1 INTRODUCTION

Bottom water property distributions provide useful insights into the complicated pathways abyssal and deep waters take throughout the global ocean, an important piece of the meridional overturning circulation (Lumpkin & Speer, 2007). The most recent summary of global bottom water properties relied on expertly hand-contoured maps from sparse measurements (Mantyla & Reid, 1983). In the intervening decades, the international World Ocean Circulation Experiment (WOCE) program, Climate Variability and Predictability-CO_2 (CLIVAR-CO_2) program, and Global Ocean Ship-Based Hydrographic Investigations Program (GO-SHIP) have greatly increased the number of high-quality observations of the deep ocean (Talley et al., 2016). Here we use machine learning (specifically an innovation on the random forest regression algorithm) to create more detailed maps of the mean bottom water property distributions based on these new observations and use them to illuminate the abyss.

The ocean has stored about 90% of the excess heat energy generated in the climate system from 2010–2018 (von Schuckmann et al., 2020) and approximately 27% of the anthropogenic carbon emitted from 1994–2010 (Talley et al., 2016). Approximately 8% of the excess heat taken up by the climate system has gone into the deep ocean below 2000 meters (von Schuckmann et al., 2020). Many recent papers have focused on discerning changes in the bottom water properties since WOCE (e.g., Desbruyères et al., 2016; Johnson et al., 2014; Kouketsu et al., 2011; Menezes et al., 2017; Purkey et al., 2019; Purkey & Johnson, 2010, 2013). Analyses of hydrographic section

data have demonstrated that Antarctic Bottom Water (AABW) in the Southern Ocean has warmed and freshened significantly over the last few decades (e.g., Desbruyères et al., 2016; Purkey & Johnson, 2010, 2013). The timescales for the return of this heat to the atmosphere are long and not yet well constrained – though great strides have been made recently in understanding deep water upwelling in the Southern Ocean (e.g., Marshall & Speer, 2012; Tamsitt et al., 2017). By further developing our knowledge of bottom water spreading pathways, we add to our understanding this important piece of the global overturning circulation and its relationship to the global energy imbalance.

Recent work on global AABW and North Atlantic Deep Water (NADW) property distributions used a 0.5° gridded climatology of temperature, salinity, oxygen, and nutrients to quantify relative fractions of AABW and NADW (Johnson, 2008). This work found that AABW at least partially influences bottom waters in all basins except the Arctic and some of the North Atlantic. Additionally, their work suggests that throughout the entire North Atlantic, the Angola Basin, and along the full extent of the western boundary of the Atlantic, NADW is the dominant contributor to the bottom waters. AABW, however, dominates in all other basins and globally overlies approximately twice the amount of seafloor area as NADW. While this work used temperature, salinity, oxygen, and nutrient data for this analysis, it did not generate global maps of these properties in the bottom waters that could be used to examine more closely the degree of mixing with the overlying waters or to investigate other, typically more local, biogeochemical processes influencing these distributions. This paper will analyze such maps, the better to advance our understanding of the factors influencing bottom water property distributions.

Over the last few decades machine learning techniques have advanced and been shown to work well for interpolating sparsely-sampled environmental variables (Li et al., 2011) and for

modeling relationships among different oceanographic variables (Giglio et al., 2018). These methods have also become more accessible to earth scientists through open source projects like the *scikit-learn* Python library (https://scikit-learn.org/). Employing these approaches will further improve the quality of our bottom property maps by providing a quantitative and reproducible way to map the sparsely sampled fields with improved accuracy over previous methods.

By taking advantage of the greater number of deep ocean observations and the concurrent advances in computational data science methods over the past few decades, here we generate updated and improved maps of bottom water properties (conservative temperature, absolute salinity, dissolved oxygen, silicic acid, nitrate, and phosphate) throughout the global ocean using machine learning techniques. Specifically, we use a machine learning method known as random forest regression in conjuction with classical objective mapping to interpolate the observed fields to a 0.5° latitude–longitude grid. We develop a new implementation of these methods which we term the "stacked" random forest objective mapping (RFOM) method that iteratively applies the RFOM procedure to first the more well-sampled fields (e.g., temperature) and then to the increasingly poorly sampled fields (e.g., phosphate). This innovation allows us to better leverage the information from the more well-sampled fields into our maps of the less well-sampled fields. The higher quality and coverage of modern hydrographic data, in combination with the use of this new mapping procedure, allows us to explore in greater detail the bottom water spreading pathways than was possible at the time of the last global bottom water analysis (Mantyla & Reid, 1983). Section 3.2 includes descriptions of the datasets used and of the mapping methods. Section 3.3 includes in-depth discussions of the composition of bottom waters globally, the multitude of AABW and NADW spreading pathways, and global analyses of the bottom water variability in

both temperature-salinity and salinity-oxygen space. Section 3.4 includes a brief summary of key findings and further discussion.

3.2 Data and Methods

Determining how to best create property maps from irregularly sampled data is a perennial and non-trivial problem in oceanography. There are many well-established approaches of varying complexity for tackling this issue, each with its own shortcomings. For example, a fairly simple solution is to use a k-nearest neighbors interpolation to grid the data, which uses an average of the nearest k points to the grid location to generate an estimate. This approach tends to produce an estimate at each point that is quite localized, which is favorable, but noisy, since limited smoothing is applied. To get a slightly smoother map, one might use a bin average where the region to be mapped is divided into bins and then the estimate within each bin is simply the average of all the data points within the bin. However, this type of estimate is likely to be a bit choppy between bins. To reduce the choppiness of the map, one could use a Gaussian weighted average instead. An even more sophisticated map can be achieved through the use of localized interpolation/regression schemes such as locally weighted scatterplot smoothing (loess) (Cleveland & Devlin, 1988). Most of the high-quality gridded products in oceanography use objective mapping to generate their mapped fields (Bretherton et al., 1976). Objective mapping is advantageous in that it corrects a user-provided first guess for the mapped field with nearby data, with some consideration of the signal-to-noise ratio, to generate an improved estimate of the mapped field. The first guess can be produced using a variety of approaches.

In order to create the best possible global maps of conservative temperature, absolute salinity, dissolved oxygen, silicic acid, nitrate, and phosphate, we incorporate data from multiple databases and performed extensive quality control (see Sections 3.2.1, 3.2.3, and 3.2.5). While

there are many classical approaches for interpolating sparse oceanographic data, in this work we present a new method that combines a new implementation of a machine learning method known as random forest regression (Breiman, 2001) with objective mapping. We hope that successfully demonstrating the skill of this approach for mapping oceanographic variables could potentially illuminate a new and useful path for interpolation of other sparse oceanographic datasets.

3.2.1 *Conservative Temperature Data and Quality Control*

Our conservative temperature dataset is made up of data from three sources. The first contribution is from high-quality conductivity-temperature-depth (CTD) data from 81 cruises (Table 3.1) downloaded from the CLIVAR and Carbon Hydrographic Data Office (CCHDO) on 05 March 2018 (https://cchdo.ucsd.edu/). While we tried to primarily use World Ocean Circulation Experiment (WOCE) cruises, if there was a similar cruise from the 1980s than was much more complete, we used that one instead. The second contribution is from all of the available Ocean Station Data (OSD) and High Resolution CTD data in the World Ocean Database 2013 (WOD13) in locations deeper than 2000 meters, which was downloaded on 19 March 2018 (https://www.nodc.noaa.gov/OC5/WOD13). The final contribution is from the late Prof. Joe Reid's (of Scripps Institution of Oceanography) NODC Deep Ocean Station Profile dataset, which was downloaded on 02 January 2018 (https://rda.ucar.edu/datasets/ds543.0/). Across these three data sources, profiles within the Arctic Ocean were found only in the WOD13 data.

Table 3.1. List of WOCE (and earlier) cruises downloaded from the CCHDO website (https://cchdo.ucsd.edu/) used in the temperature dataset.

Ocean Basin	WOCE Identifiers and Cruise Start Date
Atlantic (25 cruises)	A01/A01E (1991), A01W/AR05/AR13 (1995), A02 (1997), A03 (1993), A05/AR01 (1998), A06 (1993), A07 (1993), A08 (1994), A09 (1991), A10 (1992), A11 (1992), A12/SR04 (1992), A13/A13.5/AJAX (1995), A14 (1995),

	A15/AR15 (1994), A16C (1989), A16N (1988), A16S/A23 (1989), A17 (1994), A20 (1997), A21/S04/SR02 (1990), A22 (1997), A23/A16S (1995), A24 (1997), A25 (1997)
Indian (13 cruises)	I01E (1995), I01W (1995), I02/I02E (1995), I02/I02W (1995), I03 (1995), I04/I05W/I07C (1995), I05/I05E/I08N (1995), I05/I05P (1987), I06S (1996), I07/I07N (1995), I08S/I09S (1994), I09N (1995), I10 (1995)
Pacific (37 cruises)	P01 (1985), P01/P01W (1993), P02/P02C (1994), P02/P02E (1993), P02/P02W/PR27 (1994), P03 (1985), P04C (1989), P04E (1989), P04W (1989), P06C (1992), P06E (1992), P06W (1992), P08N (1996), P08S (1996), P09 (1994), P10 (1993), P11A (1993), P11S (1993), P13 (1992), P14/P14C (1992), P14/P14N (1993), P14S/P15S (1996), P15N (1994), P15N/PR06 (1994), P16/P16A/P17A (1992), P16/P16N (1984), P16/P16N/P16C (1991), P16/P16S/P17S (1991), P17C (1991), P17E/P19S (1992), P17N (1993), P18 (1994), P19A (1992), P19C (1993), P21/ P21E/P21W (1994), P24 (1995), P31 (1994)
Southern (6 cruises)	S03/S04/S04I (1994), S04 (1993), S04/S04A/SR04 (1996), S04/S04I (1996), S04/S04P (1992), S05 (1994)

Though there is evidence that bottom water properties have changed over the last few decades (Purkey & Johnson, 2010, 2013), the amplitude of these changes is small enough that using data spanning over this period will still be appropriate for providing us with a steady-state picture of global bottom water property distributions. Another caveat to this analysis is that due to that difficultly of acquiring oceanographic data in foul weather, there is a seasonal bias to these data. Throughout much of global ocean, this seasonality is unlikely to affect our results substantially. However, near sites of seasonal bottom water formation and perhaps in the equatorial wave-guide its effect may be larger.

A number of quality control (QC) steps were performed on the full dataset. We only kept profiles and levels where both pressure and temperature had good QC flags (specifically, values of 2, 6, or 7 in the WOCE data). We also saved the salinity data at these temperature levels if the profile had a good salinity QC flag. Profiles whose deepest measurement was shallower than 2000 meters were removed (4,271/220,898 = 1.9% of profiles removed). There were a substantial number of profiles that were either missing a bottom depth measurement (65,422/216,627 = 30.2%

of remaining profiles) or had a recorded bottom depth over 500 meters shallower than the deepest measurement depth (279/216,621 = 0.1% of remaining profiles). While CTD measurements occasionally extend below the apparent depth of the seafloor measured by the shipboard echosounder, especially in regions of steep or rough topography, a difference of > 500 meters is unlikely. Additionally, there were 1,225 profiles from WOD13 (0.6% of the total profiles from that dataset) where the distance to the seafloor from the deepest measurement of the profile appeared to be given instead of the bottom depth. We converted these values to bottom depths by adding this recorded distance to the deepest measurement depth.

For the 65,701 profiles with bad or missing bottom depths as noted above, we developed a procedure for filling in these missing depth data. Using only the high-quality WOCE profiles, we examined the difference between the recorded bottom depths and the bottom depths from ETOPO-2 (Smith & Sandwell, 1997) linearly interpolated to the profile locations in order to determine the typical difference between these ship- and satellite-based estimates of the seafloor depth. From the distribution of these differences, we identified that 270 meters was equal to approximately three times the interquartile range, which is a common definition for the minimum value of an extreme outlier. For each of the profiles with bad or missing bottom depths as noted above, if the depth of the deepest measurement plus 10 meters (the typical distance between a WOCE CTD profile and the seafloor) was within 270 meters of the interpolated ETOPO-2 depth, then the depth of the deepest measurement plus 10 meters was used as the bottom depth. This was the case for 20,865/65,701 (31.8% in total, but 88.8% for WOCE) of profiles. For the remaining profiles, the suspicious recorded bottom depth was replaced with the interpolated ETOPO-2 depth. There were still 466/216,621 (0.2%) profiles with a bottom depth more than 500 meters shallower than the

deepest measurement after this procedure was completed. These profiles were removed from the dataset.

Not all of these profiles had high-quality salinity data at every depth level (~2.8% in total were missing at least one level of salinity data, but only 1.3% for WOCE), creating an issue for our calculation of conservative temperature, which requires coincident salinity data. We developed a simple procedure for approximating these missing salinities so that we could still estimate conservative temperature at these levels. If the nearest good salinity value in the profile was within 500 meters of the missing level, that salinity value was used. If there were no good salinity values within 500 meters of the missing value, values from the nearest profile were used to fill in for the missing data points as long as they were again within 500 meters of the missing level.

We also examined the difference between the deepest measurement depth and the recorded bottom depth in each of the high-quality WOCE profiles to inform how far away we would allow measurements to be from the bottom and still consider them bottom water measurements. Based on the distribution of these differences, we decided to only retain data within 200 meters of the seafloor (the approximate location of the "elbow" of the distribution of the differences, not shown). This value was chosen while trying to balance keeping the highest number of profiles possible with making sure that they actually measured the bottom waters. For profiles whose bottom depth was supplied by the interpolated ETOPO-2 data, their deepest measurement was required to be within 470 (i.e., 200 + 270) meters of the bottom depth. This 200-meter cut-off value retained 113,448/216,155 (52.5% in total, but 97.0% for WOCE) of the profiles.

We then subsampled the in-situ temperature and practical salinity profiles at 250-meter intervals from 2000 meters to the deepest measurement depth for each profile. Including these data from higher in the water column in addition to those from the deepest measurement substantially

improved the quality of our bottom property maps (not shown). These improvements were particularly notable in regions of steeply sloping topography (e.g., mid-ocean ridges) where additional data above the seafloor in the deeper regions adjacent to the ridge provided more information for our mapping method to incorporate into the predictions at the shallower bottom depths along the ridge.

Next, we removed any duplicate profiles among the three datasets. Profiles were considered duplicates if they were taken within 1 day, 1 minute of latitude, and 1 minute of longitude of each other. First, we removed 4747/5579 (85.1%) of the Reid profiles. We then removed 12411/100812 (12.3%) of the WOD13 profiles. Lastly, we removed any remaining duplicates in the combined dataset (10,209/96,290 = 10.6% of profiles), which must have been duplicates present within one of the original datasets. This left us with 86,081 profiles of in-situ temperature and practical salinity data from which to calculate conservative temperature profiles.

The final step of our QC process for the conservative temperature profiles was to apply an interquartile range filter to these data within 500-meter depth range, 10° latitude by 10° longitude bins. When there were at least 10 data points within one of these bins (i), we calculated the interquartile range (IQR): the difference between the values one-fourth ($q_{i,1/4}$) and three-fourths ($q_{i,3/4}$) of the way along the distribution. Any data points within the bin whose temperature value fell outside of the range, Θ_i, defined as,

$$q_{i,1/4} - 3 \times IQR < \Theta_i < q_{i,3/4} + 3 \times IQR \tag{3.8}$$

were then discarded. This IQR procedure removed 2,941/587,752 = 0.50% of the points. The remaining observations of conservative temperature (Figure 3.1a) span the global ocean with especially high coverage near major oceanographic institutions (e.g., in the North Atlantic, near the coast of California and Japan).

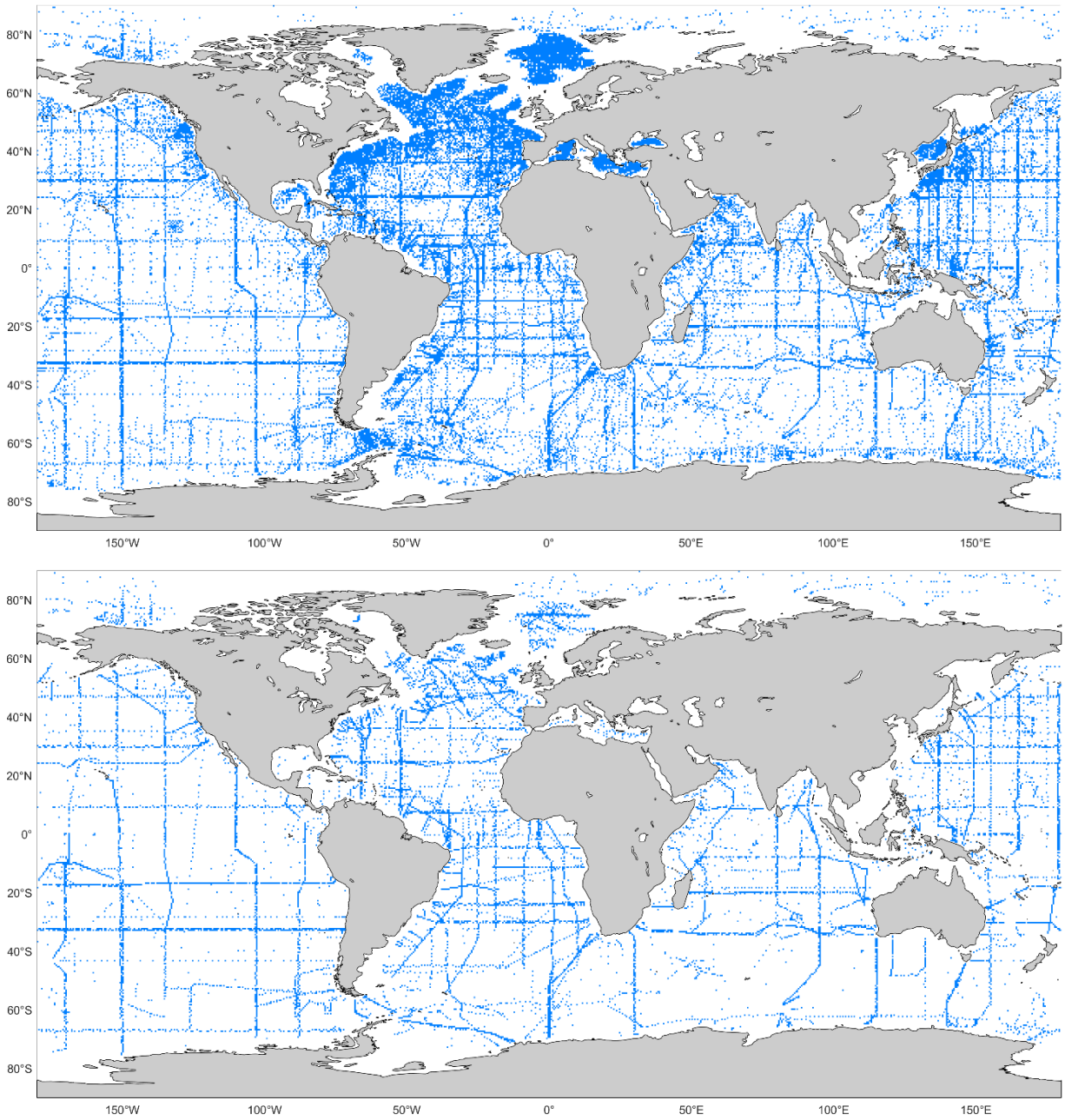

Figure 3.1. 0.5° latitude × 0.5° longitude boxes shaded blue if at least one quality-controlled near-bottom a) conservative temperature or b) phosphate measurement was present for use in RFOM mapping.

3.2.2 *Conservative Temperature Mapping*

To interpolate these profile data to an evenly-spaced 0.5° global grid of bottom conservative temperature (hereafter temperature or Θ) values, we used a supervised machine learning approach known as the random forest (RF) regression model (Breiman, 2001). RFs have many previously been shown to work well for mapping sparse oceanographic datasets (Berg et al., 2019; Giglio et al., 2018). These models are fairly robust to outliers and noise, computationally efficient, require little parameter tuning, and are not prone to overfitting. Additionally, RFs are useful for representing relationships in our sparsely-spaced, noisy data because the predictor variables (e.g., latitude, longitude, bottom depth) can vary non-monotonically with the predicted variable (e.g., bottom temperature). However, one drawback to this regression method compared to more standard methods like multiple linear regression that produce equations relating the various predictors to the predicted variable is that the RF model cannot be used to reliably extrapolate outside of the range of the data it is trained on. This will lead to potentially slightly less extensive maps from the RF approach. However, the improved accuracy from using these methods may be worth any small decreases in mapping extent.

We used the *TreeBagger* implementation in MATLAB to build the RFs for this analysis. For temperature, we built a RF that uses latitude, longitude, and depth to predict temperature (Table 3.2). The *TreeBagger* code builds a large number of decision trees where each tree is built on an independently-drawn bootstrapped replica of the data. This variety in the composition of these bootstrapped subsamples is one way in which "randomness" is added to the "forest" of decision trees. The RF approach adds further randomness to the tree-building process by restricting the algorithm to searching through a limited number of predictors at each split point in the tree instead of allowing it to always select the most optimal variable to split the data upon. The number of

predictors it is allowed to search through at each split (n_preds) is typically set to one-third the total number of predictors. Based on this heuristic, this hyperparameter should be set to 1 for the temperature RF. However, more predictors (up to 6) are used in the RFs for mapping the salinity, dissolved oxygen, and oxygen fields (Table 3.2), which would suggest setting this parameter to 2 in those RFs. For the sake of convenience and consistency across all of our mappings, we chose to set this hyperparameter to 2 in all of the RFs for this work. This choice does not significantly affect the results of the RFs.

Table 3.2. Summary of datasets, quality control procedures, RF predictor variables, and number of profiles used to generate the global map for each of the six variables. Note that here φ represent latitude, λ represents longitude, and z represents bottom depth.

Variable Mapped	Datasets Used in Random Forest	Quality Control Performed	Predictors Used	# of Profiles
Conservative temperature (Θ)	CCHDO WOCE, WOD13, Reid	Dataset quality control flags, IQR	φ, λ, z	85,404
Absolute salinity (S_A)	GLODAPv2, Reid	Dataset quality control flags, IQR	φ, λ, z, Θ	25,436
Dissolved oxygen (O_2)	GLODAPv2, Reid	Dataset quality control flags, IQR, visual check	φ, λ, z, Θ, S_A	23,802
Silica ($Si(OH)_4$)	GLODAPv2, Reid	Dataset quality control flags (GLODAPv2 only), IQR, visual check	φ, λ, z, Θ, S_A, O_2	20,665
Nitrate (NO_3^-)	GLODAPv2, Reid	Dataset quality control flags (GLODAPv2 only), IQR, visual check	φ, λ, z, Θ, S_A, O_2	19,984
Phosphate (PO_4^{3-})	GLODAPv2, Reid	Dataset quality control flags (GLODAPv2 only), IQR, visual check	φ, λ, z, Θ, S_A, O_2	18,927

In order to prevent the algorithm from trying to group data that may lie in the same latitude, longitude, or depth range but in different basins, we chose to build individual RFs for each of the following regions: the Atlantic, Indian, Pacific, and Arctic oceans; the Black, Mediterranean, and

Caribbean (which includes the Gulf of Mexico here) seas; and Baffin Bay. This regional separation is justified because we know that bottom waters should generally be more similar within each basin than between different basins. We examined the variability of the out-of-bag error with the number of trees to determine the appropriate number of trees to use in each regional RF (not shown). Typically, it is best to choose a number of trees (n_trees) greater than the number at which the out-of-bag error has stabilized and there is no risk associated with choosing too many trees other than increased computational cost. We used 1000 trees each for the Atlantic, Indian, and Pacific oceans and 500 trees each for the remaining regions.

In order to be able to evaluate the generalization performance (i.e., the "test error"; Section 3.2.5) of our regional RFs, we only built the model on data from 90% of the profile locations (training data), reserving the remaining 10% (test data) for this evaluation. The assignment of profiles to either the training or test dataset was done randomly to avoid biasing either the model or the error assessment. We then used the regional RFs to map our variable of interest (e.g. bottom temperature) by using a higher-resolution gridded field (e.g., "ETOPO-60" – the ETOPO-2 bathymetry map smoothed at 1° scales and interpolated to 0.5° resolution for locations deeper than 2000 meters) as input to the RF for each basin. We combined the RF-generated maps for all eight regions into a global map. In order to reduce the appearance of artificial, "hard" boundaries between the basins in the Southern Ocean, we set the regional bounds there such that the Atlantic, Indian, and Pacific oceans have large overlapping areas. In these regions, we combine the maps from the different basins by using a linear weighted average in longitude.

We chose to improve further the output of our RF by using objective mapping to correct this "first guess" map from the RF with nearby data. A similar approach using linearly interpolated altimetric height as a first guess for the objective mapping procedure has been shown to improve

mapped estimates of steric height (Willis, 2003). This procedure helped smooth artificially sharp gradients or rectilinear artifacts in the RF-mapped field and pulled the estimates closer to the known data as needed. ETOPO-60 was linearly interpolated to the locations of all the profiles and the bottom temperature for these latitude, longitude, and bottom depth triplets was predicted using the RF ($\Theta_{RF,ETOPO\text{-}60\ at\ data\ locations}$). These temperature predictions were subtracted from the deepest temperature observation for each profile (Θ_{data}) and then these differences were objectively mapped to the locations of the original ETOPO-60 0.5° grid assuming a Gaussian covariance function using the 99 points nearest each grid point with 1° correlation scales in latitude and longitude and error energy of 0.1 (so that the maps would not exactly agree with data at profile locations). This mapped difference field was then applied as a correction to the RF estimate on the ETOPO-60 grid ($\Theta_{RF,ETOPO\text{-}60}$), i.e.,

$$\Theta_{RFOM} = \Theta_{RF,ETOPO-60} + \langle \Theta_{\text{data}} - \Theta_{\text{RF,ETOPO}-60\ \text{at data locations}} \rangle \qquad (3.9)$$

where the angular bracket represents that objective mapping to the ETOPO-60 grid coordinates occurred and Θ_{RFOM} represents that final 0.5° grid of conservative temperature produced by our combined random forest and objective mapping (RFOM) method.

3.2.3 *Absolute Salinity Data and Quality Control*

Building a RF to predict absolute salinity from latitude, longitude, depth, and temperature, requires coincident measurements of all of these quantities. We obtained a global dataset for these variables by combining data from the Global Ocean Data Analysis Project Version 2 (GLODAPv2) data product (downloaded on 22 December 2017, https://www.nodc.noaa.gov/ocads/oceans/GLODAPv2/) and the Reid dataset described above. Salinity data typically require more QC than temperature data. While applying the IQR filter to the temperature data as described above was sufficient QC for those data, this filter alone would

have been insufficient QC for the WOD13 salinity data. GLODAPv2 applies more rigorous QC procedures for salinity than WOD13, making it the better choice for this work despite the somewhat smaller size of the dataset. GLODAPv2 profiles and levels with temperature and salinity data flagged as bad by the primary QC (i.e., with a WOCE flag of 9) were removed. The secondary QC flags were not considered. Profiles whose deepest measurement was shallower than 2000 meters were removed (19848/45164 = 44.0% profiles removed). Missing bottom depths were already filled in during the development of GLODAPv2 (Olsen et al., 2016). We removed an additional 6/25316 = 0.02% of the profiles because their bottom depth was more than 500 meters shallower than the deepest measurement. The 200-meter near-bottom cutoff retained 21734/25310 = 85.9% of the remaining points. As for the temperature-only dataset described above, we only kept the in-situ temperature and practical salinity data at 250-meter intervals from 2000 meters to the deepest measurement depth for each profile. We performed a similar QC procedure on the Reid salinity dataset as described above for the Reid temperature dataset (Table 3.2). The only difference is that we now removed the levels where the salinity data were flagged as bad in addition to levels where depth or temperature were flagged as bad.

Once the initial QC was completed, we removed any duplicate profiles between the two datasets. As with the temperature datasets, profiles were considered duplicates if they were taken within 1 day, 1 minute of latitude, and 1 minute of longitude of each other. These criteria removed 1616/5522 = 29.3% of the Reid profiles. Combining the two datasets yielded a total of 25,640 profiles (21,734 GLODAPv2, 3,906 Reid). After removing any remaining duplicates (80/25640 = 0.3% of profiles), which must have been duplicates present within one of the original datasets, 25,560 profiles remained. Lastly, we applied the same interquartile range filter describe above to both the conservative temperature and absolute salinity data. The IQR procedure for conservative

temperature removed 997/196040 = 0.51% of the total points and the IQR procedure for absolute salinity removed 944/195043 = 0.48% of the total points.

3.2.4 *Absolute Salinity Mapping*

To generate our map of absolute salinity (hereafter salinity or S_A), we used the same RFOM procedure described above except that we no longer had sufficient data to map the Black Sea. The RF for this mapping relates latitude, longitude, depth, and temperature to predict salinity (Table 3.2). To predict salinity on the 0.5° grid, we feed ETOPO-60 and the 0.5° grid of temperature produced by the RFOM described above into this new RF. This effectively "stacks" the prediction from this RF on top of the gridded results from the previous RF that were based on the high-resolution bathymetry data. Without having first mapped temperature to the 0.5° ETOPO-60 grid, we would only be able to predict salinity at the locations where we have existing coincident depth and temperature measurements instead of at the 0.5° grid locations. Alternatively, we would be limited to building a RF that uses latitude, longitude, and depth (but not temperature) to predict salinity if we still wanted to map it onto the 0.5° grid. Therefore, our novel, "stacked" RF approach allows us to map progressively more sparsely-sampled oceanographic variables to the grid of a high-resolution base field (here, the 0.5° grid of ETOPO-60) while taking advantage of as much information as possible from the more well-sampled fields earlier in the "stack"(such as temperature).

3.2.5 *Dissolved Oxygen and Nutrient Data, Quality Control, and Mapping*

Building a RF relating latitude, longitude, depth, temperature, and salinity to predict dissolved oxygen (hereafter oxygen) and then additional RFs relating all of those variables to predict silicic acid, nitrate, and phosphate (Table 3.2) requires coincident measurements of all of these quantities.

As for salinity, we combined data from the GLODAPv2 and Reid datasets for these variables. Oxygen (O_2), silicic acid ($Si(OH)_4$), nitrate (NO_3^-), and phosphate (PO_4^{3-}) were converted from units of mL L^{-1} or μgrams-atoms L^{-1} in the Reid dataset to the same units as the GLODAPv2 data (μmol kg^{-1}). In the literature, silicic acid in the ocean is often referred to as "dissolved silica" or sometimes as "silicate"; hereafter we will refer to it simply as "silica".

We performed a similar QC procedure on the GLODAPv2 and Reid datasets for these variables as described above for the GLODAPv2 and Reid salinity datasets, except that the Reid dataset lacked quality control flags for the silica, nitrate, and phosphate data (see Table 3.2 for a summary of all QC procedures for each variable). In addition to applying the IQR filter to screen for outliers, we performed a visual check of all of the bottom oxygen, silica, nitrate, and phosphate data from both GLODAPv2 and the Reid datasets. Through this visual check we removed an additional 94, 111, 204, and 144 profiles from these datasets, respectively. The fully quality-controlled nutrient datasets have sparser global coverage than the fully quality-controlled temperature dataset (Figure 3.1).

The same general procedure as described above for salinity was then followed for mapping oxygen, silica, nitrate, and phosphate data in our novel "stacked" RF framework. This enabled us to continue using the more well-sampled fields (e.g., bathymetry, temperature, and salinity) to help map the less well-sampled fields (e.g., oxygen, silica, nitrate, and phosphate) (Table 3.2).

For each of the regional RFs used in mapping each of the six variables (Θ, S_A, O_2, $Si(OH)_4$, NO_3^-, PO_4^{3-}), we conducted an error analysis. This was done both to assess how our choice of hyperparameter values (n_preds, n_trees) affected performance and to see how the RF would perform on data that were not used in building the model (i.e., on the test data). Comparing the median absolute error calculated for the RF predictions at the training data locations versus at the

test data locations, allows us to quickly check if the RF is overfitting the training data, which is likely occurring if the training error is substantially smaller than the test error. However, for all six of our mapped variables, the training and test median absolute errors are fairly comparable suggesting that the RFs are probably not overfitting the data (Table 3.3). The test error can also provide an idea of how the RF would perform at locations that were not included in the training data for the model and is sometimes referred to as the "generalization error" in this capacity. While our test data are often near the training data, it is still appropriate to consider the test error as a reasonable approximation to the mapping uncertainty farther from the training locations if we assume that our observations do not miss any anomalous bottom water regimes. We examined the test error estimates with three metrics: the median absolute error (median AE), the root-mean-squared error (RMSE), and the interquartile range of the absolute error (IQR AE) (Table 3.3). Each of these provides a unique view of the test error distribution. Both the median AE and the RMSE approximate the typical value of the test error, though the RMSE is much more sensitive to outliers, while the IQR AE gives an idea of the spread around these typical values. GO-SHIP cruises (a small subset of our total dataset) perform especially high-quality hydrographic observations so the measurement accuracies of our six mapped variables for a typical GO-SHIP cruise are provided as a point of reference for our mapping error estimates (Table 3.3). Using the median AE values from the test data predictions as the "mapping error", we find that the variables earlier in the "stack" have mapping errors either an order of magnitude larger than (for Θ) or comparable to (for S_A) the GO-SHIP measurement accuracies. However, the variables later in the "stack" (oxygen and the nutrients) have mapping errors smaller than the GO-SHIP measurement accuracies (though generally the same order of magnitude), suggesting that we are mapping these variables at high accuracy. This also suggests that as we get further along in this "stacking" the RFs' representations

of the regional relationships between different properties, which are due to the presence of different water masses, continue to improve. This complex, internal representation of these water mass relationships is what could allow this method to interpolate the most sparsely sampled fields better than conventional approaches used in oceanography.

Table 3.3. Training and test error metrics using the Atlantic-only random forests for each of the six RFOM-mapped variables. Measurement accuracies for GO-SHIP data are provided as a point of reference for these values even though not all of the data used in the mappings are measured to this accuracy. The med. AE for the test error is also referred to as the "mapping error" in the text. Med. = median, RMSE = root-mean-squared error, AE = absolute error, IQR = interquartile range, PE = percent error = 100% × (AE/observed value).

Variable	GO-SHIP Measurement Accuracy	Training Error (Med. AE)	Test Error (Med. AE)	Test Error (RMSE)	Test Error (IQR AE)
Θ (°C)	0.002	0.033	0.039	0.127	0.073
S_A (g kg^{-1})	0.002	0.002	0.002	0.007	0.004
O_2 (µmol kg^{-1})	2	0.833	1.252	3.047	1.846
Silica (µmol kg^{-1})	2.5	0.624	0.792	2.083	1.196
Nitrate (µmol kg^{-1})	0.4	0.142	0.210	0.467	0.312
Phosphate (µmol kg^{-1})	0.03	0.012	0.018	0.038	0.027

3.3 RESULTS

Consistent with previous work (e.g., Johnson, 2008; Mantyla & Reid, 1983), we find that bottom waters throughout the global ocean are mainly composed of lower NADW (hereafter, NADW), AABW, Lower Circumpolar Deep Water (LCDW), Pacific Deep Water (PDW), and Indian Deep Water (IDW) (Section 3.3.1). We assign formal definitions to these named water masses below (Section 3.3.1) using water mass properties in order to clearly differentiate between the influence of different sources in the global abyss in our discussion. Generally, NADW is relatively warm,

salty, oxygen-rich, and nutrient-poor while AABW is also oxygen-rich but is colder, fresher, and nutrient-richer than NADW. Ventilation of these two water masses occurs at sites of deep and bottom water formation in the North Atlantic and around Antarctica. LCDW makes up the densest classes of Circumpolar Deep Water which is formed in the Southern Ocean via mixing between bottom, deep, and intermediate waters, including NADW and AABW (Sverdrup, 1940). Since LCDW is not ventilated at the surface, it has lower oxygen concentrations than the recently ventilated NADW and AABW. The nutrient concentrations of LCDW closely resemble the elevated (compared to NADW) values of AABW. The temperature and salinity of LCDW lie between those of NADW and AABW, though closer to those of AABW (Figure 3.2 and see Section 3.3.6 for further discussion of the mixing between these end-members). The classes of PDW and IDW found along the bottom are typically extremely oxygen-poor and nutrient-rich, with lighter densities than the along-bottom classes of LCDW.

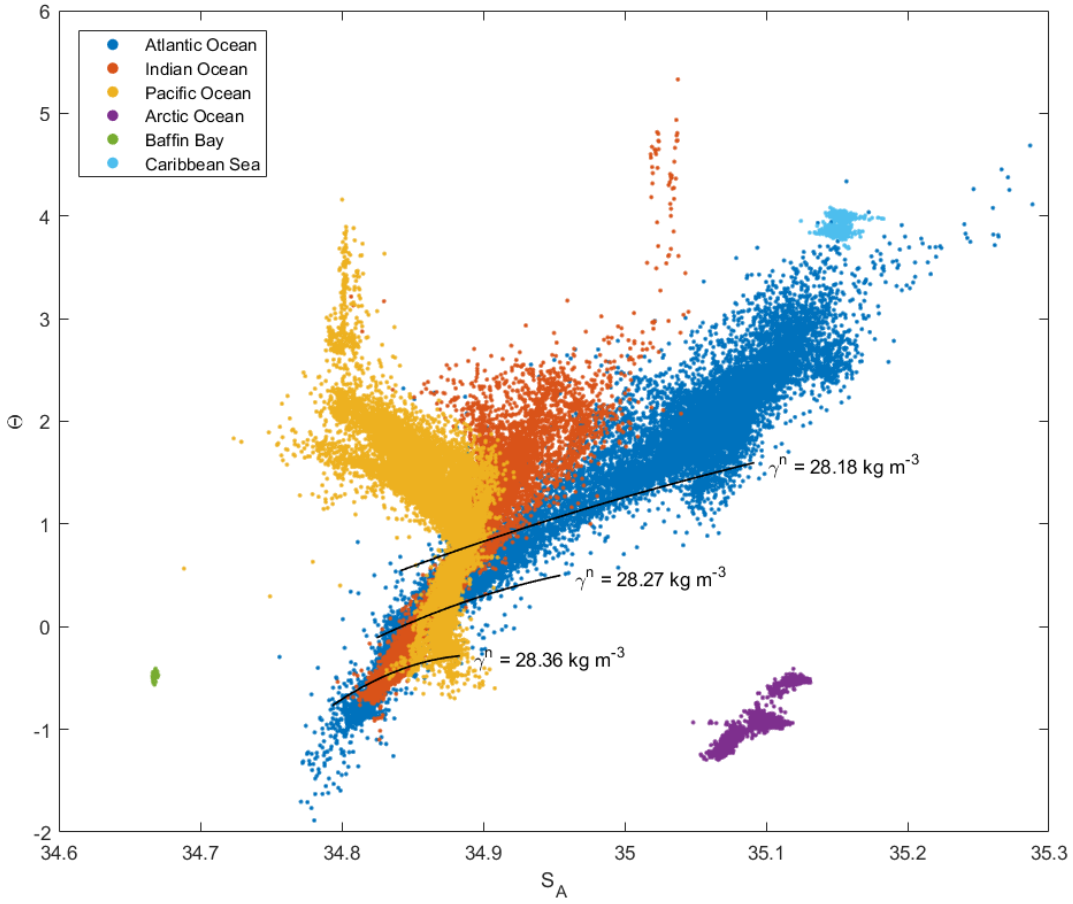

Figure 3.2. Distribution of RFOM-mapped bottom conservative temperature (°C) and absolute salinity (g kg^{-1}) values globally, colored by basin. Black curves approximating the γ^n = 28.18, 28.27, and 28.36 kg m^{-3} surfaces over the range of the data are included for reference. Note that the following basins are off-scale here: the too warm/salty Mediterranean Sea, the too fresh Sea of Japan, and the too warm Sulu Sea.

Below, we use the global bottom water property maps to set water mass boundaries (Section 3.3.1), examine in detail the main sites of bottom water formation (Sections 3.3.2 and 3.3.4), discuss the spreading pathways of these waters from their formation regions (Sections 3.3.3 and 3.3.4), and describe the distinct bottom waters of the shallower Arctic Ocean and Baffin Bay (Section 3.3.5). We then explore the mixing between different bottom water masses by looking at the RFOM-mapped datasets in Θ-S_A and O_2-S_A space (Section 3.3.6).

3.3.1 *Water Mass Definitions*

Near their formation regions, water masses have characteristic sets of property values but farther from these source regions distinguishing between different water masses is not always straightforward. Though the mixing between different named water masses along the seafloor occurs along a continuum, here we assign discrete property ranges to individual water masses of interest to make it clearer where their influence on the bottom property distributions ends. We generally follow the definitions for AABW and LCDW using neutral density (γ^n, as defined by Jackett & McDougall, 1997) proposed by Orsi et al. (1999). They define LCDW (referred to in their work as "Antarctic Circumpolar Current bottom water") as waters of southern origin with $28.18 \leq \gamma^n < 28.27$ kg m^{-3} (disregarding the densest classes of NADW that appear in this density range near Greenland) and AABW as waters with $\gamma^n \geq 28.27$ kg m^{-3}. These neutral density bounds were selected because no bottom water with $\gamma^n < 28.18$ kg m^{-3} or $\gamma^n > 28.27$ kg m^{-3} was found to flow over the shallow region of the Hero Fracture Zone (~65°W) within the Drake Passage. Therefore, since deep or bottom waters with $28.18 \leq \gamma^n < 28.27$ kg m^{-3} were found at all longitudes within the Southern Ocean (i.e., are circumpolar) this density range was used to define LCDW while waters with $\gamma^n \geq 28.27$ kg m^{-3} were designated as the non-circumpolar water mass AABW. For the purposes of our discussion we will use their LCDW definition as stated (which corresponds to waters between the thick red and cyan contours in Figure 3.3b) but further refine their AABW definition to only include waters with $28.27 \leq \gamma^n < 28.36$ kg m^{-3} (i.e., waters between the thick cyan and magenta contours in Figure 3.3b).

We then introduce the term "$AABW_{source}$" to describe the collection of denser source waters for AABW ($\gamma^n \geq 28.36$ kg m^{-3}; i.e., waters denser than those indicated by the thick magenta contour in Figure 3.3b) that Orsi et al. (1999) noted are only found in isolated patches near their formation

regions. These waters are also evident as regions of $\sigma_4 > 46.20$ kg m^{-3} in the maps of Mantyla and Reid (1983). $AABW_{source}$ represents the super-dense, recently ventilated waters at the sites of bottom water formation around Antarctica that have significantly higher oxygen values than AABW and LCDW. These are the waters that set the cold and fresh end points in temperature-salinity space for global bottom waters (Figure 3.2) and include Weddell Sea Bottom Water (WSBW), Ross Sea Bottom Water (RSBW), Adélie Land Bottom Water (ALBW), and Cape Darnley Bottom Water (CDBW), which are all discussed in more detail below. These waters are either too dense to leave their ridge-bounded formation basins without substantial mixing with overlying lighter water masses (in the case of WSBW) or they are only excessively dense near the continental shelf before rapidly entraining lighter waters as they cascade down into deeper basins (in the cases of RSBW, ALBW, and CDBW).

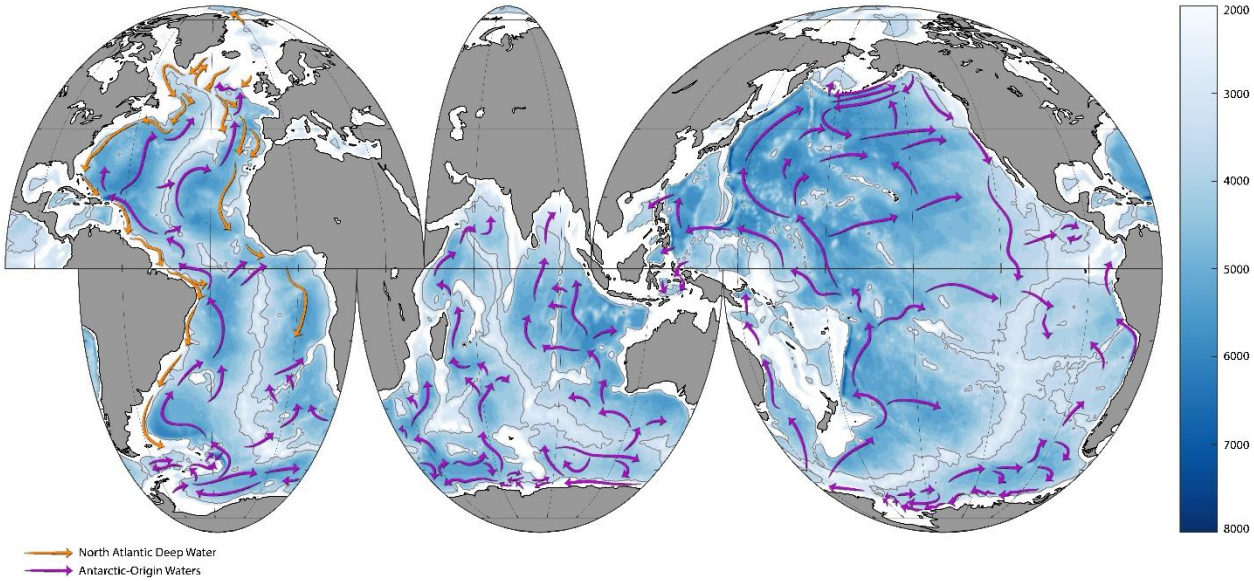
2000
3000
4000
5000
6000
7000
8000
North Atlantic Deep Water
Antarctic-Origin Waters

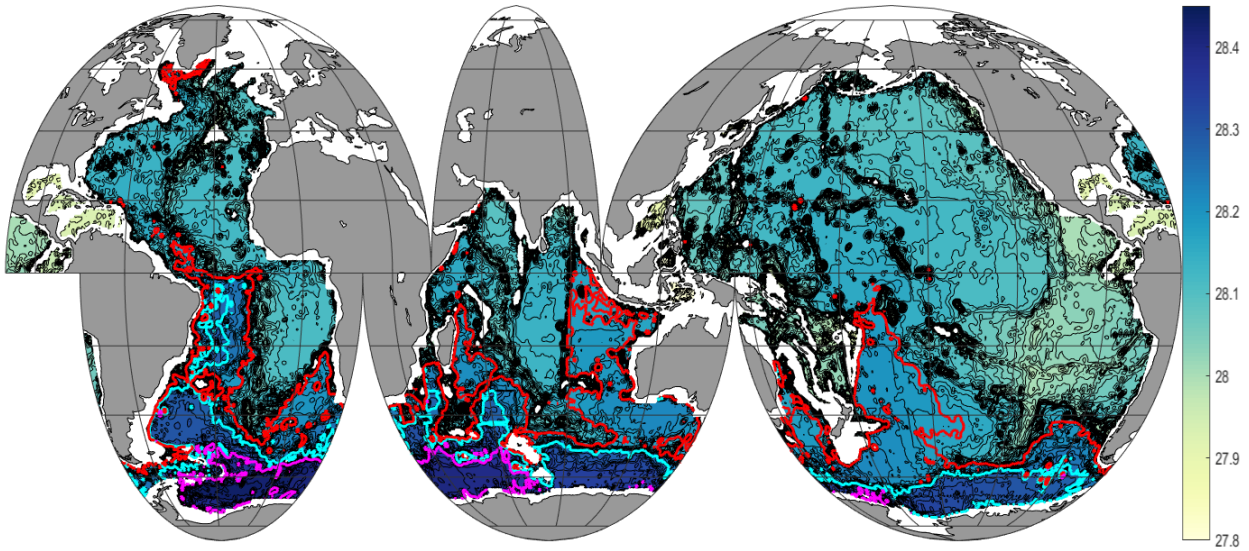
28.4
28.3
28.2
28.1
28
27.9
27.8

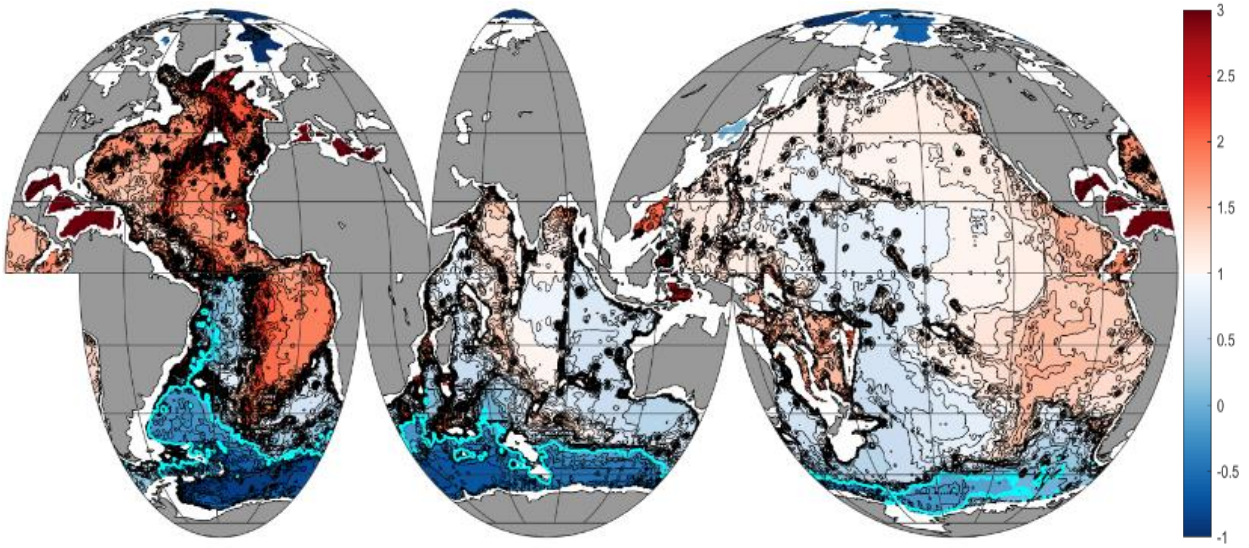
3
2.5
2
1.5
1
0.5
0
-0.5
-1

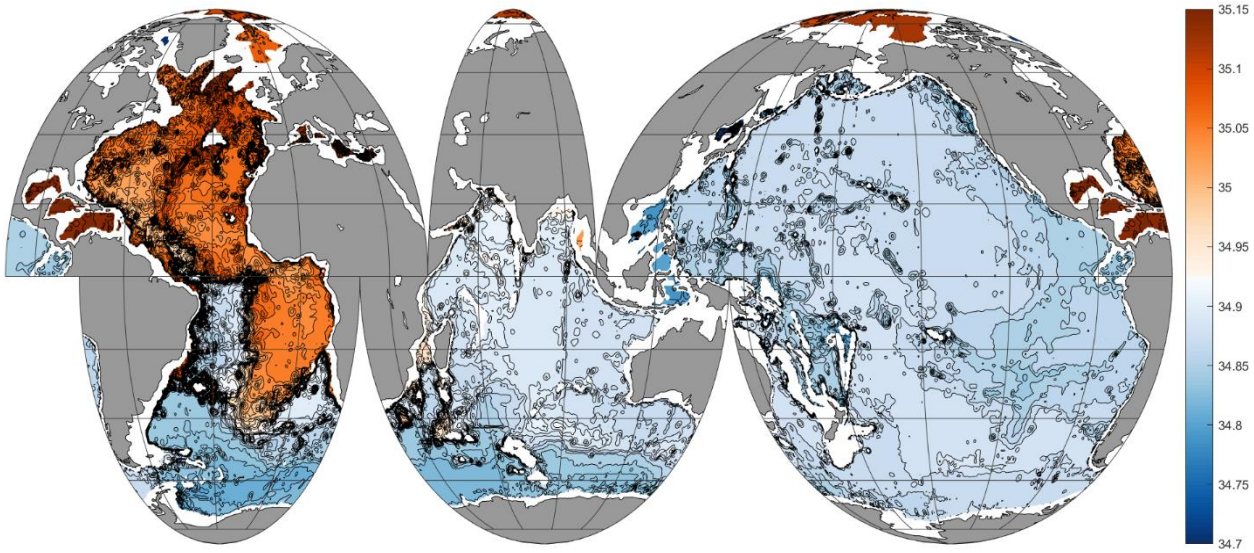
35.15
35.1
35.05
35
34.95
34.9
34.85
34.8
34.75
34.7

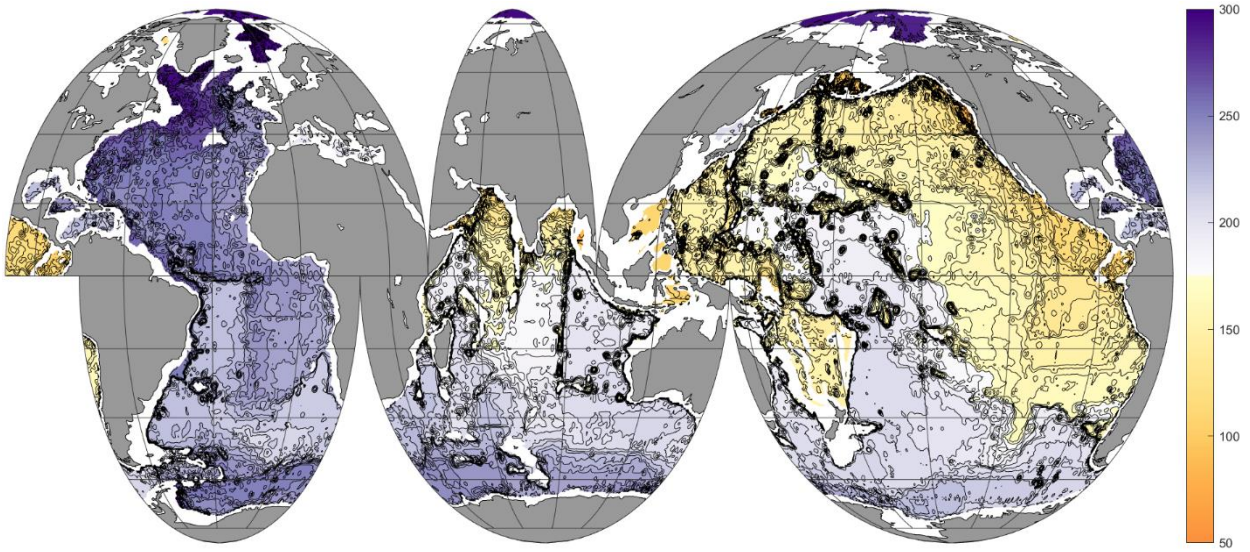
300
250
200
150
100
50

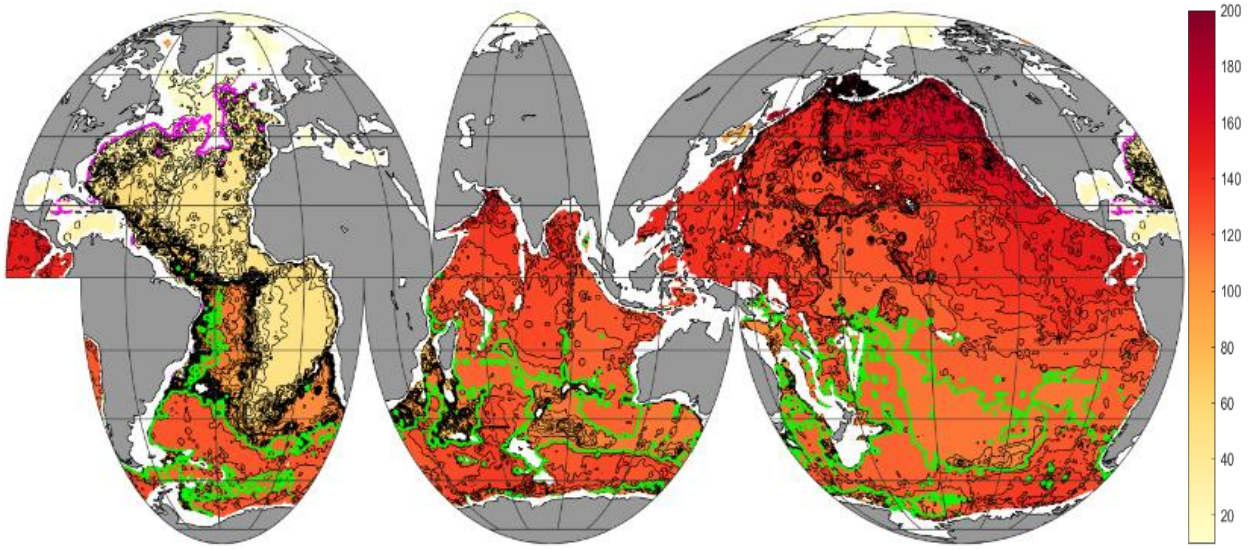
200
180
160
140
120
100
80
60
40
20

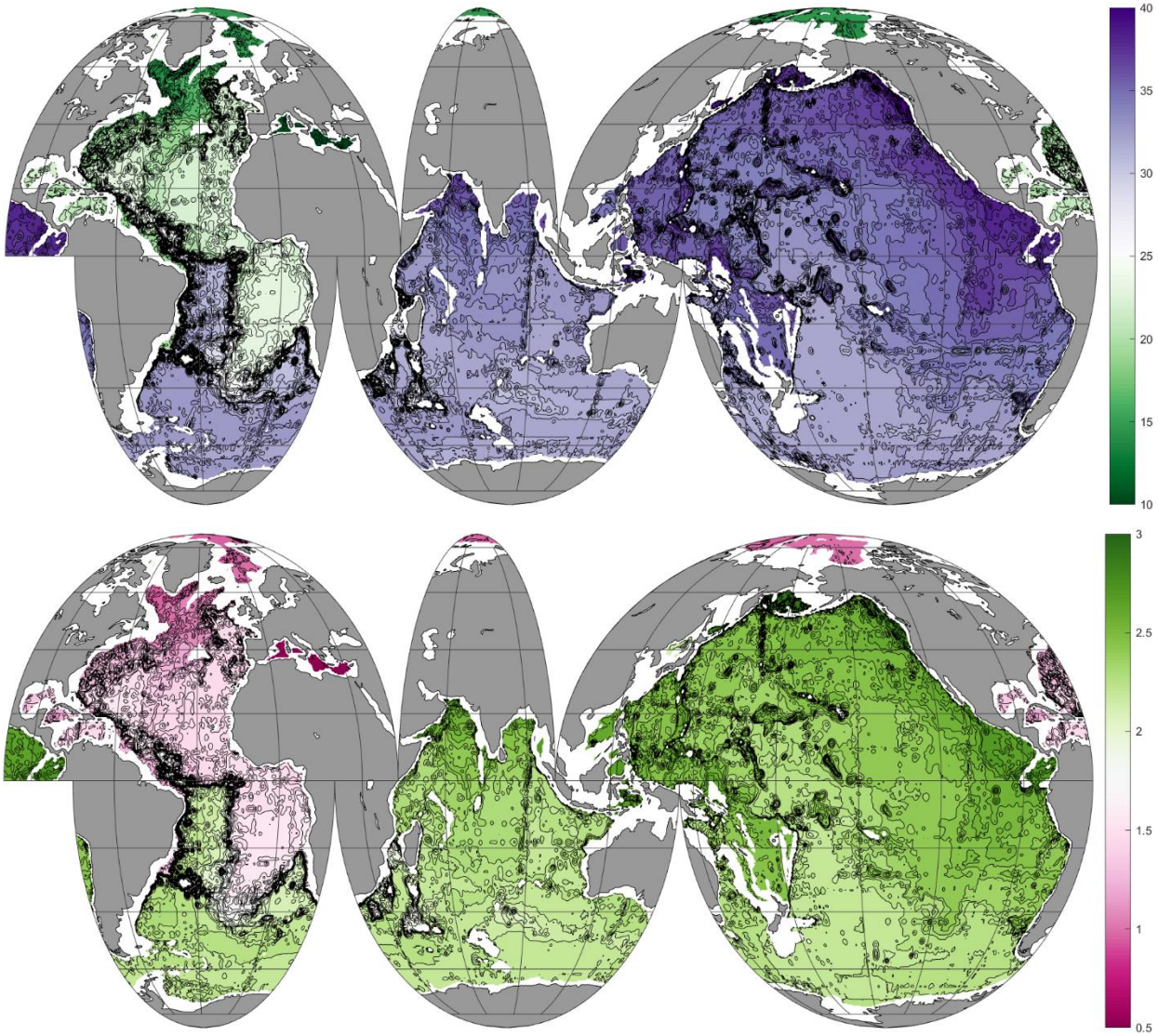

Figure 3.3. a) "ETOPO-60" – ETOPO-2 bathymetry deeper than 2000 meters interpolated to 0.5° resolution (meters, CI = 250) with the 3500-meter isobath highlighted (light grey) and arrows representing the along-bottom flow paths of North Atlantic Deep Water (NADW and AI-NADW; orange) and Antarctic-origin waters ($AABW_{source}$, AABW, LCDW, IDW, PDW; purple) discussed in the text. RFOM-generated maps at 0.5° resolution of b) neutral density (kg m^{-3}, CI = 0.01) with the γ^n = 28.18 (red), 28.27 (cyan), and 28.36 (magenta) kg m^{-3} contours highlighted, c) conservative temperature (°C, CI = 0.1) with the Θ = 0°C contour highlighted (cyan), d) absolute salinity (g kg^{-1}, CI = 0.01), e) dissolved oxygen (µmol kg^{-1}, CI = 5), f) silica (µmol kg^{-1}, CI = 5) with the $[Si(OH)_4]$ = 20 (magenta) and 120 (green) µmol kg^{-1} contours highlighted, g) nitrate (µmol kg^{-1}, CI = 0.5), and h) phosphate (µmol kg^{-1}, CI = 0.05). CI = contour interval.

AABW ($28.27 \leq \gamma^n < 28.36$ kg m^{-3}) is a mixture between the different components of $AABW_{source}$ and overlying water masses such as Weddell Sea Deep Water (WSDW) and LCDW. The boundary of northward AABW flow indicated by this definition (at $\gamma^n = 28.27$ kg m^{-3}, thick cyan contour in Figure 3.3b) is similar to the boundary of the 0°C isotherm (thick cyan contour in Figure 3.3c), a classic definition for AABW (e.g., Gordon, 1972). However, the neutral density definition used here leads to a boundary for AABW that is slightly farther north in most basins (or farther east, in the case of the Southeast Pacific Basin). Due to the mixing it undergoes with overlying, less recently ventilated water masses, AABW has significantly lower oxygen concentrations than $AABW_{source}$. This mixing also reduces the density of these bottom waters enough to enable them to flow over some of shallow sills bordering the Southern Ocean and flow northward along the western boundaries of the southwestern Atlantic and Indian oceans (Figure 3.3b). In the Argentine, Brazil, Agulhas, Natal, and Crozet basins, the AABW is a mixture among WSBW, WSDW, CDBW, and LCDW. In the Australian-Antarctic Basin, the AABW is mixture among RSBW, ALBW, and LCDW, and its northward extent is limited by the Southeast Indian Ridge. In the Southeast Pacific Basin, the AABW is a mixture between RSBW and LCDW, and its northward extent is limited by the Pacific-Antarctic Ridge.

The spreading behavior of the AABW is distinct from that of the LCDW with $28.18 \leq \gamma^n < 28.27$ kg m^{-3} (i.e., waters between the thick red and cyan contours in Figure 3.3b), which escapes northward from the Southern Ocean to fill the abyss of the Cape, Madagascar, South Australian, Tasman, Southwest Pacific, and Southeast Pacific basins. It is this LCDW, not the AABW, that fills most of the abyss globally (Mantyla & Reid, 1983). The flow of AABW into these basins is blocked by shallow sills that trap these denser waters in the basins to the south. At the sill depths, the denser classes of LCDW, which show a clear influence from the colder and fresher AABW

compared to the lighter classes of CDW, flow northward over these sills and act as the source for the abyssal waters in much of the Indian and Pacific oceans. These waters are warmer, saltier, and oxygen-poorer than the AABW that remains trapped in the Southern Ocean basins.

While the properties of NADW and $AABW_{source}$ are quite different near their respective formation regions, determining where the influence of the heavily modified $AABW_{source}$ (i.e., AABW) ends in the subtropical North Atlantic is not straightforward since the neutral densities of NADW and AABW are indistinguishable in this region. In order to meaningfully assess how far the influence of the AABW stretches into the North Atlantic basins on either side of the Mid-Atlantic Ridge, we use the 20 µmol kg^{-1} contour of silica (thick magenta contour, Figure 3.3f) as the boundary between "pure" NADW and NADW-AABW mixtures along the bottom. Hereafter, we will refer to the NADW-AABW mixtures with $\gamma^n < 28.18$ kg m^{-3} and $[Si(OH)_4] > 20$ µmol kg^{-1} as Antarctic-influenced NADW (AI-NADW) since despite their elevated nutrient concentrations and reduced oxygen concentrations (characteristic of Antarctic-origin waters), most waters in this neutral density-silica range lie closer to NADW than AABW in Θ–S_A space (Figure 3.2; Section 3.3.6 for further discussion of the mixing between these end-members). We selected this contour by simultaneously consulting our maps of bottom temperature, salinity, oxygen, and nutrients in conjunction with the regional bathymetry to identify a silica contour that would bound the signals of Antarctic-influence (i.e., relatively nutrient-rich, oxygen-poor, cold, and fresh) spreading northward while respecting the need for coherent and physically reasonable flow paths along the bottom with respect to the bathymetry. Looking at the ratio of silica to nitrate in the bottom waters was also helpful for identifying a clear boundary between the "pure" NADW and the AI-NADW since bottom waters originating from the Southern Ocean are substantially more enriched in silica relative to nitrate than the NADW (Sarmiento et al., 2007). A silica to nitrate ratio (mol mol^{-1}) of

1.2 (not shown) is nearly equivalent in spatial distribution to the silica concentration of 20 µmol kg^{-1}. While our choice of silica concentration is somewhat subjective, we discuss below how the location of our chosen boundary between the "pure" NADW and the AI-NADW is consistent with previous work that analyzed the extent of the Antarctic influence in the North Atlantic bottom waters in greater detail.

The 20 µmol kg^{-1} contour of silica suggests that the influence of Antarctic-origin waters extends up to 46.5°N on the western side of the Mid-Atlantic Ridge in a northward flow at the base of the North Atlantic Current along the western flank of the ridge just northwest of the Azores (thick magenta contour, Figure 3.3f). In the basins to the east of the Mid-Atlantic Ridge, this influence of Antarctic-origin waters reaches as far north as 56°N–57°N in tongues extending into both the Rockall Trough and the southeast corner of the Iceland Basin. A detailed analysis of the North Atlantic found northward spreading of a silica-rich layer along the bottom from the eastern side of the Newfoundland Basin into the southeast corner of the Labrador Basin (McCartney, 1992; their Figure 24b). Their findings agree with ours that this AI-NADW (termed "Lower Deep Water" in their work) flows along the broad western flank of the Mid-Atlantic Ridge up to ~46.5°N in the southeast Labrador Basin. Their work also found elevated silica, reduced temperature, and reduced salinity values relative to "pure" NADW along the bottom in the Rockall Trough and the southeast corner of the Iceland Basin, suggesting a similar distribution of AI-NADW east of the Mid-Atlantic Ridge as implied by our $[Si(OH)_4]$ = 20 µmol kg^{-1} contour. Even earlier work using the conservative tracer PO_4^* (where $PO_4^* = PO_4 + O_2/175 - 1.95$ µmol kg^{-1}) found that NADW at 4000 meters depth begins to show modification by Antarctic waters on both sides of the Mid-Atlantic Ridge at similar latitudes to those shown here (Broecker et al., 1991). Along the western boundary of the North Atlantic, the 20 µmol kg^{-1} contour of silica highlights the southward flow

of the "pure" NADW along the bottom within the Deep Western Boundary Current (thick magenta contour, Figure 3.3f). In our maps this water makes it to 27°N before interacting with Antarctic-origin waters along the bottom and generally getting displaced upwards to shallower depths (consistent with Reid & Lynn, 1971). This "pure" NADW continues to intermittently reappear along the bottom as far south as ~28°S at depths that are too shallow for the AI-NADW and AABW over the shallow continental slope on the western boundary of the Atlantic.

PDW and IDW are modified versions of LCDW that have aged and mixed extensively with the lighter, overlying water masses in their respective oceans (Sverdrup et al., 1942). Both PDW and IDW have temperature and salinity values between those of the warm and salty NADW and the cold and fresh AABW (Figure 3.2). However, PDW and IDW are not found on direct mixing lines between these two end-members because of the influence of overlying regional water masses in these basins (see Section 3.3.6 for further discussion of the mixing lines). IDW is saltier than PDW largely due to the high salt flux into the northern Indian Ocean from nearby evaporative basins (i.e., the Red Sea and Persian Gulf).

In some locations where the residence time of the bottom water flow is especially long and/or the export of organic matter from the surface to the seafloor is especially long, PDW and IDW accumulate large amounts of nutrients due to the remineralization of organic matter within either the bottom waters or the sediments (Edmond 1979). This leads to the along-bottom classes of these water masses being extremely oxygen-poor and nutrient-rich, especially at the northern boundaries of the Pacific and Indian oceans where the moderating influence of the nutrient-poorer LCDW is weaker and the residence times near the bottom are longer. The PDW and IDW found near the seafloor throughout the northeast Pacific and Bering Sea, along the northern boundary of the Arabian Sea, and in the southwest corner of the Bay of Bengal have high silica-to-nitrate ratios

($[Si(OH)_4]:[NO_3^-] \geq 4.2$ mol mol^{-1}; not shown), which indicate that larger amounts of opal dissolution than organic matter remineralization (i.e., nitrate and phosphate addition) are occurring in these basins as well (consistent with Sarmiento et al., 2007) (Sections 3.3.3.2 and 3.3.3.3). The only other basins with similarly high ratios are in the Southern Ocean, specifically the southeast Bellingshausen, southeast and east Enderby, and the central Australian-Antarctic basins as discussed below (Section 3.3.2).

Since PDW and IDW are effectively just LCDW that has been slowly modified over large subsurface regions, there are no hard boundaries between these water masses in the real ocean. However, to aid in our later discussions regarding the spread of Antarctic-origin water in the global bottom water property distributions we introduce distinct definitions of PDW, IDW, and LCDW here. We will consider any water with $\gamma^n < 28.18$ kg m^{-3} and $[Si(OH)_4] > 120$ μmol kg^{-1} (thick green contour, Figure 3.3f) in the Pacific or Indian oceans to be either PDW or IDW, respectively, while LCDW is any water with $28.18 \leq \gamma^n < 28.27$ kg m^{-3} (i.e., waters between the thick red and cyan contours in Figure 3.3b) as noted above.

As a water parcel spends more time away from the surface, its oxygen concentration decreases due to in-situ respiration. Our oxygen map suggests that the "oldest" (i.e., least recently ventilated) waters along the seafloor are found within the along-bottom classes of PDW and IDW in the northeastern and eastern equatorial Pacific Ocean, the Bering Sea, and the northern basins of Indian Ocean (Figure 3.3e). There are many factors that contribute to these basins containing the oldest bottom waters: 1) the LCDW feeding the Pacific and Indian basins is older than the AABW feeding the abyssal Atlantic, 2) there are no other bottom water sources in these basins to refresh the oxygen concentrations, and 3) there are large areas of the North Pacific where the bottom waters flow slowly and undisturbed for a much longer time than in any other basin simply

due to the basin geometry. The bottom waters of Baffin Bay and the Indonesian Seas are similarly oxygen-poor though they are fed by different water masses (Sections 3.3.5 and 3.3.6.2).

Using the water mass definitions above, we assigned the bottom waters within each 0.5° latitude × 0.5° longitude boxes to either $AABW_{source}$, AABW, LCDW, "pure" NADW, AI-NADW, PDW, IDW, Arctic Ocean/Baffin Bay/Nordic seas bottom water, Caribbean Sea/Gulf of Mexico bottom water, Mediterranean Sea bottom water, or "other bottom waters" (Figure 3.4). We then calculated the seafloor area in contact with each of these types of along-bottom water and their mean γ^n (Table 3.4). The mean γ^n for all of the along-bottom waters globally is 28.16 kg m^{-3}, reflecting the high areal coverage of a number of classes lighter than the lighter boundary of our γ^n-based LCDW definition. The largest portion of the seafloor area deeper than 2000 meters is covered by PDW (37.4%), which is not surprising given the large size of the Pacific Ocean and the relative homogeneity of these waters along the bottom. The next most prevalent types of water along the bottom are LCDW (16.6%) and AI-NADW (13.7%), which overlie comparable amounts of the seafloor. AABW (8.2%) and IDW (7.8%) cover smaller, similar portions of the seafloor. The newly-formed bottom waters $AABW_{source}$ (3.1%) and "pure" NADW (1.3%) cover even smaller areas. The bottom waters of the Arctic Ocean, Nordic seas, and Baffin Bay combined cover 1.4% of the total global area. The Caribbean Sea/Gulf of Mexico and Mediterranean Sea bottom waters cover the smallest percentages of the global area (0.7% and 0.3%, respectively). Lastly, the "other bottom waters" are found over 9.5% of the global bottom area below 2000 meters and include the remaining waters with $\gamma^n < 28.18$ kg m^{-3} and silica ≤ 120 μmol kg^{-1}. These waters are generally located in shallower regions like the Sea of Japan and over the East Pacific Rise though some are in deeper regions where the LCDW has become lighter through mixing with PDW or IDW but still has relatively low silica concentrations. In total, waters of Antarctic-origin (i.e.,

AABW, $AABW_{source}$, and LCDW) overlie approximately 1.87 times the seafloor area deeper than 2000 meters as waters dominated by NADW (i.e., "pure" NADW and AI-NADW), consistent with previous analysis suggesting that AABW covers about twice the seafloor area as NADW (Johnson, 2008). Together, the deep waters that intersect with large swaths of the bottom (i.e., PDW, IDW, LCDW, and the "other bottom waters") overlie 2.71 times the seafloor area of the classical bottom waters and their mixtures (i.e., AABW, $AABW_{source}$, "pure" NADW, and AI-NADW). The potential implications of this finding are discussed below.

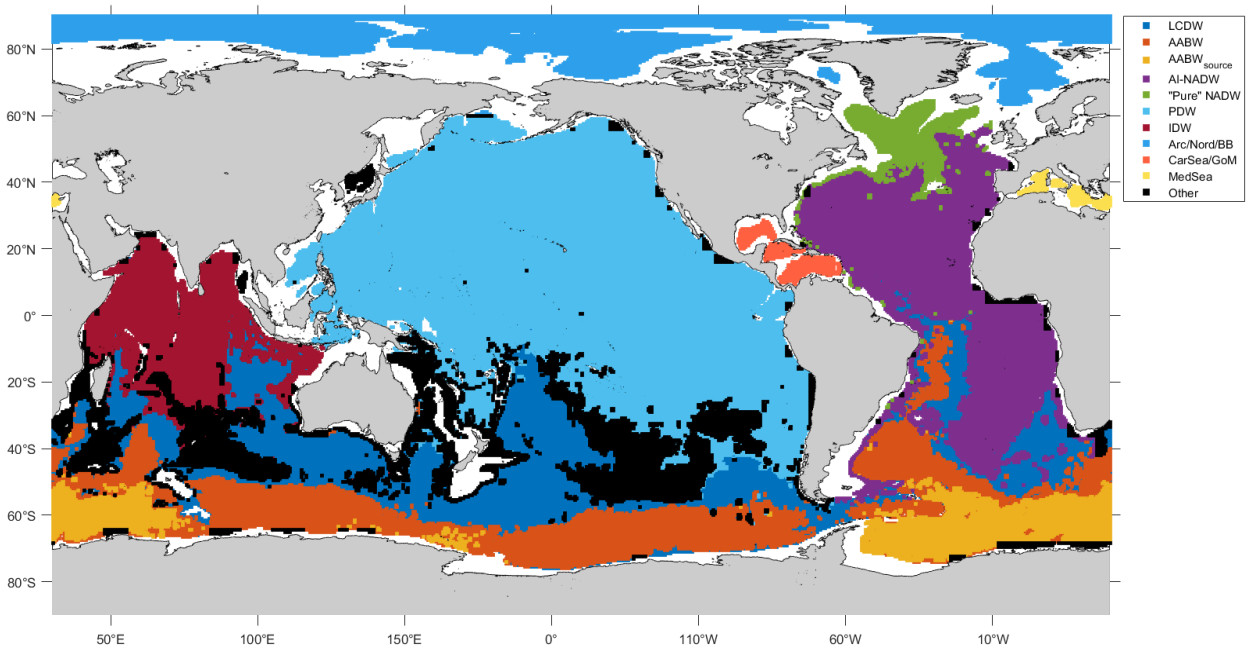

Figure 3.4. Assignments of each 0.5° latitude × 0.5° longitude boxes to one of the along-bottom water masses defined in Section 3.3.1.

Table 3.4. Seafloor area covered by the respective water masses (see definitions in Section 3.3.1 and locations in Figure 3.4) and as a percentage of the total seafloor area ≥ 2000 meters. Mean γ^n for all waters in each type. Dashes indicate basins where the neutral density calculation cannot be performed. BW = bottom water.

	Area (m^2)	Percentage of Total Area ≥ 2000 meters	Mean γ^n ($kg\ m^{-3}$)
PDW	1.14×10^{14}	37.4%	28.08
LCDW	5.07×10^{13}	16.6%	28.22
AI-NADW	4.16×10^{13}	13.7%	28.11
Other BW	2.89×10^{13}	9.5%	28.10
AABW	2.51×10^{13}	8.2%	28.31
IDW	2.38×10^{13}	7.8%	28.12
$AABW_{source}$	9.50×10^{12}	3.1%	28.40
Arctic Ocean/Nordic Seas/Baffin Bay BW	4.26×10^{12}	1.4%	-
"Pure" NADW	3.98×10^{12}	1.3%	28.10
Caribbean Sea/Gulf of Mexico BW	2.25×10^{12}	0.7%	27.93
Mediterranean Sea BW	9.23×10^{11}	0.3%	-
Total Area > 2000 meters	3.05×10^{14}	100%	28.16

3.3.2 *AABW and its Many Constituents*

The bottom waters of the Southern Ocean are dominated by AABW and $AABW_{source}$ (Figure 3.4), but their water properties vary around Antarctica due to the variety of formation mechanisms for the different $AABW_{source}$ types, topographic blocking of the densest waters by shallow sills, and varying degrees of mixing with overlying waters (Figure 3.5). The four main varieties of $AABW_{source}$ are Weddell Sea Bottom Water (WSBW), Ross Sea Bottom Water (RSBW), Adélie Land Bottom Water (ALBW), and Cape Darnley Bottom Water (CDBW) (Johnson, 2008; Ohshima et al., 2013; Orsi et al., 1999; Warren, 1981). WSBW is the dominant source of AABW (~40% of the total), while ALBW, RSBW, and CDBW contribute ~30%, ~20%, and ~10%, respectively (Meredith, 2013). All four water masses are cooler, fresher, and nutrient-richer than NADW, and are especially oxygen-rich and nutrient-poor near their formation regions (Figures

3.5c–3.5h). Below 2000 meters depth, WSBW is the densest, coldest, freshest, and oxygen-richest while RSBW is the warmest, saltiest, and oxygen-poorest. The properties of ALBW and CDBW generally lie between these extremes of WSBW and RSBW. There is relatively little variation in the phosphate and nitrate concentrations among these four water masses and within the bottom waters of the Southern Ocean in general.

Near the four main regions of bottom water formation, the bottom waters are slightly nitrate- and phosphate-poorer than farther downstream, but overall the variations in these properties within the Southern Ocean are still relatively minor (Figures 3.5g and 3.5h). Silica concentrations are also relatively low near the sites of bottom water formation (Figure 3.5f) and this property undergoes more substantial changes than the other two nutrients within the rest of the Southern Ocean, particularly in quiescent regions with heavily opaline sediments (discussed in detail below). Therefore, for the rest of this section we will leave phosphate and nitrate out of our discussion in favor of simply using the more illuminating nutrient – silica.

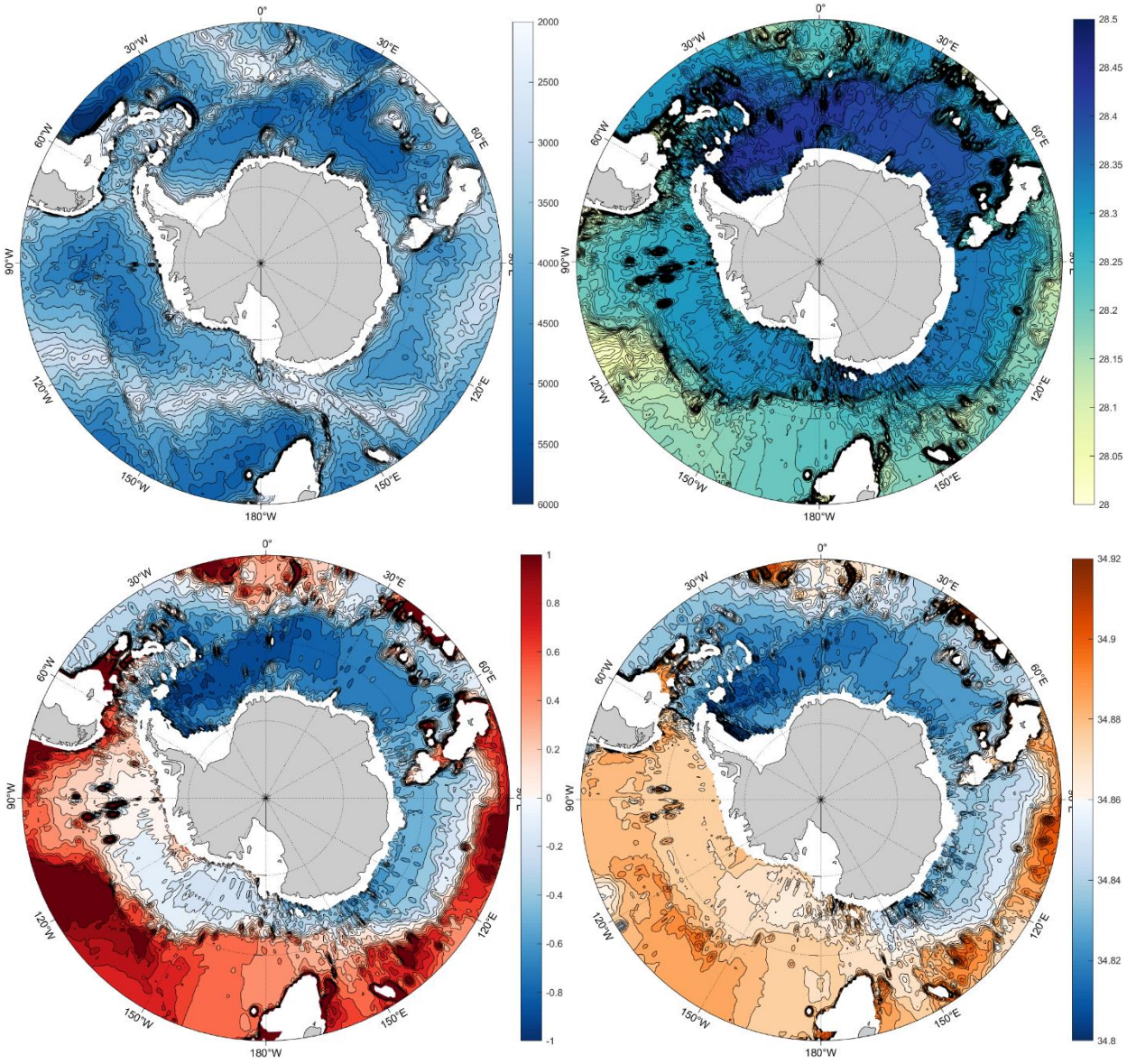
0°
30°W
30°E
60°W
60°E
90°W
90°E
120°W
120°E
150°W
150°E
180°W
2000
2500
3000
3500
4000
4500
5000
5500
6000
28.5
28.45
28.4
28.35
28.3
28.25
28.2
28.15
28.1
28.05
28
1
0.8
0.6
0.4
0.2
0
-0.2
-0.4
-0.6
-0.8
-1
34.92
34.9
34.88
34.86
34.84
34.82
34.8

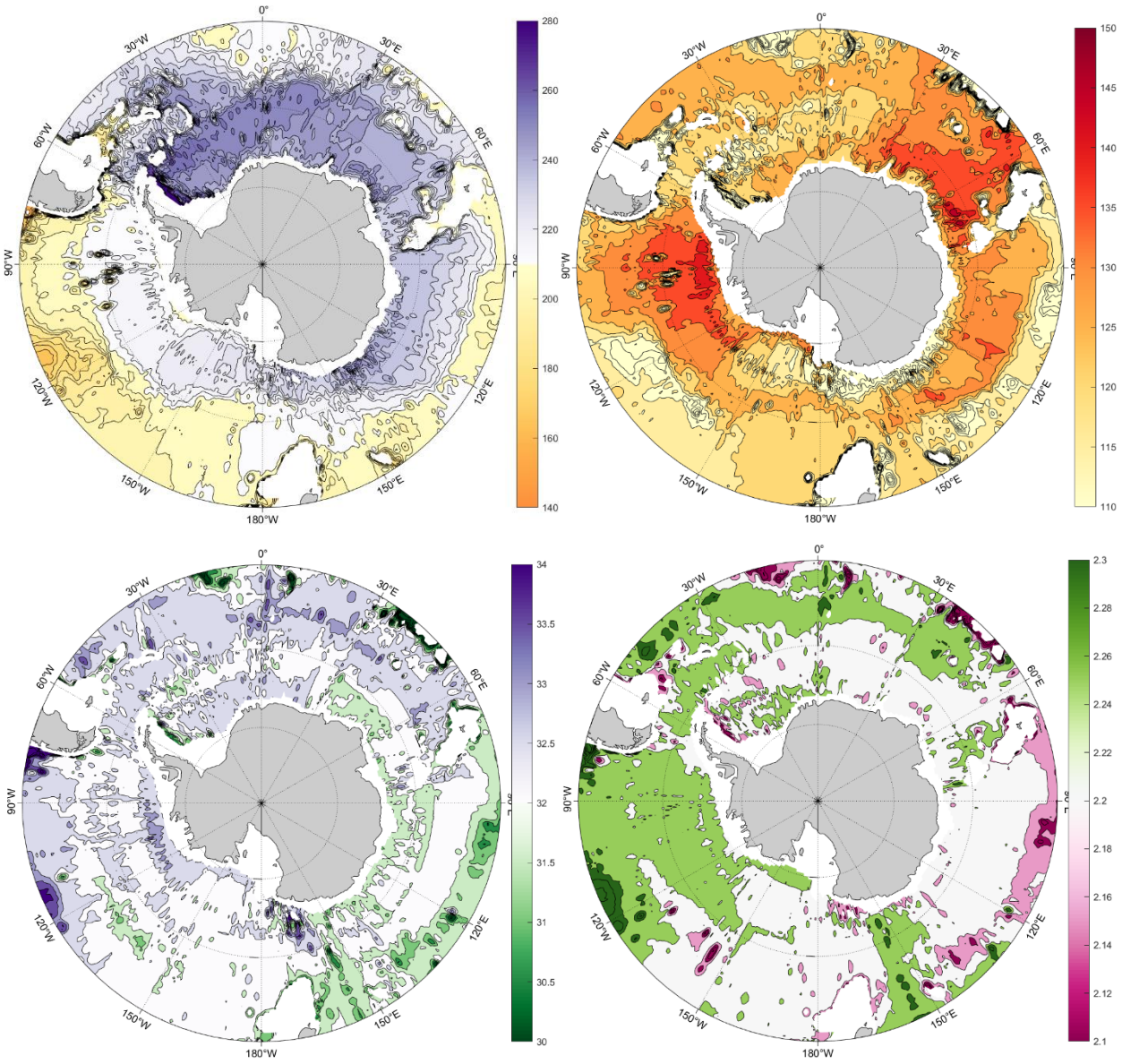

Figure 3.5. a) "ETOPO-60" – ETOPO-2 bathymetry interpolated to 0.5° resolution (meters), RFOM-generated maps at 0.5° resolution of b) neutral density (kg m^{-3}), c) conservative temperature (°C), d) absolute salinity (g kg^{-1}), e) dissolved oxygen (µmol kg^{-1}), f) silica (µmol kg^{-1}), g) nitrate (µmol kg^{-1}), and h) phosphate (µmol kg^{-1}) for the Southern Ocean. Contour intervals are the same as in Figure 3.3 except for absolute salinity (now at 0.005 g kg^{-1} intervals).

3.3.2.1 AABW Sources in the Weddell-Enderby Basin

The Weddell-Enderby Basin contains four distinct bottom water regimes: 1) a WSBW-dominated region within the northward and eastward branches of the Weddell Gyre that stretches from the

western boundary of the basin at ~60°W to ~20°E, 2) a WSBW/WSDW-mixed region along the eastern edge of the Weddell Gyre boundary (~20–30°E) and in its southward and westward return branches, 3) a WSDW-dominated region with elevated silica concentrations in the eastern Enderby Basin with especially high silica concentrations in the southeast corner of the basin, and 4) a CDBW-dominated region along the continental shelf south of the Enderby Basin.

The densest, coldest, freshest, oxygen-richest, and silica-poorest bottom waters in the Southern Ocean (WSBW) are formed on the broad continental shelves along the western and southwestern boundaries of the Weddell Basin (Foster & Carmack, 1976; Mantyla & Reid, 1983). Both the Filchner-Ronne and Larsen C ice shelves play a role in the formation of WSBW as well (e.g., Huhn et al., 2008; Schlosser et al., 1990). The properties of WSBW are modified slightly by lighter overlying waters as it cascades into the deeper areas of the basin and flows northward as a deep western boundary current (Fahrbach et al., 2001). Our maps (Figures 3.5b–3.5f) first show the newly-formed WSBW as plumes of especially dense ($\gamma^n > 28.36$), cold ($\Theta < –0.7$°C), fresh ($S_A < 34.81$ g kg^{-1}), oxygen-rich ($[O_2] > 265$ μmol kg^{-1}), and silica-poor ($[Si(OH)_4] < 95$ μmol kg^{-1}) water extending northward along the continental slope from near the outflow of the Filchner Depression (~74°S, 36°W) and from an area downslope from the Larsen C Ice Shelf (~68°S, 54.5°W). This northward flow of WSBW is eventually steered eastward by South Scotia Ridge and at ~26°W a portion of this flow branches off to the north into the South Sandwich Trench, ultimately flowing into the Georgia Basin (Gordon, 1966; Orsi et al., 1999; Reid et al., 1977; our Section 3.3.3.1). The remainder of the eastward-flowing WSBW in the Weddell Sea continues cyclonically within the Weddell Gyre to ~20°E on our maps.

Within the Weddell Gyre, WSDW overlies the WSBW and slowly mixes with it as both water masses flow around the gyre. WSDW itself is formed via mixing between WSBW and CDW

(sometimes referred to as “Warm Deep Water” within the Weddell-Enderby Basin) (Orsi et al., 1993; Reid et al., 1977). While classes of WSDW span the full mixing line between CDW and WSBW in Θ–S_A space (Section 3.3.6), the densest classes of WSDW found along the bottom in some parts of the Weddell-Enderby Basin more closely resemble WSBW, particularly in terms of their high neutral densities ($\gamma^n > 28.36$ kg m^{-3}), cold temperatures, fresh salinities, and high oxygen concentrations (Figures 3.5b–3.5e). Some of this WSDW that is strongly influenced by the newly-formed WSBW escapes northward from the eastward branch of the Weddell Gyre and into the Scotia Sea via relatively deep gaps in the South Scotia Ridge that block the northward flow of the denser WSBW (Gordon, 1966; Nowlin & Zenk, 1988; our Section 3.3.3.1). Farther from the sites of WSBW formation, the WSDW along the bottom of the Weddell-Enderby Basin has a much higher silica concentration than the WSBW due to influence of multiple bottom silica sources in the eastern and southeastern Enderby Basin (see further discussion below). We use the classical definition for WSBW ($\Theta < –0.7$°C from Carmack & Foster, 1975) to delineate between WSBW and WSDW along the bottom. Their definition actually uses potential temperature < –0.7°C but since conservative temperature is only ~0.002°C warmer than potential temperature across the entire Weddell-Enderby Basin we use the same numerical value.

Between 20°E and 30°E there is an abrupt shift in along-bottom temperature, salinity, oxygen, and silica in our maps as WSDW begins to dominate the bottom waters (Figures 3.5c–3.5f), consistent with the maps of Mantyla & Reid (1983). This increased influence of WSDW is both due to the shallow topography at 15–25°E which blocks the denser WSBW from making it farther eastward and because this is the location of the dynamical eastern boundary of the Weddell Gyre (Deacon, 1979). The densest, coldest ($\Theta < –0.8$°C), and silica-poorest classes of WSBW disappear even earlier along the eastward limb of the gyre because they are blocked by the slightly

shallower topography at 10°E. The WSBW/WSDW mixture present from 20–30°E near the gyre boundary is slightly warmer, saltier, oxygen-poorer, and silica-richer than the pure WSBW advected into this region from the west, reflecting the stronger influence of CDW in this region as noted in previous work (e.g., Mantyla & Reid, 1983). This mixture, with an additional influence of the silica-richer WSDW/CDBW mixture from the east that is discussed below, is then advected southwestward in the return branch of the Weddell Gyre as far as ~44°W generally with $\Theta \geq -0.7$°C. The shallowing topography under this southwestward branch of the gyre also contributes to some of the denser WSBW remaining trapped in the deeper northern regions of the Weddell Basin.

From 30°E to the Kerguelen Plateau (~70°E), the bottom waters of the Weddell-Enderby Basin are dominated by WSDW ($\Theta \geq -0.7$°C) with elevated concentrations of silica (Figures 3.5b and 3.5f). Previous work (e.g., Edmond et al., 1979; Mantyla & Reid, 1983) noted that the WSDW along the bottom becomes increasingly silica-rich as this water slowly continues eastward across the Enderby Basin due to the accumulation of silica flux into the bottom waters from underlying opaline sediments over a large portion of this basin. This mechanism for enhanced silica input without substantial coincident nitrate and phosphate input is consistent with a relative high silica-to-nitrate ratio as described in Section 3.3.1 and such a ratio ($[Si(OH)_4]:[NO_3^-] \geq 4.2$ mol mol^{-1}; not shown) is indeed found over the bulk of the Enderby Basin in our RFOM-mapped fields. Similar regions of high silica input by this mechanism along the seafloor in the cyclonic abyssal gyres within the Australian-Antarctic Basin and Bellingshausen Abyssal Plain are discussed below (Sections 3.3.2.2 and 3.3.2.3).

The highest concentrations of silica in our map of the Southern Ocean (up to ~150 µmol kg^{-1}; Figure 3.5f) are found in a relatively small region of sloping topography in the southeast

corner of the Enderby Basin (58°S–64°S, 62.5°E–74°E), which is bounded by the Elan Bank to the north and the Antarctic continental slope to the south. Jacobs and Georgi (1977) seem to have been the first to note the silica-rich waters immediately offshore of the Antarctic continental slope in the Enderby Basin just west of this region along a meridional section at ~60°E. They found an abrupt transition at the base of the continental slope (63°S) from silica-poor, recently ventilated waters along the continental slope (later named CDBW by Ohshima et al., 2013) to relatively silica-rich, oxygen-poor waters offshore. They proposed a number of processes that could be responsible for the input of silica into the bottom waters offshore, including: "the acquisition of silicate from the highly siliceous bottom sediments (Edmond, 1970; Heath, 1974); increased amounts of siliceous organisms and particulate matter carried down in the newly formed bottom water; high turbidity levels near bottom [sic] over the continental slope (Jacobs et al., 1970, Fig. 13) and in the bottom water (Fig. 14); and the continual input of detritus from higher up in the water column."

Our silica map (Figure 3.5f) shows that the relatively silica-rich signal observed in the bottom waters by Jacobs and Georgi (1977) at 63°S, 60°E originates farther east in a region of especially high silica input from 58°S–64°S, 62.5°E–74°E and that the "silica-rich" signal they observed is actually somewhat attenuated by mixing with CDBW at 60°E (see below). This entire region of high silica input is also at least ~5 μmol kg^{-1} poorer in oxygen that the waters immediately to the west in the Enderby Basin (Figure 3.3e). Our silica map illuminates a cyclonic circulation within this high silica input region that is fed by WSDW entering the region at ~63°E with $[Si(OH)_4] \approx 137$ μmol kg^{-1}, which then continues eastward along the southern flank of the Elan Bank (Figure 3.3f). The silica concentration of this water steadily increases as it circulates around the basin, reaching a maximum value of ~150 μmol kg^{-1} in the westward-flowing return branch.

Recent work observed elevated chlorophyll concentrations at the mouth of Prydz Bay, just south of our observed region of especially high silica input, and noted that south of the Polar Front the plankton community is dominated by diatoms (Sokolov & Rintoul, 2007). This finding, in conjunction with our observations of coincident silica gain and oxygen loss in the bottom waters, supports the idea that silica-rich diatom skeletons could be sinking down the continental shelf into this region, getting remineralized, and thereby contributing to the observed increase in silica concentrations. The localized nature of this input would also explain why this region of especially high silica input is much smaller than the broader region of enhanced silica input over the rest of the Enderby Basin. While it is also possible that the bottom waters in this region have a longer residence time than those over the rest of the Enderby Basin and that it is simply this increased contact time with the seafloor that is responsible for the especially high accumulation of silica in the bottom waters, we think the extra silica input from the coastal diatom-dominated blooms must also be playing a role because the silica-to-nitrate ratio is also somewhat higher in this small region ($[Si(OH)_4]:[NO_3^-] \geq 4.4$ mol mol^{-1}; not shown) than it is over the broader region of silica input over the Enderby Basin. This suggests the contribution of an additional source of silica input with slightly higher silica-to-nitrate ratios than the one found over the rest of the Enderby Basin.

Some of this relatively silica-rich and oxygen-poor WSDW mixes with the "younger" WSDW entering the gyre at ~63°E, slightly attenuating its anomalous signal, and then flows northwestward along isobaths on the shallow eastern edge of the Enderby Basin. Though some of the densest ($\gamma^n > 28.36$ kg m^{-3}) and silica-richest ($[Si(OH)_4] > 135$ µmol kg^{-1}) classes of this water remained trapped south of the shallow sill between the Crozet and Kerguelen islands, some of the lighter, still relatively silica-rich, classes make it into the Crozet Basin. The rest of the silica-rich and oxygen-poor WSDW flows westward out of the high silica input region and into the broader

cyclonic circulation present in the rest of the Enderby Basin. Near the continental shelf at ~60°E the influence of the newly-formed, oxygen-richer, and silica-poorer CDBW (see discussion below) becomes apparent in both the oxygen and silica maps as the WSDW continues westward (Figures 3.5e and 3.5f). At ~30°E the circulation of this modified WSDW bifurcates with some of the flow continuing farther westward to the Weddell Basin and the rest turning northward to remain in the Enderby Basin.

In both branches, the relatively high silica concentrations of the WSDW are somewhat attenuated through mixing with overlying or laterally adjacent waters with lower silica concentrations, such as the "younger" silica-poor WSDW and WSBW arriving from west via the Weddell Gyre. There are no coincident changes in oxygen from mixing with these waters, likely because the CDBW already increased the oxygen concentration in the silica-rich WSDW farther east along the continental slope to similar values as in these "younger" waters. The westward-flowing branch of silica-rich WSDW rejoins the Weddell Gyre and flows within its southwestward return branch along the continental slope as far as ~44°W. The northward-flowing silica-rich WSDW branch in the Enderby Basin ultimately turns eastward within the broad cyclonic circulation of this basin. At 33°E along the northern boundary of the basin, some of this still relatively silica-rich ($[Si(OH)_4] > 130$ μmol kg^{-1}) and dense ($28.18 \leq \gamma^n < 28.36$ kg m^{-3}) WSDW branches off to the northwest into the Agulhas and Natal basins. The fate of these waters is discussed below (Section 3.3.3.2).

The final bottom water regime of interest in the Weddell-Enderby Basin is the CDBW-dominated region along the Antarctic continental slope from approximately 68.5°E to 32°E. Brine rejection from enhanced sea ice formation in the Cape Darnley Polynya (65°E–69°E) leads to the formation of highly saline and dense shelf waters west of ~68.5°E on the continental shelf

(Ohshima et al., 2013). These dense shelf waters cascade down the continental slope, mixing with overlying CDW along the way to become CDBW. Some of this CDBW flows down into the nearby Wild (~67.5°E) and Daly canyons (~63°E–65°E), which bisect the continental shelf, via intermittent gravity currents (Ohshima et al., 2013). CDBW is first visible on our maps at these longitudes from 66.5°S to 64°S as small-scale incursions of dense ($\gamma^n > 28.36$), cold, fresh, oxygen-rich, and silica-poor water into these canyons from the continental shelf region (Figures 3.5b–3.5f). This CDBW is denser than the slightly warmer and saltier ALBW/RSBW mixture flowing into this region along the continental slope from the Princess Elizabeth Trough (described in Section 3.3.2.2). North of 64°S at these longitudes the relatively silica-rich, oxygen-poor signal of the high silica input region described above appears to dominate the bottom waters. Likely either the influence of the CDBW is much weaker than this signal in this region or a sufficient amount of the CDBW does not make it off the steep continental slope and into this region. Farther westward, the signal of CDBW along the continental slope nearly disappears from 63°E to 61°E, likely because the CDBW remains trapped on the continental shelf (specifically, shallower than the 2000-meter isobath) in this longitude range since there are no deep canyons bisecting the continental slope here. At 61°E, the cold ($\Theta < –0.6$°C), fresh, silica-poor, and oxygen-rich signal of CDBW reappears, flowing down the continental slope as far north as 63°S before continuing westward to the Weddell Basin within the Antarctic Slope Current. This downslope flow appears to coincide with the location of the Mawson Canyon (~60.5°E) that bisects the continental slope in this region suggesting that, as in the Wild and Daly canyons to the east, gravity currents transport CDBW from the continental shelf offshore via this canyon. However, we do not presently have direct velocity measurements in this canyon to support the presence of these currents as we do for the Wild and Daly canyons from Ohshima et al. (2013). Since this appears to be the main export

pathway off of the continental shelf for the CDBW that extends into the Weddell Basin, at least in our bottom water maps, a more detailed analysis of this region should be undertaken in the future.

Previous work has attempted to quantify the spread of CDBW to the west. The relatively silica-poor and oxygen-rich signature of CDBW was first noted at 63°S, 60°E by Jacobs and Georgi (1977). The existence of a westward, off-shelf, and narrow flow of CDBW along the bottom beginning at 60°E was then identified in later observations, including measurements of high oxygen concentrations and high westward velocities in meridional sections along 40°E and 60°E, and objectively-mapped measurements of high chlorofluorocarbon (CFC) concentrations in the AABW layer from the CDBW formation region to ~35°E (Aoki et al., 2020; Meijers et al., 2010; Purkey et al., 2018). This westward-propagating CDBW is visible in our maps as a narrow latitudinal band (63°S–65°S) of cold, fresh, oxygen-rich, and silica-poor water from ~61°E to 32°E (Figures 3.5c–3.5f). Since this flow appears to be constrained between roughly the 3700-meter and 4500-meter isobaths, it narrows west of ~41°E where these isopycnals become more tightly packed near the coastline. This flow continues along the continental slope when it turns northward along the eastern flank of the Gunneras Ridge but then appears to separate from the boundary at the northern flank of the ridge (~65°S, 33°E) in a zonal jet that is most clear in our oxygen map (Figure 3.5e). The presence of this plume of along-bottom CDBW extending into the interior from the northern apex of the Gunneras Ridge is supported by previous lowered acoustic Doppler current profiler (LADCP) measurements of strong northwestward and westward velocities near the bottom in this area (Aoki et al., 2020; their Figure 3). The silica-poor and oxygen-rich signal of the CDBW in this jet appears to get mixed away almost immediately after leaving the boundary when it encounters the WSDW flowing westward in the return branch of the Weddell Gyre. However, the silica-poor and oxygen-rich signature of the CDBW actually begins to impact the relatively silica-

rich and oxygen-poor WSDW flowing out of the high silica input region farther east at ~61°E as described above. The moderating influence of the CDBW on the southwestward-flowing, silica-rich WSDW likely persists as far west as ~44°W where the signal of this silica-rich WSDW is mixed away near the western boundary of the Weddell Basin as well as into the branch of WSDW that recirculates within the Enderby Basin (Figure 3.5f).

Onshore of the westward-flowing CDBW from ~59°E westward, the bottom waters are considerably oxygen-poorer but similarly silica-poor to the CDBW (Figures 3.5e and 3.5f). This signal likely corresponds to other waters from the continental shelf region that are not ventilated by the CDBW. These waters flow westward onshore of the 3700-meter isobath over the continental slope as far west as ~34°W where the signal is abruptly overwhelmed by the input of oxygen-richer and even silica-poorer WSBW from the outflow of the Filchner Depression. This signal from the oxygen-poor shelf waters along the seafloor in our maps even spreads farther north into the interior of the basin over major, shallower topographic features extending from the continental slope such as the Maud Rise and Astrid Ridge. Jacobs and Georgi (1977) noted that silica-poor waters are found in many regions near the Antarctic coastline so the presence of these such waters along the shallower portion of the continental slope here is not surprising. Aoki et al. (2020) suggested these waters over the continental slope at 30°E are CDBW. However, they use temperature and salinity to make this assertion which may not allow for distinguishing between CDBW and the less recently ventilated shelf waters as well as when using oxygen and silica as done here. Clearly there are a number of complex water mass interactions occurring along the bottom of the Weddell-Enderby Basin, including two separate regions of bottom water formation and two different regimes of silica input from the seafloor in the Enderby Basin. This situation

leads to substantial variety in the AABW and LCDW that escapes northward from this basin via the pathways described below (Section 3.3.3.1).

3.3.2.2 AABW Sources in the Australian-Antarctic Basin

The Australian-Antarctic Basin contains many different types of bottom water, including ones that are formed in this basin and others that are transported to this region from either the Weddell-Enderby or Ross basins (e.g., Donohue et al., 1999; Rintoul, 1998; Rodman & Gordon, 1982). New bottom water in the Australian-Antarctic Basin is mainly formed along the Adélie and George V Land coasts (136°E–154°E). This water, known as ALBW, is the coldest, freshest, densest ($\gamma^n \approx 28.36$ kg m^{-3}), and oxygen-richest of the bottom waters in this basin (Gordon & Tchernia, 1972; Rintoul, 1998).

There is a striking transition in the bottom waters along the continental slope around 147°E between the "high-salinity" RSBW (Section 3.3.2.3) entering this basin from the southeast and the newly formed ALBW coming off of the continental shelf (Williams et al., 2010). This shift is particularly clear in our temperature, salinity, and oxygen distributions (Figures 3.5c–3.5e). Two types of dense shelf water entrain overlying waters as they cascade down the continental slope to ultimately form ALBW (Williams et al., 2010). One is the "high-salinity" type formed in the Adélie Depression to the west and the other is the "low-salinity" type formed in the Mertz Depression to the east. In our maps, the dense shelf waters formed in the Mertz Depression are first visible at 147°E as plumes of relatively cold, fresh, oxygen-rich, and silica-poor water (Figures 3.5c–3.5f). Beginning at ~144°E the ALBW subtypes from the two sites merge and begin to extend farther offshore. This input of ALBW to bottom waters of the continental shelf region is sufficiently large that it attenuates the deep salinity maximum from RSBW by the time these waters reach 140°E (Rintoul, 1998). Recently Deep Argo float data has allowed quantification of the

interaction of these two water masses from 115°E–155°E near the ALBW formation region in greater detail (Thomas et al., 2020). As for the CDBW in the Enderby Basin, the ALBW/RSBW mixture is then advected farther westward from the ALBW formation region by the Antarctic Slope Current while maintaining a relatively cool, fresh, oxygen-rich, and silica-poor signal compared to the bottom waters farther offshore (Figures 3.5c–3.5f).

Recent work combining data from moorings, shipboard CTDs, Argo floats, and instrumented elephant seals showed that the Vincennes Bay Polynya exports a modest (up to 20% of the volume exported from the Adélie and George V Land sources) amount of AABW (Kitade et al., 2014). However, the AABW produced here is fresher and lighter than the ALBW/RSBW flowing into this region from the west along the continental slope so we do not see this newly produced AABW in our bottom water maps. Kitade et al. (2014) along with other previous work (i.e., Ohshima et al., 2013; Williams et al., 2010), suggests that there may be many smaller sites of AABW formation in East Antarctica from 75°E–135°E, including the Barrier, Shackleton, Dalton, and Dibble polynyas. While we cannot distinguish the contributions of these bottom water sources from the westward-flowing ALBW/RSBW in our maps, these medium-sized polynyas are very sensitive to global temperature changes so it may be important to understand their contributions to global totals of AABW under a changing climate (Kitade et al., 2014).

At ~90°E the westward flow of the ALBW/RSBW mixture along the continental slope bifurcates with ~20 Sv (1 Sv = 10^6 m^3 s^{-1}) of the flow with potential temperature < 0°C continuing westward through the southern Princess Elizabeth Trough and ~12 Sv turning northwestward as a bottom-intensified deep western boundary current along the eastern flank of the Kerguelen Plateau (Fukamachi et al., 2010; Heywood et al., 1999; Rodman & Gordon, 1982). Along the northern Princess Elizabeth Trough, ~3 Sv of the lighter classes of WSDW from the Enderby Basin (still

with potential temperature < 0°C; Heywood et al., 1999) flows eastward. The nearly zonal boundary between the westward-flowing ALBW/RSBW mixture on the southern edge of the trough and the eastward-flowing-WSDW on the northern edge of the trough is most readily observed at 63.5°S, 85°E in our silica map (Figure 3.5f) and is consistent with where a regional study identified this boundary in alignment with the Southern Antarctic Circumpolar Current Front (Heywood et al., 1999). The ALBW/RSBW mixture that flows westward through Princess Elizabeth Trough continues as a plume of relatively silica-poor water along the continental slope until ~67.5°E when the newly-formed, denser and slightly silica-poorer CDBW begins to dominate the bottom waters. East of the Princess Elizabeth Trough, the water entering from the Weddell-Enderby Basin is lighter than the ALBW/RSBW mixture arriving from the west so the signal of the WSDW disappears along the bottom as it is pushed above the ALBW/RSBW mixture. All of these deep and bottom waters then continue northwestward as part of the deep western boundary current along the eastern flank of the Kerguelen Plateau (Donohue et al., 1999).

These waters are eventually steered eastward by the Southeast Indian Ridge and the strong barotropic flow of Antarctic Circumpolar Current. This eastward motion makes up the northern boundary of the cyclonic circulation in the Australian-Antarctic Basin, which is bordered by the westward flow of the Antarctic Slope Current along its southern boundary and the northward flow of the deep western boundary current along its western boundary. The eastward flow is relatively slow compared to the flow at these other boundaries, leading to a steady rise in the silica concentration farther eastward due to enhanced accumulation of the silica flux into the bottom waters from the underlying opaline sediments in this basin (Edmond et al., 1979; McCartney & Donohue, 2007). Consistent with this mechanism of silica addition, the silica-to-nitrate ratio in

this basin is relatively high ($[Si(OH)_4]:[NO_3^-] \geq 4.2$ mol mol^{-1}; not shown), especially near the center of this basin (~115°E) and near its eastern boundary (~140°E).

A series of weaker cyclonic recirculations split off from this eastward flow to return this silica-richer bottom water to the western boundary (McCartney & Donohue, 2007; Stommel & Arons, 1960). We propose two possible configurations of bottom flows that could lead to the region of especially elevated silica concentrations that we see just offshore of the narrow, deep western boundary current along the Kerguelen Plateau that carries a "younger", silica-poorer variety of the ALBW/RSBW mixture as noted above (Figure 3.5f). The first bottom flow configuration is that some of the silica-richer, recirculated ALBW/RSBW mixture simply flows northwestward in a broad current immediately to the east of the narrow, deep western boundary current. The second configuration builds off of previous work (Aoki et al., 2008) that suggested that some of the "younger", silica-poorer ALBW/RSBW could branch off from deep western boundary current around 55°S to recirculate cyclonically just offshore of the boundary current. We see a relatively silica-rich signal in the center of this region (Figure 3.5f) that could be the "older" waters trapped in the interior of this recirculation gyre, lending support to the existence of this feature.

Additionally, near the northern boundary of the Australian-Antarctic Basin the bottom water slowly becomes more LCDW-like (i.e., warmer, saltier, and oxygen-poorer) as more mixing occurs between the bottom waters and the overlying LCDW, and as the bathymetry shoals northward (Figures 3.5c–3.5e). The lighter classes of this LCDW, not the ALBW/RSBW mixture, are what ultimately escape this basin around 126°E to fill the abyssal layer of the South Australian Basin (Section 3.3.3.2). However, farther east some of the recirculated, silica-rich ALBW/RSBW

does pass through the Southeast Indian Ridge via the Balleny Fracture Zone (~155°E) and into the Tasman Sea (Section 3.3.3.3).

3.3.2.3 AABW Sources in the Ross Sea

Dense shelf waters formed on the continental and ice shelves of the Ross Sea cascade down the continental slope in gravity currents, entrain overlying LCDW to transform into RSBW, and then spread from these formation regions to fill the rest of the Southeast Pacific basin via a broad cyclonic gyre circulation (Gordon, 1966; Gordon et al., 2009; Jacobs et al., 1970; Orsi et al., 1999; Purkey et al., 2018). Instead of joining this gyre circulation, some of the RSBW is instead exported westward along the continental slope to the Australian-Antarctic Basin via the Antarctic Slope Current (e.g., Orsi et al., 1999; Purkey et al., 2018).

Two varieties of RSBW with differing salinities are formed and take separate paths off of the continental shelf. “High-salinity” RSBW receives its relatively salty signature from the influence of High Salinity Shelf Waters formed within the Terra Nova Bay polynya (Budillon & Spezie, 2000). These High Salinity Shelf Waters flow down the continental shelf within energetic gravity currents in the Drygalski Trough and mix with overlying LCDW to form “high-salinity” RSBW (Gordon et al., 2009; Jacobs et al., 1970). The signature of this “high-salinity” RSBW first appears just downstream of Cape Adare along the continental slope at ~70°S, 170°E as a plume of super dense ($\gamma^n \geq 28.36$ kg m^{-3}), cold ($\Theta < -0.5$°C), salty, oxygen-rich, and silica-poor water (Figures 3.5b–3.5f). This cold and salty variety of RSBW is the densest $AABW_{source}$ formed in the Ross Sea. It then spreads both westward in a narrow plume along the continental slope (ultimately to the site of ALBW formation in the Australian-Antarctic basin as discussed above) and northward on either side of the Balleny Islands until it encounters the Pacific-Antarctic Ridge.

"Low-salinity" RSBW is formed farther east along the broad Ross Sea continental shelf and ultimately fills the abyss of the entire Southeast Pacific Basin (Gordon, 1966; Jacobs et al., 1970; Orsi et al., 1999). For a full schematic of the circulation of the shelf waters in the Ross Sea at depths shallower than the 2000-meter cut-off value used in our maps, see Figure 1 of Gordon et al. (2009). One export pathway from the shelf region for the "low-salinity" RSBW occurs within the Joides Trough just east of the Drygalski Trough (Gordon et al., 2009). As especially fresh shelf waters cascade down the continental slope in this trough, they entrain overlying LCDW and are deflected westward by the Coriolis force toward Cape Adare. A small plume of this dense ($\gamma^n \approx$ 28.35 kg m^{-3}), cold ($\Theta < -0.3$°C), relatively fresh, oxygen-rich, and silica-poor "low-salinity" RSBW is visible at ~72°S, 178.5°E (Figures 3.5b–3.5f). It spreads westward toward Cape Adare until ~170°E whereupon it turns northeastward into the deeper basin offshore and then continues farther eastward into the Ross Gyre.

Farther east, fresh, formerly supercooled Ice Shelf Waters that form under the Ross Ice Shelf descend the continental slope within the Glomar Challenger Trough, again entraining overlying LCDW during this descent to form more "low-salinity" RSBW (Gordon et al., 2009; Jacobs et al., 1970; Purkey et al., 2018). This outflow of "low-salinity" RSBW from the Glomar Challenger Trough first appears at ~74.5°S, 175°W as a plume of dense ($\gamma^n \geq 28.36$ kg m^{-3}), cold ($\Theta < -0.3$°C), fresh, oxygen-rich, and silica-poor waters (Figures 3.5b–3.5f). From there, these waters flow northwestward along the eastern flank of Iselin Bank, entraining more of the overlying LCDW along the way, which results in these waters being slightly lighter ($\gamma^n \approx 28.34$ kg m^{-3}), warmer ($\Theta \approx -0.2$°C), and silica-richer near the northern flank of Iselin Bank at ~71.5°N (Figures 3.5c and 3.5f). At the northern flank of Iselin Bank, a small portion of this "low-salinity" RSBW continues westward around the tip of the Iselin Bank while most of this water separates from the

boundary and joins the "low-salinity" RSBW from Joides Trough in a broad eastward-flowing plume of cold ($\Theta < -0.1$°C), fresh, oxygen-rich, and silica-poor water that constitutes the northern limb of the cyclonic Ross Gyre (Figures 3.5c–3.5f). This "low-salinity" RSBW flows eastward toward the Amundsen Abyssal Plain while continuing to mix with the overlying LCDW until ~140°W, which is the dynamical boundary of the Ross Gyre that is set by the core of Antarctic Circumpolar Current extending southward through the Udintsev Fracture Zone within the Pacific-Antarctic Ridge at ~56°S, 144°W (Gouretski, 1999). The densest of these waters then turn southward to recirculate within the Ross Gyre.

Only lighter classes of the "low-salinity" RSBW that have undergone substantial mixing with overlying LCDW continue past the eastern boundary of the Ross Gyre and into the weaker cyclonic circulation over the Amundsen and Bellingshausen abyssal plains. At the boundary of the Ross Gyre at ~140°W there is an abrupt transition from the especially cold ($\Theta < -0.1$°C), fresh, oxygen-rich, and silica-poor "low-salinity" RSBW in the west to the lighter ($\gamma^n < 28.32$ kg m^{-3}), warmer, saltier, oxygen-poorer, and silica-richer RSBW/LCDW mixture to the east (Figures 3.5b–3.5f). This change in properties at the eastern boundary of the Ross Gyre appears in previous maps of bottom water properties (e.g., Mantyla & Reid, 1983) though the mechanisms leading to this transition are not discussed. We suggest that a high rate of mixing between the "low-salinity" RSBW and overlying LCDW in this region may be initiated by the rapid descent of the "low-salinity" RSBW into the deeper portion of the Amundsen Abyssal Plain just east of 140°W. The strong influence of LCDW could also explain the relatively low CFC values in the bottom waters east of the gyre boundary observed in previous work (Purkey et al., 2018), though these authors suggested that these low values may simply be due to the RSBW taking a long time to cross this dynamic boundary. The continued eastward flow of the RSBW/LCDW mixture over the rest of

the Southeast Pacific Basin is slow, particularly over the Bellingshausen Abyssal Plain (Gordon, 1966; Purkey et al., 2018). The long residence time of these waters leads to a high accumulation of silica in the bottom waters due to the silica flux from the underlying opaline sediments in this basin (Edmond et al., 1979; Mantyla & Reid, 1983). Once again, the silica-to-nitrate ratio in this basin is relatively high ($[Si(OH)_4]:[NO_3^-] \geq 4.2$ mol mol^{-1}; not shown), consistent with this mechanism of silica input leading to higher relative increases in this property compared to other nutrients.

The steadily increasing concentrations of silica within the bottom waters of the Bellingshausen Abyssal Plain act to illuminate the cyclonic circulation of these waters along the seafloor in this basin – a slow eastward flow that turns southward at the eastern boundary of the basin and then westward along the continental slope (Figure 3.5f). Along this pathway, the temperature of this water increases while the oxygen concentration decreases, implying that further mixing with overlying LCDW and continued in-situ oxygen consumption is also occurring. These waters flow westward along the continental slope within the Antarctic Slope Current from ~77°W to 175°W. The silica-rich, oxygen-poor, and relatively warm ($\Theta > 0$°C) signal of these bottom waters remains clear over this entire longitude range despite continued mixing with the overlying LCDW occurring along the way.

At ~175°W the input of the more recently ventilated, "low-salinity RSBW" from the Glomar Challenger Trough into the bottom waters of the continental slope overwhelms the signal of the "older" RSBW/LCDW mixture arriving from the east. Over the broader continental shelf from approximately 130°W–115°W (offshore of the Getz Ice Shelf) there is anomalously warm ($\Theta > 0$°C), salty, oxygen-poor, and slightly nutrient-poorer water, likely the signal of some LCDW

intruding onto the continental shelf into this region with minimal interaction with dense shelf waters.

In summary, the "high-salinity" RSBW formed in the western Ross Sea makes up the AABW that flows westward along the continental slope to the site of ALBW formation while the "low-salinity" RSBW formed to the east follows a broader cyclonic circulation within the Southeast Pacific Basin. Both of these varieties of RSBW ($\gamma^n \geq 28.27$ kg m^{-3}) are too dense to overcome the shallow topography on the northern (~57°S) and eastern (~73°W) boundaries of the Southeast Pacific Basin. However, the overlying LCDW ($28.18 \leq \gamma^n < 28.27$ kg m^{-3}) does extend north of 57°S into the Mornington Abyssal Plain (bounded to the west by the East Pacific Rise) and some of this water continues even farther northward into the Chile Basin through gaps in the Chile Rise (Section 3.3.3.3).

3.3.3 *AABW/LCDW Pathways Northward*

Beginning with the bottom water spreading out of the Weddell Sea and then moving eastward around Antarctica, we will individually discuss the many northward pathways of AABW and LCDW. These include routes that begin by passing through the Argentine, Cape, Agulhas, Natal, Crozet, South Australian, Tasman, Southwest Pacific, and Southeast Pacific basins. All of these northward flows of AABW and LCDW, in addition to the southward flows of NADW (Section 3.3.4), have been summarized in a single schematic (Figure 3.3a). While much of the northward export of Antarctic-origin bottom waters occurs in deep western boundary currents, there are important transports of these waters in deep eastern boundary currents as well. These eastern boundary flows in the Indian and Pacific oceans (into the South Australian and Chile basins) are spread much farther northward than the one in the Atlantic (into the southern Angola Basin).

3.3.3.1 Atlantic AABW/LCDW Pathways

The main northward pathway of AABW along the western boundary of the Atlantic Ocean begins with flow of WSBW and WSDW from the northwestern Weddell Sea through the Scotia Sea and around its eastern boundary (e.g., Locarnini et al., 1993). Some WSBW flows through the ~3200-meter-deep gap in the South Scotia Ridge at ~42°W known as the Orkney Passage (e.g., Gordon et al., 2001). However, in order to reach the depth of this sill, the WSBW must mix with the overlying WSDW. This is why the WSBW/WSDW mixture along the bottom north of the Orkney Passage is warmer, saltier, oxygen-poorer, and silica-richer than the WSBW along the bottom in the northwestern Weddell Sea (Figures 3.3c–3.3f). Since most of the water in the Scotia Sea has $\Theta \geq -0.7$°C, hereafter we will simply refer to it as WSDW instead of as a WSBW/WSDW mixture.

Once through the gap, the WSDW flow bifurcates. One branch is steered westward by the bathymetry to ~60°W. Here, within the Shackleton Fracture Zone, these waters mix with warmer, saltier, oxygen-poorer, and silica-richer LCDW/PDW from the Southeast Pacific Basin and do not extend farther westward than the Drake Passage (Figures 3.3c–3.3f). These mixed waters then flow eastward to fill the north and central Scotia Sea north of the dynamic Southern Boundary of the Antarctic Circumpolar Current (e.g., Meredith et al., 2008). The other branch of WSDW flows northeastward from the Orkney Passage toward the ~3200-meter-deep Georgia Passage at ~56°S, 31°W. This fairly narrow northeastward-flowing branch of WSDW can be identified in our maps by its dense, cool, and fresh signature relative to the rest of the Scotia Sea bottom waters (Figures 3.3b–3.3d). More WSDW is observed in the eastern Scotia Sea, likely due to flows of WSDW through gaps in the South Sandwich Island arc.

Together, the denser classes of WSDW flowing eastward from the Orkney Passage and the lighter classes of WSDW flowing into the Scotia Sea through gaps in the South Sandwich Island arc form a branch of WSDW that flows out of the Scotia Sea via the Georgia Passage and into the

Georgia Basin (e.g., Meredith et al., 2008). In the Georgia Basin, they are met by additional, slightly denser classes of WSBW/WSDW ($\Theta \approx -0.8°C$; $\gamma^n \geq 28.36$ kg m^{-3}) that flow around the eastern side of the South Sandwich Island arc via the South Sandwich Trench (Figures 3.3b and 3.3c). Again, the densest classes of WSBW do not appear in these waters because the shallow North Weddell Ridge traps them in the Weddell Sea, although these waters that flow around the east side of the South Sandwich Island arc are notably cooler, fresher, and denser than the WSDW that travels through the Scotia Sea.

The mixture of these water masses in the Georgia Basin is quite dense ($\gamma^n \geq 28.36$ kg m^{-3}) but only waters in the AABW neutral density range ($28.27 \leq \gamma^n < 28.36$) are able to escape into the Argentine Basin via deep sills in the northern boundary of the Georgia Basin (Figure 3.3b). From the Georgia Basin, this AABW flows northward along the western boundary of the Argentine Basin with some of this flow eventually turning eastward to recirculate and fill the interior of this basin (e.g., Whitworth et al., 1991). The rest of this AABW flows through the Vema Channel and into the Brazil Basin. In this narrow trough, AABW mixes vigorously with overlying NADW as it moves northward (e.g., McDonagh et al., 2002). Some northward AABW flow from the Argentine Basin to the Brazil Basin through the Hunter Channel can be seen in the temperature map as well, consistent with previous work (e.g., Zenk et al., 1999.). The AABW in the southern Brazil Basin is a bit lighter, warmer, saltier, and nutrient-poorer than the AABW in the Georgia and Argentine basins due to the blocking of the denser AABW classes by the shallow Rio Grande Rise and enhanced mixing within the Vema and Hunter channels (Figures 3.3b–3.3d, 3.3f –3.3h). Within the Brazil Basin, the AABW flows northward to the equator along the western boundary, continuing to mix with overlying NADW along the way.

The AABW spreading pathway at the northern end of the Brazil Basin bifurcates, with some AABW making its way to the eastern equatorial Atlantic (Guinea Basin) via the Romanche and Chain Fracture Zones and the rest continuing along the western boundary into the Guiana Basin (e.g., McCartney and Curry, 1993; Mercier et al., 1994). No bottom water cooler than 0.3°C (Figure 3.3c) or within the neutral density range of AABW ($28.27 \leq \gamma^n < 28.36$ kg m^{-3}; thick cyan contour, Figure 3.3b) is observed farther north than the Brazil Basin. Instead, the bottom waters within the Guinea and Guiana basin are in the neutral density range defined above for LCDW ($28.18 \leq \gamma^n < 28.27$ kg m^{-3}) though they are actually AABW-heavy mixtures with NADW (see Section 3.3.6.1 for further discussion of these mixtures in Θ-$S_{A\ space)}$. Despite these waters being in the neutral density range of LCDW, we chose to differentiate these waters from the more characteristically oxygen-poorer LCDW that enters the Indian and Pacific oceans from the Southern Ocean and the nutrient-poorer AI-NADW in the rest of the north and southeast Atlantic, by referring to these lighter classes of Antarctic-origin water as AABW in the rest of this section. The AABW found along the bottom is warmer and saltier after traveling through the Romanche and Chain Fracture Zones due to the sills blocking the denser classes of AABW and because vigorous mixing occurs in these narrow passages with warmer and saltier waters above (Mercier et al., 1994; Mercier & Morin, 1997). The cooling and freshening influence of the AABW on the southward-flowing AI-NADW in the Guinea Basin (Section 3.3.4) is clear on our maps and extends into the in the Angola Basin (Figures 3.3c and 3.3d). A weaker cooling and freshening influence of these waters on the AI-NADW in the Sierra Leone Basin to the northeast is clear on our maps as well

The AABW flowing northwestward from the Brazil Basin flows along the western boundary of the Ceará Abyssal Plain and is steered offshore within a deep (> 4500 meters), narrow

channel until ~10°N. From the northwest corner of the Brazil Basin to where these waters first turn offshore around the Ceará Ridge into the Equatorial Channel (~3°N, 40°W), the signal of the especially cold, fresh, oxygen-poor, and nutrient-rich classes of AABW waters is substantially attenuated, likely due to enhanced mixing with the overlying NADW in this narrow channel, and a region of slightly less enhanced (though still relatively high) mixing appears to extend even farther north to ~8.5°N, 44°W (Banyte et al., 2018). In our maps, this enhanced mixing over the deep channel is well-illustrated by a change of ~0.8°C in temperature and ~50 μmol kg^{-1} in silica from the initial outflow of the Brazil Basin to the sill at ~8.5°N, 44°W.

Once in the Guiana Basin, the remaining AABW flow bifurcates once again with one branch heading east through the Mid-Atlantic Ridge via the Vema Fracture Zone (~11°N) and the other continuing along the western boundary to the Puerto Rico Trench (~20°N, 65°W). Within the narrow Vema Fracture Zone there is enhanced mixing between the eastward-flowing AABW and the overlying NADW (McCartney et al., 1991), such that the outflow into the Gambia Abyssal Plain is a substantially more NADW-like than the inflowing waters from west of the ridge. We see this attenuation of the AABW signal in our maps where the water flowing into the fracture zone is indeed much denser, cooler, fresher, oxygen-poorer, and nutrient-richer ($\gamma^n \approx 28.17$ kg m^{-3}, $\Theta \approx 1.2$°C, $[Si(OH)_4] \approx 75$ μmol kg^{-1}) than the outflow into the Gambia Abyssal Plain ($\gamma^n \leq 28.15$ kg m^{-3}, $\Theta \geq 1.7$°C, $[Si(OH)_4] \leq 55$ μmol kg^{-1}) (Figures 3.3b–3.3h).

Hereafter, we will refer to the lighter classes of AABW that flow through the Vema Fracture Zone as "Antarctic-origin waters". These waters ($\gamma^n < 28.18$ kg m^{-3}) are no longer formally AABW or LCDW under our neutral density-based definitions but still have a distinctive southern-origin cool, fresh, oxygen-poor, and nutrient-rich signal relative to NADW. Though they fall under the AI-NADW definition laid out in Section 3.3.1 we use the term "Antarctic-origin

waters" here to differentiate these northward-flowing classes of the AI-NADW from the southward-flowing classes of AI-NADW farther east in the basin (Section 3.3.4) that contain older remnants of these outflow waters from the Vema Fracture Zone. Further discussion on the locations of these waters on the Θ-S_A and O_2-S_A mixing lines between AABW and NADW is found below (Section 3.3.6).

The Antarctic-origin waters that flow into the Gambia Abyssal Plain from the Vema Fracture Zone immediately bifurcate into northward and eastward flows (McCartney et al., 1991). The eastward flow extends along the southern boundary of the Gambia Abyssal Plain (the Sierra Leone Rise) as far as the Kane Gap (~9°S, 19.5°W) before returning toward the Mid-Atlantic Ridge in a cyclonic circulation that occupies the interior of the basin. Some of the lighter classes ($\Theta > 1.8$°C) in this westward return flow turn northwestward over the Cape Verde Ridge and into the South Canary Basin (McCartney et al., 1991). Recent observations made within the Kane Gap found that the annual mean transport of "AABW" (potential temperature < 1.9°C) through this passage is almost zero, alternating between northward and southward flow multiple times over the course of the year, with small transports that only reach at most 50 km into the adjacent basins (Morozov et al., 2013). Therefore, it is not surprising that we do not resolve any exchange between the slightly more AABW-like bottom waters of the Sierra Leone Basin and the more NADW-like bottom waters of the Gambia Abyssal Plain over this gap in our maps.

The Antarctic-origin water that flows northward from the Vema Fracture Zone does so as a western boundary current along the eastern flank of the Mid-Atlantic Ridge (McCartney et al., 1991). This flow and the northwestward flow from the cyclonic recirculation gyre in the Gambia Abyssal Plain appear to combine at ~17.5°N just after entering the South Canary Basin ($\Theta \approx$ 1.85°C) before continuing northward along the western boundary of this basin. The eastern side

of this basin contains the southward-flowing AI-NADW (Section 3.3.4). The flow of Antarctic-origin water along the boundary is deflected eastward by a zonal extension of the Mid-Atlantic Ridge at ~27°N. This flow then continues northward along the eastern boundary of the North Canary Basin (McCartney et al., 1991). At this point it begins to become much harder to distinguish between the northward-flowing Antarctic-origin waters and southward flow of AI-NADW that originates in the West European Basin. However, in our temperature and salinity maps it is still possible to distinguish some plumes of the cooler and fresher Antarctic-origin water extending either northward into the Madeira Abyssal Plain or northeastward into the "dead-end" Seine Abyssal Plain.

The water that flows into the Seine Abyssal Plain goes on to mix along the bottom with a super saline variety of NADW ($S_A \geq 35.12$ g kg^{-1}; Figure 3.3c) formed near the Strait of Gibraltar due to the influence of the salty overlying Mediterranean Sea Overflow Water (Harvey & Arhan, 1988). Some of the flow into the Madeira Abyssal Plain extends even farther north, flowing through the East Azores Fracture Zone (~37°N) to reach the Iberian Basin. The influence of these waters ([$Si(OH)_4$] > 20 μmol kg^{-1}) is observed throughout the West European Basin with clear plumes of relatively fresher water with $\Theta \approx 2.3$°C extending from the West European Basin into the Rockall Trough and toward the southeast corner of the Iceland Basin. The interaction of these Antarctic-origin waters and the "pure" NADW in these basins is discussed in more detail below (Section 3.3.4).

The denser AABW that remains along the western boundary of the Guiana Basin eventually makes its way to the Puerto Rico Trench as a narrow jet of cool ($\Theta \leq 1.45$°C), fresh, oxygen-poor, and nutrient-rich ([$Si(OH)_4$] ≥ 60 μmol kg^{-1}) water (Figures 3.3c–3.3h). Some lighter classes of AABW (i.e., "Antarctic-origin waters") then continue northward along the western

boundary to ~27°N and into the Hatteras Abyssal Plain where substantial mixing occurs along the bottom with the southward-flowing NADW (Reid & Lynn, 1971). Around 20°N, another flow of these Antarctic-origin waters branches off from the western boundary, extending northeastward as a plume of relatively cool, fresh, oxygen-poor, and nutrient-rich water that become increasingly characteristic of NADW as it continues across the interior of the Nares Abyssal Plain and North American Basin (Figures 3.3c–3.3h). At ~32°N, this flow bifurcates around the Corner Rise Seamounts. One branch of this flow continues northward into the Sohm Abyssal Plain and the Newfoundland Basin to interact with NADW spreading from the western boundary therein (Section 3.3.4). The other branch continues northeastward along the western flank of the Mid-Atlantic Ridge to ~46.5°N (northern limit of the $[Si(OH)_4] = 20$ μmol kg^{-1} contour; thick magenta contour, Figure 3.3f), constrained to the eastern boundaries of the Newfoundland and southeast Labrador basins (i.e., the ridge flank) under the North Atlantic Current, before getting mixed away by the along-bottom NADW in the interior of these basins.

Another entry point for dense Antarctic-origin waters into the South Atlantic is via gaps in the southern extent of the Mid-Atlantic Ridge (e.g., at 50°S, 8°W). Some LCDW appears to make its way to the Cape Basin from the Southern Ocean through these gaps by first flowing into the basin west of Meteor Rise and then into the Cape Basin through a gap between the Discovery Seamounts and the Agulhas Ridge. None of the LCDW that arrives in the Cape Basin is cooler than 0.5°C since the shallow topography along this pathway restricts the northward flow of the denser LCDW classes more strongly influenced by the cold and fresh WSBW/WSDW. The Cape Basin is also filled by LCDW that exits the Southern Ocean via the Agulhas Basin. This pathway is discussed below (Section 3.3.3.2).

While most of the LCDW that fills the abyss of the Cape Basin remains trapped in this basin due to the presence of the shallow Walvis Ridge to the north, a small amount makes its way through gaps in this ridge to enter the Angola Basin at ~36°S, 7°W (Walvis Passage) and ~32°S, 3°W (Connary & Ewing, 1974; Shannon & Chapman, 1991). To the best of our knowledge, our maps are the first to visualize the full spreading pathway of the LCDW flow ($\Theta \leq 1.9$°C) within the southwest Angola Basin at high-resolution before its signal is mixed away by the southward-flowing AI-NADW that dominates the bottom waters in most of this basin (Sections 3.3.4 and 3.3.6). The flow through ~32°S, 3°W (Shannon & Chapman, 1991) was not discovered until after the publication of the global bottom water property maps of Mantyla and Reid (1983). In our maps (Figure 3.3), it appears that the LCDW ($\Theta \leq 1.9$°C, ($[Si(OH)_4] > 55$ µmol kg^{-1} here) that passes through the Walvis Ridge either spreads northward to ~32°S along the eastern flank of the Mid-Atlantic Ridge from the southwesternmost corner of this basin, potentially in the deep western boundary current theorized by Warren and Speer (1991), or northeastward to ~25°S, 4°E along the northern flank of the Walvis Ridge in a topographically-constrained current that has yet to be directly measured before its signal along the bottom is attenuated.

3.3.3.2 Indian AABW/LCDW Pathways

A substantial amount of WSDW enters the Agulhas Basin through a gap in the Southwest Indian Ridge at ~50°S, 30°E just northwest of Conrad Rise (e.g., Mantyla & Reid, 1995). The denser classes of WSBW and WSDW ($\gamma^n \geq 28.36$ kg m^{-3}; Figure 3.3b) remain trapped to the south due to the shallowness of this gap. The water that flows northwestward through this passageway is AABW formed via mixing between the LCDW and the WSDW from east of the Weddell Gyre boundary. This AABW is slightly silica-richer than the AABW that reaches the Argentine Basin due to influence of the older, recirculated WSDW along the seafloor which accumulates large

amounts of silica in the eastern and southeastern Enderby Basin (Figure 3.3f). The AABW that reaches the Argentine Basin is strongly influenced by the more recently ventilated, and thereby silica-poorer, WSBW and WSDW.

Once through the ridge, the AABW flow bifurcates in the Agulhas Basin. Some of the AABW continues northwestward toward the Cape Basin with the shallow topography southwest of the Agulhas Plateau blocking any classes of this water cooler than 0°C (and with $\gamma^n \geq 28.27$ kg m^{-3}) and the Agulhas Ridge blocking any classes cooler than 0.5°C. The fate of the > 0.5°C bottom waters that reach the Cape Basin is discussed above (Section 3.3.3.1). Overall, the waters that fill the abyss of the Cape Basin both via this pathway and the one discussed above are more characteristic of the warmer and saltier LCDW with $28.18 \leq \gamma^n < 28.27$ kg m^{-3} than the colder, fresher, and denser AABW. This variety of LCDW is saltier and nutrient-poorer than the LCDW found along the bottom of the Indian and Pacific basins. These attributes are due to the stronger influence of the salty and nutrient-poor NADW in the Atlantic sector of the Southern Ocean than in the Indian and Pacific sectors. The uniqueness of this heavily NADW-influenced LCDW variety is even clearer in our analysis of the property-property diagrams below (Section 3.3.6).

The rest of the AABW in the Agulhas Basin flows northeastward into the Natal Basin and is joined by a small amount of AABW that flows from the Enderby Basin via the Prince Edward Fracture Zone along ~35°E (Boswell & Smythe-Wright, 2002). This flow continues northward into the Mozambique Basin within a deep western boundary current along the Mozambique Plateau (e.g., Donohue & Toole, 2003). The northward progress of this AABW is then impeded by the shallow Mozambique Channel that extends between Madagascar and the African continent. Along this flow path, the waters north of ~33°S are slightly lighter than AABW (i.e., with $\gamma^n <$ 28.27 kg m^{-3}) and therefore more characteristic of the densest classes of the overlying warmer and

saltier LCDW. Overlying this AABW/densest LCDW is the same heavily NADW-influenced LCDW found in the Cape Basin. Some of this heavily NADW-influenced LCDW makes its way over the slightly shallower topography between the Agulhas and Mozambique plateaus to fill the abyss of the Transkei Basin. This is the only basin other than the Cape Basin where this variety of LCDW is found over a large region of the seafloor.

The strong influence of AABW and LCDW on the bottom waters in the western Indian Ocean basins originates just west of Kerguelen Plateau and extends northward to ~11°N. This pathway begins with flow of WSDW over the sill between the Crozet and Kerguelen islands. As with the flow of WSDW into the Agulhas Basin, many of the denser classes of WSDW ($\gamma^n \geq 28.36$ kg m^{-3}) remain trapped to the south of this sill in the Enderby Basin, such that only the mixtures between WSDW and LCDW (i.e., AABW, $28.27 \leq \gamma^n < 28.36$ kg m^{-3}) can escape into the Crozet Basin. This AABW then continues northeastward along the western edge of the Crozet Basin until ~33°S when the bathymetry begins to shoal toward the Central Indian Ridge and LCDW ($28.18 \leq \gamma^n < 28.27$ kg m^{-3}) starts to dominate the bottom waters.

Some of this LCDW flows northwestward through a number of gaps in the Southwest Indian Ridge and into the Madagascar Basin. Most of this transport through the ridge occurs via the Atlantis II Fracture Zone (~57°E) with lesser amounts flowing through the Melville (~60.5°E) and Indomed (~46°E) fracture zones (e.g., MacKinnon et al., 2008; Toole & Warren, 1993; Warren, 1978). The LCDW along the bottom of the Madagascar Basin is generally warmer ($\Theta >$ 0.5°C) and saltier than the LCDW along the bottom of the northern Crozet Basin likely due a combination of shallow topography blocking the flow of the denser LCDW classes and enhanced mixing with the overlying, lighter LCDW classes occurring within the fracture zones. This elevated mixing has previously been observed directly in the Atlantis II Fracture Zone

(MacKinnon et al., 2008). The LCDW that reaches the Madagascar Basin fills its abyss with relatively homogenous properties, suggesting little modification by the overlying waters occurs within the interior of this basin and making it difficult to infer from our maps the direction of the bottom flow within the basin. Previous work found that upon entering the Madagascar Basin the along-bottom LCDW flows westward until it reaches the Madagascar Ridge at which point it turns northward in a deep western boundary current, as part of a cyclonic circulation within this basin (Donohue & Toole, 2003).

As this flow continues northward over a slightly shallower sill into the Mascarene Basin, some of the slightly cooler ($\Theta < 0.6$°C) and fresher classes of LCDW remain trapped in the Madagascar Basin. The northward flow of the LCDW in the Mascarene Basin in our maps (Figure 3.3) appears to be constrained within a deep western boundary current along the coast of Madagascar consistent with previous observations (e.g., Donohue & Toole, 2003). The northern boundary of the Mascarene Basin is roughly the northern extent of our formally defined LCDW along this pathway ($28.18 \leq \gamma^n < 28.27$ kg m^{-3}; Figure 3.3b). However, previous work (Johnson et al., 1998) observed a northward flow of bottom waters that are cooler ($\Theta = 0.8$–0.9°C), fresher, oxygen-richer, and nutrient-poorer than IDW (i.e., more LCDW-like) from the Mascarene Basin to the Somali Basin via the Amirante Passage (9°S, 53°E). An identical plume of LCDW-like bottom water appears in our property maps, filling the abyssal Somali Basin from the south via the Amirante Passage (Figures 3.3c–3.3h). This LCDW-like signal extends as far north as 11°N where the Carlsberg Ridge blocks the northward flow of all but the warmest classes of this water ($\Theta \approx 1.2$°C), which then flow through the ridge via the Owen Fracture Zone at ~10°N, 57°E (e.g., Quadfasel et al., 1997) to reach the Arabian Basin.

Once in the Arabian Basin, this flow bifurcates with some of it turning southeastward to flow along the northern flank of the ridge (Johnson et al., 1991) while the rest flows northward along the western boundary of the basin. Along both of these branches these waters mix with the along-bottom classes of IDW that occupy the bulk of bottom waters in this basin. The slightly cool and fresh signal of these bottom waters along the southern and western boundaries of the Arabian Basin is evident in our maps, as is the attenuation of this signal farther from the Owen Fracture Zone (Figures 3.3c and 3.3d).

The mixture of the LCDW-like waters and the IDW found along the bottom of the northern Arabian Basin is influenced by two main overlying water masses that are much warmer and saltier. These are regional varieties of IDW that are strongly influenced by downward diffusion of either the highly saline Red Sea Water (RSW) or the highly saline Persian Gulf Water (PGW) (Beal et al., 2000) (Section 3.3.6). IDW that is especially strongly influenced by RSW appears along the bottom in our maps as a plume of water extending from the Gulf of Aden to approximately the 3500-meter isobath in the Arabian Basin. It is much warmer ($\Theta \geq 1.7°C$) and saltier than the LCDW-like bottom waters and along-bottom classes of IDW that occupy the most of the interior of the Arabian Basin (Figures 3.3c and 3.3d). These waters are also much oxygen-poorer and nutrient-richer than the LCDW-like bottom waters flowing northward (Figures 3.3e–3.3h).

As the mixture of LCDW-like bottom waters and along-bottom classes of IDW flows northward in the Arabian Basin, it becomes oxygen-poorer and nutrient-richer along the western and northern boundaries of this basin. This is due to the regeneration along the seafloor of large amounts of organic material (likely fecal pellets and diatomaceous remains) deposited under the seasonal upwelling zones in these areas (Edmond et al., 1979). At the northeastern corner of the Arabian Basin, the bathymetry shoals considerably and the bottom waters become especially warm

($\Theta \geq 2.1$°C) and salty (Figures 3.3c and 3.3d) due to a stronger influence of PGW on the bottom waters at these shallower depths (Beal et al., 2000). These bottom waters are also the oxygen-poorest and nutrient-richest waters in the Arabian Basin, reflecting their close proximity to highly productive coastal upwelling zones and riverine discharge (e.g., from the Indus River) and the associated remineralization of organic matter along the seafloor. As the oxygen-poor, nutrient-rich IDW along the seafloor turns southward to recirculate within the eastern and central Arabian Basin before ultimately being exported southward at shallower depths (e.g., Edmond et al., 1979), its anomalous oxygen and nutrient signals slowly get attenuated along the bottom as it interacts with the LCDW-like bottom waters that flow eastward from the Owen Fracture Zone.

The strong influence of LCDW ($28.18 \leq \gamma^n < 28.27$ kg m^{-3}) on the eastern and central basins of the Indian Ocean begins with flow into the South Australian Basin around 50°S, 126°E and extends as far north as ~12°N. As noted above, in the Australian-Antarctic Basin the AABW is a mixture of LCDW, ALBW, and "high-salinity" RSBW with an increasingly high proportion of LCDW as these waters extend farther northward toward the northern boundary of this basin (Section 3.3.2.2). At ~51°S, these waters encounter the Southeast Indian Ridge and some of the lighter classes ($\Theta \geq 0.4$°C) continue farther northward through the Australian-Antarctic Discordance and into the South Australian Basin, specifically through the set of deep fracture zones from ~125.5°E–127°E (Schodlok et al., 1997). The denser AABW and $AABW_{source}$ ($\gamma^n \geq 28.18$ kg m^{-3}) remain trapped to the south in the Australian-Antarctic Basin. While the LCDW that fills the bottom layer of the South Australian Basin is lighter, warmer, saltier, and oxygen-poorer than the AABW and $AABW_{source}$ found south of the ridge as one might expect, it is surprisingly ~12 μmol kg^{-1} silica-poorer than the bottom waters to the south (Figures 3.3b–3.3f). This is because the silica flux into the bottom waters that flow over the opaline sediments of the Australian-

Antarctic Basin (Section 3.3.2.2) does not reach up into these usually relatively nutrient-richer deep waters (Edmond et al., 1979).

This LCDW spreads out to fill the entirety of the abyssal South Australian Basin until it reaches shallow topography to the east (South Tasman Rise at ~145°E) or to the west (Southeast Indian Ridge at ~82°E). Its properties are fairly homogenous over the relatively deep part of the basin from ~118°E to 135°E but it becomes warmer, saltier, and oxygen-poorer (i.e., more characteristic of lighter classes of LCDW) as the bathymetry shoals on either side of this range (Figures 3.3c–3.3e). To the west, these bottom waters also become slightly oxygen-poorer and silica-richer (Figures 3.3e and 3.3f) due to mixing with the overlying oxygen-poor and silica-rich IDW that is flowing southward (e.g., Toole & Warren, 1993). Some of the westward-flowing LCDW turns northward, flowing through a deep gap between the Broken and Naturaliste plateaus at ~33°S, 103°E–108°E to enter the Perth Basin. In our maps, the LCDW north of this gap is notably warmer ($\Theta \geq 0.55$°C) and saltier than the waters immediately south in the South Australian Basin, reflecting the lightening effect of the previously observed intense near-bottom mixing over this southern boundary of the Perth Basin (Sloyan, 2006). The northward flow of these waters along the western boundary of the Perth Basin and southward recirculation in the east also observed by Sloyan (2006) are somewhat visible in our temperature and salinity maps though the alternating bands of northward and southward flow they note in the interior of the basin are not well-resolved here (Figures 3.3c and 3.3d). As these waters flow northwest into the West Australian Basin, they are again subject to bottom-intensified mixing at the northern boundary of the Perth Basin though it extends over a smaller vertical extent than the mixing at the southern boundary (Sloyan 2006), which is likely in part why the changes in the bottom water properties are less substantial than at the southern boundary.

From the West Australian Basin, the LCDW in our maps spreads out along the seafloor until it encounters shallow topography, consistent with the maps of Mantyla and Reid (1995): to the east it extends across the North Australian Basin to the continental shelves off of Indonesia and northwestern Australian (~119°E) and to the north it generally extends across the Cocos Basin until it reaches the shallow ridges or the Java Trench along its northern boundary (~5°N). Some of this water continues as far north as ~12°N in a narrow channel along the eastern flank of the Ninetyeast Ridge but the fate of this water will be discussed below. Generally, the LCDW that makes its way into the North Australian and Cocos basins is lighter ($\gamma^n \approx 28.17$ kg m^{-3}), warmer ($\Theta \geq 0.7$°C), saltier, oxygen-poorer, and nutrient-richer than the initial inflow of LCDW from the Perth Basin due to the increased influence of the overlying IDW along these pathways (Figures 3.3b–3.3h). Most of the denser classes of the LCDW that enter the West Australian Basin from the Perth Basin flow westward toward the Ninetyeast Ridge, which is the endpoint along this pathway for our formally defined LCDW ($28.18 \leq \gamma^n < 28.27$ kg m^{-3}).

However, at gaps in the Ninetyeast Ridge at 5°S, 10°S, and 28°S, some clearly LCDW-like water flows through the ridge and into the Central Indian Basin, consistent with previous analyses of the bottom flow over these deep saddles (McCarthy et al., 1997; Toole & Warren, 1993; Warren, 1982; Warren & Johnson, 2002). At 28°S, a small amount of these LCDW-like waters ($\Theta \leq 1.0$°C; Figure 3.3c), enters the Central Indian Basin and spreads only a short distance from the ridge (as far west as 85°E and as far north as 27°S). The small footprint of these waters along the seafloor at this latitude is consistent with previous observations showing that upon entering this basin ~70% of this inflowing volume upwells before it reaches 85°E (McCarthy et al., 1997). The contributions of the LCDW-like waters flowing through the gaps farther north at 5°S and 10°S to the bottom waters of the Central Indian Basin are much more substantial,

consistent with the previously observed larger volume transports through these gaps compared to the one at 28°S (Warren & Johnson, 2002). These relatively cool ($\Theta \leq 1.0$°C), fresh, oxygen-rich, and nutrient-poor waters extend from the gaps at 5°S and 10°S to the western boundary of the basin – the Chagos-Laccadive Ridge (Figures 3.3c–3.3h).

Some of the lighter classes of this water ($\gamma^n < 28.15$ kg m^{-3}) slowly spread northward over the shoaling topography to reach the Bay of Bengal, becoming increasingly characteristic of the warmer, saltier, oxygen-poorer, and nutrient-richer IDW farther northward. Much like in the Arabian Sea, the IDW along the bottom of the Bay of Bengal becomes substantially warmer ($\Theta \geq$ 1.5°C) and saltier as it approaches the northern apex of the basin due to mixing with the overlying IDW that is strongly influenced by warmer and saltier intermediate waters such as RSW and PGW (Jain et al., 2017).

Within the bottom waters of the Bay of Bengal there appear to be two sources of especially high nutrient and low oxygen concentrations along the seafloor (Figures 3.3e–3.3h). One region is northeast of Sri Lanka roughly between the 3400- and 4000-meter isobaths (Gordon et al., 2002). The bottom waters in this region are the silica-richest in the Bay of Bengal and are also oxygen-poor, relatively nitrate-rich, and relatively phosphate-rich. Previous work (e.g., Edmond et al., 1979; Gordon et al., 2002) noted that the coincident changes in the oxygen and nutrient concentrations in these bottom waters are consistent with the decomposition of diatom-rich planktonic material that is likely exported to depth by the highly productive upwelling regions of the northern Bay of Bengal. However, maps of net primary productivity (Hossain et al., 2020; their Figure 3) show that during the southwest monsoon (May–October) there is an upwelling-induced bloom of phytoplankton east of Sri Lanka, which overlies this region of elevated nutrient regeneration within the bottom waters. Given the especially high concentrations of silica within

this small region relative to the silica distribution in the rest of the Bay of Bengal, it seems likely that the diatom-rich downward particulate flux from this upwelling region offshore of Sri Lanka is the main source of the organic matter that is regenerated in the bottom waters of this area, not the upwelling regions along the northern boundary of the basin.

The other area of particularly oxygen-poor and nutrient-rich bottom waters is located throughout the northern Bay of Bengal (north of ~15°N). These signals result from the regeneration of organic matter exported from the highly-productive surface waters along the entirety of the northern boundary (again, see Figure 3 of Hossain et al., 2020 for a map of net primary productivity). Near regions of substantial river discharge over the Bengal Fan, such as the Ganges-Brahmaputra-Meghna delta at ~20°N, 89°E and the Ayeyarwady delta at ~15°N, 95°E, there are even higher rates of primary productivity and therefore likely more downward particulate flux to the seafloor as hypothesized by Mantyla & Reid (1995). The regeneration of this organic matter appears in our maps at the northeast corner of the basin (~18°N, 92°E), where the bottom waters are the oxygen-poorest, nitrate-richest, and phosphate-richest in the Bay of Bengal (Figures 3.3e–3.3h). A similar signal is observed in northwest corner of the basin, likely due to the combination of coastal upwelling and discharge from rivers off of the southeast coast of India. The silica distribution in our maps along the bottom of the northern Bay of Bengal is a bit puzzling. In the northeast corner of the basin, the silica concentration is elevated as would be expected under the upwelling regimes in this basin. However, in the northwest corner of the basin, the silica concentrations are as low as those in the LCDW-like waters that flow through the Ninetyeast Ridge at 5°S and 10°S ($[Si(OH)_4] < 135$ µmol kg^{-1}). This may have to do with the composition of the phytoplankton community in this region (i.e., perhaps they are not diatom-dominated) or it could indicate that the rivers flowing into this region are particular silica-poor.

An unrelated silica-poor and oxygen-rich bottom water plume extends from the eastern boundary of the Bay of Bengal at ~10°N, 91°E and appears to form a boundary region of well-ventilated waters between the two oxygen-poor regions described above (Gordon et al., 2002). LCDW-like waters ($\gamma^n \approx 28.17$ kg m^{-3}) in the Western Australian Basin flow northward in a narrow western boundary current along the eastern flank of the Ninety-East Ridge up to ~12°N. Some of the lighter ($\gamma^n \approx 28.13$ kg m^{-3}), relatively oxygen-rich ([O_2] ≈ 170 µmol kg^{-1}) and nutrient-poor ([$Si(OH)_4$] < 135 µmol kg^{-1}) classes of this water enter the southeastern Bay of Bengal via a depression at the northern end of the Ninetyeast Ridge. This water appears to flow westward from this entry point to ~84°E before its signal becomes indistinguishable from the along-bottom classes of IDW in the interior of this basin. While this plume likely contributes to the confinement of the oxygen-poor, nutrient-rich signal off of Sri Lanka to seafloor depths of 3400–4000 meters, as noted by Gordon et al. (2002), it seems likely that the limited extent of the phytoplankton plume overlying these waters also plays a key role in controlling the footprint of this regeneration-related feature along the seafloor. Regardless, the oxygen-poor, nutrient-rich bottom waters throughout the Bay of Bengal eventually upwell and return southward above the bottom as IDW (Edmond et al., 1979).

3.3.3.3 Pacific AABW/LCDW Pathways

AABW and LCDW flow into the Tasman Sea through fracture zones bisecting the Southeast Indian Ridge from ~150°E–160°E, especially through the Balleny Fracture Zone (~155°E) (Rodman & Gordon, 1982). While there is a small amount of AABW ($28.27 \leq \gamma^n < 28.36$ kg m^{-3}) just north of the ridge that appears to be a combination of the recirculated, silica-richer ALBW/RSBW (Section 3.3.2.2), the newly-formed ALBW, and the "high-salinity" RSBW, the bottom water found north of ~56°N in this basin is more characteristic of the lighter ($28.18 \leq \gamma^n <$

28.27 kg m^{-3}), warmer ($\Theta > 0.3$°C), saltier, and oxygen-poorer LCDW (Figures 3.3b–3.3e). As this flow continues northward down the northern flank of the Southeast Indian Ridge, it becomes even warmer, saltier, and oxygen-poorer as it entrains increasing amounts of the overlying less modified (by AABW) LCDW in this downslope flow, reaching $\Theta \approx 0.5$°C at the 4500-meter isobath (~50°S). North of ~50°S, these bottom waters flow northward as a deep western boundary current that extends to ~42°S, entraining even more of the lighter, oxygen-poorer overlying waters along the way, before turning eastward within a cyclonic recirculation gyre that fills the rest of the interior of the Tasman Basin to the east and south (Sokolov & Rintoul, 2000). In our maps this deep western boundary current and offshore recirculation gyre are well-resolved with the inflow along the western boundary containing LCDW that is distinctly cooler $\Theta \leq 0.65$°C and fresher than the recirculating waters to the east (Figures 3.3c and 3.3d). The continued warming and salinification of these waters as they flow northward along the boundary is visible in our maps as well.

Previous work has suggested that there are lighter classes of LCDW that extend farther northward within a deep western boundary current up to the northern apex of the East Australian Basin where only some of the even lighter classes of this water continue over the Cato Trough, mix with Antarctic Intermediate Water (AAIW) to become warmer and fresher, and then flow into the western Coral Sea (e.g., Sokolov & Rintoul, 2000; Wyrtki, 1960). Our maps, especially of γ^n, resolve this continuation of the LCDW-carrying boundary current up to ~24°S and further show that it is narrower than the boundary current south of ~42°S, likely due to steering by the narrow underlying bathymetric channel at these more northern latitudes (Figure 3.3b). None of the formally-defined LCDW ($28.18 \leq \gamma^n < 28.27$ kg m^{-3}) flows over the Cato Trough but we do see a clearly LCDW-like signal that is, relative to PDW, characteristically oxygen-rich ($[O_2] \geq 180$ μmol

kg^{-1}) and silica-poor ($[Si(OH)_4] \leq 110$ μmol kg^{-1}) spreading from the Cato Trough throughout the western Coral Sea (west of 160°E) with $\Theta \leq 1.5$°C (Figures 3.3b, 3.3c, 3.3e, and 3.3f). These waters do not appear to be freshened by AAIW over the Cato Trough (Figure 3.3d) as suggested by Sokolov and Rintoul (2000). This could be due to the LCDW farther above the bottom buffering this effect. Some of the LCDW-like water in the western Coral Sea appears to continue northward into the southern Solomon Sea through the Pocklington Trough at ~12°S, 155°E and even into the South Solomon Trench, consistent with the proposed circulation of Wyrtki (1961). The sources for the bottom waters of the northern Solomon Sea, New Hebrides Basin, the New Caledonia Trough, and the Fiji Basin are discussed below.

The bottom waters of the west and central basins of the Pacific Ocean originate from LCDW transported along the western boundary (e.g., Whitworth et al., 1999), while the bottom waters of the eastern basins contain only heavily modified varieties of these waters (i.e., PDW) (Mantyla & Reid, 1983). There are no other sources of new bottom water formation in the northern Pacific to ventilate these waters once they enter the basin. Though the Pacific-Antarctic Ridge blocks any AABW ($28.27 \leq \gamma^n < 28.36$ kg m^{-3}) from entering the Southwest Pacific Basin, the overlying LCDW ($28.18 \leq \gamma^n < 28.27$ kg m^{-3}) that is able to enter this basin still carries some of the relatively cool ($\Theta \geq 0.3$°C), salty, oxygen-rich, and nutrient-poor (compared to the PDW) signal of the AABW northward within its densest classes (Figures 3.3b–3.3h). This LCDW enters the Southwest Pacific from the Southern Ocean through a number of gaps in the Pacific-Antarctic Ridge south and southwest of Campbell Plateau.

Much of this LCDW flows northward as a deep western boundary current along the eastern boundaries of the Campbell Plateau, the Chatham Rise and the Tonga-Kermadec Trench. However, some of this LCDW leaves the boundary and slowly spreads eastward along the bottom

until it encounters the East Pacific Rise, mixing with overlying waters along the way to become warmer (up to $\Theta \approx 0.7°C$), saltier, and oxygen-poorer to the east. Along the eastern boundary of Chatham Rise, the isobaths down to approximately 5000 meters are relatively tightly spaced. However, near the easternmost point of the rise (~43°S, 167°W), the 5000-meter isobath breaks away from the shallower isobaths and extends eastward while the others turn northward.

Previous work suggested that some of the LCDW flow within the deep western boundary current turns offshore to follow this "wandering" isobath eastward through the Louisville Ridge before continuing northwestward along its northeastern flank as a separate deep western boundary current, which ultimately returns, at least in part, westward through the ridge north of 35°S (Whitworth et al., 1999). Some of this flow appears to continue even farther north along the northeastern flank of this ridge with strong northwestward velocities at ~32.5°S previously observed by a mooring array (Whitworth et al., 1999). On our temperature and salinity maps (Figures 3.3c and 3.3d), we see a plume of cool ($\Theta \leq 0.6°C$) and fresh LCDW extending through gaps in the Louisville Ridge east of Chatham Rise, which then continues northwestward up to ~30°S along the 5000-meter isobath on the northeastern flank of the ridge.

While our maps show a coherent flow of this water east of the ridge from 161°W to 172.5°W along the 5000-meter isobath, caution is advised regarding drawing inferences about where this flow path is truly initiated, since between 43.21°S, 159.8°W and 38.94°S, 166.8°W there are no measurements along the northeastern flank of the ridge. Over this region, the RFOM procedure may be erroneously using some of the sparse measurements from the other side of the ridge to inform the mapping. For example, our maps suggest that the southernmost flow of LCDW through the Louisville Ridge occurs at ~43°S, 162°W but examining the underlying data reveals that the RFOM procedure is likely interpolating the measurement at 43.23°S, 162.1°W on the

western side of the ridge to locations with similar depths and longitude both within the nearby ~4775-meter gap in the ridge and on the northeastern flank of the ridge. While it is possible that some LCDW is flowing through this gap, there are no measurements east of the ridge in our current dataset to support the presence of this flow at ~43°S on our maps. It is also likely that there is LCDW flow through the ridge slightly farther north via the deeper ~4925-meter gap at ~42°S, 163.5°W, but again we presently lack direct measurements of this flow. The southernmost location on the northeastern flank of the ridge where the LCDW flow is observed is farther north at 38.94°S, 166.8°W so LCDW is clearly flowing through the ridge south of this (though we currently lack direct observations of where this eastward flow occurs).

Since a number of Deep Argo floats have recently deployed in this region, perhaps we will soon have more direct measurements of the initiation of this boundary current along the northeastern flank of the Louisville Ridge. Data from these new floats have already revealed a previously unmeasured deep western boundary current with speeds up to 8 cm s^{-1} northward along a more minor ridge to the east at ~35°S, 164°W (Roemmich, Sherman, et al., 2019). North of ~39°S there are more observations in our dataset around the 5000-meter isobath so inferences from our maps about the extent of this current along the northeastern flank of the Louisville Ridge can be made there with more confidence. The rest of the LCDW that continues as a deep western boundary current along the eastern flank of the Tonga-Kermadec Trench slowly becomes lighter, warmer, and saltier to the north, reaching $\Theta \approx 0.65$°C by the time it arrives in the Samoa Basin, in part because the northward flow of the coolest and freshest (i.e., densest) classes of the LCDW is blocked by the western extent of the Louisville Ridge.

In the Samoa Basin, the remaining LCDW flowing along the western boundary splits into three branches, continuing northward either through a gap in the Robbie Ridge, through the

Samoan Passage, or along the eastern boundary of the Manihiki Plateau (e.g., Roemmich et al., 1996). Minimal water within our strict defintion for LCDW ($28.18 \leq \gamma^n < 28.27$ kg m^{-3}) escapes from the Samoa Basin in these flows, even through the Samoan Passage, which has the densest outflow of the three pathways (Figure 3.3b). However, the relatively cool, salty, oxygen-rich, and nutrient-poor influence of the LCDW along the bottom (compared to the PDW farther north) clearly continues downstream of the Samoa Basin in a coherent flow with $\gamma^n \leq 28.15$ kg m^{-3} at least as far north as the Wake Island Pasage (WIP) at ~18°N, 169°E and even somewhat farther north in additional, increasingly PDW-dominated, northward and eastward flows with $\Theta \leq 1.1$°C (Figures 3.3b–3.3h).

Some of this LCDW-like water exits the Samoa Basin through a gap in the Robbie Ridge at ~175°W and is warmer ($\Theta \geq 0.8$°C), lighter ($\gamma^n \leq 28.17$ kg m^{-3}), and nutrient-richer (e.g., [$Si(OH)_4$] > 120 μmol kg^{-1}) than the along-bottom LCDW south of the ridge, likely due to a combination of the sill blocking some of the denser LCDW classes from continuing northward and enhanced mixing between the bottom and deep waters within this gap as observed in the Samoan Passage (see below). This flow becomes indistinguishable from the outflow of the Samoan Passage within the Central Pacific Basin. The branch of northward LCDW-like flow along the eastern boundary of the Manihiki Plateau generally has similar properties to the outflow through the Robbie Ridge (i.e., $\Theta \geq 0.8$°C, $\gamma^n \leq 28.17$ kg m^{-3}) though it is slightly silica-poorer ([$Si(OH)_4$] ≤ 120 μmol kg^{-1}). This suggests that there is less vigorous mixing occurring here between the bottom waters and the overlying deep waters than in the narrower Robbie Ridge gap and the Samoan Passage where such mixing fully attenuates the especially nutrient-poor signal of the densest LCDW along the bottom in these passageways (e.g., Alford et al., 2013 for the Samoan Passage only). Our maps are consistent with previous work suggesting that the northward flow of LCDW-

like waters along the eastern boundary of the Manihiki Plateau occurs within a relatively broad, slow-moving western boundary current that extends at least as far north as ~12°S (the location of of the P31 WOCE line at this longitude) and undergoes little mixing with overlying waters (Pratt et al., 2019; Roemmich et al., 1996).

Some of this flow leaves this boundary current to fill the interior of the Penrhyn Basin to the east and its warmer ($\Theta \geq 0.9$°C) classes extend even farther eastward through gaps in the Boudeuse Ridge. This flow then bifurcates around the Marquesas Islands with some entering the Tiki Basin to the southeast ($\Theta \geq 1.1$°C, $[Si(OH)_4] < 130$ μmol kg^{-1}) and the rest flowing into the basin east of the Marquesas Islands ($\Theta \geq 1.0$°C, $[Si(OH)_4] \geq 135$ μmol kg^{-1}). From the silica distribution (Figure 3.3f) it is clear that the southward-flowing silica-rich PDW from the northeast Pacific that overlies these LCDW-like bottom waters has a stronger influence on the bottom waters east of the Marquesas Islands than those in the Tiki Basin. Ultimately, the relatively cool and silica-poor LCDW-like bottom waters east of the Marquesas Islands spread to ~110°W ($\Theta \approx 1.2$°C, $[Si(OH)_4] \approx 140$ μmol kg^{-1}) where they encounter the East Pacific Rise and the silica-rich PDW flowing southeastward along the seafloor from the northeast Pacific. These waters mix along the bottom in this region and then fill the Bauer Basin (see below).

The largest transport of LCDW from the Samoa Basin occurs via the northward flow through the Samoan Passage (10°S, 169°W) along the western side of the Manihiki Plateau. These waters undergo substantial mixing with overlying waters within, and just north of, this passage due to highly elevated levels of turbulence as the flow accelerates within the narrow passage and from hydraulic jumps downstream (to the north) of the sill (Alford et al., 2013; Freeland, 2001). This leads to the signal of bottom waters cooler than $\Theta = 0.7$°C being mixed away over this passageway (Figure 3.3c). However, the waters exiting from this pathway are still the densest (γ^n

= 28.17–28.18 kg m^{-3}; Figure 3.3b) and coolest ($\Theta \geq 0.7$°C; Figure 3.3c) waters of the three outflows from the Samoa Basin (consistent with Roemmich et al., 1996; Voet et al., 2016).

This outflow from the Samoan Passage continues northward along the western boundary of the Manihiki Plateau to ~3°S where it bifurcates such that its lighter classes ($\gamma^n < 28.17$ kg m^{-3}; $\Theta > 0.8$°C) continue northward into the Central Pacific Basin while its denser classes ($\gamma^n \geq 28.17$ kg m^{-3}; $\Theta \leq 0.8$°C) turn clockwise around the northern tip of the Manihiki Plateau. We were not able to find any previous observational-based discussions of this clockwise flow around the apex of the plateau but previous theoretical and modeling studies (Sen Gupta and England, 2004; Pratt et al., 2019) suggest that this flow should be counterclockwise, indicating a mismatch between our observations and what the current theory predicts for this flow. Our maps suggest that from the northeastern flank of the Manihiki Plateau some of this flow spreads eastward through gaps between the Line Islands to join the flow from farther south through the Boudeuse Ridge (that is originally from the southeast flank of the Manihiki Plateau) in spreading across the eastern equatorial Pacific and ultimately contributing to the bottom waters than fill the deep Bauer Basin (see above).

Much of the LCDW-like outflow from the Samoan Passage and the gap in the Robbie Ridge flows northward into the Central Pacific Basin though some of this water turns northwestward through a gap in the Gilbert Ridge at 3°S, 175°E. The flow through the Gilbert Ridge continues northwestward in the narrow basin west of the ridge (Melanesian Basin) and ultimately some of its lighter classes ($\Theta \approx 1$°C; Figure 3.3c) enter the East Mariana Basin (e.g., Johnson & Toole, 1993; Kawabe et al., 2003).

The LCDW-like water flowing northward in the Central Pacific Basin bifurcates into northwestward and eastward flows before exiting this basin. The eastward branch travels through

gaps in the ridge north of the Line Islands (e.g., the Horizon Passage at 18°N and Clarion Passage 12.5°N; Edmond et al., 1971) with the shallow sills of these passageways blocking waters with $\Theta < 0.9$°C from flowing into the Kamehameha Basin. From the Kamehameha Basin the flow of these weakly LCDW-like waters, which are most easily identified in our global maps by their relatively cool ($\Theta \leq 1.1$°C), salty, oxygen-rich, and silica-poor signal (Figures 3.3c–3.3f) compared to the PDW along the seafloor in the northeast Pacific, bifurcates into eastward and northward flows. The flow eastward continues as far as ~20°N, 128°W between the zonal Clarion (~17°N) and Molokai (~23°N) fracture zones ($\Theta \approx 1.05$°C, $[Si(OH)_4] \approx 140$ μmol kg^{-1}) to form the second major lobe of Antarctic-origin waters in our maps that spreads far into the eastern equatorial Pacific before the southward-flowing PDW closer to the eastern boundary mixes away the Antarctic-origin signal. The other outflow from the Kamehameha Basin extends northward just east of the Hawaiian Islands (steered closer to the island by the presence of the Molokai Fracture Zone) and joins the flow of LCDW-like waters through a passage north of the Hawaiian Ridge at ~31°N that is discussed below.

The northwestward flow in the Central Pacific Basin exits at the northwestern corner of the basin through two narrow gaps in the bathymetry – one at ~16.5°N, 168°E just north of the Marshall Islands and one at ~18°N, 169°E (Wake Island Passage; WIP) (Kawabe et al., 2003). The shallow topography around these gaps prevents any waters cooler than $\Theta \approx 0.9$°C from exiting the Central Pacific Basin (Figure 3.3c). The waters that flow through the gap at ~16.5°N, 168°E appear to traverse a complex set of passageways around the Marshall Seamounts before eventually joining the flow from west of the Gilbert Ridge in the East Mariana Basin. Small-scale outflows of the LCDW-like waters from the East Mariana Basin have been previously discussed in detailed regional studies and are resolved on our temperature map (Figure 3.3c) as flows of water with Θ

≈ 1.1°C into West Mariana Basin at ~11°N, 140°E through the Yap-Mariana Junction and into the "dead-end" East Carolina Basin at ~9°N, 151°E (Kaneko et al., 1998; Siedler et al., 2004).

The flow into the West Mariana Basin bifurcates (Kaneko et al., 1998) with much of it spreading northward and then westward to fill the Shikoku and Philippine basins, respectively, ($\Theta \leq 1.2$°C; Figure 3.3c) and the rest turning southwestward through the Yap Trench to fill the West Caroline Basin ($\Theta \approx 1.1$°C; Figure 3.3c). Kaneko et al. (1998) suggested that some of this bottom water in the West Caroline Basin then flows into the Philippine Basin via a deep (> 4000 meters) channel near its southern boundary. While there appears to be some of this water ($\Theta \leq 1.2$°C) on our map within the southern Philippine Basin, its path from the West Caroline Basin is not well resolved here. Within the Philippine Basin these bottom waters eventually upwell across isopycnals and leave this basin at shallower depths as PDW.

The LCDW-like water that flows through the WIP (~18°N, 169°E) spreads throughout the Northwest Pacific Basin (Kawabe et al., 2003) with its densest ($\gamma \geq 28.13$ kg m^{-3}) and coolest ($\Theta \leq 1$°C) classes remaining constrained east of ~160°E by the Shatsky Rise and a slightly shallow sill extending southeastward from it (Figures 3.3b and 3.3c). Some of these LCDW-like waters ($\Theta \leq 1.05$°C) flow eastward at ~31°N, 177°E through a passage between Hess Rise and the Hawaiian Ridge before encountering the shallow Liliuokalani Ridge that extends southeastward from the Hess Rise over ~177°W–172°W and blocks the continued eastward progression of most of these waters. A small portion of these waters appear to make it through this shallow topography and into the basin between the Liliuokalani Ridge and the Musician Seamounts (~163°W) where they mix with some of the water that flows northward along the eastern boundary of the Hawaiian Islands as described above (which has similar properties to the LCDW-like waters flowing though the passage at ~31°N, 177°E) and a bit of the slightly warmer, fresher, and oxygen-poorer water from

the abyssal cyclonic gyre in the Northeast Pacific Basin (described below) that flows anticyclonically in a narrow boundary current around the eastern boundary of the Hess Rise to enter this basin (Figures 3.3c–3.3e). This narrow boundary current is just barely discernible in the meridional sections along 179°E from Roden (2000). East of the Musician Seamounts, the bottom water is dominated by the water flowing northward along the eastern boundary of the Hawaiian Islands. This water then continues eastward as a third lobe of Antarctic-origin water extending across the Pacific bounded by the Murray Fracture Zone (~32°N) to the south and by the Mendocino Fracture Zone (~40°N) to the north. While the signal of these waters is slowly diminished by the overlying warmer and silica-richer PDW as they spread across the Pacific, a narrow plume of these waters extends to ~37°N, 130°W (the base of the continental rise off of California) with a distinct LCDW-like signal ($\Theta \approx 1.13$°C, $[Si(OH)_4] \approx 155$ μmol kg^{-1}) compared to the PDW-dominated waters ($[Si(OH)_4] \geq 170$ μmol kg^{-1}) found immediately north and south along the adjacent shallower topography. Lighter remnants of the LCDW-like water that have mixed a bit more with the overlying PDW may extend even farther eastward to ~38°N, 126°W ($\Theta \approx 1.15$°C, $[Si(OH)_4] \approx 160$ μmol kg^{-1}) within this relatively deep basin but it is difficult to distinguish between these waters and those flowing eastward into this region along the Mendocino Fracture Zone from the broad cyclonic gyre to the north. In summary, our maps, especially of oxygen and silica, illustrate a potential pathway for changes near sites of bottom water formation in the Southern Ocean to propagate all the way to the eastern boundary of the Northeast Pacific at ~38°N.

The LCDW-like waters that flow into the Northwest Pacific Basin at the WIP can also exit this basin as a northward flow between the Shatsky and Hess rises (e.g., Owens & Warren, 2001). However, the shallow topography of the zonally oriented Ojin Rise Seamounts along ~37°N blocks

the northward transport of the densest classes of these waters (Owens & Warren, 2001). The remaining, lighter ($\gamma^n < 28.11$ kg m^{-3}) LCDW-like waters continue northward on west side of the Emperor Seamount Chain with some of this flow ($\Theta \leq 1.1$°C, $[Si(OH)_4] \leq 155$ μmol kg^{-1}) transiting to the east side of this seamount chain via the Main Gap (Nintoku Passage) at ~39°N (Figures 3.3b, 3.3c, and 3.3f). This eastward flow has been observed directly in previous work (e.g., Komaki & Kawabe, 2009). This previous study also found that most of these waters continue flowing eastward along the northern flank of the Hess Rise to join the eastward-flowing southern limb of the broad cyclonic gyre within the abyssal Northeast Pacific Basin (discussed below). However, a portion of these waters appear to split off from this main flow and turn southeastward around the eastern boundary of the Hess Rise in the narrow boundary current discussed above to ultimately flow into the basin between the Liliuokalani Ridge and the Musician Seamounts instead of joining the gyre circulation. The remaining LCDW-like waters west of the Emperor Seamount Chain that do not flow through the Main Gap appear to continue northward along the seamount chain up to the Aleutian Trench. The fate of these waters once they reach the trench is discussed below.

From the silica distribution (Figure 3.3f), it is clear that some of the LCDW-like waters ($[Si(OH)_4] \leq 140$ μmol kg^{-1}) from both the WIP outflow and from a northward flow out of the East Marina Basin at ~25°N, 151°E (seemingly from a western boundary current within that basin) continue northward in a boundary current along the eastern edges of the Izu-Ogasawara, Japan, and Kuril-Kamchatka trenches, and over the axes of the Japan and Kuril-Kamchatka trenches, up to the northwest corner of the basin (~55°N, 164°E). This flow and the related flows in the Aleutian Trench are discussed in great detail in previous work (e.g., Owens & Warren, 2001). At the northern end of the Kuril-Kamchatka Trench, these waters likely mix with those that extend along the western side of the Emperor Seamount Chain in the flow described above. The mixture of these

LCDW-like waters from these two northward pathways is still relatively silica-poor ($[Si(OH)_4] \leq$ 150 μmol kg^{-1}; Figure 3.3f). These waters turn southeastward around the northern apex of the Emperor Seamount Chain and then continue to ~175°E within the Aleutian Trench. Near 175°E, the zonal extension of the relatively silica-rich ($[Si(OH)_4] \geq 160$ μmol kg^{-1}) Alaskan Stream that separates from the boundary near the dateline (e.g., Warren & Owens, 1988) temporarily interrupts this eastward flow of LCDW-like waters within the Aleutian Trench, pushing this signal farther offshore in our maps (Figure 3.3f). This disruption of the abyssal eastward jet by the zonal extension of the Alaskan Stream does not appear to be discussed in previous work.

East of ~177°E, the flow of the relatively silica-poor LCDW-like water from the western boundary resumes as a narrow, northeastward-flowing jet over the Aleutian Trench and the northern flank of the Aleutian Rise (Warren & Owens, 1988). This flow extends to ~56°N, 152°W (just south of Kodiak Island), with little modification of its relatively cool ($\Theta \leq 1.1$°C) and silica-poor signal ($[Si(OH)_4] \leq 150$ μmol kg^{-1}) (Figures 3.3c and 3.3f), consistent with the work of Warren and Owens (1988) who traced this flow to ~150°W. East of 152°W, the signal of the LCDW-like water gets weaker due to mixing with the overlying PDW that is warmer, oxygen-poorer, and silica-richer, though the northeastward flow of the LCDW-like water can still be traced to the eastern end of the Aleutian Trench at ~59°N, 144°W (Figure 3.3c, 3.3e, and 3.3f).

Near 59°N, 144°W, the flow of the LCDW-like water turns southward, roughly following the meridionally oriented 4000-meter isobath just east of the Patton Seamounts. South of the Patton Seamounts, between ~50°N–53°N, the relatively oxygen-rich and silica-poor signal (Figures 3.3e and 3.3f) of these waters turns back to the northwest along slightly deeper isobaths. From there, this flow is steered along the southern flank of the Aleutian Rise to become a broad, southwestward jet just offshore of the northeastward jet of "younger" LCDW-like water described above. The

existence of this westward flow was first hypothesized by Warren & Owens (1988). This flow makes up the northern limb of the cyclonic gyre within the Northeast Pacific Basin that appears to be bounded by the Aleutian Rise to the north, the Emperor Seamount Chain to the west, the Mendocino Fracture Zone to the south, and ~155°W to the east in our maps, consistent with previous inverse modeling results (Hautala, 2018). Due to the high-resolution of our maps, we are also able to resolve that some of the "younger" LCDW-like water appears to exit the Aleutian Trench at a number of locations from ~180° to 152°W to join the westward-flowing recirculation jet over the southern flank of the Aleutian Rise. The largest of these intrusions appears to be at ~51°N, 168°W where there is a deeper connection between the Aleutian Trench and the interior of the basin, allowing this "younger" water to extend farther into the interior. We believe that our maps are the first to fully trace the complicated, anticyclonic circulation of the LCDW-like waters along the seafloor from the eastern limit of the Aleutian Trench, around the Patton Seamounts, and into the recirculating westward jet that makes up the northern limb of the abyssal cyclonic gyre of the Northeast Pacific Basin. This pathway is important to understand because it supplies recently ventilated Antarctic-origin waters to the abyssal interior of this basin.

Recent work found that in the Northeast Pacific Basin the Péclet number is large (advection >> diffusion), which means that flows parallel to tracer isolines instead of flowing down tracer "tongues" (i.e., parallel to tracer gradients) (Hautala, 2018). We use this frame of reference when inferring flow paths from our property maps throughout this basin. For example, the southwestward flow of the "older" LCDW-like waters discussed above (i.e., the northern limb of the cyclonic gyre located between the Emperor Seamount Chain and ~155°W) flows along northeast-southwest oriented isolines of oxygen and silica (Figures 3.3 e and 3.3f). Near 180°, these isolines transition to a north-south orientation then to a northwest-southeast orientation.

Therefore, we can infer that the flow turns south then southeast, seemingly following the bathymetry of the Emperor Trough, which is consistent with the modeled flow paths of Hautala (2018). This flow then turns eastward along the northern flank of Hess Rise, intersecting with the "younger" LCDW-like waters that flow eastward through the Main Gap as described above.

The mixture of these water masses continues eastward over the Mendocino Fracture Zone (~37°N–40°N) along the zonally oriented isolines that extend from the eastern boundary of Hess Rise to ~126°W in our property maps. Some of this flow continues all the way to ~126°W where it turns southeastward and mixes with the much "younger" LCDW-like water that flows into this relatively deep basin from the south as discussed above. The rest of the eastward flow turns northward farther west (around 155°W) to close the cyclonic recirculation gyre, again consistent with the modeled flow paths of Hautala (2018). This northward flow is perhaps easiest to see in our oxygen map (Figure 3.3e) where the plume of oxygen-richer, LCDW-like water returning northward around 155°W is evident compared to the "older", oxygen-poorer LCDW-like water found immediately to the west within the center of the gyre or the oxygen-poorer PDW found over the shallow topography to the east. The water in the center of the western gyre is silica-richer as well with $[Si(OH)_4]:[NO_3^-] \geq 4.4$ mol mol^{-1}. This is consistent with previous work (e.g., Edmond et al., 1979) that observed extra silica addition from the dissolution of opaline sediments in the Northeast Pacific Basin in locations where the bottom water flow is especially slow, such as in the center of this gyre.

In the northeast corner of the Northeast Pacific Basin, the mid-depth silica maximum within PDW can appear along the bottom when isopycnals incrop on the continental slope (Hautala & Hammond, 2020). These waters are extremely oxygen-poor ($[O_2] \leq 100$ μmol kg^{-1}; Figure 3.3e) and silica-rich ($[Si(OH)_4] \geq 170$ μmol kg^{-1}; Figure 3.3f). The bottommost classes of the westward-

flowing Alaskan Stream are comprised of this PDW, which is slightly warmer ($\Theta \geq 1.2$°C) and much fresher, oxygen-poorer, and nutrient-richer than the LCDW-like waters that flow eastward over the Aleutian Trench and northern flank of the Aleutian Rise (Figures 3.3c–3.3h). The Alaskan Stream is a narrow western boundary current which, as noted in previous work (e.g., Warren and Owens, 1988), extends southwestward over the northern flank of the Aleutian Trench to ~180° at which point much of the flow separates from the boundary due to the changing orientation of the boundary. The deep (>2000 dbar) flow within this current is substantial, especially at 175°W (Chapter 2; Table 2.2). The width of the silica-rich signal of the PDW in the Alaskan Stream (Figure 3.3f) indicates that this current narrows substantially between 150°W and 155°W along the bottom, consistent with previous observations of the flow at 2000 dbar narrowing between these longitudes (Chapter 2; Figure 2.4). At ~180°, this flow continues westward as a zonal jet toward the Emperor Seamount Chain that is ultimately steered northward back to the Aleutian Island Arc (e.g., Warren and Owens, 1988). The remaining along-bottom PDW flow ($[Si(OH)_4] \geq 165$ μmol kg^{-1}; Figure 3.3f) then splits with part of it continuing northward through Near Strait (~54°N, 169.5°E) to enter the Bering Sea and the rest turning continuing westward along the Aleutian Island Arc to join the southward-flowing Kamchatka Current (as previously noted by Warren & Owens, 1988).

The flow through Near Strait bifurcates with some turning westward to fill the Komandor Basin in conjunction with a portion of PDW that flows through the deeper Kamchatka Strait (~56°N, 164°E) farther west. The remainder of the flow through Near Strait turns eastward along the northern slope of the Aleutian Island Chain to fill the Bowers Basin (still with $[Si(OH)_4] \geq 165$ μmol kg^{-1}). Despite the high nutrient and low oxygen concentrations of this PDW, it is actually relative nutrient-poor and oxygen-rich compared to the bulk of the bottom water in the “dead-end”

Bering Sea which is extremely oxygen-poor ($[O_2] \leq 100$ μmol kg^{-1}) and nutrient-rich due to the long residence time of the bottom waters in this basin (Figures 3.3e–3.3h). In the northeast Aleutian Basin, the silica concentrations in the bottom waters reach as high as 240 μmol kg^{-1}, an increase of ~70 μmol kg^{-1} from the PDW that enters the Bering Sea ($[Si(OH)_4] \approx 170$ μmol kg^{-1}) (Figure 3.3f). This large increase is due to dissolution of biogenic opal both along the seafloor and in the sediments (e.g., Tsunogai et al., 1979) and accordingly the silica-to-nitrate ratio in this basin reaches its highest values for the bottom waters globally ($[Si(OH)_4]:[NO_3^-] \geq 6$ mol mol^{-1}).

Northward flow of the PDW through gaps in the Aleutian Island Arc also occurs farther east when flow splits off from the Alaskan Stream through the > 1000-meter deep Amchitka Pass (~51.5°N, 180°) (Stabeno et al., 2005). This flow is first evident in our oxygen and nutrient maps (Figures 3.3e–3.3h) at 52.5°N, 177°W and these waters are then advected cyclonically within the Aleutian Basin by the Aleutian North Slope Current and the Bering Slope Current. The PDW that instead flows westward along the Aleutian Island Arc to join the Kamchatka Current continues along the western boundary in a narrow jet onshore of the northward flow of the LCDW-like waters discussed above (Warren & Owens, 1988). This jet extends southward over the inshore flank of the Kuril-Kamchatka, Japan, and Izu-Ogasawara trenches as far south as 30°N, 140°E with the signature of PDW ($\Theta \geq 1.1$°C, $[Si(OH)_4] \geq 155$ μmol kg^{-1}) intact.

Within the Northeast Pacific Basin, the rest of the near-bottom PDW that does not join the westward flow of the Alaskan Stream turns to flow southward then southeastward along the broad topographic slope east of 155°W. This flow has been identified in previous inverse modeling work (Hautala, 2018) to continue as far south as Mendocino Fracture Zone (~40°N). On our maps, this flow can be inferred by the meridionally oriented isolines (e.g., of oxygen or neutral density) in this region east of the cyclonic circulation that occupies the rest of the basin to the west. Additional

silica is added from a seafloor source along this pathway (Hautala & Hammond, 2020) such that our silica isolines are not parallel to the direction of the flow. The silica-to-nitrate ratio in the bottom waters (not shown; $[Si(OH)_4]:[NO_3^-] \geq 4.6$ mol mol^{-1}) reveals that this extra silica addition is from dissolution of opaline sediments within the southward-flowing PDW between 153°W–134°W. A large amount of silica addition, with a similarly high silica-to-nitrate ratio, occurs within the shallow (< 3000 meters) Cascadia Basin offshore of Washington state resulting in silica concentrations ≥ 190 μmol kg^{-1}. South of the Mendocino Fracture Zone, the southward flow of the PDW can be inferred from the orientation of the isolines along the eastern boundary. For example, between the Mendocino and Murray fracture zones, the extremely oxygen-poor and silica-rich PDW is constrained to a relatively narrow continental slope (Figures 3.3e and 3.3f). However, south of the Murray Fracture Zone, the topographic slope becomes broad again and the signal of this PDW spreads over a much larger seafloor area.

This broad southeastward flow of PDW continues along the eastern boundary at depths generally shallower than ~4000 meters until it encounters the shallow topography of the East Pacific Rise. Some of the classes of this PDW at depths slightly above the bottom flow over the East Pacific Rise at the Galapagos triple junction (~2°N) and within the Siqueiros Fracture Zone (~8°N) to fill the Guatemala Basin (Mantyla, 1975). Our maps only resolve the inflow at the Galapagos triple junction (~2°N, 101°W), which then appears to flow northeastward upon entering the Guatemala Basin to initiate an abyssal cyclonic circulation within this basin (Figure 3.3e highlights this feature the best). Farther south, the southward-flowing PDW mixes with LCDW-like waters that flow eastward from the western boundary (see above) to form water with $[Si(OH)_4]$ ≈ 145 μmol kg^{-1}, approximately 5 μmol kg^{-1} richer in silica than the inflowing LCDW-like waters. This mixture then enters the Bauer Basin through a number of fracture zones bisecting the East

Pacific Rise from ~3°S–10°S (Lonsdale, 1976). On our maps, most of this flow appears to enter this basin through the Quebrada Fracture Zone at ~3.5°S, 103°W ($\Theta \approx 1.4$°C, $[Si(OH)_4] \leq 145$ μmol kg^{-1}; Figures 3.3c and 3.3f). Two additional smaller inflows of these waters appear on our maps as well: a warmer ($\Theta \approx 1.5$°C) inflow through the Wilkes Fracture Zone (~10.5°S, 105°W) and a fresher ($S_A \leq 34.855$ g kg^{-1}) inflow through the Yaquina Fracture Zone (~6.5°S, 109°W). These waters that fill the Bauer Basin are not only warmer but also substantially fresher and oxygen-poorer ($S_A \leq 34.86$ g kg^{-1}, $[O_2] \leq 140$ μmol kg^{-1}) than the flow of LCDW-like waters ($S_A \geq 34.865$ g kg^{-1}, $[O_2] \geq 155$ μmol kg^{-1}) along the eastern boundary of the Peru and Chile basins that is discussed below (Figures 3.3c–3.3e). Only on our salinity map (Figure 3.3d) is any outflow from the Bauer Basin clear, with a plume of the PDW/LCDW-like water mixture with $S_A \leq 34.86$ g kg^{-1} extending into the Yupanqui Basin through a gap in the Galapagos Ridge at ~17°S, 105°W.

The bottom waters of the Chile and Peru basins are fed by LCDW from the Southeast Pacific Basin (e.g., Lonsdale, 1976). LCDW ($\Theta \leq 1.1$°C) branches off from the Antarctic Circumpolar Current to flow northward through several fracture zones that cut across the Chile Rise; mainly through the Valdivia Fracture Zone (~41°S, 87°W) and to a lesser degree through the Chile Fracture Zone (~36°S, 99°W) and an unnamed fracture zone farther south (~45°S, 80°W). This "LCDW" is slightly lighter ($\gamma^n \leq 28.16$ kg m^{-3}) than our formal definition of LCDW ($28.18 \leq \gamma^n < 28.27$ kg m^{-3}) but is clearly cooler, saltier, oxygen-richer, nitrate-poorer, and phosphate-poorer than the mixture of PDW and LCDW-like waters from the western boundary that is found in the Bauer Basin (Figures 3.3b–3.3e, 3.3g, 3.3h). We will refer to the waters in the Chile and Peru basins with $\gamma^n \geq 28.04$ kg m^{-3} as "LCDW-like waters" since they are more characteristic of the "newer" LCDW that enters from the Southeast Pacific Basin than of the PDW/"older" LCDW-like water mixture found in the Bauer Basin ($\gamma^n \leq 28.03$ kg m^{-3}). These LCDW-like waters have

previously been observed to flow into the Peru Basin both over a sill between the Sala-y-Gomez and Nazca ridges (~24°S, 84°W) and through the narrow Peru-Chile Trench along the eastern boundary (Lonsdale, 1976). On our maps the flow of LCDW-like waters through the former pathway is somewhat warmer ($\Theta > 1.4$°C) than through the latter pathway ($\Theta \leq 1.4$°C) (Figure 3.3c).

The northward flow of LCDW-like waters along the eastern boundary within the Peru-Chile Trench bifurcates with some spreading westward to fill the interior of the Peru Basin and the rest continuing northward into the Ecuador Trench. Near the Carnegie Ridge at ~1°S, the sill depth affecting the flow along the boundary is 2920 meters causing the waters that go on to fill the Panama Basin to be more characteristic of the overlying warmer and fresher PDW than LCDW-like waters in the Ecuador Trench (e.g., Lonsdale, 1976). This flow is supported by our maps where the bottom waters of the Panama Basin are not only warmer and fresher than the LCDW-like bottom waters of the Peru Basin but also substantially oxygen-poorer and silica-richer, consistent with this abyss of this basin being fed by "older" classes PDW from far above the bottom (Figures 3.3c–3.3e). These waters become lighter within the Panama Basin via geothermal heating and enhanced rates of vertical mixing due to tides to escape this basin after a relatively short residence time (Lonsdale, 1976).

3.3.4 *NADW and its Pathways Southward*

NADW is warmer, saltier, nutrient-poorer, and oxygen-richer than the AABW it interacts with in the Atlantic Ocean (Mantyla & Reid, 1983). The classes of NADW seen in our bottom water property maps are fed by dense waters from three different Nordic Seas overflow pathways over the Greenland-Scotland Ridge: the Denmark Strait, the Iceland-Faroe Ridge, and the Faroe-Shetland Channel. Generally, the NADW along the seafloor is a mixture of Denmark Strait

Overflow Water (DSOW) and Iceland Scotland Overflow Water (ISOW) (Dickson & Brown, 1994; Eldevik et al., 2009). Once this bottom flow of NADW extends far enough south to meet with bottom waters of Antarctic origin (roughly when $[Si(OH)_4]$ = 20 μmol kg^{-1}; thick magenta contour, Figure 3.3f), some of it gets displaced to higher in the water column while its densest classes mix with the AABW along the bottom to form AI-NADW.

On the eastern edge of the Greenland-Scotland Ridge, a substantial amount of ISOW flow occurs through the deepest gap in this ridge complex, the Faroe-Shetland Channel, and into the basins to the south (Hansen & Østerhus, 2007). Once at the southeastern tip of the Faroe Plateau, the ISOW flow bifurcates with the lighter, warmer, fresher, and oxygen-poorer classes traveling southward into the Rockall Trough over the < 600-meter deep Wyville Thomson Ridge and the denser classes traveling westward to the Iceland Basin via the 840-meter deep Faroe Bank Channel (Ellett & Roberts, 1973; Hansen & Østerhus, 2007). Within the Rockall Trough, the Wyville Thomson Ridge overflow water mixes with the Sub-Arctic Intermediate Water and Mediterranean Sea Overflow Water, as well as the denser Labrador Sea Water and the relatively nutrient-rich AI-NADW from the south (Holliday et al., 2000; Sherwin et al., 2015). Previous work (McCartney, 1992), suggested that some of the dominantly AI-NADW along-bottom classes of this mixture exit the southern end of the Rockall Trough and turn northwestward to flow as a boundary current along the southern flank of the Rockall Plateau toward the southeastern Iceland Basin. While it is difficult to distinguish between these waters leaving the Rockall Trough and the younger AI-NADW entering it, there is a clear plume of relatively nutrient-rich AI-NADW flowing northwestward toward the southeastern Iceland Basin in our maps. The $[Si(OH)_4]$ = 20 μmol kg^{-1} contour (thick magenta contour, Figure 3.3f) marks the approximate transition between this

relatively fresh northwestward-flowing AI-NADW and the much saltier southwestward-flowing ISOW that is found over most of the seafloor in the Iceland Basin.

In the northern Iceland Basin, the waters that flow through the Faroe Bank Channel meet waters from smaller dense overflows over the Iceland-Faroe Ridge and mix (Beaird et al., 2013; Saunders, 1996). By the time they descend to 2000 meters (the shallowest depth on our maps) around 62.5°N, the waters from these two sources have combined and are together referred to as Iceland Scotland Overflow Water (ISOW). These waters are the saltiest contributor to NADW and can be readily observed in the salinity map (Figure 3.3d) spreading southwestward along the Reykjanes Ridge, the western boundary of the Iceland Basin (Kanzow & Zenk, 2014; Saunders, 1996). There appears to be southward ISOW flow in the interior of the Iceland Basin as well, which has been noted in some model simulations (e.g., Chang et al., 2009). The interior and eastern side of this basin contain the densest (coldest and saltiest) classes of ISOW (Figures 3.3b–3.3d).

There are several pathways by which the ISOW exits the Iceland Basin. Some of the lighter classes of ISOW make their way into the Irminger Basin via gaps in the Reykjanes Ridge (Zou et al., 2017). However, most of the ISOW reaches the southern tip of the ridge. From there the flow trifurcates with some ISOW continuing southward along the eastern flank of the Mid-Atlantic Ridge, some recirculating cyclonically within the Iceland Basin, and the lightest remaining classes traveling westward to the Irminger Basin via the Charlie Gibbs Fracture Zone (Bower & Furey, 2017; Fleischmann et al., 2001; Saunders, 1994; Smethie et al., 2000; Zou et al., 2017).

The ISOW flow that continues southward along the eastern flank of the Mid-Atlantic Ridge is readily observed in our temperature and salinity maps (Figures 3.3c and 3.3d). From there, some of it flows eastward into the West European Basin, likely entraining some of the denser ISOW from the interior of the Iceland Basin along the way (Figure 3.3b). Within the West European

Basin this water mixes with relatively nutrient-rich Antarctic-origin water that flows northward from the eastern equatorial Atlantic, thereby cooling and freshening the ISOW and transforming it into AI-NADW (Figures 3.3c, 3.3d, and 3.4). The continued southward flow of this AI-NADW from the West European Basin is discussed below.

The ISOW flow that heads westward within the Charlie Gibbs Fracture Zone is immediately steered northeastward by the bathymetry to flow along the western flank of the Reykjanes Ridge. On our maps, the presence of ISOW on the eastern side of the Irminger Basin is clear from its relatively warm ($\Theta > 2°C$), salty, and low oxygen signal compared to the DSOW on the western side of the basin (Figures 3.3c–3.3e; see further discussion of DSOW below). However, it is difficult to determine from our maps whether this ISOW arrived via gaps in the Reykjanes Ridge or via the longer route through the Charlie Gibbs Fracture Zone. Regardless of the pathway traveled, the near-bottom signal of this water mass disappears in the western Irminger Sea when it interacts with the denser DSOW and gets pushed higher in the water column.

The coolest ($\Theta < 2°C$) and densest ($\gamma^n \geq 28.18$ kg m^{-3}) contributor to NADW first appears on our maps offshore of the southeastern Greenland coast in the Irminger Sea. This cold, oxygen-rich, and nutrient-poor water is known as Denmark Strait Overflow Water (DSOW) and it enters the Irminger Sea where dense waters from the Greenland, Iceland, and Norwegian seas cascade over the Greenland-Iceland Ridge within the Denmark Strait (Swift, 1984). This water travels southward within the Deep Western Boundary Current (DWBC) around the tip of Greenland and mixes with lighter ISOW from the eastern Irminger Sea along the way (Figure 3.3b). Once this mixing occurs and the flow turns northwestward around Cape Farewell, the combined water mass is typically referred to as NADW (Dickson & Brown, 1994). This water mass then flows along the eastern and western boundaries of the Labrador Sea, though the coolest and freshest classes do not

seem to reach onto the shallow topography in the northwest portion of the basin near Davis Strait, before continuing farther southeast along the western boundary to the Flemish Cap (McCartney, 1992; Swift, 1984). While the bathymetry of the Labrador Basin generally deepens to the southeast until just east of the Flemish Cap, the bottom waters become paradoxically warmer and lighter over this region, suggesting that relatively substantial mixing with the overlying waters occurs as the NADW flows along this pathway (Figures 3.3a, 3.3c, and 3.3d). Specifically, no bottom water denser than $\gamma^n = 28.18$ kg m^{-3} or cooler than $\Theta = 1.5$°C is observed farther south than the Orphan Knoll (~50.5°N, 46.5°W).

Just southeast of the Flemish Cap, the topography shoals in the transition from the southeast Labrador Basin to the Newfoundland Basin at the Milne Seamount Complex, trapping the denser, cooler ($\Theta \leq 1.7$°C), oxygen-richer, nutrient-poorer NADW to the north. The NADW that remains in the southeast Labrador Basin appears to spread eastward to fill the rest of this basin while becoming warmer, and lighter due to further mixing with the overlying waters as the topography shoals toward the western flank of the Mid-Atlantic Ridge. Some of the AI-NADW bearing the elevated silica signal from Antarctic-origin waters ([$Si(OH)_4$] > 20 μmol kg^{-1}) flows into the southeastern corner of this basin along the western flank of the Mid-Atlantic Ridge and mixes with these waters (Sections 3.3.1 and 3.3.3.1).

The lighter NADW that escapes the southeast Labrador Basin via a deep, narrow channel along the western boundary continues southwestward within the DWBC along the continental slope of the Newfoundland Basin. Some of this NADW makes its way into the deeper interior of this basin where it mixes along isopycnals with the remnants of Antarctic-origin waters flowing northward to transform into AI-NADW ([$Si(OH)_4$] > 20 μmol kg^{-1}). The NADW within the DWBC along the edge of Newfoundland Basin continues to flow equatorward in a narrow jet along

the continental slope, briefly turning northwestward along the Tail of the Grand Banks before continuing southwestward along the North American continental slope. The narrowness of this "pure" NADW flow south of the Newfoundland Basin is especially clear in the silica maps by the proximity of the 20 μmol kg^{-1} contour to the continental margin.

However, some of the more recently ventilated (oxygen-richer and nutrient-poorer) and denser (colder and fresher) classes of the NADW in the DWBC do not make the turn around the Tail of the Grand Banks and instead remain trapped in the Newfoundland Basin (Figures 3.3b–3.3f), consistent with previous work using CFC data (Smethie et al., 2000). While much of the NADW to the south remains along the North American continental slope within the DWBC, some of it leaves the boundary and enters the interior, where its oxygen-rich and nutrient-poor signal is attenuated as it mixes with northward-flowing AABW to become the AI-NADW that is found over most of Sohm and Hatteras abyssal plains.

The rest of the NADW continues equatorward along the coast as a coherent signal within the DWBC as far south as ~27°N, before it begins to disappear from our bottom water maps as it mixes with AABW or gets displaced higher in the water column (consistent with Reid & Lynn, 1971). Since "pure" NADW continues southward above the bottom along the length of the western boundary of the Atlantic, we see the nutrient-poor signal of these waters occasionally reappear in our bottom water property maps over the continental slope as far south as ~28°S when the bottom is too shallow for AI-NADW or AABW to be present. Previous work has also shown that the influence of NADW on bottom waters reappears in parts of the Indian and Pacific oceans as the bottom waters mix with overlying NADW in these regions (Johnson, 2008). However, on our maps it is difficult to identify when this mixing occurs with NADW versus other overlying water masses

in those basins, though our property-property analysis (Section 3.3.6) may offer some additional insight into the along-bottom water mass interactions in those basins.

The ISOW-heavy AI-NADW formed within the West European Basin flows southward along the central and eastern portions of the east Atlantic basins, entraining large amounts of the denser, cooler, fresher, and nutrient-richer AABW near 11°N and the equator where these waters flow eastward across the Mid-Atlantic Ridge within deep fracture zones (Figures 3.3b–3.3d, 3.3f–3.3h). This AI-NADW along the bottom ultimately makes it as far south as the southern boundary of the Angola Basin (Walvis Ridge) where it mixes with a small amount of LCDW from the Cape Basin (Section 3.3.3.1). Between the West European Basin and the Walvis Ridge, the oxygen and nutrient concentrations of the AI-NADW are also strongly influenced by biogeochemical processes occurring along the African coast. Over most of the African continental slope from 33°N to 5°N the bottom waters are somewhat oxygen-poor ($[O_2] < 242$ μmol kg^{-1}) compared to those in the interior of the east Atlantic basins (Figure 3.3e). These relatively oxygen-poor bottom waters are located directly underneath the highly-productive coastal upwelling regimes of the Canary Current system (~21°N–33°N), the region off of the Mauritania and Senegal coasts (~14°N–21°N), and the region off the Sierra Leone and Liberia coasts (~5°N–8.5°N) (e.g., Carr, 2001). This oxygen-poor signal is also evident in the bottom waters slightly farther offshore under the highly productive Guinea Dome (~10°N–15°N, 20°W–28°W; Figure 3.3e) and highly-productive band around 20°N extending from the Canary Current (e.g., Carr & Kearns, 2003; Siedler et al., 1992). Oxygen minimum zones are typically found beneath such tropical upwelling regions near the eastern boundary (e.g., Karstensen et al., 2008). Given the lack of coincidently high along-bottom nutrient concentrations in these regions, it seems likely that the relatively low oxygen concentrations we see in the bottom waters near the African coast compared to the interior of the

eastern Atlantic basins from 5°N–33°N are due to the downward diffusion of the low oxygen signal from the oxygen minimum zones above, not in-situ dissolution of nutrients along the bottom. This signal then diffuses laterally (offshore) along the bottom to influence the southward-flowing AI-NADW in the interior of the east Atlantic basins from ~5°N–33°N.

Farther south, along the eastern boundary of the Angola Basin and the northern boundary of the Guinea Basin, two additional coastal regions of especially low oxygen are observed within the AI-NADW (Figure 3.3e). One of these regions extends to the southeast/east from the continental slope at ~4°N, 1°W into the interior of the Guinea Basin as far south as ~0.5°S, 2°E and as far east as 3°N, 4.5°E. This signal also appears to diffuse westward to ~3°N, 4.5°W, consistent with previous observations at 4°W (Arhan et al., 1998). This entire region of oxygen-poor bottom waters is likely associated with the upstream (to the west) highly productive Ivory Coast/Ghana coastal upwelling region (e.g., Nieto & Mélin, 2017). While a permanent oxygen minimum zone is not present beneath this upwelling region, the oxygen concentrations become nearly suboxic around 300 meters (Lebrato & Jones, 2009). These low oxygen concentrations in the upper water column below the upwelling region likely contribute somewhat (via diffusion) to the oxygen-poor signal in the bottom waters farther offshore. However, the presence of elevated nutrient concentrations within this near-bottom, oxygen-poor plume suggests that a substantial amount of oxygen is probably being consumed by the remineralization of this organic material at the seafloor in the offshore region. Previous work observed that organic material from the Ivory Coast/Ghana upwelling regime can be exported off the shelf to depths of ~1200 meters via downslope, along-bottom flow in canyons bisecting the continental slope (Lebrato & Jones, 2009). Though they did not make measurements below 1200 meters, they used regional bathymetric maps to note that many of these canyons extend to depths > 2000 meters. In our maps, it appears that

organic matter exported via these canyons can be found along that seafloor as deep as the 4800-meter isobath, suggesting that the link between this coastal upwelling regime and enhanced deposition of organic material along the seafloor extends farther offshore in the Guinea Basin than previously discussed. This presents an alternate explanation to that of the current literature (e.g., Vangriesheim, Pierre, et al., 2009) that instead suggests that the oxygen-poor signal from the outflow of the Congo canyon (see further discussion below) is somehow being advected over a great distance with minimal modification to this region by an along-isobath flow. It is also likely that nutrient input from nearby rivers such as the Volta and Niger rivers contributes both to the high productivity of the coastal regions bordering the Guinea Basin and to the higher concentrations of nutrients found along the seafloor in the interior of the basin (e.g., Araujo et al., 2014; Nieto & Mélin, 2017).

The other area of especially oxygen-poor and nutrient-rich bottom waters extends from ~2°S to ~21°S along the continental rise and is related to the highly productivity within the Congo (formerly Zaire) River plume, Angola Dome, and Benguela Current upwelling system regions; and the nutrient-rich outflow of the Cuanza River. The presence of such oxygen and nutrient anomalies along the seafloor from 6°S–8°S was discussed in an analysis of hydrographic and piston core data that sampled along the Congo canyon and its outflow (Van Bennekom & Berger, 1984). That analysis suggested that decomposing organic matter from the highly productive Congo River plume region is exported within a bottom nepheloid layer from the Congo canyon to the base of the continental slope (at ~3500 meters) and can be found offshore as far as ~6.5°E (nearly the 5000-meter isobath). It cited enhanced turbulence in the inner part of the canyon as the reason this organic matter does not settle therein. Just outside of the inner canyon, this enhanced deposition of organic material leads to anomalously oxygen-poor and nutrient-rich bottom waters

as oxygen is consumed in the remineralization of this organic matter either within the near-bottom waters or the sediments (Vangriesheim, Pierre, et al., 2009). Van Bennekom and Berger (1984) noted that phosphate concentrations there are not only affected by the oxidation of organic material but also by a process related to the high turbidity of the along-canyon flow. They found that phosphate is absorbed on suspended material in the hypoxic inner canyon and then desorbs in the relatively oxygen-richer conditions in the bottom water downstream to contribute as much as 80% of the observed increase in phosphate concentrations seen at ~3500 meters. In our maps (Figures 3.3e–3.3h) we see the core of this oxygen-poor, nutrient-rich signal over approximately the same depth range of 3600–4600 meters (6°S–8°S, 6.5°E–9°E) as in this earlier work and can trace this signal as it diffuses farther offshore to interact with the southward-flowing AI-NADW. This signal can also be advected either northwestward to ~2°S or southeastward to ~10.5°S along these isobaths by as-yet unmeasured extensions of the frequently oscillating currents measured near the Congo canyon by Vangriesheim, Khripounoff, et al. (2009).

Analysis of a high-resolution zonal hydrographic section at 11°S identified an along-bottom oxygen minimum and nutrient maximum on the continental rise from 10°E–11°E and showed that this signal diffuses offshore along the bottom to ~6°E, 11°S (Warren & Speer, 1991). At 11°S on our maps we find that this signal diffuses offshore from the continental rise to ~6°E (approximately the 5300-meter isobath) as well. Warren and Speer (1991) showed that the ratio of the changes in oxygen, nitrate, and phosphate (i.e., the Redfield ratio) within this plume indicates that this signal is due to the remineralization of organic material that likely occurs within the sediments, with the altered concentrations resulting from this process later diffusing across the sediment-water interface. They also note that the signal of silica along the bottom is a bit more elevated than expected from the oxidative ratios, potentially due to enhanced accumulation of

diatom skeletons on the bottom relative to other sources of organic material in this region. A high proportion of silica compared to nitrate and phosphate has also been observed in the siliceous sediments of the Bay of Bengal (Edmond et al., 1979). The current literature (e.g., Warren & Speer, 1991 and Vangriesheim, Pierre, et al., 2009) suggests that the oxygen-poor and nutrient-rich signal related to outflow of the Congo canyon is advected as far north as 3°N, 3°E and as far south as 11°S in along-isobath flows over the continental rise. However, our maps (Figures 3.3e–3.3h) suggest that the signal previously observed at 3°N, 3°E is actually due the southeastward advection of the oxygen-poor, nutrient-rich signal associated with the highly productive Ivory Coast/Ghana coastal upwelling regime as described above and that the Congo canyon-derived signal is instead constrained to ~2°S–10°S along the continental rise. It is not clear from our maps whether this signal is advected as far south as 11°S as suggested by Warren & Speer, 1991 because there seems to be another bolus of oxygen-poor along-bottom water centered along the continental rise at ~11.5°S, 10.5°E that may be contributing to the low oxygen concentrations observed at 11°S. The localized, especially high nutrient concentrations within this plume suggest that this signal is not simply from southward advection of the Congo River signal but instead originates from a different source. This source could be the decomposition of the large amounts of organic matter deposited by the highly productive Angola Dome (e.g., Karstensen et al., 2008) and the outflow of the nutrient-rich Cuanza River (e.g., Hanz et al., 2019). The core of this signal extends southward along the continental rise to ~14.5°S, which is the approximate northern boundary of the Angola-Benguela Frontal Zone (Meeuwis & Lutjeharms, 1990).

Farther south, from ~17°S–19°S there is another plume of especially oxygen-poor and nutrient-rich water along the continental slope. This signal likely corresponds to the decomposition of organic matter that accumulates under the highly productive Benguela Current upwelling

system (e.g., Carr & Kearns, 2003) and spreads northward along the continental slope to meet the signal from the Angola Dome/Cuanza River in the Angola-Benguela Frontal Zone from ~14.5°S–16.5°S. There is another small region of especially oxygen-poor and nutrient-rich bottom waters that is likely related to the Benguela Current upwelling system in our maps centered over the continental rise at 23°S, 9°E in the northernmost region of the Cape Basin (consistent with previous observations by Warren & Speer, 1991).

There are many processes contributing to the especially oxygen-poor and sometimes nutrient-rich bottom waters along the eastern boundary of the Atlantic that can affect the properties of the southward-flowing AI-NADW. These include the downward diffusion of oxygen-poor signals from oxygen minimum zones and the remineralization of especially large amounts of organic matter deposited along the seafloor from both river discharge and highly productive coastal upwelling zones. While one might expect to see a similar, oxygen-poor signal in the NADW flowing southward over the continental slope beneath the outflow of the Amazon River in the western equatorial Atlantic basins, such a signal is not obvious in our maps. This could be because the bottom water flow is too rapid in this region to allow for similar amounts of nutrient accumulation (and thereby oxygen consumption when these nutrients are remineralized) to occur or because it occurs at depths shallower than our 2000-meter cut-off for our maps.

Farther south, recent observations at 34.5°S confirmed the presence of recently ventilated "NADW" (AI-NADW by our definition since $[Si(OH)_4] > 20$ µmol kg^{-1}) along the seafloor within the eastern boundary current bordering the Cape Basin, which was likely transported to this region from the western boundary of the Atlantic via interior pathways (Kersalé et al., 2019). The rapid transition between the substantially warmer, saltier, oxygen-richer, and nutrient-poorer AI-NADW over the continental slope of the Cape Basin and the LCDW within the deeper interior of the basin

is clear on our maps and we are able to see the full plume of the flow along the boundary (Figures 3.3c–3.3f). However, we find the offshore extent of the AI-NADW at 34.5°S to be ~1.5° longitude closer to the coast (at ~16.5°E) than observed in their work (at ~15°E). The high resolution of our mapped fields allows us to resolve boundary features of interest such as this throughout much of the global ocean.

3.3.5 *Bottom Waters of the Arctic*

The bottom water distribution of the Arctic Ocean is governed by its topography, exchanges with the Pacific and Atlantic oceans, and the broad continental shelves on its boundaries. The Arctic is split into two main basins, the Amerasian and Eurasian basins, separated by the Lomonosov Ridge that roughly follows the 135°E and 45°W meridians (Figure 3.6a). The Amerasian Basin contains two important sub-basins, the Canada and Makarov basins, separated by the Alpha-Mendeleev Ridge. The Eurasian Basin also contains two key sub-basins, the Nansen and Amundsen basins, separated by the Gakkel Ridge. The paradigm for the bottom-water spreading pathways in the Arctic is that flow through the Fram Strait fills the bottom of the Nansen and Amundsen basins with waters from the Nordic seas at the sill depth (2600 meters) and then this flow proceeds to fill the Makarov and Canada basins (Aagaard et al., 1985; Bluhm et al., 2015). Dense waters flowing from the shelf regions likely also contribute to the bottom waters of the Arctic (e.g., Ikeda et al., 2018; Jones et al., 1995).

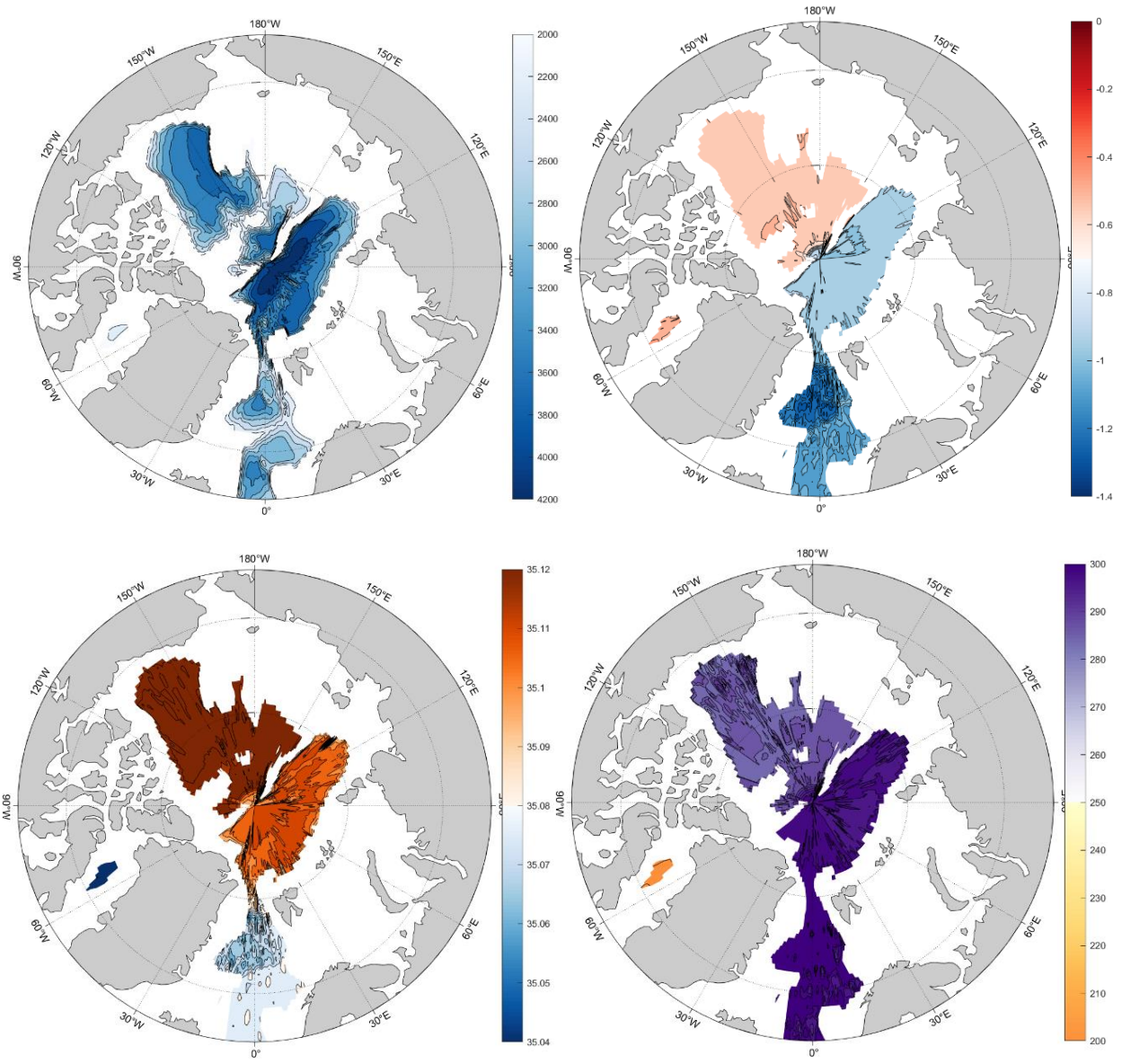
180°W
150°W
150°E
120°W
120°E
90°W
60°W
60°E
30°W
30°E
0°
2000
2200
2400
2600
2800
3000
3200
3400
3600
3800
4000
4200
0
-0.2
-0.4
-0.6
-0.8
-1
-1.2
-1.4
35.12
35.11
35.1
35.09
35.08
35.07
35.06
35.05
35.04
300
290
280
270
260
250
240
230
220
210
200

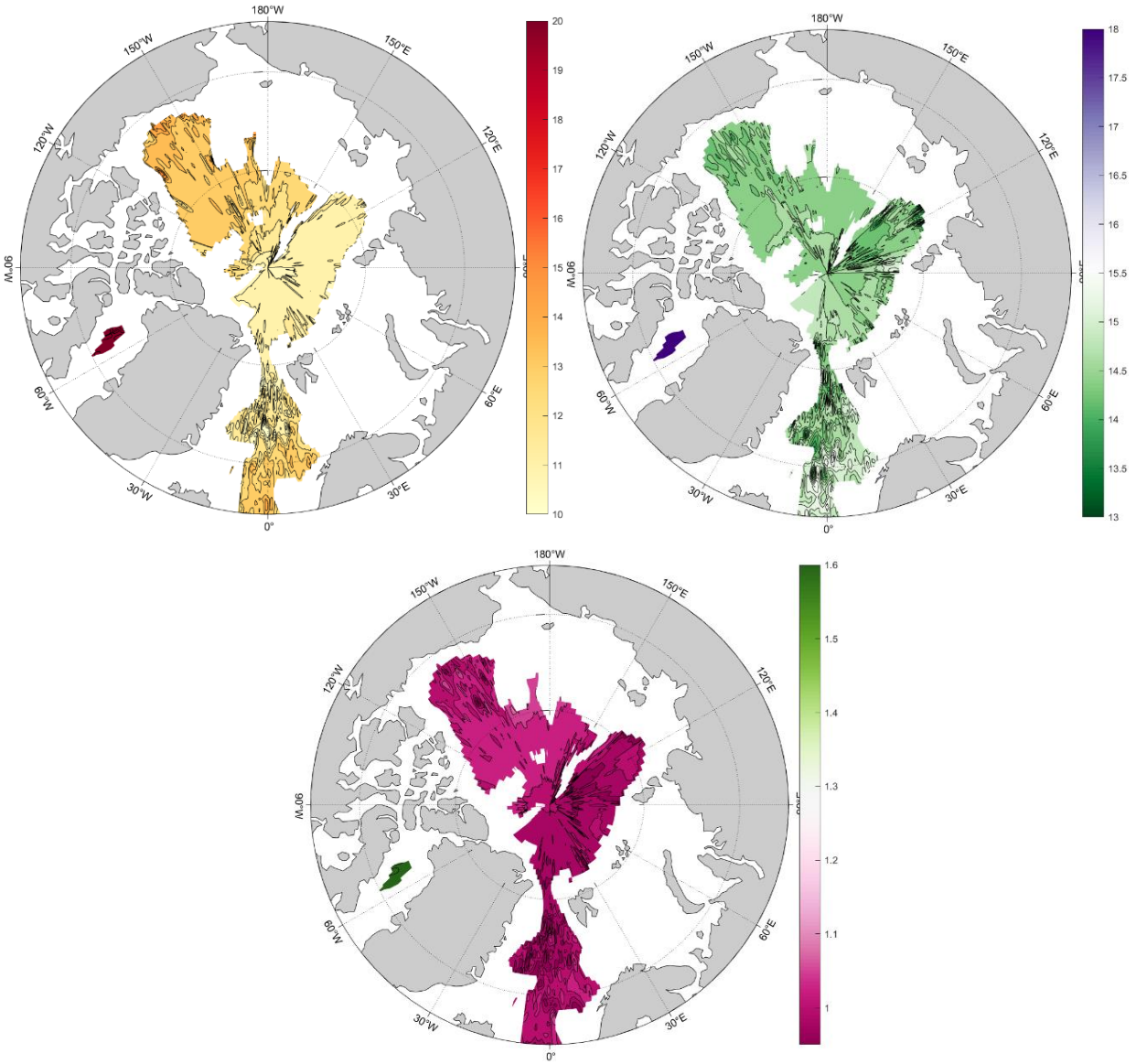

Figure 3.6. a) "ETOPO-60" – ETOPO-2 bathymetry interpolated to 0.5° resolution (meters, CI = 250), RFOM-generated maps at 0.5° resolution of b) conservative temperature (°C, CI = 0.05), c) absolute salinity (g kg^{-1}, CI = 0.005), d) dissolved oxygen (µmol kg^{-1}, CI = 2), e) silica (µmol kg^{-1}, CI = 0.5), f) nitrate (µmol kg^{-1}, CI = 0.2), and g) phosphate (µmol kg^{-1}, CI = 0.025) for the Arctic Ocean. Note that many of these contour intervals (CI's) are different from those used in Figures 3.3 and 3.5. The values of these properties in Baffin Bay are more accurately depicted in Figure 3.3.

Our maps are consistent with deep inflow to the Arctic through the Fram Strait, where the bottom waters north of the strait are lighter, warmer, and saltier, as found at the sill depth in the Nordic Seas, compared to the denser, cooler, and fresher bottom waters south of the strait (Figures 3.6b and 3.6c). The waters that make it into the Arctic abyss are also slightly less recently ventilated (i.e., oxygen-poorer) than those by the seafloor in the Nordic seas (Figure 3.6d). Our maps suggest these waters slowly spread throughout the Nansen and Amundsen basin before potentially finding deep gaps in the Lomonosov Ridge near the North Pole. Previous work suggests a maximum sill depth through this ridge of ~1870 meters near 88.7°N, 156.0°E, which would allow for bottom water flow between these basins (Björk et al., 2007). We see a small plume of bottom water with similar silica and oxygen values, but not temperature and salinity values, to those of the Eurasian Basin extending from this gap in the ridge into the Makarov Basin (Figures 3.6b–3.6e). The flow from the Amundsen to the Makarov Basin implied by the silica and oxygen distributions has been suggested by many previous studies (e.g., Jones et al., 1995; Timmermans et al., 2005). Timmermans et al., 2005 estimated this over-sill flow to be 0.25 Sv by combining hydrographic observations and hydraulic theory. However, Björk et al., 2007 found observational evidence of flow in the opposite direction, from the Makarov to the Amundsen Basin. Since this gap in the Lomonosov Ridge is at the northernmost boundary of our mapping domain and our RF method can be unreliable along the boundaries caution is advised regarding drawing inferences from our maps about the true direction of this trans-basin flow.

The bottom waters of the Makarov Basin likely flow via the ~2600 m deep sill at the Cooperation Gap within the Alpha-Mendeleev Ridge into the remainder of the Amerasian Basin and there is some suggestion of this flow in our silica map (Figure 3.6e). Farther from the Lomonosov Ridge, the bottom waters of the Amerasian Basin are distinctly warmer, saltier,

oxygen-poorer, phosphate-richer, and silica-richer than those of the Eurasian Basin (Figures 3.6b–3.6e and 3.6g), consistent with previous work (Aagaard et al., 1985; Ikeda et al., 2018; Worthington, 1953). However, there is substantial variability in the nitrate concentrations within both of these basins in our map (Figure 3.6f) with notable regions of especially low nitrate and phosphate around 120°E in both the Amundsen Basin and in the Beaufort Sea. The basin-scale property trends of oxygen and silica (Figures 3.6d and 3.6e) suggest that the bottom waters of the Amerasian Basin are older than those in the Eurasian Basin, further supporting the idea that the flow through the Lomonosov Ridge is from the Eurasian Basin to the Amerasian Basin.

Within the Canada Basin, the bottom waters are fairly homogenous on our maps, making inferences of flow direction within this basin impossible. Previous work suggested the bottom waters in this sub-basin move extremely slowly and can be lightened via geothermal heating and ultimately exported back to the Eurasian Basin at shallower depths (Carmack et al., 2012). There are some suggestions of this mechanism on our conservative temperature map around 120°W (Figure 3.6b) but it is difficult to determine whether the warming pattern is due to shallowing of the bathymetry or geothermal heating. Based on the bottom slope, it seems more likely to be the former.

Recent work mapped the deep nutrient distributions of the Arctic using data from the Hydrochemical Atlas of the Arctic Ocean (HAAC) (Ikeda et al., 2018). This dataset contains more oxygen and nutrient data than the datasets used in our work but no associated temperature and salinity information. Thus, we could not use the HAAC data since our methodology requires coincident temperature and salinity data at the locations of the oxygen and nutrient data in order to build the first two layers of our “stacked” RF. Their maps show the same large-scale differences in silica, phosphate, and oxygen between the Eurasian and Amerasian basins as seen in this work.

In terms of smaller-scale features, our maps show the same silica-rich, oxygen-poor region in the southern Canada Basin likely due to the dissolution of sinking organic matter from Alaskan coastal waters, but not the silica-rich region north of the Barents Sea seen in their work. Additionally, their analysis of PO_4^* distributions throughout the Arctic further supports the discussion above of the bottom water flow paths implied by our maps, but we do not see the region of especially high phosphate in the southern Canada Basin present in their maps.

The Arctic water that flows through the Canadian Arctic Archipelago and enters Baffin Bay is not the same as that observed along the seafloor in the Canada Basin but is instead from higher in the water column in that basin (e.g., Bluhm et al., 2015). This water enters Baffin Bay via the Nares Strait (sill depth ≈ 250 meters) and the Lancaster and Jones sounds (sill depths ≈ 150 meters) and is a modified version of the especially fresh near-surface water from the Canada Basin (Tremblay et al., 2002). Due to this highly fresh input, of the basins we mapped, only the Sea of Japan has fresher bottom water than Baffin Bay (Figure 3.3d). The Arctic inflow to Baffin Bay has nutrient concentrations that are somewhat higher than those of the Canada Basin waters due to nutrient regeneration as these waters flow over the continental shelves. Once in Baffin Bay, these waters likely cascade down the slope to fill the abyss where they remain trapped due to the shallow sills bordering the basin. There may also be a contribution to the bottom waters from dense waters formed on the continental shelf, though a flow of such waters down the slope has not yet been directly observed (e.g., Tang et al., 2004). The especially low oxygen concentration of the bottom waters throughout this basin on our map supports the idea that these waters remain trapped in this basin for some time (Figure 3.3e). This long residence time leads to a large amount of silica accumulation in the bottom waters due to the dissolution of biogenic silica with the concentration of silica increasing from ~26 μmol kg^{-1} in the shallow Arctic inflow (not shown, from Trembley

et al., 2002) to ~101 µmol kg^{-1} in the bottom waters of the ≥ 2000-meter deep portion of Baffin Bay (Figure 3.3f). This deep regeneration of organic matter could be contributing to the low oxygen concentrations as well.

3.3.6 *Property-Property Analysis of Global Bottom Waters*

Bottom water property-property plots (e.g., Θ-S_A, O_2-S_A) illuminate the degree of mixing among different water masses, including local end-members created by the near-bottom remineralization of organic matter. Here we will focus specifically on the Θ-S_A and O_2-S_A relationships in our RFOM-mapped fields, using bivariate areal censuses to gain insights into these processes.

3.3.6.1 Θ-S_A Relationships

In Θ-S_A space, the bottom waters of the Atlantic, Indian, and Pacific oceans radiate outward in three different directions from a shared $AABW_{source}$/AABW/LCDW (i.e., Southern Ocean water) set of end-members (Figure 3.2). The general shape of the Θ-S_A distribution for the bottom waters is identical to that of the potential temperature-practical salinity distribution presented by Worthington (1981) for waters throughout the water column that are cooler than 4°C (their Figure 2.8). More detailed comparisons to their work are made below in the discussion of our bivariate areal census. In our bottom water Θ-S_A distribution (Figure 3.2), the Atlantic sector of the Southern Ocean contains the coolest and freshest varieties of AABW/$AABW_{source}$ while the Pacific sector contains the warmest and saltiest varieties. The Indian sector of the Southern Ocean contains AABW/$AABW_{source}$ with temperature and salinity values between those for these water masses in the other two basins. However, within most of the neutral density range of LCDW the opposite pattern holds with the Pacific sector containing the coolest and freshest type and the Atlantic sector containing the warmest and saltiest type. This pattern reflects the stronger influence of relatively salty NADW on the LCDW in the Atlantic sector (Orsi et al., 1999). As for AABW/$AABW_{source}$,

the temperature and salinity for the LCDW in the Indian sector lies between the Pacific and Atlantic values. Extending northward from the Southern Ocean, the bottom waters of the Indian and Atlantic basins become warmer and saltier while those of the Pacific become warmer and fresher. The bottom waters of the Arctic Ocean, Baffin Bay, the Sea of Japan, the Gulf of Mexico and the Mediterranean, Caribbean, Andaman, and Sulu seas are disconnected from the rest of the global bottom waters in Θ-S_A space since they are filled by waters from higher in the water column that are not found along the bottom in any other basins (Figure 3.2, see caption for which of these basins are off-scale).

In shallower regions of our mapped dataset, waters along the bottom may be dominated by other deep or intermediate water masses than those highlighted in this work (i.e., not LCDW, PDW, or IDW). To exclude these less globally prevalent along-bottom waters from our property-property analysis, we limit it to bottom waters at locations deeper than 3500 meters in the remainder of this section and in Section 3.3.6.2. This restriction removes some shallower basins of note such as Baffin Bay and the Andaman Sea from the analysis.

We analyze the Θ-S_A distributions for the entire ocean as well as for the Atlantic, Indian, and Pacific oceans individually to better understand the breakdown between AABW, LCDW, NADW, PDW, and IDW within each basin. For this purpose, we designate the boundaries between these three basins in the Southern Ocean (defined as the region south of 55°S as in Worthington, 1981) to be at 25.2°E (Atlantic-Indian, eastern edge of Weddell Gyre), 146.8°E (Indian-Pacific, southern tip of Tasmania), and 64.3°W (Pacific-Atlantic, Shackleton Fracture Zone within Drake Passage).

By combining our global RFOM-mapped fields of bottom water Θ and S_A with the seafloor areas within each 0.5° latitude × 0.5° longitude box, we constructed a Θ-S_A diagram where each

0.1°C × 0.01 g kg^{-1} rectangle is shaded by the log of the area of the seafloor touched by waters of that class (Figure 3.7a). This analysis is reminiscent of previous work that created a volumetric bivariate census for the full-depth global ocean, excluding the Arctic Ocean and all marginal seas, using the same-sized bins but in potential temperature-practical salinity (θ-S_P) space (Worthington, 1981, hereafter W81). However, since our work focuses on only the bottommost waters we analyze area, not volume. Additionally, there are substantially more observations of the deep ocean presently than were available in 1981 so we have more confidence in the accuracy of our census since we did not need to do as much extrapolation as did W81. For example, in the dataset used in the W81 census only 28.7% of 5° latitude × 5° longitude squares in the North Pacific had at least one high-quality deep station while in our dataset 97.1% of these squares contain at least one high-quality observation of both bottom conservative temperature and absolute salinity (not shown). W81 assumed that the remaining 71.3% of the North Pacific was distributed across the same θ-S_P classes as the measured waters. Similar assumptions were used for regions of missing data throughout the Atlantic and Indian basins as well leading to further uncertainty in the class distributions of W81.

Our analysis further differs from W81 in that we use the updated Thermodynamic Equation of Seawater - 2010 (TEOS-10, http://www.teos-10.org/) variables of absolute salinity and conservative temperature instead of practical salinity and potential temperature. We are not aware of any previous efforts to summarize the global areal coverage of specific temperature-salinity classes using these newer variables.

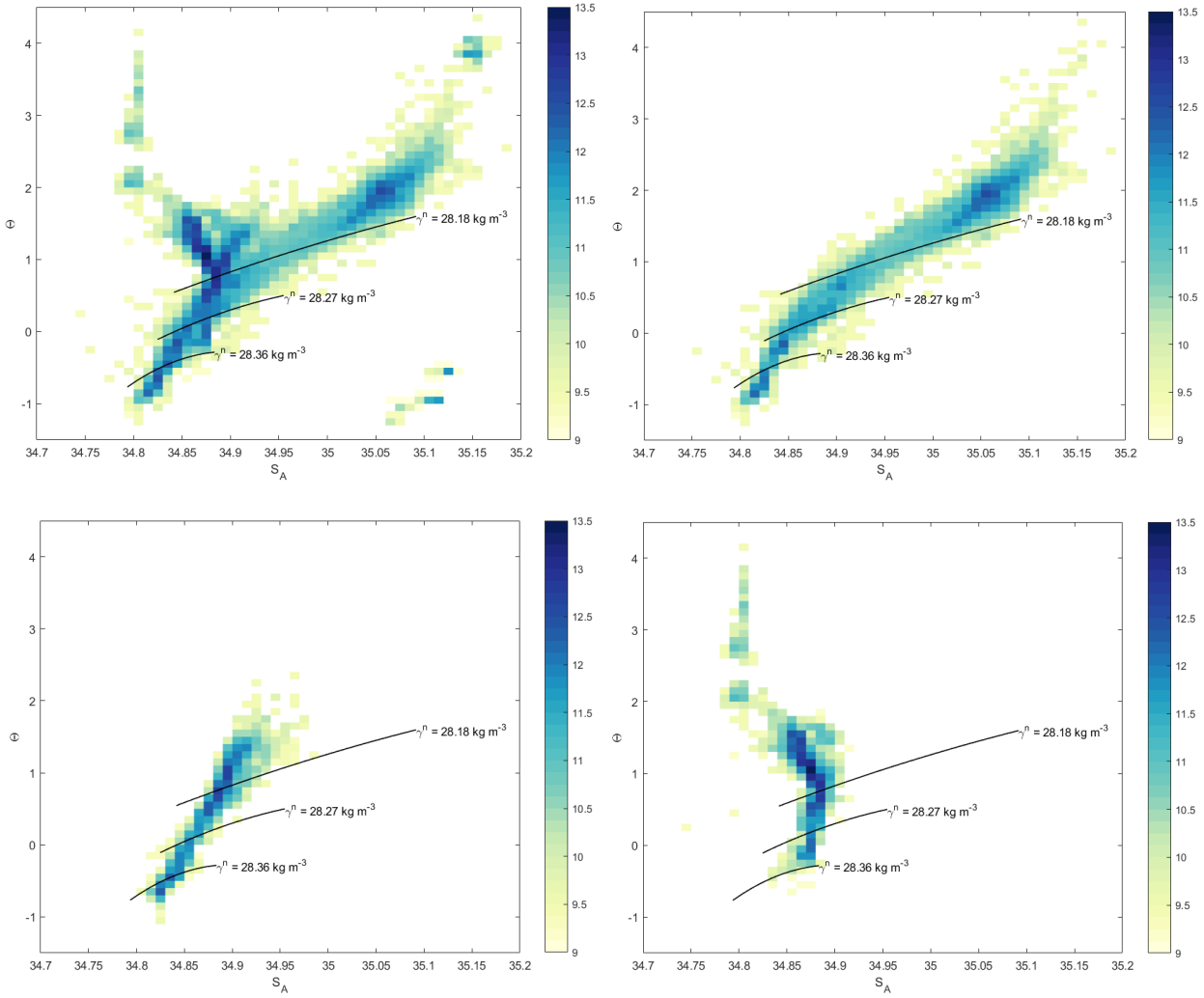

Figure 3.7. $\log_{10}$ of seafloor area within each 0.1°C by 0.01 g kg^{-1} box in conservative temperature-absolute salinity space for the a) global, b) Atlantic, c) Indian, and d) Pacific oceans for locations with seafloor depths ≥ 3500 meters. Black curves approximating the γ^n = 28.18, 28.27, and 28.36 kg m^{-3} surfaces over the range of the data are included for reference. Note that the following basins are off-scale here: the too warm/salty Mediterranean Sea, the too fresh Sea of Japan, and the too warm Sulu Sea.

Our bivariate area census for locations deeper than 3500 meters highlights many key aspects of the global bottom water mass distribution (Figures 3.7a–3.7d). The highest area regions form a “y”-like shape with a Southern Ocean $AABW_{source}$/AABW/LCDW base, a fresher Pacific

"leg", and a saltier Atlantic "leg". A shorter "leg" of middling salinities in the Indian basin lies between the more prominent Pacific and Atlantic branches. A summary of the geographic distribution of the 30 highest area classes (all which have $\Theta \leq 2°C$) helps bridge between the maps of temperature and salinity discussed above and this bivariate area census (Table 3.5). In total, these 30 classes cover ~66.0% of the seafloor deeper than 3500 meters. W81 included a similar table ranking the most voluminous classes they identified (though only until 75% of the global ocean volume had been classified). We matched our 30 highest area classes to their counterparts in the W81 table for reference, converting from S_A to S_P based on where the majority of the points in each class were located. Seven of our ten highest-area classes are included in their ten highest-volume classes, though in a different order. Given that these classes correspond to PDW and LCDW (see further discussion below) this agreement is not surprising.

When bottom waters are formed around Antarctica or in the North Atlantic (via the mechanisms discussed in Sections 3.3.2 and 3.3.4), the "pure" version of these water masses typically only exists in a small region right around the formation region (i.e., the $AABW_{source}$ and the "pure" NADW on Figure 3.4). These newly formed bottom waters undergo substantial mixing with overlying or laterally adjacent water masses as they exit these regions. It is at these less extreme property values that these water masses flow over much larger areas in the downstream basins.

Table 3.5. Geographical breakdown of the area within each of the 30 highest area Θ-S_A classes shown in Figure 3.7a. Some rows do not sum to 100% due to rounding. The equator serves as the boundary between the North and South Pacific as well as the North and South Atlantic oceans. The boundaries between the different sectors of the Southern Ocean are noted in the text. Only classes 17, 21, and 25 are not discussed specifically in the text. The total seafloor area for locations with seafloor depth ≥ 3500 meters is 2.39×10^{14} m^2.

Rank	Rank (W81)	Θ (°C)	S_A (g kg^{-3})	Mean γ^n (kg m^{-3})	% of Total Area ≥3500 meters	N. Pac. (%)	S. Pac. (%)	S.O. Pac. (%)	Ind. (%)	S.O. Ind. (%)	N. Atl. (%)	S. Atl. (%)	S.O. Atl. (%)
1	6	1.0–1.1	34.87–34.88	28.11	10.08	82	18	-	-	-	-	-	-
2	68	0.9–1.0	34.87–34.88	28.13	4.71	79	21	-	-	-	-	-	-
3	5	1.1–1.2	34.87–34.88	28.10	4.47	80	20	-	-	-	-	-	-
4	10	0.8–0.9	34.88–34.89	28.16	4.22	37	52	-	11	-	-	-	-
5	3	0.7–0.8	34.88–34.89	28.18	4.22	1	53	1	45	-	-	-	-
6	7	0.6–0.7	34.88–34.89	28.20	4.18	-	56	2	41	-	-	1	-
7	1	1.1–1.2	34.86–34.87	28.09	4.05	75	25	-	-	-	-	-	-
8	4	1.2–1.3	34.86–34.87	28.07	3.08	61	39	-	-	-	-	-	-
9	29	1.4–1.5	34.86–34.87	28.04	2.28	4	96	-	-	-	-	-	-
10	42	0.5–0.6	34.87–34.88	28.21	2.17	-	44	11	43	-	-	1	1
11	14	0.9–1.0	34.89–34.90	28.15	2.04	-	7	-	93	-	-	-	-
12	11	1.0–1.1	34.89–34.90	28.14	1.91	-	4	-	96	-	-	-	-
13	35	1.9–2.0	35.05–35.06	28.12	1.64	-	-	-	-	-	27	73	-
14	32	0.4–0.5	34.87–34.88	28.22	1.63	-	18	21	57	-	-	4	-
15	27	0.9–1.0	34.88–34.89	28.14	1.43	39	56	-	5	-	-	-	-
16	26	1.3–1.4	34.86–34.87	28.06	1.39	30	70	-	-	-	-	-	-
17	24	0.5–0.6	34.88–34.89	28.21	1.25	-	51	10	33	-	-	6	-
18	119	-0.7– -0.6	34.82–34.83	28.40	1.20	-	-	-	3	61	-	5	30
19	75	-0.2– -0.1	34.84–34.85	28.30	1.15	-	-	-	30	2	-	68	-
20	8	1.5–1.6	34.85–34.86	28.02	1.09	38	62	-	-	-	-	-	-
21	61	1.9–2.0	35.06–35.07	28.12	0.98	-	-	-	-	-	95	5	-
22	9	1.3–1.4	34.85–34.86	28.05	0.90	41	59	-	-	-	-	-	-
23	17	0.8–0.9	34.89–34.90	28.17	0.88	1	9	1	88	-	-	1	-
24	193	-0.5– -0.4	34.83–34.84	28.35	0.88	-	-	-	17	70	-	10	2
25	123	1.8–1.9	35.05–35.06	28.13	0.74	-	-	-	-	-	97	3	-
26	129	0.0–0.1	34.87–34.88	28.30	0.73	-	-	96	1	-	-	3	-
27	15	1.4–1.5	34.85–34.86	28.04	0.69	24	76	-	-	-	-	-	-
28	191	-0.1–0.0	34.87–34.88	28.31	0.69	-	-	100	-	-	-	-	-
29	99	-0.6– -0.5	34.82–34.83	28.37	0.65	-	-	-	15	35	-	13	37
30	166	1.7–1.8	35.04–35.05	28.13	0.64	-	-	-	-	-	94	6	-

Given the vastness of the Pacific compared to the other oceanic basins, it is not surprising that many of the classes covering the highest area are found exclusively in the Pacific (e.g., classes 1–3, $\gamma^n < 28.18$ kg m^{-3}, $\Theta = 0.9–1.2$°C, $S_A = 34.87–34.88$ g kg^{-1}, Table 3.5) where bottom waters can flow relatively unperturbed over large areas. These classes represent PDW, some of which has mixed with the lighter classes of LCDW. W81 also found that PDW within the same Θ-S_A range made up several of the highest volume classes (their classes 5, 6, and 68 with $\theta = 0.9–1.2$°C, $S_p = 34.69–34.70$) even though their census used data from all depths. Many classes of even warmer and fresher PDW ($\gamma^n < 28.18$ kg m^{-3}) occupy substantial portions of the global bottom area as well (e.g., classes 7–9, 16, 20, 22, 27 in Table 3.5).

Another set of especially high area classes in our census are within the neutral density range of LCDW ($28.18 \leq \gamma^n < 28.27$ kg m^{-3}) and are found in both the Pacific and Indian basins (e.g., classes 5–6, $\Theta = 0.6–0.8$°C, $S_A = 34.88–34.89$ g kg^{-1}, Table 3.5). These classes were also found by W81 to be some of the most voluminous in their census (their classes 3 and 7 with $\theta = 0.6–0.8$°C, $S_P = 34.71–34.72$). The initial outflow of LCDW from the Southern Ocean to the South Australian, Tasman, and Southwest Pacific basins is of slightly cooler and fresher waters that cover a smaller, though still substantial, area of the bottom (e.g., classes 10 and 14, $28.18 \leq \gamma^n < 28.27$ kg m^{-3}, $\Theta = 0.4–0.6$°C, $S_A = 34.87–34.88$ g kg^{-1}, Table 3.5). This LCDW also overlies the AABW that fills the abyssal Crozet Basin so downstream it appears at the bottom in the Madagascar and northeastern Crozet basins once the AABW has been trapped farther south by topography.

There are some additional high-area classes found almost exclusively in the Indian basin that are slightly warmer and saltier than the Pacific-Indian shared classes of LCDW (e.g., classes 11–12 and 23, $\Theta = 0.8–1.1$°C, $S_A = 34.89–34.90$ g kg^{-1}, Table 3.5). These high-area classes are

slightly lighter than the γ^n = 28.18 kg m^{-3} upper boundary of our LCDW definition and represent IDW along the bottom in the Somali and Central Indian basins. As for the PDW within the high-area classes noted above, the IDW within these high-area classes flows across large distances within these basins with relatively slow modification by the overlying water masses. Since these waters are quite similar to the overlying IDW that occupies a substantial volume in the global ocean, it is not surprising that W81 found that the waters within these classes occupied some of their highest-volume classes (their classes 11, 14, and 17 with θ = 0.8–1.1°C, S_P = 34.72–34.73).

Since the main northward pathway into the abyssal South Atlantic (i.e., into the Argentine Basin) is filled by AABW, a substantial area of the seafloor in the South Atlantic, specifically in the Argentine Basin and Scotia Sea, is covered by Θ-S_A classes corresponding to the cooler and fresher WSDW/AABW (e.g., class 19, 28.27 $\leq \gamma^n <$ 28.36 kg m^{-3}, Θ = -0.2– -0.1°C, S_A = 34.84–34.85 g kg^{-1}, Table 3.5). More water within this Θ-S_A class is found throughout the entire Agulhas Basin and smaller portions of the region north of Conrad Rise (i.e., along the northern boundary of the Enderby Basin), the southwest corner of the Crozet Basin, and the northwest corner of the Australian-Antarctic basin. While there is still a cluster of high-area classes in the LCDW neutral density range in the South Atlantic (e.g., 28.18 $\leq \gamma^n <$ 28.27 kg m^{-3}, Θ = 0.6–0.8°C, S_A = 34.90–34.91 g kg^{-1}, Figure 3.7b), these waters are saltier than the high-area LCDW classes shared by the Pacific and Indian basin due to the stronger influence of NADW on the LCDW in the Atlantic sector of the Southern Ocean. This variety of LCDW is only found over large areas of the bottom in the Cape and Transkei basins. Moreover, it is found on a mixing line slightly offset from that of the AABW/NADW mixing that occurs along the bottom spreading pathways extending from the Argentine Basin to the North Atlantic.

Another cluster of high-area classes in the Atlantic lies near the NADW end of the mixing line between NADW and AABW (Figure 3.7b). These classes correspond to the Antarctic-influenced NADW (AI-NADW) described in Section 3.3.1. Downstream of the Argentine Basin the northward-flowing AABW is continuously being modified by the overlying NADW and the presence of shallow sills at many locations along the different flow paths forces the denser classes of the AABW to be trapped in the basins to the south. The combination of these processes leads to a lack of high-area classes between the WSDW/AABW of the Argentine Basin (e.g., class 19, $28.27 \leq \gamma^n < 28.36$ kg m^{-3}, Θ = -0.2– -0.1°C, S_A = 34.84–34.85 g kg^{-1}, Table 3.5) and the AI-NADW mixture found over the Hatteras and Sohm abyssal plains and in the Cape Verde, Sierra Leone, and Guinea basins (e.g., class 30, $\gamma^n < 28.18$ kg m^{-3}, Θ = 1.7–1.8°C, S_A = 35.04–35.05 g kg^{-1}, Table 3.5). W81 also noted a similar lack of high-volume classes in this region of temperature-salinity space suggesting that bottom mixing may be influential in setting interior water mass properties. The highest-area class within the cluster of AI-NADW high-area classes corresponds to the bottom waters of the Angola Basin and the basin just west of the Sierra Leone Rise (class 13, $\gamma^n < 28.18$ kg m^{-3}, Θ = 1.9–2.0°C, S_A = 35.05–35.06 g kg^{-1}, Table 3.5) and is the highest area Atlantic-only class found in our census. This class was found to have the highest volume of any Atlantic-only class in W81 too (their class 35 with θ = 1.9–2.0°C, S_P = 34.88–34.89).

Like the $AABW_{source}$ varieties, the "pure" NADW (defined above as having $[Si(OH)_4] \leq$ 20 µmol kg^{-1}) covers a much smaller area than its mixtures with AABW and is therefore not a prominent feature in our Θ-S_A distributions (Figures 3.7a and 3.7b). The areal coverage of the "pure" NADW is further reduced because the Irminger and Iceland basins, which contain a substantial amount of this water mass along the bottom, are not included in our Θ-S_A distributions

since these basins are shallower than 3500 meters. However, some of the DSOW-dominated NADW ($\Theta < 2°C$) within the Labrador Basin is visible as a cluster of low-area Θ-S_A classes (e.g., Θ = 1.2–1.4°C, S_A = 35.05–35.06 g kg^{-1}, Figures 3.7a and 3.7b). Some of the more ISOW-dominated NADW ($\Theta > 2°C$) that flows into the West European Basin is also visible as a cluster of low-area classes (e.g., Θ = 2.2–2.4°C, S_A = 35.13–35.15 g kg^{-1}, Figures 3.7a and 3.7b).

Examining the Southern Ocean region of Θ-S_A space for each of the three main basins (Atlantic, Indian, and Pacific; Figures 3.7b–3.7d) allows us to analyze where the bulk of the water in each basin falls on the mixing lines between the regional varieties of $AABW_{source}$ and LCDW. In the Atlantic, there are two clusters of high-area Θ-S_A classes within the Southern Ocean portion of Θ-S_A space (Figure 3.7b). The first cluster includes some classes corresponding to the WSBW found in the eastward-flowing branch of the Weddell Gyre (e.g., γ^n > 28.36 kg m^{-3}, Θ = -0.9– -0.7°C, S_A = 34.81–34.82 g kg^{-1}, Figure 3.7b). The second cluster contains classes corresponding to the WSDW found in the westward-flowing return limb of the gyre, in the Enderby Basin east of gyre boundary, and in the basin east of the South Sandwich Trench (e.g., classes 18 and 29, γ^n > 28.36 kg m^{-3}, Θ = -0.7– -0.5°C, S_A = 34.82–34.83 g kg^{-1}, Table 3.5). CDBW in the Enderby Basin is found within some of the same high-area Θ-S_A classes as the WSDW, thereby further contributing to the high areal coverage of these classes. The classes corresponding WSBW and WSDW are not present in the bottom waters of the North Atlantic or the Pacific basins (Table 3.5; Figure 3.7d).

In the Indian sector of the Southern Ocean, there are two clusters of high-area classes (Figure 3.7c). The first corresponds to newly formed ALBW ($\gamma^n \approx$ 28.36 kg m^{-3}) just downstream of its formation region (e.g., class 18, Θ = -0.7– -0.6°C, S_A = 34.82–34.83 g kg^{-1}, Table 3.5). As noted above, this class also corresponds to the WSDW and CDBW in the Enderby Basin (a basin

considered part of the Indian basin in both Table 3.5 and Figure 3.7c), which cover a much larger area than the ALBW in this Θ-S_A range. The other high-area classes in the Indian sector of the Southern Ocean correspond to both a WSDW/LCDW mixture along the eastern boundary of the Enderby Basin and to an ALBW/LCDW mixture that occupies most of the abyss in the Australian-Antarctic Basin (e.g., class 24, Θ = -0.5– -0.4°C, S_A = 34.83–34.84 g kg^{-1}, Table 3.5). Along the eastern boundary of the Enderby Basin, the waters within this Θ-S_A class have γ^n > 28.36 kg m^{-3} ($AABW_{source}$) while in the Australian-Antarctic Basin these waters are lighter with 28.27 ≤ γ^n < 28.36 kg m^{-3} (AABW). The waters within this Θ-S_A class cover a much larger portion of the Australian-Antarctic Basin than the "purer" (i.e., colder and fresher) ALBW classes noted above.

In the Pacific basin (Figure 3.7d), the single cluster of high-area classes (e.g., classes 26 and 28, 28.27 ≤ γ^n < 28.36 kg m^{-3}, Θ = -0.1–0.1°C, S_A = 34.87–34.88 g kg^{-1}, Table 3.5) within the Southern Ocean represents the mixture of "low-salinity" RSBW and LCDW found along the bottom in most of the Amundsen and Bellingshausen abyssal plains and in the westward return flow that extends along the continental slope as far west as 175°W. This mixture of "low-salinity" RSBW and LCDW is not found along the bottom in any other basin. However, a small amount of AABW in the same Θ-S_A range is found along the bottom in the Brazil Basin and along the spreading pathway from the Southern Ocean to the Natal Basin. The newly-formed "low-salinity" RSBW that flows from Iselin Bank and into the eastward limb of the Ross Gyre (e.g., 28.27 ≤ γ^n < 28.36 kg m^{-3}, Θ = -0.2– -0.1°C, S_A = 34.86–34.87 g kg^{-1}, Figure 3.7d) occupies a smaller bottom area than the "low-salinity" RSBW/LCDW mixture. The "high-salinity" RSBW (e.g., γ^n > 28.36 kg m^{-3}, Θ = -0.3– -0.2°C, S_A = 34.88–34.89 g kg^{-1}, Figure 3.7d) occupies an even smaller bottom area, most of which is shallower than 3500 meters and therefore not included in our census.

The Θ-S_A distributions within each of the three main basins (Figures 3.7b–3.7d) can be used to infer the relative mixing between various water masses along the seafloor. When two water masses meet along a given isopycnal the resulting mixed water mass is often denser than either of the original water masses due to cabbeling (Stommel, 1960; Witte, 1902). This causes the mixing lines between end-member water masses to generally be straight lines in Θ-S_A space instead of curves along isopycnals. Therefore, we can infer that any "kinks" in the observed mixing lines are due to the presence of another water mass.

Of the three main basins, the Indian Ocean has the simplest set of mixing lines. All of the bottom waters of the Indian Ocean lie on a single mixing line in Θ-S_A space that transitions neatly from the fresh, cool ALBW to the warm, salty, and heavily intermediate water-influenced classes of IDW, passing through a mode of LCDW classes along the way. There are relatively high area values among all of the classes present along this mixing line.

The Atlantic contains multiple high-area mixing lines, each with a different slope, including ones between WSBW and WSDW, between the heavier WSDW in the Southern Ocean and the lighter WSDW in the Argentine/Brazil basins, and between the different AI-NADW classes. As noted above, the part of the mixing line between the high-area classes of the lighter WSDW/AABW and the AI-NADW contains only fairly low-area classes. This minimum is due to the continuous and relatively rapid modification of the northward-flowing AABW downstream of the Argentine Basin by both the overlying NADW and a series of sills. The heavily NADW-influenced LCDW found along the bottom in the Cape and Transkei basins falls along a mixing line between LCDW and NADW that typically only contains waters above the bottom. The high-area classes noted above for these basins (Θ = 0.6–0.8°C, S_A = 34.90–34.91 g kg^{-1}, Figure 3.7b)

occupy the denser portion of this mixing line, which is the only portion in contact with a large seafloor area.

The Pacific has two sets of fairly high-area mixing lines. The first is between the "low-salinity" RSBW and the LCDW. The second is between the warmer/saltier classes of LCDW and the PDW. This mixing line extends further to lower-area classes that are warmer and fresher than the bulk of the along-bottom PDW and represent more heavily intermediate water-influenced classes of PDW. These are closer to the surface-derived water masses that lie at the true end of this mixing line. The bottom waters of the South China Sea contain some of these classes at the warm/fresh end of this mixing line (e.g., Θ = 2.0–2.3°C, S_A = 34.79–34.81 g kg^{-1}, Figure 3.7d) since they are sourced by lighter Pacific waters from ~2000 meters depth that flow across Luzon Strait (e.g., Qu et al., 2006). Directly above these waters in Θ-S_A space, there are a set of classes that correspond to the warmer bottom waters of the Banda and Celebes (formerly Sulawesi) seas (e.g., Θ = 2.5–4.2°C, S_A = 34.78–34.82 g kg^{-1}, Figure 3.7d). These classes are not connected to the other Pacific classes in our Θ-S_A diagram because they are filled by intermediate waters near the sill depths (~1350–1940 meters, Gordon et al., 2003), which are not present along the bottom in any other of the basins included in our census.

Overall, 10 of the 30 highest area classes are found exclusively in the Pacific Ocean north of 55°S (classes 1–3, 7–9, 16, 20, 22, 27, Table 3.5) while two more of these classes have at least 89% of their area in this region (classes 4, 15, Table 3.5). All twelve of these classes have γ^n < 28.18 kg m^{-3} and combined they cover ~38.4% of the seafloor in regions deeper than 3500 meters. The high areal coverage of these classes that correspond to PDW highlights that these waters undergo relatively slow modification over large regions of the seafloor in the Pacific. This is

consistent with the areal coverage of all Θ-S_A classes of PDW for locations deeper than 2000 meters (~37.4% of global area) as described in Section 3.3.1 and Table 3.4.

Likewise, the LCDW and IDW that occupy the abyssal Indian Ocean are modified relatively slowly by the overlying waters, especially within the individual sub-basins of this ocean basin. However, there are a number of ridges along the spreading pathways of LCDW along both the western and eastern edges of the Indian Ocean that induce slightly more abrupt transitions between the high-area LCDW/IDW classes of the different sub-basins than those observed between the various high-area LCDW/PDW classes in the Pacific.

The AABW that flows northward from the Southern Ocean into the Atlantic is continually modified by the overlying NADW and the effects of dense water-blocking sills such that it gains ~1.8°C in temperature and ~0.19 g kg^{-1} in salinity before a single Θ–S_A class spreads laterally over a large enough area to stand out in our bivariate area census.

In both the Weddell-Enderby and the Amundsen-Bellingshausen basins, the bulk of the seafloor area is covered by relatively homogenous water masses that are a mixture of their respective $AABW_{source}$ varieties (i.e., WSBW and RSBW) and the overlying water masses (i.e., WSDW and LCDW). These mixtures occupy the bottom waters in most of the central and eastern aspects of these basins as well as in the westward-flowing return branches of the Weddell and Ross gyres. The unmodified eastward-flowing WSBW and "low-salinity" RSBW occupy a much smaller portion of these basins by comparison. In the Australian-Antarctic basin, mixtures between ALBW and LCDW comprise substantially more of the bottom waters than the "pure" ALBW. This trend continues in the North Atlantic with a substantially larger area of the seafloor being covered by the AI-NADW classes than the "pure" NADW classes. This pattern is consistent with our area analysis in Section 3.3.1 for all of the bottom waters deeper than 2000 meters where we found that

AABW covers approximately 2.64 times the seafloor area of $AABW_{source}$ and that AI-NADW covers approximately 10.45 times the area of the "pure" NADW (Table 3.4).

3.3.6.2 O_2-S_A Relationships

While Θ-S_A diagrams are a classic way to examine water mass distributions, since dissolved oxygen is non-conservative in the ocean, O_2-S_A diagrams can highlight additional relationships among different water masses, such as how their mixing varies along different pathways within a given basin, and if local biogeochemical processes are affecting the bottom waters. As done above for Θ and S_A we combined the RFOM-mapped O_2 and S_A fields with the seafloor areas within each 0.5° latitude × 0.5° longitude box to create O_2-S_A diagrams where each 2 μmol kg^{-1} × 0.01 g kg^{-1} rectangle is shaded by the area of the seafloor deeper than 3500 meters touched by waters of that class in the global ocean and in the Atlantic, Indian, and Pacific oceans individually (Figures 3.8a–3.8d).

To summarize the geographic distributions of the highest area classes, we assess the regional breakdown for each of the 30 largest area classes using the same boundaries between the basins as in Table 3.5 (Table 3.6). These 30 highest area O_2-S_A classes cover ~ 36.6% of the total seafloor area deeper than 3500 meters, much less than the area covered by the 30 highest area Θ-S_A classes described above. To try and leverage the benefits of both Θ-S_A and O_2-S_A diagrams, we also incorporated Θ, S_A, and O_2 data into one view (Figures 3.9a–3.9d). Analyzing these two types of O_2-S_A diagrams in tandem allows for more detailed exploration of the degree of mixing between different bottom waters than possible in Θ-S_A space alone. While relatively straight mixing lines between different water masses do appear in O_2-S_A space despite oxygen being non-conservative, there are a number of instances where the oxygen concentrations change substantially with little coincident change in temperature and salinity, suggesting that these oxygen changes are not due

to mixing between water masses. Instead strong biological activity or long residence times with little mixing with overlying waters of different salinity may be implicated.

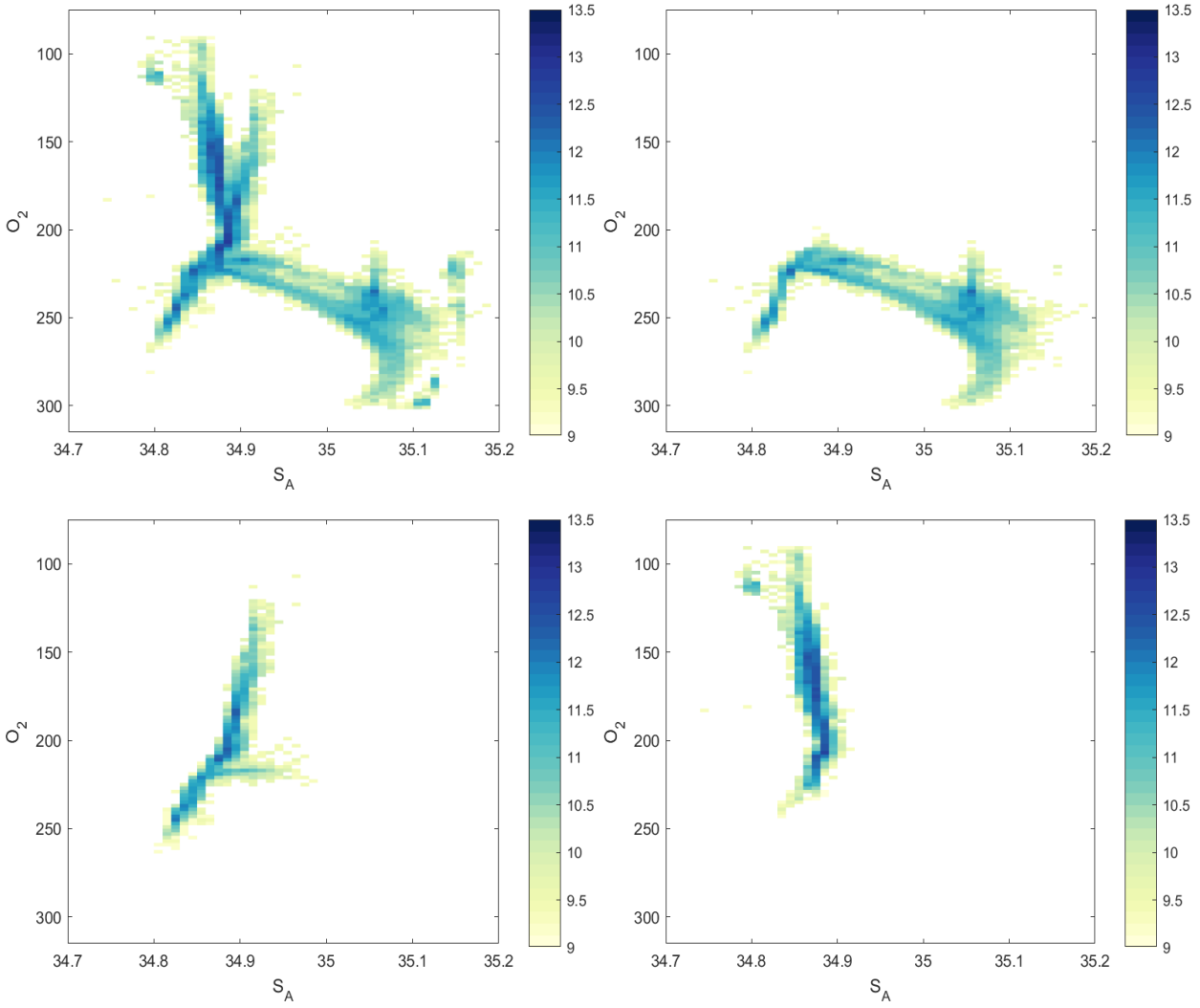

Figure 3.8. $\log_{10}$ of seafloor area within each 2 μmol kg^{-1} by 0.01 g kg^{-1} box in dissolved oxygen-absolute salinity space for the a) global ocean, b) Atlantic Ocean, c) Indian Ocean, and d) Pacific Ocean for locations with seafloor depths ≥ 3500 meters. Note that the following basins are off-scale here: the too salty Mediterranean Sea and the too fresh Sea of Japan.

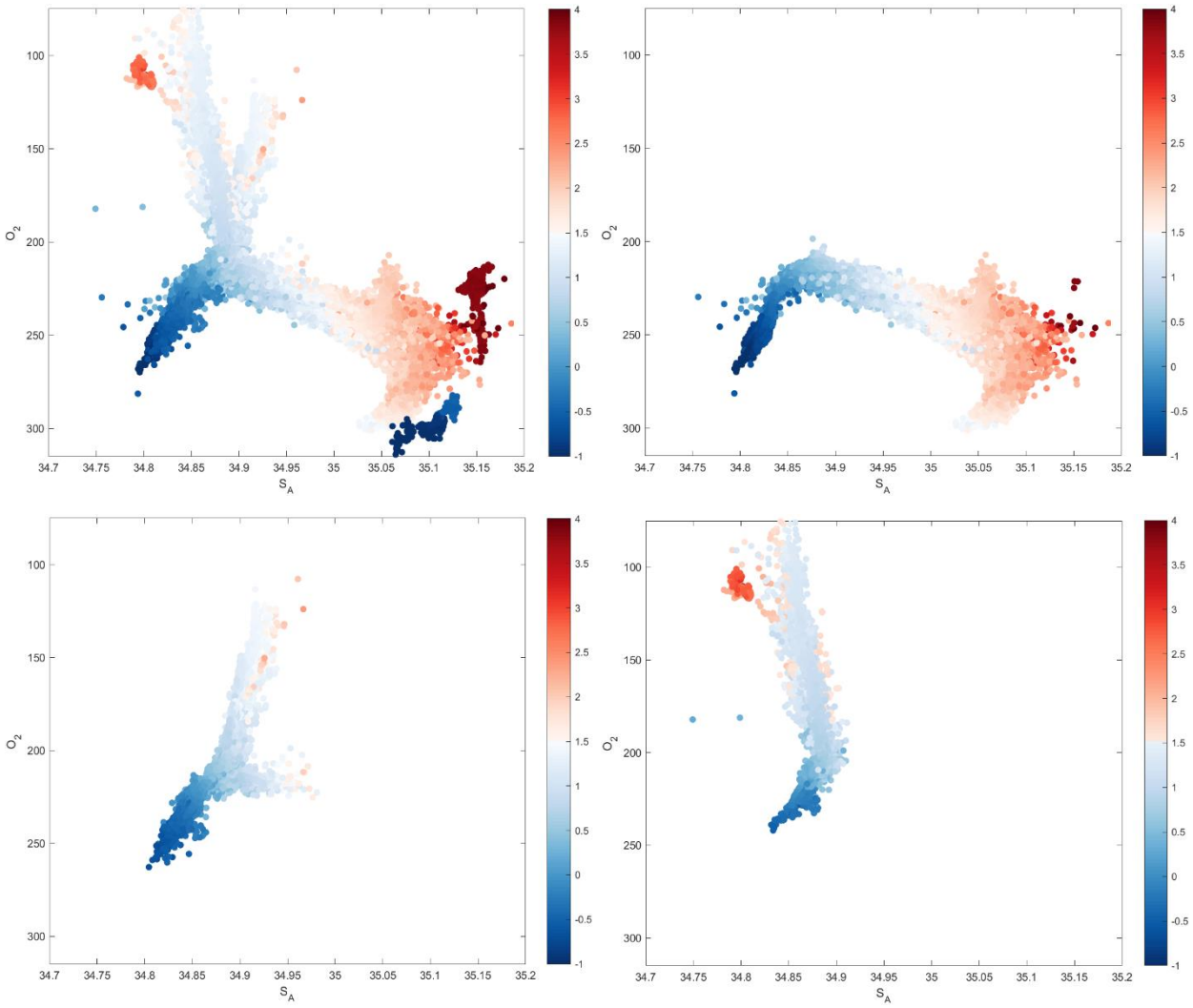

Figure 3.9. Distributions of RFOM-mapped bottom dissolved oxygen (μmol kg^{-1}) and absolute salinity (g kg^{-1}) values at locations with seafloor depths ≥ 3500 meters, colored by conservative temperature (°C) for the a) global ocean, b) Atlantic Ocean, c) Indian Ocean, and d) Pacific Ocean. Note that the following basins are off-scale here: the too salty Mediterranean Sea and the too fresh Sea of Japan.

Table 3.6. Geographical breakdown of the area within each of the 30 highest area O_2-S_A classes shown in Figure 3.8a. Some rows do not sum to 100% due to rounding. The equator serves as the boundary between the North and South Pacific as well as the North and South Atlantic oceans. The boundaries between the different sectors of the Southern Ocean are noted in the text. The total seafloor area for locations with seafloor depth ≥ 3500 meters is 2.39×10^{14} m^2.

Rank	O_2 (μmol kg^{-1})	S_A (g kg^{-3})	Mean γ^n (kg m^{-3})	% of Total Area ≥3500 meters	N. Pac. (%)	S. Pac. (%)	SO. Pac. (%)	Ind. (%)	S.O. Ind. (%)	N. Atl. (%)	S. Atl. (%)	SO. Atl. (%)
1	206–208	34.88–34.89	28.20	2.77	-	69	6	25	-	-	-	-
2	204–206	34.88–34.89	28.19	2.05	-	58	3	38	-	-	-	-
3	210–212	34.87–34.88	28.23	1.98	-	22	27	49	-	-	1	1
4	202–204	34.88–34.89	28.18	1.77	-	69	2	29	-	-	-	-
5	208–210	34.87–34.88	28.22	1.69	-	44	17	39	-	-	-	-
6	170–172	34.87–34.88	28.12	1.32	69	31	-	-	-	-	-	-
7	174–176	34.87–34.88	28.13	1.32	89	11	-	-	-	-	-	-
8	200–202	34.88–34.89	28.18	1.32	-	64	1	35	-	-	-	-
9	172–174	34.87–34.88	28.12	1.29	83	17	-	-	-	-	-	-
10	198–200	34.88–34.89	28.17	1.24	-	65	-	35	-	-	-	-
11	164–166	34.87–34.88	28.11	1.24	82	18	-	-	-	-	-	-
12	166–168	34.87–34.88	28.11	1.19	78	22	-	-	-	-	-	-
13	196–198	34.88–34.89	28.17	1.18	2	63	-	34	-	-	-	-
14	176–178	34.87–34.88	28.13	1.15	88	12	-	-	-	-	-	-
15	162–164	34.87–34.88	28.11	1.14	87	13	-	-	-	-	-	-
16	158–160	34.87–34.88	28.11	1.13	91	9	-	-	-	-	-	-
17	160–162	34.87–34.88	28.11	1.11	92	8	-	-	-	-	-	-
18	208–210	34.88–34.89	28.21	1.05	-	38	12	49	-	-	-	-
19	152–154	34.86–34.87	28.06	1.05	47	53	-	-	-	-	-	-
20	192–194	34.88–34.89	28.16	1.01	38	48	-	14	-	-	-	-
21	168–170	34.87–34.88	28.12	0.92	79	21	-	-	-	-	-	-
22	156–158	34.86–34.87	28.08	0.90	74	26	-	-	-	-	-	-
23	154–156	34.86–34.87	28.08	0.90	71	29	-	-	-	-	-	-
24	182–184	34.89–34.90	28.14	0.90	-	2	-	98	-	-	-	-
25	194–196	34.88–34.89	28.16	0.88	7	68	-	25	-	-	-	-
26	190–192	34.88–34.89	28.15	0.88	57	29	-	14	-	-	-	-
27	212–214	34.87–34.88	28.26	0.85	-	6	60	26	-	-	7	1
28	150–152	34.86–34.87	28.06	0.83	44	56	-	-	-	-	-	-
29	184–186	34.89–34.90	28.14	0.79	-	3	-	96	-	-	-	-
30	156–158	34.87–34.88	28.10	0.78	97	3	-	-	-	-	-	-

As in the Θ-S_A area plots, the Southern, Atlantic, Indian, and Pacific oceans have distinct high-area branches in the O_2-S_A domain (Figures 3.8a–3.8d). The most recently ventilated water masses of the Southern Ocean and North Atlantic/Arctic oceans occupy the lower left and lower right corners of the global O_2-S_A diagram, respectively. Those in the North Atlantic/Arctic oceans have much higher oxygen concentrations (~300 μmol kg^{-1}) than those of the Southern Ocean (~270 μmol kg^{-1}) because the many varieties of $AABW_{source}$ all entrain a substantial amount of oxygen-poor LCDW as they descend from their formation regions along the continental shelf to depths below 3500 meters (the cut-off for this analysis). A small portion of WSBW along the seafloor near the top of the continental slope (at depths between 2000 and 3500 meters) has oxygen concentrations of ~300 μmol kg^{-1} (Figure 3.8b). By the time these waters reach the base of the continental slope at ~3500 meters their oxygen concentration has decreased by ~30 μmol kg^{-1}, demonstrating how much the mixing with LCDW can attenuate the oxygen-rich signal of $AABW_{source}$.

The high-area classes within the oxygen-rich AABW/$AABW_{source}$ range of O_2-S_A space correspond to these regional varieties of AABW (i.e., $AABW_{source}$/LCDW mixtures). It is these slightly oxygen-poorer waters, not the highest-oxygen $AABW_{source}$ waters, that occupy the bulk of the abyssal Southern Ocean. The water overlying the NADW along the seafloor of the Irminger and Labrador basins is not as oxygen-poor as the LCDW overlying the $AABW_{source}$ so the NADW retains its especially high oxygen signature over a much larger area of seafloor below 3500 meters.

Of the 30 highest area classes in our O_2-S_A census (Table 3.6), 15 correspond exclusively to PDW found along the bottom in the Pacific (e.g., class 6, $\gamma^n < 28.18$ kg m^{-3}, $[O_2] = 170–172$ μmol kg^{-1}, $S_A = 34.87–34.88$ g kg^{-1}). However, unlike in Θ-S_A space where PDW dominated the highest area classes, here the five highest area classes are LCDW classes that are found in both the

Pacific and Indian basins (e.g., classes 1–2, $28.18 \leq \gamma^n < 28.27$ kg m^{-3}, [O_2] = 204–208 μmol kg^{-1}, S_A = 34.88–34.89 g kg^{-1}, Table 3.6). Another cluster of especially high-area classes corresponds to IDW found exclusively along the bottom in the Indian (e.g., classes 24 and 29, $\gamma^n < 28.18$ kg m^{-3}, [O_2] = 182–186 μmol kg^{-1}, S_A = 34.89–34.90 g kg^{-1}, Table 3.6) that is saltier and oxygen-poorer than the shared Pacific/Indian LCDW. Consistent with our other area analyses in Sections 3.3.1 and 3.3.6.1, homogenous O_2-S_A classes of LCDW, IDW, and PDW occupy large areas of the seafloor with relatively slow modification by overlying waters.

In the Pacific Ocean (Figures 3.8d and 3.9d), there are two key high-area mixing lines in O_2-S_A space (as in Θ-S_A space). The first line is between the lower area classes of the cooler, fresher, and more oxygen-rich "low-salinity" RSBW (e.g., [O_2] = 224–226 μmol kg^{-1}, S_A = 34.86–34.87 g kg^{-1}) and the higher area classes of the warmer, saltier, and less oxygen-rich LCDW (e.g., class 1, $28.18 \leq \gamma^n < 28.27$ kg m^{-3}, [O_2] = 206–208 μmol kg^{-1}, S_A = 34.88–34.89 g kg^{-1}, Table 3.6). The second line is between the LCDW and PDW (e.g., class 6, $\gamma^n < 28.18$ kg m^{-3}, [O_2] = 170–172 μmol kg^{-1}, S_A = 34.87–34.88 g kg^{-1}). As LCDW spreads northward it also becomes slightly warmer, fresher, and oxygen-poorer due to entrainment of overlying waters, eventually becoming dominantly characteristic of PDW.

Farther from the AABW sources, Pacific waters along the seafloor continue to become even warmer, fresher, and oxygen-poorer as they mix with the overlying water or are affected by other processes such as in-situ respiration and geothermal heating (Figures 3.8d and 3.9d). Throughout most of the Pacific these overlying waters are strongly influenced by North Pacific Intermediate Water or AAIW but near the eastern boundary current upwelling regimes additional, smaller volume intermediate water masses, such as California Intermediate Water, are present. Due to the variety in the properties of the overlying water masses that PDW may entrain as it flows

through the abyssal Pacific and the large number of potential pathways it can follow, PDW occupies a broad range of classes in O_2-S_A space.

Generally, the saltiest and most oxygenated classes of PDW are found in the central basins closer to the outflow from the Samoan Passage while the freshest and least oxygenated classes of PDW are located farther from the Samoan Passage, particularly near the continental slope in the northeastern and eastern equatorial Pacific and in the shallower sub-basins west of 160°E. However, similar ranges of O_2 and S_A values can be achieved through very different sets of water mass interactions in the distinct sub-basins of the Pacific. One nice example of this is class 19 (γ^n < 28.18 kg m^{-3}, [O_2] = 152–154 μmol kg^{-1}, S_A = 34.86–34.87 g kg^{-1}, Table 3.6), the waters of which are found in four main areas of the Pacific: the Peru Basin, the Philippine Sea, the shallow area north of the Hawaiian Islands, and along the 3500-meter isobath just south of the Clipperton Fracture Zone (~10°N, 117°W). The bottom waters in the Philippine Sea and the shallow region north of the Hawaiian Islands have similar temperature values and are approximately equidistant from the Samoan Passage along the bottom water flow paths so they likely are dominantly PDW of similar age. South of the Clipperton Fracture Zone, the bottom waters are a mix of the older, oxygen-poorer PDW flowing southward from the northeast Pacific and the younger, oxygen-richer LCDW flowing eastward from the Penrhyn Basin, resulting in oxygen concentrations between these two end-members equivalent to a younger apparent age of PDW than that of the PDW from the northeast Pacific. The Peru Basin is dominated by some of the lighter classes of LCDW from the Southeast Pacific Basin that have mixed somewhat with the overlying PDW, resulting in the warmest waters (~1.5°C) within this O_2-S_A class.

The bottom waters of several marginal seas stand out in the Pacific O_2-S_A diagrams (Figures 3.8d and 3.9d). The cluster of relatively high area classes at the oxygen-poorer end of the

LCDW-PDW mixing line corresponds to the extremely old bottom waters of the Bering Sea (e.g., $[O_2]$ = 94–104 μmol kg^{-1}, S_A = 34.85–34.86 g kg^{-1}). At slightly higher oxygen concentrations and slightly fresher salinities, there is a cluster of relatively high area classes corresponding to the warm bottom waters of the South China, Sulu, Celebes, and Banda seas (e.g., $[O_2]$ = 108–118 μmol kg^{-1}, S_A = 34.79–34.81 g kg^{-1}, Figures 3.8d and 3.9d). As in Θ-S_A space, the classes corresponding to these basins are somewhat separated in O_2-S_A space from the bottom waters from the other Pacific basins since the abyss of these basins is filled by Pacific intermediate waters at the shallower (< 2000 meters) sill depths. These intermediate waters dominate the along-bottom waters in some of the shallower regions of the western tropical Pacific and these locations correspond to the warm, low-area classes (e.g., $[O_2]$ = 112–122 μmol kg^{-1}, S_A = 34.81–34.84 g kg^{-1}, Figures 3.8d and 3.9d) connecting the high-area LCDW/PDW structure to the moderately high area classes of the South China, Sulu, Celebes, and Banda seas. This relationship is easier to discern here than in the Θ-S_A diagram (Figure 3.7d).

The bottom waters of the Indian Ocean generally become warmer, saltier, and oxygen-poorer as they spread northward from the Southern Ocean (Figures 3.8c and 3.9c). In the Southern Ocean portion of the Indian O_2-S_A diagrams, there is a relatively high-area mixing line between low-area classes of the cold, fresh, and oxygen-rich ALBW/CDBW/WSDW (e.g., $[O_2]$ = 254–264 μmol kg^{-1}, S_A = 34.8–34.83 g kg^{-1}) and the high-area classes of the warm, salty, and less oxygen-rich LCDW (e.g., class 3, 28.18 < γ^n < 28.27 kg m^{-3}, $[O_2]$ = 210–212 μmol kg^{-1}, S_A = 34.87–34.88 g kg^{-1}), similar to the one described in the Θ-S_A census above. Another high-area mixing line exists between this LCDW and the even warmer, saltier, and oxygen-poorer IDW (e.g., class 24, γ^n < 28.18 kg m^{-3}, $[O_2]$ = 182–184 μmol kg^{-1}, S_A = 34.89–24.90 g kg^{-1}). This mixing line corresponds to the northward bottom water flow along both the Crozet-Madagascar-Mascarene basin and the

South Australian-Perth-West Australian basin pathways. As the IDW continues to fill the rest of the abyssal Indian Ocean, its oxygen concentration decreases and its salinity increases further as it entrains more of the older and saltier overlying waters.

Within the "dead-end" deep Arabian Basin, additional moderate-area mixing lines exist that correspond to mixing between the "younger" IDW that enters this basin at the Owen Fracture Zone and the "older" IDW on the western and northern edges of the basin that has been strongly influenced by both the saltier, overlying intermediate waters (i.e., RSW and PGW) and by the consumption of oxygen during especially high amounts of organic matter remineralization along the seafloor (Section 3.3.3.2). The warmest ($\Theta > 2.0°C$), saltiest ($S_A > 34.94$ g kg^{-1}), and oxygen-poorest ([O_2] < 100 μmol kg^{-1}) classes of this "older" IDW along the bottom are found at shallower depths (2000–3500 meters) in the Gulf of Aden and along the northern boundary of the Arabian Basin (Figures 3.3c–3.3e). However, even over just the part of the Arabian Basin deeper than 3500 meters, the impact of the "older" IDW on the oxygen concentrations of the "younger" IDW is substantial, causing the oxygen concentrations of these waters to decrease by ~42 μmol kg^{-1} (from [O_2] = 162–164 μmol kg^{-1} to 120–122 μmol kg^{-1}) with minimal changes to salinity (S_A = 34.90–34.91 g kg^{-1} to 34.91–34.92 g kg^{-1}) (Figure 3.8c). For reference, an equivalent decrease in oxygen within the bottom waters (from 206–208 μmol kg^{-1} to 162–164 μmol kg^{-1}) due to more typical amounts of in-situ respiration and mixing with the overlying oxygen-poorer waters occurs over the full flow path of the LCDW/IDW from the Mascarene Basin to the Arabian Basin (via the Somali Basin) (Figure 3.3e). These waters simultaneously experience a much larger change in salinity class over this distance (from 34.88–34.89 g kg^{-1} to 34.91–34.92 g kg^{-1}, Figure 3.3d) than the bottom waters of the Arabian Basin that undergo an equivalent change in oxygen concentration. This further supports the previous evidence (e.g., Edmond et al., 1979) that a local biogeochemical

process must be contributing to the large change in the oxygen concentrations within the bottom waters of Arabian Basin (assuming no large differences in bottom speeds between these basins).

Similarly, within the "dead-end" Bay of Bengal, there is another moderate-area mixing line between the "younger" IDW entering from the Central Indian Basin and the somewhat "older" IDW found northeast of Sri Lanka. This "older" IDW is relatively oxygen-poor due to the regeneration of organic matter that is exported to the seafloor from the overlying region of high seasonal productivity (Section 3.3.3.2). The "older" IDW ($[O_2]$ = 148–150 μmol kg^{-1}, S_A = 34.90–34.91 g kg^{-1}) is only slightly saltier but ~24 μmol kg^{-1} oxygen-poorer than the "younger" IDW ($[O_2]$ = 172–174 μmol kg^{-1}, S_A = 34.89–34.90 g kg^{-1}). The warmest ($\Theta > 2°C$), saltiest (S_A > 34.94 g kg^{-1}), and oxygen-poorest ($[O_2] < 120$ μmol kg^{-1}) bottom waters in the Bay of Bengal are found along the seafloor at shallower depths (< 3500 meters) near the northern boundary of the basin (Section 3.3.3.2; Figures 3.3c–3.3e). An additional moderate-area mixing line exists between these waters and the IDW within the central Bay of Bengal but it is found at bottom depths too shallow to be included on our O_2-S_A diagrams.

The uniqueness of the heavily NADW-influenced variety of LCDW found along the bottom of the Transkei and Cape basins (e.g., $[O_2]$ = 216–218 μmol kg^{-1}, S_A = 34.90–34.91 g kg^{-1}) relative to that of the LCDW that feeds the rest of the Indian sub-basins is much clearer in O_2-S_A space than it is in Θ-S_A space (Section 3.3.6.1). In the Indian O_2-S_A diagrams (Figures 3.8c and 3.9c), there is a distinct mixing line extending laterally from the main AABW/LCDW/IDW structure to the relatively high area classes corresponding to this heavily NADW-influenced variety of LCDW. The saltiest and lowest area end-members of this mixing line are the even more heavily NADW-influenced (i.e., saltier and oxygen-richer) LCDW classes found along the shallower edges of these basins.

The Atlantic O_2-S_A distributions looks much different than those of the Pacific and Indian basins due to the presence of the oxygen-rich NADW end member outside of the Southern Ocean (Figures 3.8b and 3.9b). The oxygen-rich end member within the Southern Ocean is the cold and fresh WSBW. These waters mix with the warmer, saltier, and oxygen-poorer LCDW in a relatively tight range of O_2-S_A space, leading to the formation of a number of high-area classes of WSDW (e.g., [O_2] = 244–246 μmol kg^{-1}, S_A = 34.82–34.83 g kg^{-1}). A cluster of especially high area classes closer to the LCDW end of this mixing line (e.g., [O_2] = 222–224 μmol kg^{-1}, S_A = 34.84–34.85 g kg^{-1}) corresponds to the WSDW/AABW found along the bottom in the Argentine, Agulhas, northern Enderby, and southern Crozet basins. This water is the Southern Ocean end member of the main (i.e., higher area) AABW-NADW mixing line in O_2-S_A space.

In Θ-S_A space (Figure 3.7b), identifying the different end members of NADW is difficult since they lie along the cooler, low area fringes of the AABW-NADW mixing line. However, in O_2-S_A space (Figures 3.8b and 3.9b) it is easier to identify both the cooler, fresher, and oxygen-richer low area classes of DSOW (e.g., [O_2] = 294–302 μmol kg^{-1}, S_A = 35.02–35.04 g kg^{-1}) and the warmer, saltier, and oxygen-poorer low area classes of ISOW (e.g., [O_2] = 268–274 μmol kg^{-1}, S_A = 35.11–35.14 g kg^{-1}). There is a cluster of high-area classes along the mixing line between these two end members, generally closer to the DSOW end member. These relatively high area classes represent along-bottom classes of NADW (e.g., [O_2] = 286–288 μmol kg^{-1}, S_A = 35.07–35.08 g kg^{-1}), which contain more of the fresher DSOW due to its higher density.

Over the southern Labrador Basin east of the Flemish Cap and the Newfoundland Basin, the oxygen concentration of the NADW along the bottom decreases by ~20 μmol kg^{-1} while undergoing minimal changes in Θ and S_A to transform into the salty end member of the main NADW-AABW mixing line (e.g., [O_2] = 266–268 μmol kg^{-1}, S_A = 35.07–35.08 g kg^{-1}). This

relatively rapid change in oxygen is likely due a combination of topographic blocking of the heaviest, oxygen-richest classes of NADW to the north as the flow turns southwestward into the Newfoundland Basin and stronger mixing with the overlying, oxygen-poorer recirculated NADW. The former process likely controls the rapid change in O_2 between the southern Labrador Basin and the Newfoundland Basin while the latter process controls the somewhat more gradual O_2 change within the bottom waters of the southeastern Labrador Basin as the bathymetry shoals toward the western flank of the Mid-Atlantic Ridge. In both instances, the oxygen concentration ultimately decreases by ~20 μmol kg^{-1}. This pattern demonstrates that the end-members of the main mixing line between the recently ventilated Southern Ocean and North Atlantic waters are not truly the $AABW_{source}$ and initial DSOW/ISOW mixtures but instead modified versions of these water masses that have both lost a significant amount of oxygen before they begin to mix with one another.

Two distinct high-area mixing lines between the $AABW_{source}$/AABW/LCDW structure and different vintages of NADW are visible in the Atlantic O_2-S_A distributions (Figures 3.8b and 3.9b). The high-area mixing line at higher oxygen concentrations represents mixing in the basins west of the Mid-Atlantic Ridge between the WSDW/AABW flowing northward from the Argentine Basin (e.g., $[O_2]$ = 222–224 μmol kg^{-1}, S_A = 34.84–34.85 g kg^{-1}) and the warmer, saltier, and more recently ventilated NADW flowing southward. The moderate area of the classes along this mixing line is because this AABW is continuously being modified as it flows northward by NADW and a series of sills. The second, oxygen-poorer mixing line represents mixing between a LCDW end-member and an older (and thereby oxygen-poorer) vintage of NADW, most of which occurs above the bottom. The high-area classes near the fresh end of this mixing line correspond to the heavily NADW-influenced LCDW within the bottom waters of the Transkei and Cape basins (e.g., $[O_2]$ =

216–218 μmol kg^{-1}, S_A = 34.90–34.91 g kg^{-1}) that is present on the Indian Ocean O_2-S_A diagrams as well (Figures 3.8c and 3.9c). As noted in our earlier discussions of these waters, it appears that it is only in these basins that a substantial portion of these LCDW-NADW mixtures come in contact with the bottom.

The high-area class near the saltier apparent end of this mixing line ([O_2] = 234–236 μmol kg^{-1}, S_A = 35.05–35.06 g kg^{-1}) corresponds to a mode of AI-NADW found along the bottom in a large portion of the Angola Basin. The NADW overlying these waters has similar oxygen and salinity values to the above-bottom NADW that mixes with the LCDW to form the heavily NADW-influenced LCDW of the Cape and Transkei basins, hence the apparent position of the fairly similar underlying AI-NADW as the end-member of this mixing line. The low area classes over most of the saltier portion of the LCDW/"older" NADW mixing line correspond to waters found over various shallower regions in the South Atlantic such as the continental slope and the Mid-Atlantic Ridge. The presence of these lighter classes over shallower topography further supports the idea that most of the mixing between LCDW and the "older" NADW occurs in lighter density classes that are only found along the bottom in regions where the denser AABW or AI-NADW are not present either because the region is too shallow or, as is the case for the Cape and Transkei basins, because the sills surrounding the basin block the inflow of these denser waters.

There are several high-area classes of AI-NADW (S_A > 35.04 g kg^{-1} and [O_2] < 252 μmol kg^{-1}) that appear to be offset from the AABW-NADW mixing line of the western basins in O_2-S_A space. These classes correspond to the relatively oxygen-poorer varieties of AI-NADW found throughout the basins east of Mid-Atlantic Ridge that contain higher proportions of ISOW than DSOW. Within this O_2-S_A range, the AI-NADW generally loses oxygen while undergoing little change in temperature and salinity as it flows southward in the basins north of the ~20°N. This

loss of oxygen is mainly due to normal amounts of in-situ respiration though mixing with the oxygen-poorer bottom waters near the African continental rise from 5°N to 33°N (Section 3.3.4) likely contributes as well. The lighter classes of AABW that flow through the Mid-Atlantic Ridge via the fracture zones at 11°N and the equator freshen and cool the bulk of the southward-flowing AI-NADW ($[O_2] \approx 244–246$ μmol kg^{-1}) to form a new variety of AI-NADW that is found throughout the Guinea and Angola basins. The lighter classes of AABW that make it into these eastern basins are warmer, saltier, and oxygen-poorer than the AABW that mixes with the NADW in the western basins, hence the position of the newly formed AI-NADW classes offset from that mixing line. This slightly cooler and fresher AI-NADW flows southward into the Angola Basin where it spreads over a large portion of this basin with relatively little modification by overlying waters, resulting in the especially high area class within this basin noted above ($[O_2] = 234–236$ μmol kg^{-1}, $S_A = 35.05–35.06$ g kg^{-1}).

A string of increasingly lower area classes within the same salinity range ($S_A = 35.05–35.06$ g kg^{-1}) extends from this high-area class to an extremely low area class ($[O_2] = 206–208$ μmol kg^{-1}) and are all found within this basin. This reflects the presence of another set of O_2-S_A end-members in the Angola Basin – the relatively oxygen-poor ($[O_2] < 218$ μmol kg^{-1}) near-bottom plumes over the continental rise from ~2°S to ~21°S discussed above (Section 3.3.4; Figure 3.3e). These plumes result from the large amount of oxygen consumption along the seafloor in these regions during the remineralization of organic matter deposited beneath nearby river outflows and highly productive coastal upwelling zones. The oxygen concentrations within these plumes are as much as 28 μmol kg^{-1} lower than in the waters offshore. The classes between $[O_2] = 206–208$ μmol kg^{-1} and $[O_2] = 234–236$ μmol kg^{-1} with $S_A = 35.05–35.06$ g kg^{-1} represent the diffusion of the anomalously oxygen-poor signal from these plumes offshore into waters with similar salinities in

the interior of the Angola Basin. Another mixing line with classes of moderate area is present at salinities of S_A = 35.02–35.03 g kg^{-1} and similarly reflects the lateral mixing that occurs with little change in salinity between the relatively oxygen-rich AI-NADW flowing into the Guinea Basin (O_2 = 244–246 μmol kg^{-1}) and the ~14 μmol kg^{-1} oxygen-poorer end-member (O_2 = 230–232 μmol kg^{-1}) farther east in the Guinea Basin that originates from remineralization of organic matter at the seafloor from the Ivory Coast/Ghana coastal upwelling region (Section 3.3.4).

The influence of another end member in the eastern Atlantic is evident by the presence of some especially salty AI-NADW classes within the S_A > 35.04 g kg^{-1} and [O_2] < 252 μmol kg^{-1} range. These low area, warm, and salty classes (e.g., Θ > 2°C, [O_2] = 238–252 μmol kg^{-1}, S_A = 35.12–35.19 g kg^{-1}) correspond to a unique subtype of AI-NADW that is strongly influenced by the overlying highly saline Mediterranean Sea Overflow Water and to a lesser degree by the saltier NADW end member (ISOW). The bottom waters of the Caribbean Sea and Gulf of Mexico (e.g., [O_2] = 216–224 μmol kg^{-1}, S_A = 35.14–35.16 g kg^{-1}) are saltier, substantially warmer (Θ > 3.6°C), and somewhat oxygen-poorer than the majority of the AI-NADW classes. This is not surprising since they are sourced by less recently ventilated deep and intermediate waters from the western Atlantic. Compared to the DSOW, the bottom waters of the Arctic Ocean (e.g., [O_2] = 296–300 μmol kg^{-1}, S_A = 35.1–35.12 g kg^{-1}) are slightly saltier, much colder (Θ < 0°C), and similarly oxygen-rich since they are also sourced from relatively recently ventilated waters from the Nordic Seas.

3.4 Discussion

In this work, we have introduced a new “stacked” random forest and objective mapping approach for mapping sparse oceanographic variables. By using this approach on all of the publicly-available high-quality, full-depth profiles we could access, we were able to create updated global

maps of Θ, S_A, O_2, NO_3^-, PO_4^{3-}, and $Si(OH)_4$ distributions just above the ocean floor for all basins deeper than 2000 meters. The combination of a larger dataset, our machine learning-based interpolation method, and the use of higher-resolution bathymetry in the mapping procedure led to improvements over previous maps (e.g., Mantyla & Reid, 1983). Specifically, our maps better illustrate the considerable role of small-scale topography, such as fracture zones, sills, and submarine canyons, in steering bottom water spreading pathways globally and show the impact of biogeochemical processes (typically related to rivers, upwelling zones, or the composition of the underlying sediments) on regional property distributions. Several important narrow jets along topographic boundaries such as the Antarctic Slope Current, the Alaskan Stream, the unnamed eastward flow over the Aleutian Rise, and many others were well-resolved in our maps and the importance of the thse flows in driving the abyssal circulation was made clear by their ability to transport water masses between basins with little modification in their characteristics. Due to the increase in nutrient data collected over the past few decades, we were able to generate detailed global maps of phosphate and nitrate in the bottom waters for the first time as well. The improved quality of our silica map allowed us to use this nutrient to trace the weaker abyssal cyclonic circulations in a number of basins with heavily opaline sediments (e.g., the Bellingshausen Abyssal Plain). Additionally, our mapping and analyses included the Arctic Ocean and many marginal seas that were excluded from previous global bottom water analyses (e.g., Mantyla & Reid, 1983; Worthington, 1981).

Among our more detailed findings is a small region of especially high silica input in the southeast corner of the Enderby Basin (58°S–64°S, 62.5°E–74°E) that is bounded by the Elan Bank to the north and the Antarctic continental slope to the south. While previous work has discussed the elevated silica concentrations in the along-bottom WSDW in the eastern Enderby

Basin due to enhanced silica flux from opaline sediments (Edmond et al., 1979; Mantyla & Reid, 1983), to the best of our knowledge our maps are the first to show an additional, more localized high silica input region (with a higher silica-to-nitrate ratio) for the WSDW that is likely related to enhanced deposition of diatomaceous organic matter from the highly productive surface waters near Prydz Bay (Figures 3.5e and 3.5f). The oxygen and silica observations that we used to map this high silica input region were measured after 1983, which would explain why the discussion of this feature was missing from the earlier detailed studies. Jacobs & Georgi (1977) first observed relatively high concentrations of silica in the northward bottom flow of WSDW across a zonal section between the Crozet and Kerguelen islands and were able to trace this silica-rich bottom water back to a "source" at 63°S, 60°E along a meridional section but here we show that the source of these waters is slightly farther east (our so-called high silica input region). Their northwesterly/southeasterly section over the channel between the Agulhas and Mozambique basins depicts similarly silica-rich water flowing northward along the bottom though they did not mention this feature nor its link to their "source" for the silica-rich signal at 63°S, 60°E. On our silica map (Figure 3.5f) we can trace the influence of our newly-described high silica input region as far west as 44°W in the Weddell Gyre and as far north as 33°S along the northward spreading pathways in the Natal and Crozet basins. However, the fingerprint of this high silica input region is not present in the WSDW that enters the South Atlantic since those waters are dominated by "newer" WSDW and WSBW that are much silica-poorer.

Recent observing campaigns undertaken since previous efforts to map the global abyss have greatly advanced our understanding of the formation of CDBW (Ohshima et al., 2013). However, the influence of the recently ventilated CDBW on the oxygen, silica, and CFC concentrations of WSDW above the seafloor was observed as far west as ~20°W in hydrographic

and tracer section data long before the formation region for CDBW was directly observed by Ohshima et al. (2013) (e.g., Hoppema et al., 2001; Meijers et al., 2010; Meredith et al., 2000). Yet, to the best of our knowledge, our silica map is the first to clearly illustrate the complete pathway along the bottom from 61°E to 44°W of the CDBW influence on the silica-rich WSDW that originates from our newly-described high silica input region. Our maps suggest that the main export pathway for CDBW off of the continental shelf is via as-yet unsampled gravity currents in the Mawson Canyon (~60.5°E), slightly farther west than the Wild and Daly canyon outflows, which appear to be more minor in comparison despite the focus on them in CDBW studies to date (e.g., Ohshima et al., 2013). It is also possible that the outflows from these other canyons are simply getting overwhelmed along the bottom by the stronger signal of the high silica input region farther offshore. Our work also seems to be the first to note the overlap between previous observations of strong northwestward and westward velocities in the bottom water at the northern apex of the Gunneras Ridge (from Aoki et al., 2020) with property maps (mainly those of oxygen and silica; Figures 3.5e and 3.5f) that suggest CDBW leaves the continental slope at this location to join the silica-rich WSDW in the southwestward return branch of the Weddell Gyre. Recent work observed a freshening trend in the CDBW exported from its formation region to 60°E so understanding the full export pathway of this water mass may be important when investigating basin-wide changes in bottom water properties (Aoki et al., 2020).

We examined in detail the numerous coastal sources of oxygen-poor, and sometimes nutrient-rich, waters along the eastern boundary of the Atlantic Ocean that can influence the southward-flowing AI-NADW farther offshore. Based on our property maps and the local bathymetry, we suggest that the oxygen-poor bottom waters in the Gulf of Guinea do not originate from the advection of oxygen-poor waters from the outflow of the Congo Canyon but instead from

the regeneration of organic matter exported directly from the Ivory Coast/Ghana upwelling regime and adjacent rivers. This export off the shelf to depths deeper than 2000 meters could occur via downslope flow in canyons that bisect the continental slope, in a similar fashion to the export of particulate matter from the Congo Canyon. We further suggest that the spread of the oxygen-poor Congo Canyon signal to the south might be more limited than previously described and identify the Angola Dome, the Cuanza River, the Benguela Current upwelling system as potentially important contributors to the oxyen-poor signal in the bottom waters along the continental slope of the Angola Basin south of ~11°S.

Our analysis of the areal coverage of the different water masses showed that South Ocean-origin waters (AABW, $AABW_{source}$, and LCDW) cover ~1.87 times the seafloor as the NADW-dominated waters ("pure" NADW and AI-NADW), highlighting the relative importance of the Southern Ocean deep and bottom waters in the ventilating the gloal abyss, consistent with previous work (e.g., Johnson, 2008; Mantyla & Reid, 1983). However, this analysis also revealed that PDW, IDW, and LCDW overlie a majority (61.8%) of the seafloor deeper than 2000 meters. These "deep" water masses are able to flow over large portions of the seafloor with little modification by mixing with overlying waters or topographic blocking. The "other bottom waters", generally mixtures of these named deep water masses, make up another 9.5% of the the global, along-bottom waters. Accordingly, in any future work exploring variability in the bottom water properties in the basins where the abyss is dominated by these "deep" waters (Figure 3.4) it may be worthwhile to investigate not only any changes affecting the $AABW_{source}$ waters that are the southern source of the LCDW/PDW/IDW but also any affecting the overlying intermediate waters that contribute to the properties of these deep water masses. The remaining 28.7% of the seafloor is mainly covered by AI-NADW (13.7% of global total), which is dominantly characteristic of NADW though with

a clear influence of Antarctic waters in the nutrient fields and AABW (8.2%), the set of mixtures between $AABW_{source}$ and LCDW. The newly formed bottom waters ($AABW_{source}$ and "pure" NADW) cover a very small percentage of the global seafloor in comparison (3.1% and 1.3%, respectively). Our O_2-S_A analysis showed that both of these source water masses are substantially modified before they begin to mix along the main mixing line in the western Atlantic basins. Along this bulk of this mixing line, there are few high-area Θ-S_A or O_2-S_A classes because the northward-flowing AABW is nearly continuously modified by the overlying NADW and the effects of sills between deep basins. Exploring the mapped fields in O_2-S_A space also highlighted the uniqueness of the bottom waters of the Cape and Traskei basins. These waters contain the densest mixtures along the generally above-bottom mixing line between the LCDW (not the AABW found along the seafloor in the western Atlantic basins) and an older vintage of NADW that is similar to the one found at middepths over the Angola Basin. These mixtures correspond to a variety of LCDW that is substantially different from the LCDW found along the seafloor in other Indian and Pacific basins in our maps.

There have been many previous efforts to create full-depth climatologies of various ocean properties (e.g., the World Ocean Atlas; Boyer et al., 2018). Unfortunately, given the relative paucity of measurements in the deep ocean (de Lavergne, Madec, Capet, et al., 2016) it is difficult to accurately map abyssal properties, especially oxygen, which is more sparsely sampled than temperature and salinity, and nutrients, which are even more sparsely sampled than oxygen. The fields we map further along in our "stacking" of the random forests (i.e., oxygen and nutrients) should show the largest improvements in accuracy compared to existing climatologies. This is because the random forests used to map these fields contain highly complex, internal representations of the regional relationships between the previously mapped variables (first

temperature and then salinity) that correspond to different water masses and their mixtures. The improved accuracy of the maps for the variables further in the "stack" is suggested by the smaller mapping errors (relative to the GO-SHIP measurement accuracies) for the salinity, oxygen, and nutrient fields compared to those of the temperature field (Table 3.3).

However, the mapping of the fields earlier in the "stack", such as temperature and possibly salinity, likely do not represent a great improvement over mapping done with conventional oceanographic methods (e.g., those employed in generating the World Ocean Atlas 2019). For example, to predict the bottom temperature distribution the only inputs to the random forest are the bathymetric data (latitude, longitude, and depth) from ETOPO-60. This temperature prediction is then corrected toward the temperature measurements using objective mapping as described above. This mapping procedure should not yield substantially different results from conventional mapping approaches, but does sometimes result in rectilinear mapping artifacts in areas with a lower data density. One example of such an artifact is in the interior of the West Australian Basin at 16°S where the 0.7°C contour extends perfectly zonally from 93°E to 107°E despite the topography of the basin suggesting it should extend farther north at some of the longitudes in this range. However, strictly meridional or zonal isolines in the property maps are not always the result of such artifacts and may be appropriate based on the orientation of the underlying topography that can steer the bottom flow. The reader is encouraged to consult the bathymetric maps provided when in doubt about a set of isolines. For example, in all of the property maps there are seemingly suspicious zonal isolines at 40°N extending from ~145°W to 126°W but consulting the bathymetric map shows that they are reasonable features due to the presence of the underlying, nearly perfectly zonal Mendocino Fracture Zone. We plan to explicitly compare our bottom water climatology to the bottommost levels of previous full-depth climatologies in future work.

There has recently been a renewed interest in the deep ocean with the launch of the Deep Argo program (Roemmich, Alford, et al., 2019), recent observations of interannual variability in bottom water properties (e.g., Desbruyères et al., 2016; Johnson et al., 2014; Kouketsu et al., 2011; Menezes et al., 2017; Purkey et al., 2019; Purkey & Johnson, 2010, 2013), and recent work pointing to the bottom boundary layer as a potentially significant site of AABW transformation (e.g., Ferrari et al., 2016). Here we provide a timely and thorough overview of the mean state of the abyss, together with an improved bottom water climatology, to support these avenues of future research.

3.5 Acknowledgements

We thank all those who participated in the collection, calibration, processing, and archiving of the CTD and nutrient data used here across a number of different programs over the past few decades. Data used in this study can be downloaded from the URLs given in the text. Sarah Battle is thanked for preparing the bottom flow schematic. We also thank Susan Hautala for valuable discussions that improved the manuscript. P.D.L. and G.C.J. are supported by the Global Ocean Monitoring and Observing (GOMO) Program of the National Oceanic and Atmospheric Administration (NOAA), U.S. Department of Commerce, and NOAA Research. P.D.L. was also supported under the NASA Earth and Space Science Fellowship Program – Grant NNX16AO60H.

Chapter 4. BOTTOM MIXED LAYERS IN THE NORTH ATLANTIC OCEAN

4.1 INTRODUCTION

The generally northward flows of Antarctic Bottom Water (AABW) and southward flows of North Atlantic Deep Water (NADW) from their formation regions are the drivers of the climatically-important bottom and deep limbs of the meridional overturning circulation (Lumpkin & Speer, 2007). The ocean is a large sink for excess heat energy and anthropogenic carbon within the climate system, taking up ~90% of this extra energy added from 2010–2018 (von Schuckmann et al., 2020) and ~27% of the extra anthropogenic carbon added from 1994–2010 (Talley et al., 2016). The deep ocean (> 2000 meters depth) specifically has absorbed ~8% of the excess heat within the climate system (von Schuckmann et al., 2020). While we have a fairly complete picture of the lateral bottom water spreading pathways from the main sites of bottom water formation in the North Atlantic and Southern oceans (e.g., Chapter 3), there is still substantial work to be done in understanding and observing how these waters return to the surface. Recent work has illuminated some pathways for deep water upwelling in the Southern Ocean (e.g., Marshall & Speer, 2012; Tamsitt et al., 2017) but here we will focus on characterizing the density structure near the bottom of the ocean, which may be important for another, recently-highlighted mechanism for substantial upwelling of abyssal waters – diapycnal transport via bottom mixed layers along basin boundaries.

Recent theoretical and modeling work has suggested that there is substantial vertical transport of abyssal water masses within the bottom boundary layer over regions of sloping topography (Ferrari et al., 2016; de Lavergne, Madec, Le Sommer, et al., 2016; McDougall et al., 2017). The foundation of these recent discussions is a revised perspective of how diapycnal mixing varies near the seafloor (Ferrari et al., 2016). Observations have shown that diapycnal mixing due

to breaking internal waves is enhanced closer to the seafloor, especially over rough topography and abrupt, isolated ridges such as the Hawaiian Ridge (e.g., St. Laurent et al., 2012; Polzin, 1997; Waterhouse et al., 2014). This mixing profile acts to increase the density of abyssal waters due to relatively enhanced entrainment of the denser, underlying waters thereby leading to net downwelling in the abyss.

To reconcile this abyssal downwelling with the need for bottom waters to be raised to depths of at least 2000 meters for the global meridional overturning circulation to close (e.g., Marshall & Speer, 2012), Ferrari et al. (2016) proposed that within the weakly stratified, turbulent bottom boundary layer below this interior mixing regime the small-scale mixing decays toward the bottom in order to satisfy the bottom boundary condition of zero density flux at the seafloor. This leads to lightening of the bottom waters within the bottom boundary layer and diapycnal upwelling in these layers along the sloped oceanic boundaries such as the continental margins and ridges. They refer to the region of strong mixing and diapycnal downwelling that is near the seafloor but above the bottom boundary layer as the stratified mixing layer (SML) and we will follow this convention here. They further note that in their theoretical framework these SMLs are typically hundreds of meters thick while the bottom boundary layers over sloping topography are generally on the order of tens of meters thick, consistent with previous observations of both of these layers (e.g., St. Laurent et al., 2012; Polzin, 1997; Weatherly & Martin, 1978). Additionally, in regions with substantial input from geothermal heat flux to the bottom waters (i.e., where the buoyancy flux at the base of the bottom boundary layer is instead non-zero), the diapycnal upwelling within bottom boundary layer over sloped topography is moderately enhanced since this heat flux acts to further lighten these waters within this along-bottom layer (Ferrari et al., 2016; de Lavergne, Madec, Le Sommer, et al., 2016; McDougall et al., 2017).

Analysis of a global buoyancy and volume budget for the bottom boundary layer and SML found that the upwelling volume flux in the bottom boundary layer is up to five times that of the net dianeutral upwelling of bottom waters in the abyss (for waters with neutral density of 27.95–28.2 kg m^{-3}) while the downward diapycnal volume flux in the SML is only up to four times the net dianeutral upwelling of bottom waters in the abyss (McDougall et al., 2017). This results in a net upwelling of abyssal waters within the turbulent bottom boundary layer. McDougall et al. (2017) further suggested that little significant diapycnal transport of either sign occurs in the interior and that instead these strong upward (in the bottom boundary layer) and downward (in the SML) diapycnal transports are limited to regions within a few hundred kilometers laterally of the continental boundaries.

We will use the term "bottom mixed layer" (BML) to denote the weakly stratified bottom boundary layer described in the theoretical and modeling works cited above and in previous observational studies discussed below. Specifically, we define the BML as a well-mixed region near the bottom with nearly uniform density and nutrient concentrations over its depth range, consistent with previous observational studies (Armi & Millard, 1976; Lentz & Trowbridge, 1991; Stahr & Sanford, 1999). In many locations, especially where the BML thickness is relatively small, this layer is the same as the region of elevated turbulence near the seafloor (e.g., Lentz & Trowbridge, 1991). However, in flat, smooth areas of the seafloor this well-mixed region can be much larger (e.g. > 1000 meters thick in the interior of the North Pacific and Angola basins; Banyte et al., 2018) and relatively quiescent.

There have been a number of detailed regional, observational studies exploring the variation in the bottom mixed layer over the abyssal plain compared to over the continental slope. Observations in the North Atlantic showed that the thickest, least stratified BMLs are found over

the smooth, flat topography in the interior of the basin while thinner, more stratified BMLs are located on the sloped and/or rough topography on the edges of the basin (Armi & Millard, 1976). A study in the northern California coastal upwelling region observed BMLs with typical thicknesses of 5–15 meters (though sometimes exceeding 50 meters) whose thicknesses are related to the stratification of the layer directly above, i.e. the SML (Lentz & Trowbridge, 1991). They also showed that the BML can be weakly stratified, though still clearly more well-mixed than the overlying SML, such that Richardson number may exceed 0.25. Lastly, they found a stronger relationship between the thickness of the BML and both the current speed and direction than with the interior stratification, with a clear relationship of poleward flows (downwelling) leading to thicker BMLs and equatorward flows (upwelling) leading to thinner BMLs over sloped topography. This tendency is due to the associated buoyancy fluxes with each of these types of flows. Equatorward flows have an upslope bottom Ekman flux that enhances the local stratification and thereby limits BML thickness, while poleward flows have a downslope bottom Ekman flux that reduces the local stratification and thereby encourages the growth of a thicker BML. This relationship was proposed by Weatherly & Niiler (1974), with supporting numerical and laboratory analyses later performed by Weatherly & Niiler (1978) and MacCready & Rhines (1991), and may have important implications for when BMLs along sloped boundaries are the site of upwelling within the bottom limb of the meridional overturning circulation. Geothermal heating can also affect the stratification and thickness of the BML (e.g., Thompson & Johnson, 1996).

Recent work (Banyte et al., 2018), produced maps of BML thickness for the Atlantic, Indian, and Pacific oceans north of 40°S using conductivity-temperature-depth (CTD) profiles from the World Ocean Database 2013. However, their use of a density gradient threshold ($\Delta\sigma = 1 \times 10^{-5}$ kg^{-4}) calculated over 100-meter intervals limited their approach to only detecting bottom

mixed layers thicker than 50 meters in the CTD profile data (which they interpolated to make their regional maps). The main conclusions that they were able to draw from their BML thickness distribution were, 1) that thin (< 100 meters thick) BMLs are generally found along the side walls of the basins – i.e., continental margins and ridges and 2) that sub-basins toward the end of the along-bottom flow paths of AABW/LCDW, such as the Angola, Philippine, and North Pacific basins, tend to contain especially large BMLs (> 1000 meters thick) with especially weak stratification. However, it appears that the BMLs within the "dead-end" basins of the Indian Ocean, such as the Arabian Basin, are not as thick though they do not discuss why this may be. This could occur because of strong abyssal advective features in these basins (e.g., the boundary current in the Arabian Basin noted by Johnson et al. (1991)) or because of downward diffusion of salt from overlying salty water masses, such as the Red Sea Water or Persian Gulf Water, enhancing the abyssal stratification (e.g., You, 2002) and thereby limiting the BML thickness.

In this work we introduce a new method, modified from the surface mixed layer literature, for identifying the BML and SML in CTD profiles. One advantage of this method compared to that of Banyte et al. (2018) is that it can identify BMLs thinner than 100 meters, which are prevalent in the ocean, as shown below. Additionally, our approach allows for identification of the SML. Understanding the structure (i.e., thickness and stratification) of the SML could be helpful in understanding the processes controlling the BML thickness and stratification in different regions. We expect BML structure to be strongly influenced by many factors including, but certainly not limited to, the overlying velocity structure (i.e. swift deep boundary current vs. quiescent interior), the slope and roughness of the underlying topography, topographically controlled overflows over sills, as well as boundary forcings such as geothermal heating and potential even internal processes such as salt fingering. Therefore, we combine the identified

bottom mixed layer thicknesses with information about the underlying seafloor (slope, roughness) to help characterize different BML dynamical regimes. Here we only use CTD data from the North Atlantic but we plan to later extend this analysis globally.

4.2 Data and Methods

Previous work examining bottom mixed layers (BMLs) in observational data (e.g., Banyte et al., 2018; Lentz & Trowbridge, 1991; Stahr & Sanford, 1999) uses either a specific density difference or a density gradient to delineate the BML from the overlying waters. In this work, we adapt a method from the surface mixed layer literature known as the split-and-merge method (Thomson & Fine, 2003) to identify the BML and the overlying stratified mixing layer (SML) simultaneously. Once these layers have been identified, we input information about these layers (thickness, N^2) and relevant information about the underlying bathymetry (slope, roughness) into two unsupervised clustering algorithms to try to identify dynamical regimes of these BML, which are likely associated with varying amounts and directions of diapycnal transport.

4.2.1 *Density Profiles and Quality Control*

High-quality, full-depth conductivity-temperature-depth (CTD) profiles from 10 cruises (Table 4.1) in the North Atlantic were downloaded from the Climate Variability and Predictability (CLIVAR) and Carbon Hydrographic Data Office (CCHDO) on 05 March 2018 (https://cchdo.ucsd.edu/). We primarily used the World Ocean Circulation Experiment (WOCE)-era occupations of the North Atlantic hydrographic sections though one occupation we used (A16N; 2003) is from the CLIVAR-CO_2 program occupation shortly after the end of the WOCE program. We limited the data used to locations with bottom depths deeper than 2000 meters since we are interested in BMLs that could be relevant for the diapycnal upwelling of AABW and lower

NADW, which are generally found below this depth. The CTD casts from these cruises aim to reach to within 10 meters of the seafloor and the median distance to bottom in the dataset used here is approximately 20 meters. Therefore, we expect that these profiles sample at least the upper portion of the BML in most regions.

Table 4.1. List of WOCE and CLIVAR-CO_2 cruises downloaded from the CCHDO website (https://cchdo.ucsd/edu/) and used in the CTD dataset.

WOCE Identifiers and Cruise Start Date	EXPCODE
A01/A01E (1991)	06MT18_1
A01W/AR05/AR13 (1995)	18HU95011_1
A02 (1997)	06MT039_3
A05/AR01 (1998)	31RBOACES24N_2
A06 (1993)	35A3CITHER1_2
A16N (2003)	33RO200306_01
A20 (1997)	316N151_3
A22 (1997)	316N151_4
A24 (1997)	316N151_2
A25 (1997)	74DI230_1

To ensure that these CTD measurements sampled the BML and to make the dataset less noisy so that the BML would easier to detect automatically, we performed a number of quality control (QC) steps on these CTD data. We only kept profiles and levels where pressure, temperature, and salinity had good WOCE QC flags (specifically, values of 2, 6, or 7), resulting in the inclusion of 793 profiles. To reduce the spikiness of the profiles to make BML detection easier, we smoothed the initial profiles of in-situ temperature and practical salinity using a 20-decibar Hanning filter before converting these variables to the Thermodynamic Equation of Seawater - 2010 (TEOS-10, http://www.teos-10.org/) variables of absolute salinity and conservative temperature. We then calculate $\sigma_{deepest}$ from these fields, which is the potential density of the water referenced to the pressure of the deepest measurement of the profile. Using these

$\sigma_{deepest}$ profiles will allow us to use a single method across all of the profiles (which are taken over a range of bottom depths) and aid in our visualization of these data.

Almost a third of these profiles (240/793 = 30.3%) did not have a recorded bottom depth, which is problematic for determining if they reached close enough to the seafloor to adequately sample the BML as needed for this analysis. We used the same procedure for filling in these missing depth data as described above (Section 3.2.1) using bottom depths from ETOPO-2 (Smith & Sandwell, 1997) as needed. Ultimately, 21/240 (8.8%) profiles were assigned the interpolated ETOPO-2 bottom depth and the remaining profiles were assigned the depth of the deepest measurement plus 10 meters as the bottom depth. By examining the difference between the deepest measurement depth and recorded bottom depth for each profile, in addition to the profiles themselves, we determined that if the deepest measurement was within 50 meters of the seafloor then we should include it in this analysis. This limit was chosen in order to balance keeping as many profiles as possible with ensuring that they sampled the BML. If the bottom depth for the profile was supplied from the ETOPO-2 data as descripted above, then the deepest measurement was required to be within 320 (i.e., 50 + 270) meters of the bottom depth. This cut-off value retained 88.5% (702/793 profiles) though 63.6% of the profiles are actually within 20 meters of the seafloor (504/793 profiles).

4.2.2 *Split-and-Merge Algorithm*

To automatically identify the BML and SML in the $\sigma_{deepest}$ profiles, we adapted the split-and-merge method – an approach that has been used successfully to identify ocean surface mixed layers (Thomson & Fine, 2003). This algorithm acts to approximate a given curve with a set of simplified line segments that capture significant changes in slope or any step-like offsets (Figure 4.1). When applied to our $\sigma_{deepest}$ profiles, the bottommost of the resulting line segment corresponds to the

BML while the next deepest line segment corresponds to the SML. We used the somewhat more computationally-efficient Douglas-Peucker algorithm (Douglas & Peucker, 1973) to do this analysis which is effectively identical to the split-and-merge method described by Thomson & Fine (2003) except that instead of randomly setting the initial break point, it draws a line between the end points of the initial profile and then sets the initial break point at the point in the profile that is farthest from this line. This approach for identifying the BML and SML is extremely flexible and is able to automatically identify these layers throughout the global ocean where the thicknesses and stratification can vary substantially (see below). This method is advantageous compared to previous approaches for identifying the BML that used a threshold value of density or temperature (e.g., $\Delta T = 0.02°C$; Lentz & Trowbridge, 1991) or a set density gradient ($\frac{\Delta \sigma}{\Delta z} = 1 \times 10^{-5}$ kg m^{-4}; Banyte et al., 2018), which may not be applicable throughout the global ocean and do not allow for simultaneous identification of the overlying SML. Once we have identified the BML and SML in each profile using our implementation of the split-and-merge algorithm, we calculate the thickness of each layer and the buoyancy frequency (N^2) between the top and bottom points of each layer.

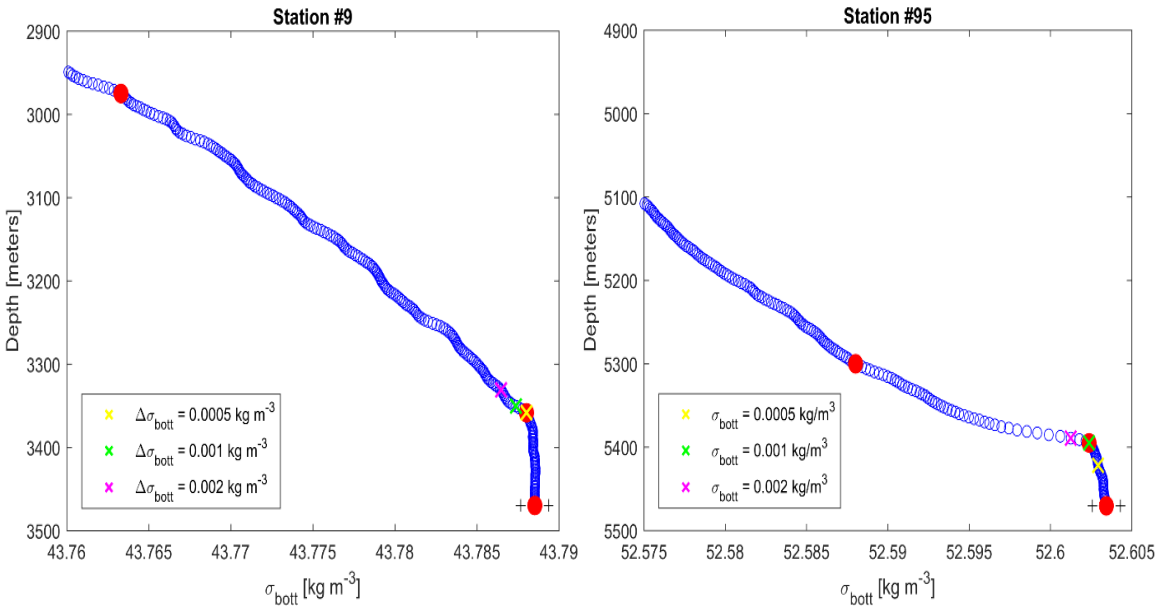

Figure 4.1. Profiles of $\sigma_{deepest}$ at stations 9 (a) and 95 (b) of the 1998 occupation of the A05/AR01 trans-Atlantic line at 24.5°N showing the top of the BML identified using different density differences from the deepest measurement (x's, legend) and end points of the BML and SML identified by the split-and-merge algorithm (red circles) with an upper bound on the precision of the bottom $\sigma_{deepest}$ value for reference (black pluses), calculated assuming a precision of 0.001 g kg^{-1} in absolute salinity and 0.0005°C in conservative temperature.

4.2.3 *Seafloor Slope and Roughness*

As discussed above, the slope and roughness of the seafloor should have a strong influence of the size and stratification of the BML and SML. In order to investigate these relationships, we calculate these quantities at the location of each of our profiles from a high-resolution bathymetric product (ETOPO-1; Smith & Sandwell, 1997). We followed the approach of Gille et al. (2000) for calculating the roughness, first high-pass filtering (λ > 160 km) the bathymetry (effectively as a band pass filter since the altimeter measurements of gravity underlying this field do not resolve features with wavelengths (λ) less than ~20 km). Next, we square the filtered bathymetry, apply a low-pass filter (λ < 160 km), and take the square root in order to compute the roughness. In order

to calculate the slope of the bathymetry, we take a similar approach. We first low-pass filter ($\lambda <$ 160 km) the bathymetry and then compute the 2-D derivative to obtain the slope.

4.2.4 *k-means Clustering*

By combining information from the density profiles (e.g., the thickness and N^2 of the BML and SML) with information about the underlying bathymetry, we use the k-means clustering algorithm to identify clusters of similar values of these properties that could correspond to different BML dynamical regimes. The k-means algorithm requires setting the number of desired clusters a priori. Our process for determining this number is discussed below. We perform two sets of clustering runs: one with the profile-based parameters only (i.e., BML thickness, SML thickness, BML N^2, and SML N^2) and the other with both the profile-based parameters and the bathymetric variables (slope and roughness). In the k-means algorithm, an iterative approach assigns each profile to one of the clusters and then adjust these assignments based on the Euclidean distance from each profile to the multi-dimensional "center of mass" of each cluster. This process is repeated until the cluster assignments cease to change significantly. We used the MATLAB function *kmeans* which uses the k-means++ implementation of this algorithm (Arthur & Vassilvitskii, 2007).

To determine how many clusters were appropriate for our dataset we used the silhouette score, which compares how similar the profiles in an individual cluster are to one another and how dissimilar each of those profiles are from the next nearest cluster (see Rousseeuw, 1987 for more details). If the silhouette score is equal to 1 then the profile is close to the others within its assigned cluster and far from those in the next nearest cluster. If it is equal to –1 then it is closer to another cluster than its assigned cluster (representing a failure of the clustering algorithm). A silhouette score of 0 indicates that the profile lies on the border between two clusters and could reasonable be assigned to either one. We assess the average silhouette score across all of the profiles in our

dataset using the clusters generated from the k-means algorithm (attempted for 2–16 clusters) to determine the appropriate number of clusters based on the profile-based parameter set (Figure 4.2a). We did this analysis for the combined profile-based and bathymetric parameter set as well (Figure 4.2b).We find that the maximum of the silhouette score occurs for 4 clusters when using the profile-based parameter set and for 3 clusters when using the combined profile-based and bathymetric parameter set. In order to make it easier to compare between the clustering results from the two parameter sets we use 4 clusters for both. We also found that the addition of a fourth cluster for both parameter sets did resolve an additional dynamic regime compared to those found using only 3 clusters (a consideration not necessarily well-quantified by the silhouette score), further justifying this choice of cluster number.

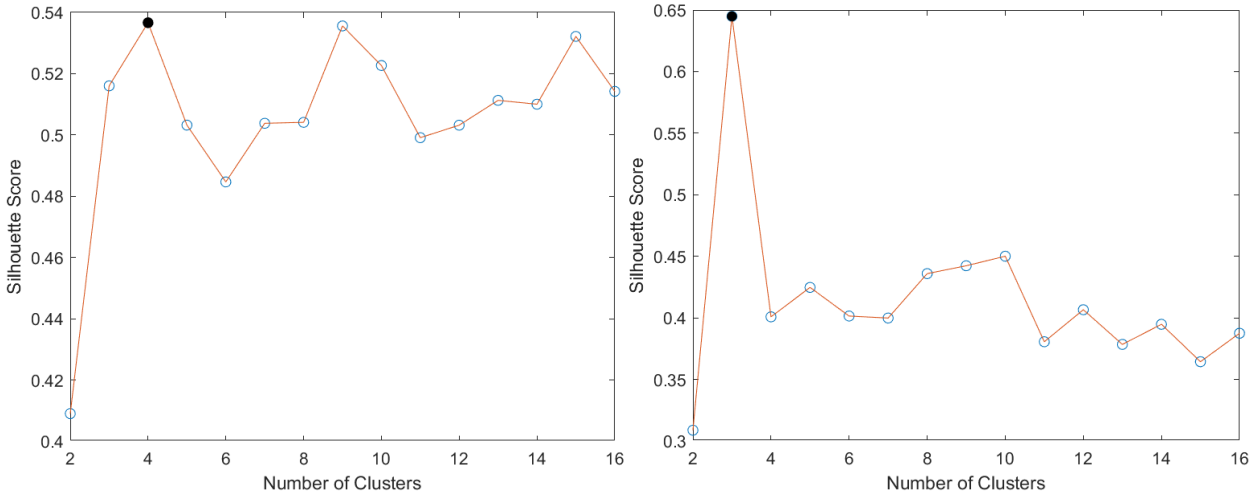

Figure 4.2. Mean silhouette score across all profiles for different numbers of clusters when using the k-means algorithm on our a) profile-based parameter set (BML thickness, SML thickness, BML N^2, and SML N^2 values) and b) our combined profile-based and bathymetric parameter set (BML thickness, SML thickness, BML N^2, and SML N^2 values, slope, and roughness). Maximum values of the silhouette score are indicated by the filled black dots.

4.3 RESULTS

Along the ten cruise tracks, there is substantial variability in the thicknesses of both the BML and the SML identified by the split-and-merge method (Figure 4.3). We find that the Caribbean Sea contains especially thick (> 1000 m) and unstratified BMLs and SMLs because the density profiles in this basin are nearly exponential in shape. This density structure occurs because the abyss of this basin is entirely filled by episodic overflows over Jungfern-Grappler Sill complex, which has a maximum depth of 1815 meters (MacCready et al., 1999). Banyte et al. (2018) (hereafter B18) found thinner (≤ 600 meters) BMLs in this basin, suggesting that the value for the density gradient threshold they selected for identifying the BML might not work well in every basin. Other regions with especially thick BMLs identified by our method include the interiors of the Canary and Iberian basins, while profiles along the boundaries of these basins have much thinner BMLs, consistent with the dichotomy presented in the literature (e.g., B18). However, in some deep basins, such as the Guiana and Newfoundland basins, the BMLs appear to remain relatively thin even in the interior in both our results and those of B18. This could be due high local rates of abyssal water mass transformation (as proposed for the Guiana Basin by B18) or by the strong influence of the deep western boundary current in these basins.

In the western subtropical North Atlantic and in the shallower subpolar basins, we find some substantial differences between the BML thicknesses we identified and those found by B18. For example, from ~27°N–33°N along the ~52.3°W section within the North American Basin, we found a clear region of thicker BMLs (~600 meters) in our dataset while B18's map of BML thicknesses was quite noisy in this region without a discernable trend. Farther west over the Hatteras Abyssal Plain from 20°N–30°N, our method identifies much thinner BMLs than those found by B18, which ranged from 800–1000 meters in thickness over a large portion of this region.

Apart from the interior of the West European Basin, we find that in the relatively shallower (< 4000 m depth) basins north of ~45°N, such as the Labrador, Irminger, Iceland basins and the Rockall Trough (hereafter the "northern North Atlantic basins"), the BMLs and SMLs are generally much thinner than in the basins farther south. This trend of thinner BMLs in these basins was not well-captured by the method of B18, especially in the Irminger and Labrador basins.

We also find that for both the SML and BML there is a strong inverse relationship between the observed thicknesses and N^2 values for each of these layers throughout the North Atlantic (Figures 4.4a and 4.4b). However, the relationships between the thicknesses and N^2 values of the two different layers are more complicated (Figures 4.4c and 4.4d). Unsupervised clustering methods can help us to identify patterns in the multi-dimensional data that may be difficult to identify by eye.

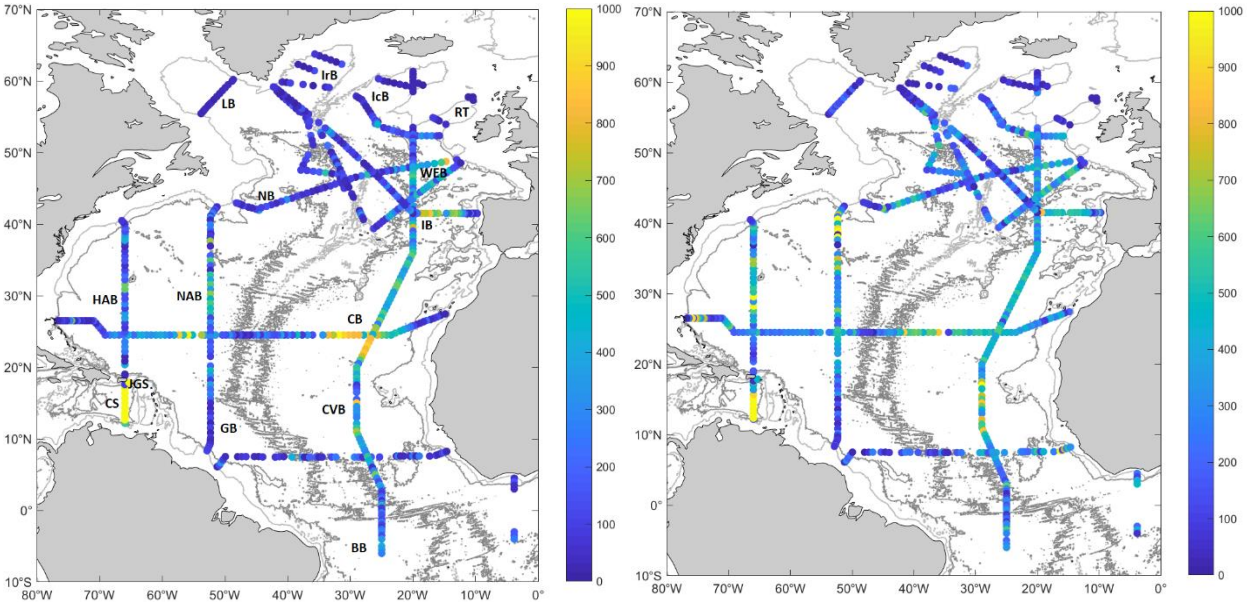

Figure 4.3. Thickness of the a) bottom mixed layer (BML) and b) stratified mixing layer (SML) at each profile location. BB: Brazil Basin; CB: Canary Basin; CVB: Cape Verde Basin; CS: Caribbean Sea; GB: Guiana Basin; HAB: Hatteras Abyssal Plain; IB: Iberian Basin; IcB: Iceland Basin; IrB: Irminger Basin; JGS: Jungfern-Grappler Sill; LB: Labrador Basin; NAB: North American; NB: Newfoundland Basin; RT: Rockall Trough; WEB: West European Basin.

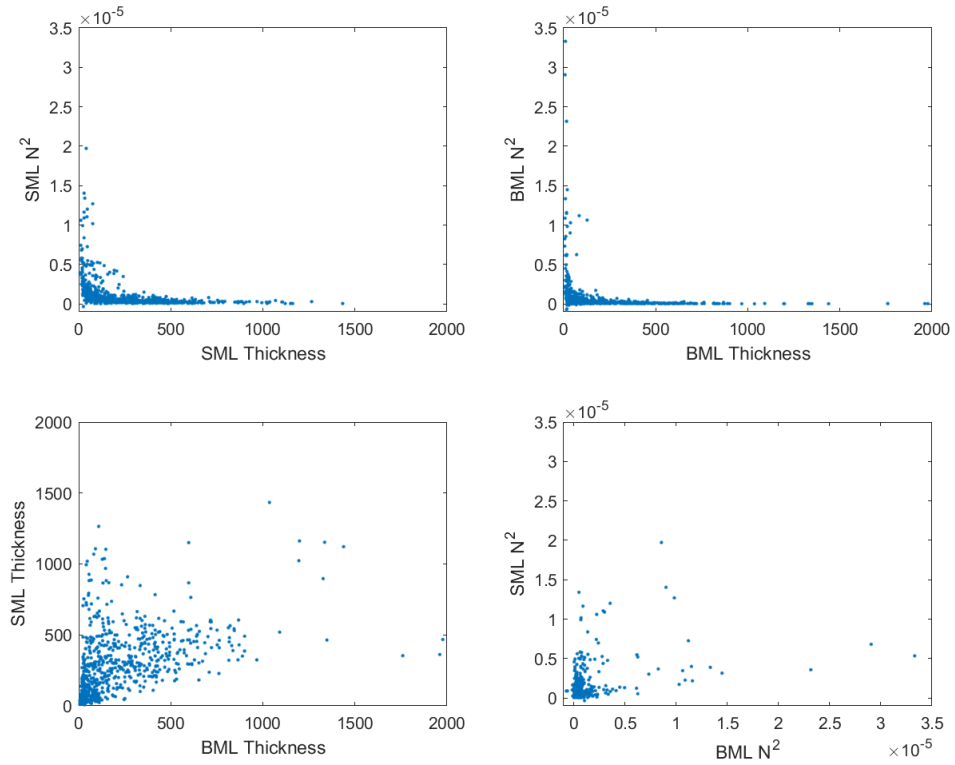

Figure 4.4. For the 702 profiles in our dataset, the distributions of a) SML thickness and SML N^2, b) BML thickness and BML N^2, c) BML thickness and SML thickness, and BML N^2 and SML N^2.

We performed k-means clustering on the BML thickness, SML thickness, BML N^2, and SML N^2 values for all 702 profiles in our dataset using 4 clusters (Figures 4.5a, 4.6a, 4.6c, and 4.6e). This analysis resulted in three clusters (clusters 2, 3, and 4) with at least one clear property extrema (e.g., the especially stratified SMLs in cluster 2) and one "catch-all" cluster containing profiles with properties in between these more distinct clusters (cluster 1). Cluster 3 generally contains profiles that are exponential-like (such as those in the Caribbean Sea) with thick BMLs and/or thick SMLs that are relatively unstratified. Clusters 2 and 4 both contain profiles with BMLs and SMLs thinner than ~100 meters though in the cluster 2 profiles the SML was more stratified than the BML while in the cluster 4 profiles the BML was more stratified than the SML. Both of these clusters were found nearly exclusively in the northern North Atlantic basins and are therefore likely related to the Denmark Strait Overflow Water and Iceland Scotland Overflow Water plumes

that flow along (or near) the bottom of these basins (e.g., Dickson & Brown, 1994; Eldevik et al., 2009). Two profiles within cluster 2 are found in the Guiana Basin and likely correspond to locations within the along-bottom northward flow of AABW in this basin (Chapter 3). Cluster 1 contains BMLs and SMLs covering a wide range of thickness- and N^2-space, generally between the more extreme values of clusters 2, 3, and 4. Outside of the northern North Atlantic basins, the profiles are typically assigned to either cluster 3 (unstratified BMLs and SMLs, thicker SMLs) or cluster 1 (more stratified BMLs and/or SMLs, thinner SMLs). The profiles in cluster 3 are mainly found over the flat, abyssal plains (e.g., the interior of the Canary and Cape Verde basins) but some other flat-bottomed basins (e.g., interior of the Guiana Basin, portions of the Hatteras Abyssal Plain) instead contain profiles with more stratified BMLs and SMLs that correspond to cluster 1. None of these 4 clusters have a clear slope or roughness dependence (Figure 4.6e).

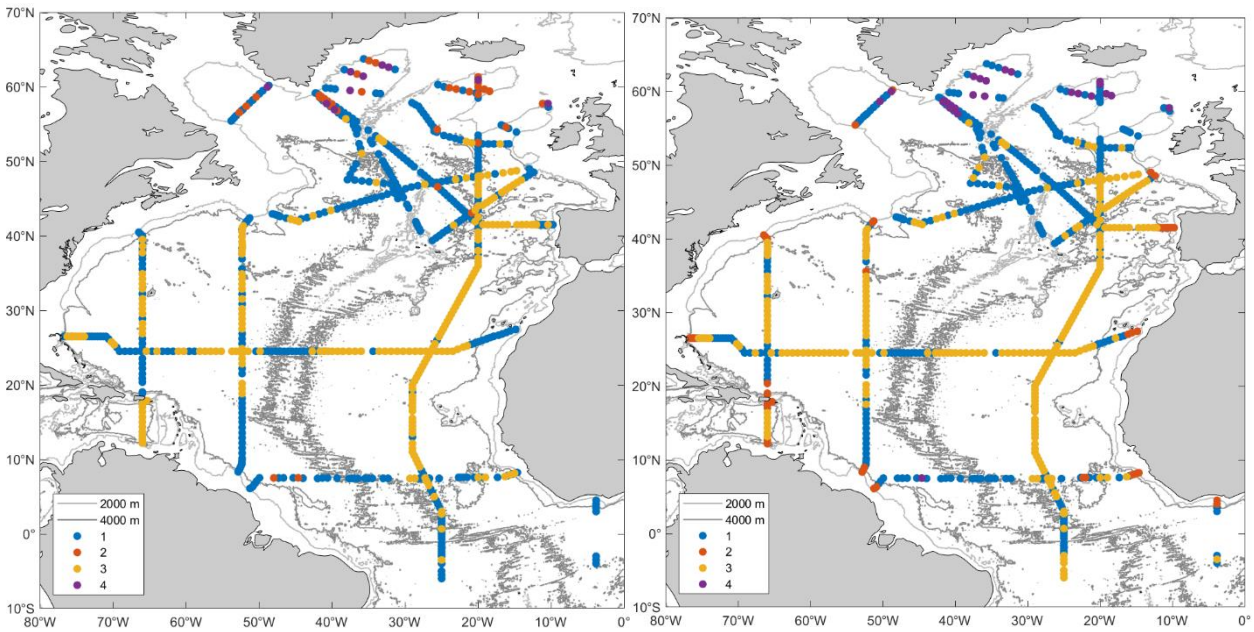

Figure 4.5. The cluster assignments from the k-means algorithm when using the input variables, a) BML thickness, SML thickness, BML N^2, and SML N^2 or b) BML thickness, SML thickness, BML N^2, SML N^2, seafloor slope, and seafloor roughness.

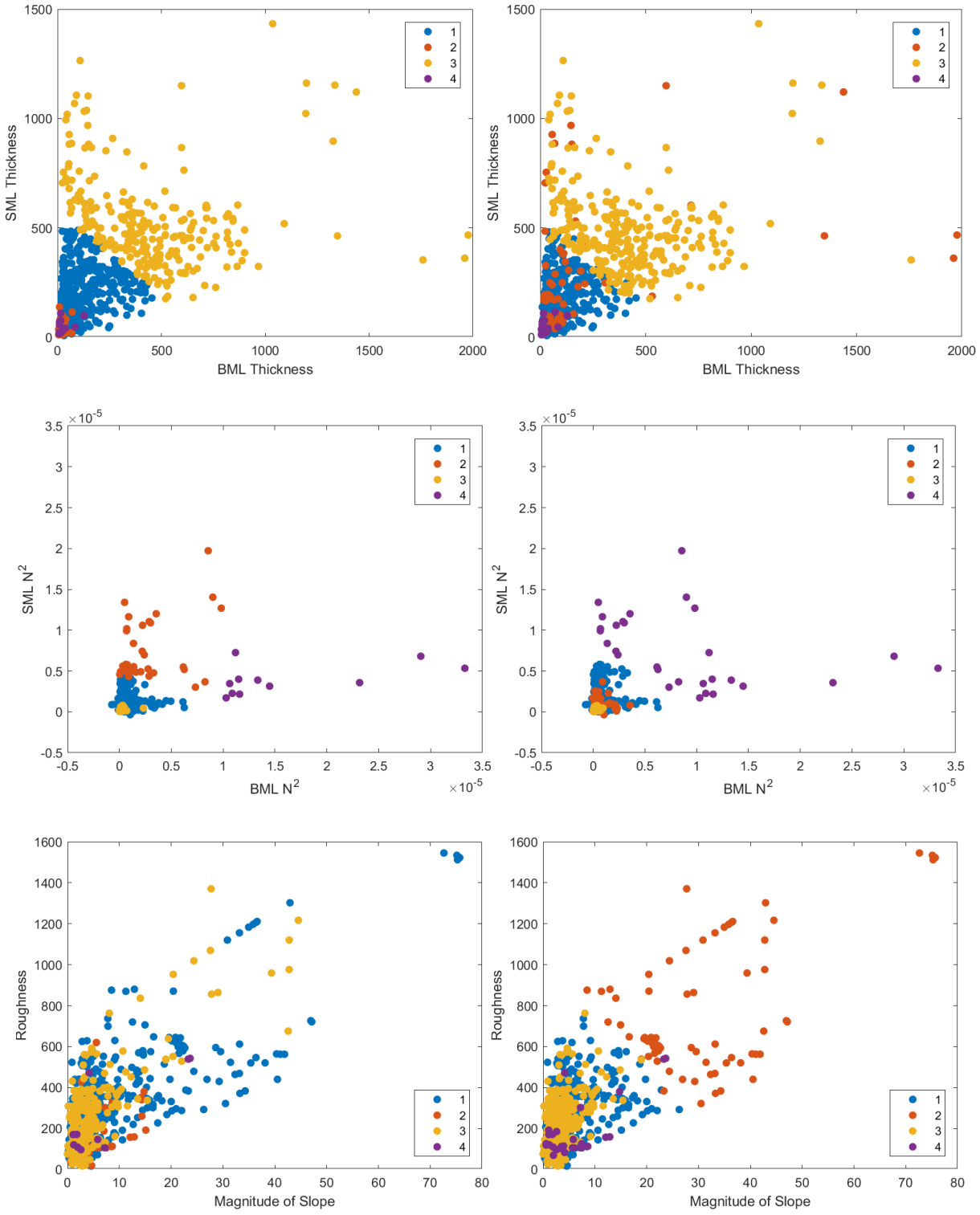

Figure 4.6. For the 702 profiles in our dataset, the distributions of a, b) BML thickness and SML thickness, c, d) BML N^2 and SML N^2, and e, f) seafloor slope and roughness, with the cluster assignments from either the run with 4 variables (a, c, e) or with 6 variables (b, d, f).

To further investigate the relationships between the BML and SML properties and the bottom topography, we performed another k-means clustering with 4 clusters with the bottom slope and roughness at the profile locations now included in the input variables as well (Figures 4.5b, 4.6b, 4.6d, and 4.6f). Cluster 3 in this set of results look similar to that of the cluster 3 from the previous set of clusters, generally containing profiles that are exponential-like with thick BMLs and/or thick SMLs that are relatively unstratified. However, here this cluster is further limited to profiles that lie over a flat bottom (with no strong correlation to roughness), which only removes a handful of profiles from the prior version of this cluster. Here, cluster 4 is a combination of clusters 2 and 4 from the previous set of clusters, containing profiles with very thin BMLs and SMLs where either the BML N^2 or the SML N^2 value is especially large. The profiles in cluster 4 are generally found over relatively flat and smooth bathymetry. Cluster 2 contains the profiles found over the steepest and roughest bathymetry sampled by our dataset. These profiles contain BMLs that are generally thin and weakly stratified, and SMLs that are also weakly stratified and of variable thickness. Cluster 1 is again a "catch-all" cluster to a degree, containing profiles with either a BML or a SML that is more stratified than those found in the cluster 2 profiles but less stratified than those in cluster 4. The profiles in cluster 1 contain BMLs and SMLs with moderate thicknesses and are located over moderately rough bathymetry compared to the other clusters.

4.4 DISCUSSION

In previous observational analyses of the bottom mixed layer, profiles within a given basin were generally classified into one of two types: 1) thick, well-mixed BMLs found over the flatter and smoother abyssal plains and 2) thinner, more stratified BMLs found over the sloped and often rougher bathymetry of the basin boundaries (e.g., mid-ocean ridges or the continental margins).

Here, we find that while this simple dichotomy holds to first order there are additional dynamical regimes of interest that are highlighted by using our approach for examining the BML and SML. For example, in the region of turbulent flow of AABW from the Brazil Basin to the Guiana Basin (B18; Chapter 3) the BMLs are anomalously thin in the interior. Additionally, throughout the northern North Atlantic basins, the BMLs and SMLs are always relatively thin with one of these layers substantially more stratified than the other (i.e., clusters 2 and 4 from the clustering for the profile-based parameter set).

The differences between the BML thickness observed here and those found by B18 can be attributed to either the differences in the BML detection algorithms or in the datasets used. Our split-and-merge method may be more appropriate for usage across a large region such as the North Atlantic since the effective density gradient threshold changes with each profile while the method of B18 uses a set value for all profiles. The identification of much thinner BMLs in the northern North Atlantic basins and over some of the Hatteras Abyssal Plain in this work is likely due to a difference in data quality since we only used profiles that extended to within 50 meters of the seafloor while B18 used all profiles in the World Ocean Database 2013 (https://www.nodc.noaa.gov/OC5/WOD13), many of which do not reach this close to the seafloor. This could explain why their dataset may not capture the < 100-meter-thick BMLs we found in these basins.

Based on previous theoretical and modeling studies, the combination of properties that is needed for diapycnal upwelling to occur within the BML is a significant bathymetric slope along with a SML that is more stratified than the BML. We do find a number of profiles in clusters 1 and 2 from both clusterings that fit these criteria (though there are also some in these clusters that do

not). We had hoped that these diapycnal upwelling-favorable BMLs would emerge as a single cluster in our analysis but this was not the case.

While this dataset spans a number of interesting dynamical regimes in the North Atlantic (e.g., deep western boundary current, sites of overflow plumes) it is still a relatively small dataset. In future work we plan to add more CTD profiles from WOCE cruises in the other major ocean basins to, 1) explore whether these BML/SML regimes are unique to the North Atlantic (unlikely), 2) hopefully improve our signal-to-noise ratio for detecting different BML/SML regimes, and 3) potentially augment the set of BML/SML/bathymetry relationships described here with others from processes not well-sampled in this basin (e.g., from geothermal heating).

We also hope to experiment with other clustering methods such as Gaussian mixture models (GMM) and density-based spatial clustering of applications with noise (DBSCAN) which, respectively, may be better equipped to handle transitions between different BML regimes and noisy oceanographic data than k-means (Ester et al., 1996; Hastie et al., 2009). Eventually we hope to build a set of relationships relating the BML and SML thickness and stratification values to fields that have previous been mapped to high resolution such as the bottom depth, slope, roughness, and bottom water density (Chapter 3). This could enable us to map these key BML and SML properties with higher accuracy than previous work (e.g., B18) and then use these mapped fields to estimate the amount of potential diapycnal upwelling of bottom waters that is occurring within the turbulent BMLs over sloped topography. While previous work has estimated the dianeutral transports in the BMLs by analyzing the seafloor areas covered by different neutral density surfaces (de Lavergne et al., 2017), this proposed future work would provide additional information about the BML and SML structure that would inform what portion of these seafloor areas actually have BMLs and SMLs with properties conducive to the diapycnal upwelling of

interest. This would provide a critical link between this modeled upwelling pathway and observations of BMLs globally.

4.5 Acknowledgements

We thank all those who participated in the collection, calibration, processing, and archiving of the CTD data during the WOCE and CLIVAR-CO_2 programs. Data used in this study can be downloaded from the CCHDO website (https://cchdo.ucsd.edu/). P.D.L. and G.C.J. are supported by Global Ocean Monitoring and Observing (GOMO) Program of the National Oceanic and Atmospheric Administration (NOAA), U.S. Department of Commerce, and NOAA Research. P.D.L. was also supported under the NASA Earth and Space Science Fellowship Program – Grant NNX16AO60H.

Chapter 5. CONCLUSION

This dissertation uses the explosion of in-situ observations from the past few decades to investigate the mean state of a number of important aspects of water-property distributions, ocean circulation, and mixing within the ocean. We introduce a number of new methods to accomplish this, many of which come from the machine learning literature. While we gain a number of new insights through this work, there are a variety of future pathways for the application of these methods to these data in other regions for further analysis of the circulation and mixing regimes of interest.

The main takeaway from Chapter 2 is that the velocity structure of the Alaskan Stream changes substantially over its extent. This current becomes narrower, stronger, and more barotropic to the west. We found that concentration of Pacific Equatorial Water decreases westward in this current, consistent with previous work. However, we were able to determine that this decrease in concentration is not from these waters leaving the current but instead from the increased entrainment of other waters from the interior as this current flows westward. Accurately modeling both the changing transport of the Alaskan Stream and the presence of Pacific Equatorial Water within the current, could be important in work that aims to model the downstream influence of this current on the ecosystem and dynamics of the Bering Sea and Sea of Okhotsk. The approach used here to map Argo and shipboard CTD data to across-current transects could be replicated in other boundary current systems to assess the mean state of those currents.

In Chapter 3, the newly-generated, high-resolution maps of bottom water properties improve upon previous global analyses by highlighting both the importance of small-scale bathymetric features (e.g., sill, fracture zones, and deep submarine canyons) and of regional biogeochemical process on setting global property distributions. For instance, in both the Enderby Basin and the

Bay of Bengal, our analysis reveals that there are two distinct biogeochemical processes influencing the bottom oxygen and nutrient distributions in these basins. We were able to match regions of especially silica-rich waters in both of these basins to highly productive surface regions identified in other work examining surface chlorophyll distributions. Similarly, along the eastern boundary of the Atlantic Ocean, a variety of sources for the oxygen-poor (and sometimes nutrient-rich) waters along the continental shelf are well-illustrated by our maps.

In another example, detailed analysis using our maps of the spreading pathway of bottom water from Cape Darnley, the least well-studied of the four Antarctic sites of bottom water formation, shows that the main export pathway for these waters off of the continental shelf is likely the Mawson Canyon that bisects the continental slope, which is farther west than the previously suggested export pathways. These waters continue westward along the continental slope to ~33°E before leaving the continental boundary to mix with the westward-flowing WSDW along the seafloor in the interior. This location of this separation point is clear on our maps and we found that it coincides with strong downslope along-bottom velocities observed but not described in previous work, lending support to our novel observation of the waters joining the interior at this location.

Examining our climatology in property-property space (e.g., Θ-S_A, O_2-S_A) revealed additional insights about the different named water masses mix along the seafloor. For example, this analysis highlighted that the bottom water in the Cape and Transkei basins is unique, corresponding to the densest of the LCDW-NADW mixtures, which are typically found far above the bottom. Overall, this work gives us a detailed baseline from which to infer changes in the abyssal circulation as the Deep Argo array grows in size and as we continue to sample the deep ocean with the GO-SHIP

program. Furthermore, the mapping procedure here could be used to map other important, sparse datasets near the seafloor such as chlorofluorocarbons.

Though Chapter 3 contains a detailed description of the properties and inferred flows of bottom water along the seafloor, Chapter 4 aims to study the bottom mixed layer (BML) and stratified mixing layer (SML) just above to provide some insight into where these waters might begin their convoluted journey back to the surface by flowing across isopycnals within BMLs over sloped bathymetry. In much of the North Atlantic, our results are consistent with previous work, finding that there are broadly two types of BMLs – thick, well-mixed BMLs over relatively smooth and flat topography and thin, more stratified BMLs found over sloped and sometimes relatively rougher regions of the seafloor. These BMLs generally correspond to the basin interior or the basin boundaries, respectively.

However, in the more northern basins of this region (i.e., in the Labrador, Irminger, and Iceland basins and the Rockall Trough) two additional configurations of BMLs and SMLs appear. In one, the BML is more stratified than the SML though both layers are quite thin. In the other, both layers are again quite thin but the SML is more stratified than the BML (though the BML is sometimes still weakly stratified). These patterns suggest that a simple two-category classification of BMLs may be insufficient for capturing the complex dynamics of these layers. In future work we plan to extend this analysis to other basins and expect to find additional BML/SML regimes such as those related to geothermal heating. Combining the information about these different dynamical regimes, the bottom bathymetry, and our property maps from Chapter 3, should allow us to eventually estimate the amount of diapycnal upwelling occurring in the BMLs globally. Critically, this will provide observational evidence to support the theoretical and modeling work that has suggested this pathway as a means for closing the meridional overturning circulation.

BIBLIOGRAPHY

Aagaard, K., Swift, J. H., & Carmack, E. C. (1985). Thermohaline circulation in the Arctic Mediterranean Seas. *Journal of Geophysical Research*, *90*(C3), 4833. https://doi.org/10.1029/jc090ic03p04833

Alford, M. H., Girton, J. B., Voet, G., Carter, G. S., Mickett, J. B., & Klymak, J. M. (2013). Turbulent mixing and hydraulic control of abyssal water in the Samoan Passage. *Geophysical Research Letters*, *40*(17), 4668–4674. https://doi.org/10.1002/grl.50684

Aoki, S., Fujii, N., Ushio, S., Yoshikawa, Y., Watanabe, S., Mizuta, G., et al. (2008). Deep western boundary current and southern frontal systems of the Antarctic Circumpolar Current southeast of the Kerguelen Plateau. *Journal of Geophysical Research: Oceans*, *113*(8), 8038. https://doi.org/10.1029/2007JC004627

Aoki, S., Katsumata, K., Hamaguchi, M., Noda, A., Kitade, Y., Shimada, K., et al. (2020). Freshening of Antarctic Bottom Water Off Cape Darnley, East Antarctica. *Journal of Geophysical Research: Oceans*, *125*(8), e2020JC016374. https://doi.org/10.1029/2020JC016374

Araujo, M., Noriega, C., & Lefèvre, N. (2014). Nutrients and carbon fluxes in the estuaries of major rivers flowing into the tropical Atlantic. *Frontiers in Marine Science*, *1*, 10. https://doi.org/10.3389/fmars.2014.00010

Arhan, M., Mercier, H., Bourlès, B., & Gouriou, Y. (1998). Hydrographic sections across the Atlantic at 7°30N and 4°30S. Deep-Sea Research Part I: Oceanographic Research Papers, 45(6), 829–872. https://doi.org/10.1016/S0967-0637(98)00001-6

Armi, L., & Millard, R. C. (1976). The bottom boundary layer of the deep ocean. *Journal of Geophysical Research*, *81*(27), 4983–4990. https://doi.org/10.1029/JC081i027p04983

Arthur, D., & Vassilvitskii, S. (2007). k-means++: the advantages of careful seeding. In *Proceedings of the 18th Annual ACM-SIAM Symposium on Discrete Algorithms* (pp. 1027–1035). New Orleans, Louisiana, USA.

Banyte, D., Smeed, D. A., & Morales Maqueda, M. (2018). The Weakly Stratified Bottom Boundary Layer of the Global Ocean. *Journal of Geophysical Research: Oceans*, *123*(8), 5587–5598. https://doi.org/10.1029/2018JC013754

Beaird, N. L., Rhines, P. B., & Eriksen, C. C. (2013). Overflow Waters at the Iceland–Faroe Ridge Observed in Multiyear Seaglider Surveys. *Journal of Physical Oceanography*, *43*(11), 2334–2351. https://doi.org/10.1175/JPO-D-13-029.1

Beal, L. M., Ffield, A., & Gordon, A. L. (2000). Spreading of Red Sea overflow waters in the Indian Ocean. *Journal of Geophysical Research: Oceans*, *105*(C4), 8549–8564. https://doi.org/10.1029/1999JC900306

Berg, R. D., Solomon, E. A., & Teng, F. Z. (2019). The role of marine sediment diagenesis in the modern oceanic magnesium cycle. *Nature Communications*, *10*(1), 1–10. https://doi.org/10.1038/s41467-019-12322-2

Björk, G., Jakobsson, M., Rudels, B., Swift, J. H., Anderson, L., Darby, D. A., et al. (2007).

Bathymetry and deep-water exchange across the central Lomonosov Ridge at 88–89°N. *Deep Sea Research Part I: Oceanographic Research Papers*, *54*(8), 1197–1208. https://doi.org/10.1016/J.DSR.2007.05.010

Bluhm, B. A., Kosobokova, K. N., & Carmack, E. C. (2015). A tale of two basins: An integrated physical and biological perspective of the deep Arctic Ocean. *Progress in Oceanography*, *139*, 89–121. https://doi.org/10.1016/J.POCEAN.2015.07.011

Boswell, S. M., & Smythe-Wright, D. (2002). The tracer signature of Antarctic Bottom Water and its spread in the Southwest Indian Ocean: Part I - CFC-derived translation rate and topographic control around the Southwest Indian Ridge and the Conrad Rise. *Deep-Sea Research Part I: Oceanographic Research Papers*, *49*(3), 555–573. https://doi.org/10.1016/S0967-0637(01)00066-8

Bower, A., & Furey, H. (2017). Iceland-Scotland Overflow Water transport variability through the Charlie-Gibbs Fracture Zone and the impact of the North Atlantic Current. *Journal of Geophysical Research: Oceans*, *122*(9), 6989–7012. https://doi.org/10.1002/2017JC012698

Boyer, T. P., Antonov, J. I., Baranova, O. K., Coleman, C., Garcia, H. E., Grodsky, A., et al. (2013). World Ocean Database 2013. *Sydney Levitus, Ed.; Alexey Mishonoc, Technical Ed.*, *NOAA Atlas*(72), 209 pp. https://doi.org/http://doi.org/10.7289/V5NZ85MT

Boyer, T. P., Garcia, H. E., Locarnini, R. A., Zweng, M. M., Mishonov, A. V., Reagan, J. R., et al. (2018). World Ocean Atlas 2018. NOAA National Centers for Environmental Information. Dataset. https://accession.nodc.noaa.gov/NCEI-WOA18.

Breiman, L. (2001). Random Forests. *Machine Learning*, *45*(1), 5–32. https://doi.org/10.1023/A:1010933404324

Bretherton, F. P., Davis, R. E., & Fandry, C. B. (1976). A technique for objective analysis and design of oceanographic experiments applied to MODE-73. *Deep Sea Research and Oceanographic Abstracts*, *23*(7), 559–582. https://doi.org/10.1016/0011-7471(76)90001-2

Broecker, W. S., Blanton, S., Smethie, W. M., & Ostlund, G. (1991). Radiocarbon decay and oxygen utilization in the Deep Atlantic Ocean. *Global Biogeochemical Cycles*, *5*(1), 87–117. https://doi.org/10.1029/90GB02279

Budillon, G., & Spezie, G. (2000). Thermohaline structure and variability in the Terra Nova Bay polynya, Ross Sea. *Antarctic Science*, *12*(4), 493–508. https://doi.org/10.1017/s0954102000000572

Carmack, E. C., & Foster, T. D. (1975). On the flow of water out of the Weddell Sea. *Deep-Sea Research and Oceanographic Abstracts*, *22*(11), 711–724. https://doi.org/10.1016/0011-7471(75)90077-7

Carmack, E. C., Williams, W. J., Zimmermann, S. L., & McLaughlin, F. A. (2012). The Arctic Ocean warms from below. *Geophysical Research Letters*, *39*(7), L07604. https://doi.org/10.1029/2012GL050890

Carr, M. E. (2001). Estimation of potential productivity in Eastern Boundary Currents using remote sensing. *Deep-Sea Research Part II: Topical Studies in Oceanography*, *49*(1–3), 59–80. https://doi.org/10.1016/S0967-0645(01)00094-7

Carr, M. E., & Kearns, E. J. (2003). Production regimes in four Eastern Boundary Current systems. *Deep-Sea Research Part II: Topical Studies in Oceanography*, *50*(22–26), 3199–3221. https://doi.org/10.1016/j.dsr2.2003.07.015

Chang, Y. S., Garraffo, Z. D., Peters, H., & Özgökmen, T. M. (2009). Pathways of Nordic Overflows from climate model scale and eddy resolving simulations. *Ocean Modelling*, *29*(1), 66–84. https://doi.org/10.1016/J.OCEMOD.2009.03.003

Chen, S., & Firing, E. (2006). Currents in the Aleutian Basin and subarctic North Pacific near the dateline in summer 1993. *Journal of Geophysical Research: Oceans*, *111*(3), C03001. https://doi.org/10.1029/2005JC003064

Cleveland, W. S., & Devlin, S. J. (1988). Locally Weighted Regression: An Approach to Regression Analysis by Local Fitting. *Journal of the American Statistical Association*, *83*(403), 596. https://doi.org/10.2307/2289282

Connary, S. D., & Ewing, M. (1974). Penetration of Antarctic bottom water from the Cape Basin into the Angola Basin. *Journal of Geophysical Research*, *79*(3), 463–469. https://doi.org/10.1029/JC079i003p00463

Crawford, W. R., Cherniawsky, J. Y., & Foreman, M. G. G. (2000). Multi-year meanders and eddies in the Alaskan Stream as observed by TOPEX/Poseidon altimeter. *Geophysical Research Letters*, *27*(7), 1025–1028. https://doi.org/10.1029/1999GL002399

Davis, R. E. (2005). Intermediate-Depth Circulation of the Indian and South Pacific Oceans Measured by Autonomous Floats. *Journal of Physical Oceanography*, *35*(5), 683–707. https://doi.org/10.1175/JPO2702.1

Deacon, G. E. R. (1979). The Weddell gyre. *Deep Sea Research Part A, Oceanographic Research Papers*, *26*(9), 981–995. https://doi.org/10.1016/0198-0149(79)90044-X

Desbruyères, D. G., Purkey, S. G., McDonagh, E. L., Johnson, G. C., & King, B. A. (2016). Deep and abyssal ocean warming from 35 years of repeat hydrography. *Geophysical Research Letters*, *43*(19), 10,356-10,365. https://doi.org/10.1002/2016GL070413

Dickson, R. R., & Brown, J. (1994). The production of North Atlantic Deep Water: Sources, rates, and pathways. *Journal of Geophysical Research*, *99*(C6), 12319. https://doi.org/10.1029/94JC00530

Donohue, K. A., & Toole, J. M. (2003). A near-synoptic survey of the Southwest Indian Ocean. *Deep-Sea Research Part II: Topical Studies in Oceanography*, *50*(12–13), 1893–1931. https://doi.org/10.1016/S0967-0645(03)00039-0

Donohue, K. A., Hufford, G. E., & McCartney, M. S. (1999). Sources and transport of the Deep Western Boundary Current East of the Kerguelen Plateau. *Geophysical Research Letters*, *26*(7), 851–854. https://doi.org/10.1029/1999GL900099

Douglas, D. H., & Peucker, T. K. (1973). Algorithms for the reduction of the number of points required to represent a digitized line or its caricature. *Cartographica: The International Journal for Geographic Information and Geovisualization*, *10*(2), 112–122. https://doi.org/10.3138/fm57-6770-u75u-7727

de Lavergne, C., Madec, G., Capet, X., Maze, G., & Roquet, F. (2016). Getting to the bottom of the ocean. *Nature Geoscience*. Nature Publishing Group. https://doi.org/10.1038/ngeo2850

de Lavergne, C., Madec, G., Le Sommer, J., Nurser, A. J. G., & Naveira Garabato, A. C. (2016). On the Consumption of Antarctic Bottom Water in the Abyssal Ocean. *Journal of Physical Oceanography*, *46*(2), 635–661. https://doi.org/10.1175/JPO-D-14-0201.1

de Lavergne, C., Madec, G., Roquet, F., Holmes, R. M., & McDougall, T. J. (2017). Abyssal ocean overturning shaped by seafloor distribution. *Nature*, *551*(7679), 181–186. https://doi.org/10.1038/nature24472

Edmond, J. M. (1970). Comments on the paper by T. L. Ku, Y. H. Li, G. G. Mathieu, and H. K. Wong, "Radium in the Indian-Antarctic Ocean south of Australia." *Journal of Geophysical Research*, *75*(33), 6878–6883. https://doi.org/10.1029/jc075i033p06878

Edmond, J. M., Chung, Y., & Sclater, J. G. (1971). Pacific Bottom Water: Penetration east around Hawaii. *Journal of Geophysical Research*, *76*(33), 8089–8097. https://doi.org/10.1029/JC076i033p08089

Edmond, J. M., Jacobs, S. S., Gordon, A. L., Mantyla, A. W., & Weiss, R. F. (1979). Water column anomalies in dissolved silica over opaline Pelagic sediments and the origin of the deep silica maximum. *Journal of Geophysical Research*, *84*(C12), 7809. https://doi.org/10.1029/JC084iC12p07809

Efron, B., & Stein, C. (1981). The Jackknife Estimate of Variance. *The Annals of Statistics*, *9*(3), 586–596. https://doi.org/10.1214/aos/1176345462

Eldevik, T., Nilsen, J. E. Ø., Iovino, D., Anders Olsson, K., Sandø, A. B., & Drange, H. (2009). Observed sources and variability of Nordic seas overflow. *Nature Geoscience*, *2*(6), 406–410. https://doi.org/10.1038/ngeo518

Ellett, D. J., & Roberts, D. G. (1973). The overflow of Norwegian sea deep water across the wyville-thomson Ridge. *Deep Sea Research and Oceanographic Abstracts*, *20*(9), 819–835. https://doi.org/10.1016/0011-7471(73)90004-1

Ester, M., Kriegel, H.-P., Sander, J., & Xu, X. (1996). *A Density-Based Algorithm for Discovering Clusters in Large Spatial Databases with Noise*. Retrieved from www.aaai.org

Ezer, T., & Oey, L. Y. (2010). The role of the Alaskan Stream in modulating the Bering Sea climate. *Journal of Geophysical Research: Oceans*, *115*(4), C04025. https://doi.org/10.1029/2009JC005830

Fahrbach, E., Harms, S., Rohardt, G., Schröder, M., & Woodgate, R. A. (2001). Flow of bottom water in the northwestern Weddell Sea. *Journal of Geophysical Research: Oceans*, *106*(C2), 2761–2778. https://doi.org/10.1029/2000JC900142

Favorite, F. (1967). The Alaskan Stream. International North Pacific Fisheries Commission Bulletin, 21, 20.

Ferrari, R., Mashayek, A., McDougall, T. J., Nikurashin, M., & Campin, J.-M. (2016). Turning Ocean Mixing Upside Down. *Journal of Physical Oceanography*, *46*(7), 2239–2261. https://doi.org/10.1175/JPO-D-15-0244.1

Ferreira, M. L. de C., & Kerr, R. (2017). Source water distribution and quantification of North Atlantic Deep Water and Antarctic Bottom Water in the Atlantic Ocean. *Progress in Oceanography*, *153*, 66–83. https://doi.org/10.1016/J.POCEAN.2017.04.003

Fleischmann, U., Hildebrandt, H., Putzka, A., & Bayer, R. (2001). Transport of newly ventilated deep water from the Iceland Basin to the Westeuropean Basin. *Deep Sea Research Part I: Oceanographic Research Papers*, *48*(8), 1793–1819. https://doi.org/10.1016/S0967-0637(00)00107-2

Foster, T. D., & Carmack, E. C. (1976). Frontal zone mixing and Antarctic Bottom water formation in the southern Weddell Sea. *Deep-Sea Research and Oceanographic Abstracts*, *23*(4), 301–317. https://doi.org/10.1016/0011-7471(76)90872-X

Freeland, H. (2001). Observations of the Flow of Abyssal Water through the Samoa Passage. *Journal of Physical Oceanography*, *31*(8), 2273–2279. https://doi.org/10.1175/1520-0485(2001)031<2273:OOTFOA>2.0.CO;2

Freeland, H. J. (2006). What proportion of the north pacific current finds its way into the Gulf of Alaska? *Atmosphere-Ocean*, *44*(4), 321–330. https://doi.org/10.3137/ao.440401

Fukamachi, Y., Rintoul, S. R., Church, J. A., Aoki, S., Sokolov, S., Rosenberg, M. A., & Wakatsuchi, M. (2010). Strong export of Antarctic Bottom Water east of the Kerguelen plateau. *Nature Geoscience*, *3*(5), 327–331. https://doi.org/10.1038/ngeo842

Giglio, D., Lyubchich, V., & Mazloff, M. R. (2018). Estimating Oxygen in the Southern Ocean Using Argo Temperature and Salinity. *Journal of Geophysical Research: Oceans*, *123*(6), 4280–4297. https://doi.org/10.1029/2017JC013404

Gill, A. E. (1982). *Atmosphere-ocean dynamics* (Vol. 30). Academic Press.

Gille, S. T., Yale, M. M., & Sandwell, D. T. (2000). Global correlation of mesoscale ocean variability with seafloor roughness from satellite altimetry. *Geophysical Research Letters*, *27*(9), 1251–1254. https://doi.org/10.1029/1999GL007003

Gordon, A. L. (1966). Potential temperature, oxygen and circulation of bottom water in the Southern Ocean. *Deep-Sea Research and Oceanographic Abstracts*, *13*(6), 1125–1138. https://doi.org/10.1016/0011-7471(66)90704-2

Gordon, A. L. (1972). Spreading of Antarctic Bottom Waters, II. In *Studies in Physical Oceanography— a tribute of George Wüst on his 80th birthday* (Vol. II, pp. 1–17). New York: Gordon and Breach.

Gordon, A. L., & Tchernia, P. L. (1972). Waters of the continental margin off Adélie Coast, Antarctica. In D. E. Hayes (Ed.), *Antarctic Oceanology II: The Australian-New Zealand Sector, Antarct. Res. Ser., vol. 19* (pp. 59–69). Washington, D.C.: American Geophysical Union (AGU). https://doi.org/10.1029/AR019p0059

Gordon, A. L., Visbeck, M., & Huber, B. (2001). Export of Weddell Sea Deep and Bottom Water. *Journal of Geophysical Research: Oceans*, *106*(C5), 9005–9017. https://doi.org/10.1029/2000jc000281

Gordon, A. L., Giulivi, C. F., Takahashi, T., Sutherland, S., Morrison, J., & Olson, D. (2002).

Bay of Bengal nutrient-rich benthic layer. *Deep-Sea Research Part II: Topical Studies in Oceanography*, *49*(7–8), 1411–1421. https://doi.org/10.1016/S0967-0645(01)00161-8

Gordon, A. L., Giulivi, C. F., & Ilahude, A. G. (2003). Deep topographic barriers within the Indonesian seas. *Deep Sea Research Part II: Topical Studies in Oceanography*, *50*(12–13), 2205–2228. https://doi.org/10.1016/S0967-0645(03)00053-5

Gordon, A. L., Orsi, A. H., Muench, R., Huber, B. A., Zambianchi, E., & Visbeck, M. (2009). Western Ross Sea continental slope gravity currents. *Deep-Sea Research Part II: Topical Studies in Oceanography*, *56*(13–14), 796–817. https://doi.org/10.1016/j.dsr2.2008.10.037

Gouretski, V. (1999). The Large-Scale Thermohaline Structure of the Ross Gyre. In G. Spezie & G. M. R. Manzella (Eds.), Oceanography of the Ross Sea Antarctica (pp. 77–100). Springer, Milan. https://doi.org/10.1007/978-88-470-2250-8_6

Hansen, B., & Østerhus, S. (2007). Faroe Bank Channel overflow 1995–2005. *Progress in Oceanography*, *75*(4), 817–856. https://doi.org/10.1016/J.POCEAN.2007.09.004

Hanz, U., Wienberg, C., Hebbeln, D., Duineveld, G., Lavaleye, M., Juva, K., et al. (2019). Environmental factors influencing benthic communities in the oxygen minimum zones on the Angolan and Namibian margins. *Biogeosciences*, *16*(22), 4337–4356. https://doi.org/10.5194/bg-16-4337-2019

Harvey, J., & Arhan, M. (1988). The Water Masses of the Central North Atlantic in 1983–84. *Journal of Physical Oceanography*, *18*(12), 1855–1875. https://doi.org/10.1175/1520-0485(1988)018<1855:TWMOTC>2.0.CO;2

Hastie, T., Tibshirani, R., & Friedman, J. (2009). *The Elements of Statistical Learning. Data Mining, Inference,and Prediction. Springer Series in Statistics*.

Hautala, S. L. (2018). The abyssal and deep circulation of the Northeast Pacific Basin. *Progress in Oceanography*, *160*, 68–82. https://doi.org/10.1016/j.pocean.2017.11.011

Hautala, S. L., & Hammond, D. E. (2020). Abyssal Pathways and the Double Silica Maximum in the Northeast Pacific Basin. *Geophysical Research Letters*, *47*(19), e2020GL089010. https://doi.org/10.1029/2020GL089010

Heath, G. R. (1974). Dissolved Silica and Deep-Sea Sediments. In W. W. Hay (Ed.), *Studies in Paleo-Oceanography* (pp. 77–93). SEPM (Society for Sedimentary Geology). https://doi.org/10.2110/pec.74.20.0077

Heywood, K. J., Sparrow, M. D., Brown, J., & Dickson, R. R. (1999). Frontal structure and Antarctic Bottom Water flow through the Princess Elizabeth Trough, Antarctica. *Deep-Sea Research Part I: Oceanographic Research Papers*, *46*(7), 1181–1200. https://doi.org/10.1016/S0967-0637(98)00108-3

Holliday, N. P., Pollard, R. T., Read, J. F., & Leach, H. (2000). Water mass properties and fluxes in the Rockall Trough, 1975–1998. *Deep Sea Research Part I: Oceanographic Research Papers*, *47*(7), 1303–1332. https://doi.org/10.1016/S0967-0637(99)00109-0

Hoppema, M., Klatt, O., Roether, W., Fahrbach, E., Bulsiewicz, K., Rodehacke, C., & Rohardt, G. (2001). Prominent renewal of Weddell Sea Deep Water from a remote source. *Journal of*

Marine Research, *59*(2), 257–279. https://doi.org/10.1357/002224001762882655

Hossain, M. S., Sarker, S., Sharifuzzaman, S. M., & Chowdhury, S. R. (2020). Primary productivity connects hilsa fishery in the Bay of Bengal. Scientific Reports, 10(1), 1–16. https://doi.org/10.1038/s41598-020-62616-5

Huhn, O., Hellmer, H. H., Rhein, M., Rodehacke, C., Roether, W., Schodlok, M. P., & Schröder, M. (2008). Evidence of deep- and bottom-water formation in the western Weddell Sea. *Deep-Sea Research Part II: Topical Studies in Oceanography*, *55*(8–9), 1098–1116. https://doi.org/10.1016/j.dsr2.2007.12.015

Ikeda, M., Tanaka, S. S., & Watanabe, Y. W. (2018). Circulation patterns in the lower Arctic Ocean derived from geochemical data. *Journal of Oceanography*, *74*(5), 453–470. https://doi.org/10.1007/s10872-018-0472-2

IOC, SCOR, & IAPSO. (2010). The international thermodynamic equation of seawater – 2010: Calculation and use of thermodynamic properties. *Intergovernmental Oceanographic Commission, Manuals and Guides*, 196 pp.

Jackett, D. R., & McDougall, T. J. (1997). A neutral density variable for the world's oceans. *Journal of Physical Oceanography*, *27*(2), 237–263. https://doi.org/10.1175/1520-0485(1997)027<0237:ANDVFT>2.0.CO;2

Jacobs, S. S., & Georgi, D. T. (1977). Observations on the southwest Indian/Antarctic Ocean. In M. Angel (Ed.), *Voyage of discovery* (pp. 43–85). New York: Pergamon Press.

Jacobs, S. S., Amos, A. F., & Bruchhausen, P. M. (1970). Ross Sea oceanography and Antarctic Bottom Water formation. *Deep-Sea Research and Oceanographic Abstracts*, *17*(6), 935–962. https://doi.org/10.1016/0011-7471(70)90046-X

Jain, V., Shankar, D., Vinayachandran, P. N., Kankonkar, A., Chatterjee, A., Amol, P., et al. (2017). Evidence for the existence of Persian Gulf Water and Red Sea Water in the Bay of Bengal. Climate Dynamics, 48(9–10), 3207–3226. https://doi.org/10.1007/s00382-016-3259-4

Johnson, G. C. (2008). Quantifying Antarctic Bottom Water and North Atlantic Deep Water volumes. *Journal of Geophysical Research*, *113*(C5), C05027. https://doi.org/10.1029/2007JC004477

Johnson, G. C., & Toole, J. M. (1993). Flow of deep and bottom waters in the Pacific at 10°N. *Deep-Sea Research Part I*, *40*(2), 371–394. https://doi.org/10.1016/0967-0637(93)90009-R

Johnson, G. C., Warren, B. A., & Olson, D. B. (1991). A deep boundary current in the Arabian Basin. *Deep Sea Research Part A, Oceanographic Research Papers*, *38*(6), 653–661. https://doi.org/10.1016/0198-0149(91)90004-Y

Johnson, G. C., Musgrave, D. L., Warren, B. A., Ffield, A., & Olson, D. B. (1998). Flow of bottom and deep water in the Amirante Passage and Mascarene Basin. *Journal of Geophysical Research: Oceans*, *103*(C13), 30973–30984. https://doi.org/10.1029/1998JC900027

Johnson, G. C., Schmidtko, S., & Lyman, J. M. (2012). Relative contributions of temperature

and salinity to seasonal mixed layer density changes and horizontal density gradients. *Journal of Geophysical Research: Oceans*, *117*, C04015. https://doi.org/10.1029/2011JC007651

Johnson, G. C., McTaggart, K. E., & Wanninkhof, R. (2014). Antarctic Bottom Water temperature changes in the western South Atlantic from 1989 to 2014. *Journal of Geophysical Research: Oceans*, *119*(12), 8567–8577. https://doi.org/10.1002/2014JC010367

Johnson, G. C., Lyman, J. M., & Purkey, S. G. (2015). Informing deep argo array design using argo and full-depth hydrographic section data. *Journal of Atmospheric and Oceanic Technology*, *32*(11), 2187–2198. https://doi.org/10.1175/JTECH-D-15-0139.1

Jones, E. P., Rudels, B., & Anderson, L. G. (1995). Deep waters of the Arctic Ocean: origins and circulation. *Deep-Sea Research Part I*. https://doi.org/10.1016/0967-0637(95)00013-V

Kaneko, I., Takatsuki, Y., Kamiya, H., & Kawae, S. (1998). Water property and current distributions along the WHP-P9 section (137°–142°E) in the western North Pacific. *Journal of Geophysical Research: Oceans*, *103*(C6), 12959–12984. https://doi.org/10.1029/97JC03761

Kanzow, T., & Zenk, W. (2014). Structure and transport of the Iceland Scotland Overflow plume along the Reykjanes Ridge in the Iceland Basin. *Deep Sea Research Part I: Oceanographic Research Papers*, *86*, 82–93. https://doi.org/10.1016/J.DSR.2013.11.003

Karstensen, J., Stramma, L., & Visbeck, M. (2008). Oxygen minimum zones in the eastern tropical Atlantic and Pacific oceans. *Progress in Oceanography*, *77*(4), 331–350. https://doi.org/10.1016/j.pocean.2007.05.009

Kawabe, M., Fujio, S., & Yanagimoto, D. (2003). Deep-water circulation at low latitudes in the western North Pacific. *Deep-Sea Research Part I: Oceanographic Research Papers*, *50*(5), 631–656. https://doi.org/10.1016/S0967-0637(03)00040-2

Kersalé, M., Perez, R. C., Speich, S., Meinen, C. S., Lamont, T., Le Hénaff, M., et al. (2019). Shallow and Deep Eastern Boundary Currents in the South Atlantic at 34.5°S: Mean Structure and Variability. *Journal of Geophysical Research: Oceans*, *124*(3), 1634–1659. https://doi.org/10.1029/2018JC014554

Kitade, Y., Shimada, K., Tamura, T., Williams, G. D., Aoki, S., Fukamachi, Y., et al. (2014). Antarctic Bottom Water production from the Vincennes Bay Polynya, East Antarctica. *Geophysical Research Letters*, *41*(10), 3528–3534. https://doi.org/10.1002/2014GL059971

Komaki, K., & Kawabe, M. (2009). Deep-circulation current through the Main Gap of the Emperor Seamounts Chain in the North Pacific. *Deep-Sea Research Part I: Oceanographic Research Papers*, *56*(3), 305–313. https://doi.org/10.1016/j.dsr.2008.10.006

Kouketsu, S., Doi, T., Kawano, T., Masuda, S., Sugiura, N., Sasaki, Y., et al. (2011). Deep ocean heat content changes estimated from observation and reanalysis product and their influence on sea level change. *Journal of Geophysical Research: Oceans*, *116*(3). https://doi.org/10.1029/2010JC006464

Ladd, C., & Stabeno, P. J. (2009). Freshwater transport from the Pacific to the Bering Sea

through Amukta Pass. *Geophysical Research Letters*, *36*(14), L14608. https://doi.org/10.1029/2009GL039095

St. Laurent, L., Naveira Garabato, A. C., Ledwell, J. R., Thurnherr, A. M., Toole, J. M., & Watson, A. J. (2012). Turbulence and diapycnal mixing in drake passage. *Journal of Physical Oceanography*, *42*(12), 2143–2152. https://doi.org/10.1175/JPO-D-12-027.1

Lebedev, K. V, Yoshinari, H., Maximenko, N. A., & Hacker, P. W. (2007). YoMaHa'07: Velocity data assessed from trajectories of Argo floats at parking level and at the sea surface. *IPRC Technical Note*, *2*(4), 20.

Lebrato, M., & Jones, D. O. B. (2009). Mass deposition event of *Pyrosoma atlanticum* carcasses off Ivory Coast (West Africa). *Limnology and Oceanography*, *54*(4), 1197–1209. https://doi.org/10.4319/lo.2009.54.4.1197

Lentz, S. J., & Trowbridge, J. H. (1991). The Bottom Boundary Layer Over the Northern California Shelf. *Journal of Physical Oceanography*, *21*(8), 1186–1201. https://doi.org/10.1175/1520-0485(1991)021<1186:TBBLOT>2.0.CO;2

Li, J., Heap, A. D., Potter, A., & Daniell, J. J. (2011). Application of machine learning methods to spatial interpolation of environmental variables. *Environmental Modelling & Software*, *26*(12), 1647–1659. https://doi.org/10.1016/j.envsoft.2011.07.004

Locarnini, R. A., Whitworth, T., & Nowlin, W. D. (1993). The importance of the Scotia Sea on the outflow of Weddell Sea Deep Water. *Journal of Marine Research*, *51*(1), 135–153. https://doi.org/10.1357/0022240933223846

Lonsdale, P. (1976). Abyssal circulation of the southeastern Pacific and some geological implications. *Journal of Geophysical Research*, *81*(6), 1163–1176. https://doi.org/10.1029/JC081i006p01163

Lumpkin, R., & Speer, K. (2007). Global Ocean Meridional Overturning. *Journal of Physical Oceanography*, *37*(10), 2550–2562. https://doi.org/10.1175/JPO3130.1

Lyman, J. M., & Johnson, G. C. (2015). Anomalous eddy heat and freshwater transport in the Gulf of Alaska. *Journal of Geophysical Research: Oceans*, *120*(2), 1397–1408. https://doi.org/10.1002/2014JC010252

MacCready, P., & Rhines, P. B. (1991). Buoyant inhibition of Ekman transport on a slope and its effect on stratified spin-up. Journal of Fluid Mechanics, 223, 631–661. https://doi.org/10.1017/S0022112091001581

MacCready, P., Johns, W. E., Rooth, C. G., Fratantoni, D. M., & Watlington, R. A. (1999). Overflow into the deep Caribbean: Effects of plume variability. *Journal of Geophysical Research: Oceans*, *104*(C11), 25913–25935. https://doi.org/10.1029/1999JC900206

MacKinnon, J. A., Johnston, T. M. S., & Pinkel, R. (2008). Strong transport and mixing of deep water through the Southwest Indian Ridge. *Nature Geoscience*, *1*(11), 755–758. https://doi.org/10.1038/ngeo340

Mantyla, A. W. (1975). On the potential temperature in the abyssal Pacific Ocean. *Journal of Marine Research*, *33*(3), 341–354.

Mantyla, A. W., & Reid, J. L. (1983). Abyssal characteristics of the World Ocean waters. *Deep Sea Research Part A. Oceanographic Research Papers*, *30*(8), 805–833. https://doi.org/10.1016/0198-0149(83)90002-X

Mantyla, A. W., & Reid, J. L. (1995). On the origins of deep and bottom waters of the Indian Ocean. *Journal of Geophysical Research*, *100*(C2), 2417. https://doi.org/10.1029/94JC02564

Marshall, J., & Speer, K. (2012). Closure of the meridional overturning circulation through Southern Ocean upwelling. *Nature Geoscience*, *5*(3), 171–180. https://doi.org/10.1038/ngeo1391

McCarthy, M. C., Talley, L. D., & Baringer, M. O. (1997). Deep upwelling and diffusivity in the southern central Indian Basin. *Geophysical Research Letters*, *24*(22), 2801–2804. https://doi.org/10.1029/97GL02112

McCartney, M. S. (1992). Recirculating components to the deep boundary current of the northern North Atlantic. *Progress in Oceanography*, *29*(4), 283–383. https://doi.org/10.1016/0079-6611(92)90006-L

McCartney, M. S., & Curry, R. A. (1993). Transequatorial Flow of Antarctic Bottom Water in the Western Atlantic Ocean: Abyssal Geostrophy at the Equator. *Journal of Physical Oceanography*, *23*(6), 1264–1276. https://doi.org/10.1175/1520-0485(1993)023<1264:TFOABW>2.0.CO;2

McCartney, M. S., & Donohue, K. A. (2007). A deep cyclonic gyre in the Australian-Antarctic Basin. *Progress in Oceanography*. Pergamon. https://doi.org/10.1016/j.pocean.2007.02.008

McCartney, M. S., Bennett, S. L., & Woodgate-Jones, M. E. (1991). Eastward Flow through the Mid-Atlantic Ridge at 11°N and Its Influence on the Abyss of the Eastern Basin. *Journal of Physical Oceanography*, *21*(8), 1089–1121. https://doi.org/10.1175/1520-0485(1991)021<1089:efttma>2.0.co;2

McDonagh, E. L., Arhan, M., & Heywood, K. J. (2002). On the circulation of bottom water in the region of the Vema Channel. *Deep Sea Research Part I: Oceanographic Research Papers*, *49*(7), 1119–1139. https://doi.org/10.1016/S0967-0637(02)00016-X

McDougall, T. J., & Krzysik, O. A. (2015). Spiciness. *Journal of Marine Research*, *73*(5), 141–152.

McDougall, T. J., Ferrari, R., McDougall, T. J., & Ferrari, R. (2017). Abyssal Upwelling and Downwelling Driven by Near-Boundary Mixing. *Journal of Physical Oceanography*, *47*(2), 261–283. https://doi.org/10.1175/JPO-D-16-0082.1

Meeuwis, J. M., & Lutjeharms, J. R. (1990). Surface thermal characteristics of the Angola-Benguela front. *South African Journal of Marine Science*, *9*(1), 261–279. https://doi.org/10.2989/025776190784378772

Meijers, A. J. S., Klocker, A., Bindoff, N. L., Williams, G. D., & Marsland, S. J. (2010). The circulation and water masses of the Antarctic shelf and continental slope between 30 and 80°E. *Deep-Sea Research Part II: Topical Studies in Oceanography*, *57*(9–10), 723–737. https://doi.org/10.1016/j.dsr2.2009.04.019

Menezes, V. V., Macdonald, A. M., & Schatzman, C. (2017). Accelerated freshening of Antarctic Bottom Water over the last decade in the Southern Indian Ocean. *Science Advances*, *3*(1), e1601426. https://doi.org/10.1126/sciadv.1601426

Mercier, H., & Morin, P. (1997). Hydrography of the Romanche and Chain Fracture Zones. *Journal of Geophysical Research: Oceans*, *102*(C5), 10373–10389. https://doi.org/10.1029/97JC00229

Mercier, H., Speer, K. G., & Honnorez, J. (1994). Flow pathways of bottom water through the Romanche and Chain fracture zones. *Deep-Sea Research Part I*, *41*(10), 1457–1477. https://doi.org/10.1016/0967-0637(94)90055-8

Meredith, M. P. (2013). Oceanography: Replenishing the abyss. *Nature Geoscience*. Nature Publishing Group. https://doi.org/10.1038/ngeo1743

Meredith, M. P., Locarnini, R. A., Van Scoy, K. A., Watson, A. J., Heywood, K. J., & King, B. A. (2000). On the sources of Weddell Gyre Antarctic Bottom Water. *Journal of Geophysical Research: Oceans*, *105*(C1), 1093–1104. https://doi.org/10.1029/1999jc900263

Meredith, M. P., Garabato, A. C. N., Gordon, A. L., & Johnson, G. C. (2008). Evolution of the Deep and Bottom Waters of the Scotia Sea, Southern Ocean, during 1995–2005. *Journal of Climate*, *21*(13), 3327–3343. https://doi.org/10.1175/2007JCLI2238.1

Mordy, C. W., Stabeno, P. J., Ladd, C., Zeeman, S., Wisegarver, D. P., Salo, S. A., & Hunt, G. L. (2005). Nutrients and primary production along the eastern Aleutian Island Archipelago. *Fisheries Oceanography*, *14*(s1), 55–76. https://doi.org/10.1111/j.1365-2419.2005.00364.x

Morozov, E. G., Tarakanov, R. Y., & Van Haren, H. (2013). Transport of Antarctic bottom water through the Kane Gap, tropical NE Atlantic Ocean. *Ocean Science*, *9*(5), 825–835. https://doi.org/10.5194/os-9-825-2013

Musgrave, D. L., Weingartner, T. J., & Royer, T. C. (1992). Circulation and hydrography in the northwestern Gulf of Alaska. *Deep Sea Research Part A. Oceanographic Research Papers*, *39*(9), 1499–1519. https://doi.org/10.1016/0198-0149(92)90044-T

Nieto, K., & Mélin, F. (2017). Variability of chlorophyll-a concentration in the Gulf of Guinea and its relation to physical oceanographic variables. *Progress in Oceanography*, *151*, 97–115. https://doi.org/10.1016/j.pocean.2016.11.009

Nowlin, W. D., & Zenk, W. (1988). Westward bottom currents along the margin of the South Shetland Island Arc. *Deep Sea Research Part A, Oceanographic Research Papers*, *35*(2), 269–301. https://doi.org/10.1016/0198-0149(88)90040-4

Ohshima, K. I., Fukamachi, Y., Williams, G. D., Nihashi, S., Roquet, F., Kitade, Y., et al. (2013). Antarctic Bottom Water production by intense sea-ice formation in the Cape Darnley polynya. *Nature Geoscience*, *6*(3), 235–240. https://doi.org/10.1038/ngeo1738

Olsen, A., Key, R. M., Van Heuven, S., Lauvset, S. K., Velo, A., Lin, X., et al. (2016). The global ocean data analysis project version 2 (GLODAPv2) - An internally consistent data product for the world ocean. *Earth System Science Data*, *8*(2), 297–323. https://doi.org/10.5194/essd-8-297-2016

Onishi, H., & Ohtani, K. (1999). On seasonal and year to year variation in flow of the Alaskan Stream in the central North Pacific. *Journal of Oceanography*, *55*(5), 597–608. https://doi.org/10.1023/A:1007840802296

Orsi, A. H., Nowlin, W. D., & Whitworth, T. (1993). On the circulation and stratification of the Weddell Gyre. *Deep-Sea Research Part I*, *40*(1), 169–203. https://doi.org/10.1016/0967-0637(93)90060-G

Orsi, A. H., Johnson, G. C., & Bullister, J. L. (1999). Circulation, mixing, and production of Antarctic Bottom Water. *Progress in Oceanography*, *43*(1), 55–109. https://doi.org/10.1016/S0079-6611(99)00004-X

Owens, W. B., & Warren, B. A. (2001). Deep circulation in the northwest corner of the Pacific Ocean. *Deep-Sea Research Part I: Oceanographic Research Papers*, *48*(4), 959–993. https://doi.org/10.1016/S0967-0637(00)00076-5

Polzin, K. L. (1997). Spatial Variability of Turbulent Mixing in the Abyssal Ocean. *Science*, *276*(5309), 93–96. https://doi.org/10.1126/science.276.5309.93

Prants, S. V., Andreev, A. G., Budyansky, M. V., & Uleysky, M. Y. (2015). Impact of the Alaskan Stream flow on surface water dynamics, temperature, ice extent, plankton biomass, and walleye pollock stocks in the eastern Okhotsk Sea. *Journal of Marine Systems*, *151*, 47–56. https://doi.org/10.1016/j.jmarsys.2015.07.001

Pratt, L. J., Voet, G., Pacini, A., Tan, S., Alford, M. H., Carter, G. S., et al. (2019). Pacific Abyssal Transport and Mixing: Through the Samoan Passage versus around the Manihiki Plateau. *Journal of Physical Oceanography*, *49*(6), 1577–1592. https://doi.org/10.1175/JPO-D-18-0124.1

Purkey, S. G., & Johnson, G. C. (2010). Warming of Global Abyssal and Deep Southern Ocean Waters between the 1990s and 2000s: Contributions to Global Heat and Sea Level Rise Budgets. *Journal of Climate*, *23*(23), 6336–6351. https://doi.org/10.1175/2010JCLI3682.1

Purkey, S. G., & Johnson, G. C. (2013). Antarctic Bottom Water Warming and Freshening: Contributions to Sea Level Rise, Ocean Freshwater Budgets, and Global Heat Gain. *Journal of Climate*, *26*(16), 6105–6122. https://doi.org/10.1175/JCLI-D-12-00834.1

Purkey, S. G., Smethie, W. M., Gebbie, G., Gordon, A. L., Sonnerup, R. E., Warner, M. J., & Bullister, J. L. (2018). A Synoptic View of the Ventilation and Circulation of Antarctic Bottom Water from Chlorofluorocarbons and Natural Tracers. *Annual Review of Marine Science*, *10*(1), 503–527. https://doi.org/10.1146/annurev-marine-121916-063414

Purkey, S. G., Johnson, G. C., Talley, L. D., Sloyan, B. M., Wijffels, S. E., Smethie, W., et al. (2019). Unabated Bottom Water Warming and Freshening in the South Pacific Ocean. *Journal of Geophysical Research: Oceans*, *124*(3), 1778–1794. https://doi.org/10.1029/2018JC014775

Qu, T., Girton, J. B., & Whitehead, J. A. (2006). Deepwater overflow through Luzon Strait. *Journal of Geophysical Research*, *111*(C1), C01002. https://doi.org/10.1029/2005JC003139

Quadfasel, D., Fischer, J., Schott, F., & Stramma, L. (1997). Deep water exchange through the Owen Fracture Zone in the Arabian Sea. *Geophysical Research Letters*, *24*(22), 2805–2808.

https://doi.org/10.1029/97GL01544

Reed, R. K. (1984). Flow of the Alaskan Stream and its variations. *Deep Sea Research Part A, Oceanographic Research Papers*, *31*(4), 369–386. https://doi.org/10.1016/0198-0149(84)90090-6

Reed, R. K., & Stabeno, P. J. (1993). The recent return of the Alaskan Stream to Near Strait. *Journal of Marine Research*, *51*(3), 515–527. https://doi.org/10.1357/0022240933224025

Reed, R. K., & Stabeno, P. J. (1994). Flow along and across the Aleutian Ridge. *Journal of Marine Research*, *52*(4), 639–648. https://doi.org/10.1357/0022240943076957

Reed, R. K., & Stabeno, P. J. (1999). A recent full-depth survey of the Alaskan Stream. *Journal of Oceanography*, *55*(1), 79–85. https://doi.org/10.1023/A:1007813206897

Reid, J. L. (1997). On the total geostrophic circulation of the Pacific Ocean: Flow patterns, tracers, and transports. *Progress in Oceanography*. Elsevier Ltd. https://doi.org/10.1016/S0079-6611(97)00012-8

Reid, J. L., & Lynn, R. J. (1971). On the influence of the Norwegian-Greenland and Weddell seas upon the bottom waters of the Indian and Pacific oceans. *Deep-Sea Research and Oceanographic Abstracts*, *18*(11), 1063–1088. https://doi.org/10.1016/0011-7471(71)90094-5

Reid, J. L., Nowlin, W. D., & Patzert, W. C. (1977). On the Characteristics and Circulation of the Southwestern Atlantic Ocean. *Journal of Physical Oceanography*, *7*(1), 62–91. https://doi.org/10.1175/1520-0485(1977)007<0062:otcaco>2.0.co;2

Rintoul, S. R. (1998). On the Origin and Influence of Adélie Land Bottom Water. In S. Jacobs & R. Weiss (Eds.), *Ocean, Ice, and Atmosphere: Interactions at the Antarctic Continental Margin, Antarct. Res. Ser., vol. 75* (pp. 151–171). Washington, D.C.: American Geophysical Union (AGU). https://doi.org/10.1029/AR075p0151

Roden, G. I. (1995). Aleutian Basin of the Bering Sea: Thermohaline, oxygen, nutrient, and current structure in July 1993. *Journal of Geophysical Research*, *100*(C7), 13539. https://doi.org/10.1029/95JC01291

Roden, G. I. (2000). Flow and water property structures between the Bering Sea and Fiji in the summer of 1993. *Journal of Geophysical Research: Oceans*, *105*(C12), 28595–28612. https://doi.org/10.1029/1999jc000030

Rodman, M. R., & Gordon, A. L. (1982). Southern ocean bottom water of the Australian-New Zealand sector. *Journal of Geophysical Research*, *87*(C8), 5771. https://doi.org/10.1029/JC087iC08p05771

Roemmich, D., Hautala, S., & Rudnick, D. (1996). Northward abyssal transport through the Samoan passage and adjacent regions. *Journal of Geophysical Research: Oceans*, *101*(C6), 14039–14055. https://doi.org/10.1029/96JC00797

Roemmich, D., Sherman, J. T., Davis, R. E., Grindley, K., McClune, M., Parker, C. J., et al. (2019). Deep SOLO: A full-depth profiling float for the Argo program. *Journal of Atmospheric and Oceanic Technology*, *36*(10), 1967–1981. https://doi.org/10.1175/JTECH-

D-19-0066.1

Roemmich, D., Alford, M. H., Claustre, H., Johnson, K. S., King, B., Moum, J., et al. (2019). On the future of Argo: A global, full-depth, multi-disciplinary array. *Frontiers in Marine Science*. Frontiers Media S.A. https://doi.org/10.3389/fmars.2019.00439

Rousseeuw, P. J. (1987). Silhouettes: A graphical aid to the interpretation and validation of cluster analysis. *Journal of Computational and Applied Mathematics*, *20*(C), 53–65. https://doi.org/10.1016/0377-0427(87)90125-7

Sarmiento, J. L., Simeon, J., Gnanadesikan, A., Gruber, N., Key, R. M., & Schlitzer, R. (2007). Deep ocean biogeochemistry of silicic acid and nitrate. *Global Biogeochemical Cycles*, *21*(1). https://doi.org/10.1029/2006GB002720

Saunders, P. M. (1994). The flux of overflow water through the Charlie-Gibbs Fracture Zone. *Journal of Geophysical Research*, *99*(C6), 12343. https://doi.org/10.1029/94JC00527

Saunders, P. M. (1996). The Flux of Dense Cold Overflow Water Southeast of Iceland. *Journal of Physical Oceanography*, *26*(1), 85–95. https://doi.org/10.1175/1520-0485(1996)026<0085:TFODCO>2.0.CO;2

Schlosser, P., Bayer, R., Foldvik, A., Gammelsrød, T., Rohardt, G., & Münnich, K. O. (1990). Oxygen 18 and helium as tracers of ice shelf water and water/ice interaction in the Weddell Sea. *Journal of Geophysical Research*, *95*(C3), 3253. https://doi.org/10.1029/JC095iC03p03253

Schmidtko, S., Johnson, G. C., & Lyman, J. M. (2013). MIMOC: A global monthly isopycnal upper-ocean climatology with mixed layers. *Journal of Geophysical Research: Oceans*, *118*(4), 1658–1672. https://doi.org/10.1002/jgrc.20122

Schodlok, M. P., Tomczak, M., & White, N. (1997). Deep sections through the South Australian Basin and across the Australian-Antarctic Discordance. *Geophysical Research Letters*, *24*(22), 2785–2788. https://doi.org/10.1029/97GL01929

Sen Gupta, A., & England, M. H. (2004). Evaluation of interior circulation in a high-resolution global ocean model. Part I: Deep and bottom waters. *Journal of Physical Oceanography*, *34*(12), 2592–2614. https://doi.org/10.1175/jpo2651.1

Shannon, L. V., & Chapman, P. (1991). Evidence of Antarctic bottom water in the Angola Basin at 32°S. *Deep Sea Research Part A, Oceanographic Research Papers*, *38*(10), 1299–1304. https://doi.org/10.1016/0198-0149(91)90028-E

Sherwin, T. J., Aleynik, D., Dumont, E., & Inall, M. E. (2015). Deep drivers of mesoscale circulation in the central Rockall Trough. *Ocean Science*, *11*(3), 343–359. https://doi.org/10.5194/os-11-343-2015

Siedler, G., Zangenberg, N., Onken, R., & Morlière, A. (1992). Seasonal changes in the tropical Atlantic circulation: Observation and simulation of the Guinea Dome. *Journal of Geophysical Research*, *97*(C1), 703. https://doi.org/10.1029/91JC02501

Siedler, G., Holfort, J., Zenk, W., Müller, T. J., & Csernok, T. (2004). Deep-water flow in the Mariana and Caroline Basins. *Journal of Physical Oceanography*, *34*(3), 566–581.

https://doi.org/10.1175/2511.1

Sloyan, B. M. (2006). Antarctic bottom and lower circumpolar deep water circulation in the eastern Indian Ocean. *Journal of Geophysical Research*, *111*(C2), C02006. https://doi.org/10.1029/2005JC003011

Smethie, W. M., Fine, R. A., Putzka, A., & Jones, E. P. (2000). Tracing the flow of North Atlantic Deep Water using chlorofluorocarbons. *Journal of Geophysical Research: Oceans*, *105*(C6), 14297–14323. https://doi.org/10.1029/1999JC900274

Smith, W. H. F., & Sandwell, D. T. (1997). Global Sea Floor Topography from Satellite Altimetry and Ship Depth Soundings. *Science*, *277*(5334), 1956–1962. https://doi.org/10.1126/science.277.5334.1956

Sokolov, S., & Rintoul, S. (2000). Circulation and water masses of the southwest Pacific: WOCE section P11, Papua New Guinea to Tasmania. *Journal of Marine Research*, *58*(2), 223–268. https://doi.org/10.1357/002224000321511151

Sokolov, S., & Rintoul, S. R. (2007). On the relationship between fronts of the Antarctic Circumpolar Current and surface chlorophyll concentrations in the Southern Ocean. *Journal of Geophysical Research*, *112*(C7), C07030. https://doi.org/10.1029/2006JC004072

Stabeno, P. J., & Hristova, H. G. (2014). Observations of the Alaskan Stream near Samalga Pass and its connection to the Bering Sea: 2001–2004. *Deep Sea Research Part I: Oceanographic Research Papers*, *88*, 30–46. https://doi.org/10.1016/j.dsr.2014.03.002

Stabeno, P. J., & Reed, R. K. (1991). Recent lagrangian measurements along the Alaskan stream. *Deep Sea Research Part A. Oceanographic Research Papers*, *38*(3), 289–296. https://doi.org/10.1016/0198-0149(91)90069-R

Stabeno, P. J., & Reed, R. K. (1992). A major circulation anomaly in the western Bering Sea. *Geophysical Research Letters*, *19*(16), 1671–1674. https://doi.org/10.1029/92GL01688

Stabeno, P. J., Kachel, D. G., Kachel, N. B., & Sullivan, M. E. (2005). Observations from moorings in the Aleutian Passes: temperature, salinity and transport. *Fisheries Oceanography*, *14*(s1), 39–54. https://doi.org/10.1111/j.1365-2419.2005.00362.x

Stahr, F. R., & Sanford, T. B. (1999). Transport and bottom boundary layerobservations of the North Atlantic Deep Western Boundary Current at the Blake Outer Ridge. *Deep Sea Research Part II: Topical Studies in Oceanography*, *46*(1–2), 205–243. https://doi.org/10.1016/S0967-0645(98)00101-5

Stommel, H. (1960). *The Gulf Stream*. Berkeley, Calif.: Univ. of Calif. Press.

Stommel, H., & Arons, A. B. (1960). On the abyssal circulation of the world ocean-I. Stationary planetary flow patterns on a sphere. *Deep Sea Research*, *6*, 140–154. https://doi.org/10.1016/0146-6313(59)90065-6

Sverdrup, H. U. (1940). Hydrology, Section 2, discussion. Report B.A.N.Z. In *Antarctic Research Expedition 1921–31* (Series A, pp. 88–126). Oceanography, Part 2, Section 2.

Sverdrup, H. U., Johnson, M. W., & Fleming, R. H. (1942). *The Oceans: Their Physics,*

Chemistry, and General Biology. New York: Prentice Hall.

Swift, J. H. (1984). The circulation of the Denmark Strait and Iceland-Scotland overflow waters in the North Atlantic. *Deep Sea Research Part A. Oceanographic Research Papers*, *31*(11), 1339–1355. https://doi.org/10.1016/0198-0149(84)90005-0

Talley, L. D., Feely, R. A., Sloyan, B. M., Wanninkhof, R., Baringer, M. O., Bullister, J. L., et al. (2016). Changes in Ocean Heat, Carbon Content, and Ventilation: A Review of the First Decade of GO-SHIP Global Repeat Hydrography. *Annual Review of Marine Science*, *8*, 185–215. https://doi.org/10.1146/annurev-marine-052915-100829

Tamsitt, V., Drake, H. F., Morrison, A. K., Talley, L. D., Dufour, C. O., Gray, A. R., et al. (2017). Spiraling pathways of global deep waters to the surface of the Southern Ocean. *Nature Communications*, *8*(1), 172. https://doi.org/10.1038/s41467-017-00197-0

Tang, C. C. L., Ross, C. K., Yao, T., Petrie, B., DeTracey, B. M., & Dunlap, E. (2004). The circulation, water masses and sea-ice of Baffin Bay. *Progress in Oceanography*. https://doi.org/10.1016/j.pocean.2004.09.005

Thomas, G., Purkey, S. G., Roemmich, D., Foppert, A., & Rintoul, S. R. (2020). Spatial Variability of Antarctic Bottom Water in the Australian Antarctic Basin From 2018–2020 Captured by Deep Argo. *Geophysical Research Letters*, *47*(23), e2020GL089467. https://doi.org/10.1029/2020GL089467

Thompson, L., & Johnson, G. C. (1996). Abyssal currents generated by diffusion and geothermal heating over rises. *Deep-Sea Research Part I: Oceanographic Research Papers*, *43*(2), 193–211. https://doi.org/10.1016/0967-0637(96)00095-7

Thomson, R. E., & Fine, I. V. (2003). Estimating Mixed Layer Depth from Oceanic Profile Data. *Journal of Atmospheric and Oceanic Technology*, *20*(2), 319–329. https://doi.org/10.1175/1520-0426(2003)020<0319:EMLDFO>2.0.CO;2

Thomson, R. E., & Krassovski, M. V. (2010). Poleward reach of the California Undercurrent extension. *Journal of Geophysical Research: Oceans*, *115*(9), 1–9. https://doi.org/10.1029/2010JC006280

Tibby, R. B. (1941). The water masses off the west coast of North America. *Journal of Marine Research*, *4*(2), 112–121.

Timmermans, M.-L., Winsor, P., & Whitehead, J. A. (2005). Deep-Water Flow over the Lomonosov Ridge in the Arctic Ocean. *Journal of Physical Oceanography*, *35*(8), 1489–1493. https://doi.org/10.1175/JPO2765.1

Todd, R. E., Rudnick, D. L., Mazloff, M. R., Cornuelle, B. D., & Davis, R. E. (2012). Thermohaline structure in the California Current System: Observations and modeling of spice variance. *Journal of Geophysical Research: Oceans*, *117*, C02008. https://doi.org/10.1029/2011JC007589

Toole, J. M., & Warren, B. A. (1993). A hydrographic section across the subtropical South Indian Ocean. Deep-Sea Research Part I, 40(10), 1973–2019. https://doi.org/10.1016/0967-0637(93)90042-2

Tremblay, J.-É., Gratton, Y., Carmack, E. C., Payne, C. D., & Price, N. M. (2002). Impact of the large-scale Arctic circulation and the North Water Polynya on nutrient inventories in Baffin Bay. *Journal of Geophysical Research*, *107*(C8), 26-1-26–14. https://doi.org/10.1029/2000JC000595

Tsunogai, S., Kusakabe, M., Iizumi, H., Koike, I., & Hattori, A. (1979). Hydrographic features of the deep water of the Bering Sea-the sea of Silica. *Deep Sea Research Part A, Oceanographic Research Papers*, *26*(6), 641–659. https://doi.org/10.1016/0198-0149(79)90038-4

Uehara, H., Kruts, A. A., Mitsudera, H., Nakamura, T., Volkov, Y. N., & Wakatsuchi, M. (2014). Remotely propagating salinity anomaly varies the source of North Pacific ventilation. *Progress in Oceanography*, *126*, 80–97. https://doi.org/10.1016/j.pocean.2014.04.016

Ueno, H., Sato, K., Freeland, H. J., Crawford, W. R., Onishi, H., Oka, E., & Suga, T. (2009). Anticyclonic Eddies in the Alaskan Stream. *Journal of Physical Oceanography*, *39*(4), 934–951. https://doi.org/10.1175/2008JPO3948.1

Van Bennekom, A. J., & Berger, G. W. (1984). Hydrography and silica budget of the Angola Basin. *Netherlands Journal of Sea Research*. Elsevier. https://doi.org/10.1016/0077-7579(84)90047-4

Vangriesheim, A., Pierre, C., Aminot, A., Metzl, N., Baurand, F., & Caprais, J. C. (2009). The influence of Congo River discharges in the surface and deep layers of the Gulf of Guinea. *Deep-Sea Research Part II: Topical Studies in Oceanography*, *56*(23), 2183–2196. https://doi.org/10.1016/j.dsr2.2009.04.002

Vangriesheim, A., Khripounoff, A., & Crassous, P. (2009). Turbidity events observed in situ along the Congo submarine channel. *Deep-Sea Research Part II: Topical Studies in Oceanography*, *56*(23), 2208–2222. https://doi.org/10.1016/j.dsr2.2009.04.004

Voet, G., Alford, M. H., Girton, J. B., Carter, G. S., Mickett, J. B., Klymak, J. M., et al. (2016). Warming and Weakening of the Abyssal Flow through Samoan Passage. *Journal of Physical Oceanography*, *46*(8), 2389–2401. https://doi.org/10.1175/JPO-D-16-0063.1

von Schuckmann, K., Cheng, L., Palmer, M. D., Hansen, J., Tassone, C., Aich, V., et al. (2020). Heat stored in the Earth system: Where does the energy go? *Earth System Science Data*, *12*(3), 2013–2041. https://doi.org/10.5194/essd-12-2013-2020

Warren, B. A. (1978). Bottom water transport through the Southwest Indian Ridge. Deep-Sea Research, 25(3), 315–321. https://doi.org/10.1016/0146-6291(78)90596-9

Warren, B. A. (1981). Deep circulation of the world ocean. In B. A. Warren & C. Wunsch (Eds.), *Evolution of Physical Oceanography* (pp. 6–41). Cambridge, Mass.: MIT Press.

Warren, B. A. (1982). The deep water of the Central Indian Basin. *Journal of Marine Research*, *40*(Suppl.), 823–859.

Warren, B. A., & Johnson, G. C. (2002). The overflows across the Ninetyeast Ridge. *Deep-Sea Research Part II: Topical Studies in Oceanography*, *49*(7–8), 1423–1439. https://doi.org/10.1016/S0967-0645(01)00156-4

Warren, B. A., & Owens, W. B. (1988). Deep Currents in the Central Subarctic Pacific Ocean. *Journal of Physical Oceanography*, *18*(4), 529–551. https://doi.org/10.1175/1520-0485(1988)018<0529:DCITCS>2.0.CO;2

Warren, B. A., & Speer, K. G. (1991). Deep circulation in the eastern South Atlantic Ocean. *Deep Sea Research Part A. Oceanographic Research Papers*, *38*, S281–S322. https://doi.org/10.1016/s0198-0149(12)80014-8

Waterhouse, A. F., Mackinnon, J. A., Nash, J. D., Alford, M. H., Kunze, E., Simmons, H. L., et al. (2014). Global patterns of diapycnal mixing from measurements of the turbulent dissipation rate. *Journal of Physical Oceanography*, *44*(7), 1854–1872. https://doi.org/10.1175/JPO-D-13-0104.1

Weatherly, G. L., & Martin, P. J. (1978). On the structure and dynamics of the oceanic bottom boundary layer. *Journal of Physical Oceanography*, *8*(4, Jul. 1978), 557–570. https://doi.org/10.1175/1520-0485(1978)008<0557:otsado>2.0.co;2

Weatherly, G. L., & Niiler, P. P. (1974). Bottom homogeneous layers in the Florida Current. *Geophysical Research Letters*, *1*(7), 316–319. https://doi.org/10.1029/GL001i007p00316

Whitworth, T., Nowlin, W. D., Pillsbury, R. D., Moore, M. I., & Weiss, R. F. (1991). Observations of the Antarctic Circumpolar Current and deep boundary current in the southwest Atlantic. *Journal of Geophysical Research*, *96*(C8), 15105. https://doi.org/10.1029/91jc01319

Whitworth, T., Warren, B. A., Nowlin, W. D., Rutz, S. B., Pillsbury, R. D., & Moore, M. I. (1999). On the deep western-boundary current in the Southwest Pacific Basin. *Progress in Oceanography*, *43*(1), 1–54. https://doi.org/10.1016/S0079-6611(99)00005-1

Williams, G. D., Aoki, S., Jacobs, S. S., Rintoul, S. R., Tamura, T., & Bindoff, N. L. (2010). Antarctic Bottom Water from the Adélie and George V Land coast, East Antarctica (140–149°E). *Journal of Geophysical Research*, *115*(C4), C04027. https://doi.org/10.1029/2009JC005812

Willis, J. K. (2003). Combining altimetric height with broadscale profile data to estimate steric height, heat storage, subsurface temperature, and sea-surface temperature variability. *Journal of Geophysical Research*, *108*(C9), 3292. https://doi.org/10.1029/2002JC001755

Witte, E. (1902). *Zur Theorie der Strom Kabbelungen* (pp. 484–487). Gaea, Cologne, Germany.

Worthington, L. (1981). The Water Masses of the World Ocean: Some Results of a Fine-Scale Census. In B. A. Warren & C. Wunsch (Eds.), *Evolution of Physical Oceanography, Scientific Surveys in Honor of Henry Stommel* (pp. 42–60). Cambridge, Mass.: MIT Press.

Worthington, L. V. (1953). Oceanographic results of project Skijump I and Skijump II in the Polar Sea, 1951–1952. *Transactions, American Geophysical Union*, *34*(4), 543. https://doi.org/10.1029/TR034i004p00543

Wyrtki, K. (1960). *The surface circulation in the Coral and Tasman Seas* (Tech. Pap.8). Australia: Commonwealth Sci. and Ind. Res. Organ., Div. of Fish. and Oceanogr.

You, Y. (2002). A global ocean climatological atlas of the Turner angle: Implications for double-

diffusion and water-mass structure. *Deep-Sea Research Part I: Oceanographic Research Papers*, *49*(11), 2075–2093. https://doi.org/10.1016/S0967-0637(02)00099-7

Zenk, W., Siedler, G., Lenz, B., & Hogg, N. G. (1999). Antarctic Bottom Water flow through the Hunter Channel. *Journal of Physical Oceanography*, *29*(11), 2785–2801. https://doi.org/10.1175/1520-0485(1999)029<2785:ABWFTT>2.0.CO;2

Zou, S., Lozier, S., Zenk, W., Bower, A., & Johns, W. (2017). Observed and modeled pathways of the Iceland Scotland Overflow Water in the eastern North Atlantic. *Progress in Oceanography*, *159*, 211–222. https://doi.org/10.1016/J.POCEAN.2017.10.003

VITA

Paige D. Lavin

EDUCATION

California Institute of Technology (Caltech), Pasadena, CA
B.S. with Honor: Geophysics; Environmental Science and Engineering (2014)

University of Washington (School of Oceanography), Seattle, WA
MS: Oceanography (2016)

University of Washington (School of Oceanography), Seattle, WA
PhD: Oceanography: Advanced Data Option (expected April 2021)
Graduate Certificate in Climate Science (2019)

PROFESSIONAL EXPERIENCE

• **Graduate Research Assistant** (July 2014-present), School of Oceanography, University of Washington *and* Cooperative Institute for Climate, Ocean, and Ecosystem Studies, Pacific Marine Environmental Laboratory, National Oceanic and Atmospheric Administration (joint appointment)
• **Summer Student Fellow** (June 2013-Aug. 2013), Department of Physical Oceanography, Woods Hole Oceanographic Institution
• **Summer Research Intern** (June 2012-Aug. 2012), Phenomenology, Algorithms, and Software Division, Areté Associates
• **Summer Undergraduate Research Fellow** (June 2011-August 2011), Division of Geological and Planetary Sciences, California Institute of Technology
• **Freshman Summer Research Institute Fellow** (June 2010-July 2010), Division of Geological and Planetary Sciences, California Institute of Technology
• **Summer Research Intern** (June 2009-August 2009), Hopkins Marine Station, Stanford University

AWARDS

• NASA Earth and Space Science Fellowship (2016–2019)
• NSF Antarctica Service Medal (2016)
• Campus Life and Master's Award for Student Government (2013) – California Institute of Technology

FIELDWORK

• R/V New Horizon, 6 Sept-16 Sept, 2011 (10 DAS), Asthenospheric and Lithospheric Broadband Architecture from the California Offshore Region Experiment (ALBACORE) cruise, San Diego-San Diego, CA, OBS watch-stander
• NOAA Ship Ronald H. Brown, 30 Dec, 2016-3 Feb, 2017 (36 DAS), GO-SHIP P18 cruise, Hanga Roa, CL-Punta Arenas, CL, CTD watch-stander, salt analyst, drifter/float deployments

PUBLICATIONS

• **Logan, P. D.**, and G. C. Johnson (2017), Zonal evolution of Alaskan Stream structure and transport quantified with Argo data, *J. Geophys. Res. Ocean., 122(2),* doi:10.1002/2016JC012302

PRESENTATIONS AND POSTERS

• Ocean Sciences Meeting 2020: **Lavin, P.D.**; Johnson, G.C.; *A New Bottom Water Climatology Using a Stacked Random Forest and Objective Mapping Approach*, presentation
• Ocean Sciences Meeting 2020: Thompson, L.; **Lavin, P.D.**; Proistosescu, C.; *Provinces of Air-Sea Interaction in the North Atlantic Ocean*, presentation

• Gateways to the Ocean - A Symposium Celebrating Arnold Gordon's Contributions to Physical Oceanography 2020: **Lavin, P.D.**; Johnson, G.C.; *Tracing Abyssal Flow Pathways in a New Global Bottom Water Climatology*, presentation
• Northwest Climate Conference 2019: **Lavin, P.D.**; Roop, H.; Morgan, H.; Cory, D.; Correll, M.; Kosara, R.; Rofo Hill, J.; Grodnik-Nagle, A.; Purnell, D.; *New Interactive Data Visualizations of Washington's Sea Level Rise Projections Using Tableau*, presentation
• Graduate Climate Conference 2018: **Lavin, P.D.**; Johnson, G.C.; *Random Forests in the Ocean: Using Machine Learning to Improve Our Understanding of the Deep Ocean*, poster
• Ocean Sciences Meeting 2018: **Lavin, P.D.**; Johnson, G.C.; *Bottom Mixed Layer Property Maps Using Machine Learning and Objective Mapping*, presentation
• Graduate Climate Conference 2016: **Logan, P.D.**; Johnson, G.C.; *The Alaskan Stream: Zonal Evolution of Structure and Transport Quantified with Argo Data*, poster
• Ocean Sciences Meeting 2016: **Logan, P.D.**; Johnson, G.C.; *The Alaskan Stream: Zonal Evolution of Structure and Transport Quantified with Argo Data*, presentation
• Ocean Sciences Meeting 2014: **Logan, P.D.**; Bower, A.S.; *Formation and Propagation of Anticyclonic Eddies Near the Tail of the Grand Banks*, poster

OTHER SCIENTIFIC PRODUCTS

• **Lavin, P.D.**; Roop, H.A., Neff, P.D., Morgan, H., Cory, D., Correll, M., Kosara, R., and Norheim, R. (2019), Interactive Washington State Sea Level Rise Data Visualizations. https://cig.uw.edu/our-work/applied-research/wcrp/sea-level-rise-data-visualization/

EDUCATIONAL ACTIVITIES

• Tutor, *Physics Across Oceanography: Fluid Mechanics & Waves*, Susan Hautala, University of Washington, 2016
• Teaching Assistant, *Integrative Oceans (OCEAN 210)*, Curtis Deutsch, University of Washington, 2015
• Teaching Assistant, *Energy and Society (EST 2)*, David Rutledge, California Institute of Technology, 2014
• Teaching Assistant, *Earth and Environment (Ge 1)*, Paul Asimow, California Institute of Technology, 2013

PROFESSIONAL SERVICE ACTIVITIES

• Reviewer, Journal of Geophysical Research - Oceans
• Abstract Committee Chair, Graduate Climate Conference, Pack Forest, WA, 2016, 2018
• Graduate Student Representative, Program on Climate Change Board, University of Washington, 2016-2018
• Committee Member, PCC Graduate Student Steering Committee, University of Washington, 2016-2018
• Committee Member, Society for Women in Marine Science (SWMS) - Seattle Steering Committee, 2017-2021

OUTREACH ACTIVITIES

• Orca Bowl (Regional Ocean Sciences Bowl), Science Judge, University of Washington, 2015-2020
• NOAA Science Camp, Activity Leader, NOAA/PMEL, 2016-2019
• Discover Science Weekend, Activity Leader, Seattle Aquarium, 2016-2018
• AP Environmental Science Classes, Visiting Speaker, Mount Si High School, 2016, 2017
• STEM EXPO, Presenter, Magnuson Park Community Center, 2015
• State Science Olympiad, Dynamic Planet Event Supervisor, Highline College, 2015
• Regional Science Olympiad, Dynamic Planet Event Supervisor, Highline College, 2015, 2016
• Sally Ride Science/Inspire STEM Festival, Workshop Leader, University of Washington-Bothell, 2014, 2015

PROFESSIONAL MEMBERSHIPS

• American Geophysical Union